UNIVERSITÀ
DEGLI STUDI
DI PADOVA

Sede Amministrativa: Università degli Studi di Padova

Dipartimento di Ingegneria Industriale

CORSO DI DOTTORATO DI RICERCA IN: INGEGNERIA INDUSTRIALE

CURRICOLO: INGEGNERIA CHIMICA, MECCANICA E DEI MATERIALI

29 ° CICLO

CCS AND EOR HAZARD ANALYSIS. EXPERIMENTAL INVESTIGATION AND MODELING OF MULTIPHASE CO_2 PRESSURIZED RELEASES.

Coordinatore: Ch.mo Prof. Giovanni Meneghetti

Supervisore: Ch.mo Prof. Giuseppe Maschio

Dottorando : Paolo Mocellin

Abstract

Il presente lavoro muove dalla necessità di colmare alcune lacune esistenti riguardanti l'Analisi Quantitativa di Rischio (AQR) applicata ad infrastrutture di movimentazione di CO_2. La recente diffusione di complessi sistemi per la cattura e lo stoccaggio della CO_2 e per lo spurgo di pozzi petroliferi esausti ha posto il problema di garantire adeguati standard di sicurezza in fase di trasporto mediante pipelines, dato il carattere asfissiante della sostanza movimentata.

Per quanto riguarda l'AQR preliminare e di esercizio applicata al caso della CO_2, essa risente della carenza di modelli ad-hoc e di dati sperimentali di supporto utili allo sviluppo di idonei strumenti di calcolo descrittivi dei fenomeni di rapida depressurizzazione. La CO_2, infatti, è caratterizzata da un peculiare comportamento termodinamico che in fase di depressurizzazione può portare alla comparsa di fase liquida e solida, rendendo di fatto inadatti e imprecisi i modelli tradizionali attualmente disponibili.

Volendo pertanto trattare tali carenze, il lavoro di ricerca ha previsto la raccolta di dati sperimentali relativi a rapide depressurizzazioni di CO_2 nonché la formulazione di un modello comprensivo a scopi di AQR.

L'apparecchiatura sperimentale predisposta ha pertanto consentito di indagare i fenomeni transitori meccanici e termici che seguono ad un rilascio pressurizzato così come fare luce sui meccanismi competitivi di scambio termico che determinano la trasformazione risultante di espansione. I dati relativi a cariche liquide hanno altresì evidenziato le peculiarità derivanti dai meccanismi di cambio di fase sulla determinazione dei profili di pressione e di temperatura all'interno del serbatoio e all'orifizio. Allo scopo di supportare lo sviluppo del modello, sia il coefficiente di scarico che i dettagli sulla trasformazione di espansione sono stati derivati, dipendentemente dalle condizioni di carico del serbatoio.

Il modello proposto si articola in un complesso sistema di equazioni di bilancio unite a specifiche correlazioni utili a descrivere i meccanismi di scambio termico e di transizione di fase che, nel caso della CO_2, possono coinvolgere l'ebollizione, la solidificazione e la sublimazione. Specifiche equazioni di stato per la CO_2 contribuiscono ad una robusta descrizione del fenomeno. È stata dedicata particolare attenzione all'indagine preliminare della fluidodinamica dei moti soggetti a rilevanti gradienti termici nonché al peculiare comportamento della CO_2 in regime di choked flow.

La corrispondenza quantitativa e qualitativa con i dati sperimentali raccolti è buona. Inoltre, il modello ha permesso di ricavare dettagli sul grado di reversibilità dei percorsi di espansione e

sui principali parametri richiesti in fase di AQR quali i profili di pressione e di temperatura, l'evoluzione della portata massiva rilasciata dal sistema e il tempo totale di scarico.

L'estensione del modello a domini su scala reale ha previsto l'indagine dell'incidenza delle condizioni operative, della dimensione della pipeline così come di quella del foro di scarico sull'evoluzione del fenomeno di depressurizzazione. I risultati hanno consentito di fare luce sulle condizioni che determinano la comparsa di fase solida in fase di rilascio, spesso trascurata dai modelli tradizionali.

Diverse simulazioni hanno evidenziato come sia le condizioni operative che la dimensione dell'orifizio rappresentino i parametri chiave nel governare i processi di cambiamento di fase e le modalità di espansione. Inoltre, l'analisi ha consentito di stabilire sotto quali condizioni sia possibile semplificare l'intera modellazione adottando l'ipotesi di isotermia e di scambio termico trascurabile mostrando come pipeline molto lunghe soggette a piccoli fori soddisfino a tali requisiti.

Infine, il perfezionamento del modello mediante l'introduzione di concetti legati sia a fenomeni di non-equilibrio che di processi irreversibili che accompagnano le transizioni di fase, ha mostrato come per pressioni moderate e piccole pipelines ciò sia del tutto superfluo. Negli altri casi, invece, l'adozione di questo approccio supplementare mostra importanti deviazioni nella stima sia della dinamica termica che del tempo totale di scarico.

Table of contents

Introduction

CO_2 handling operations are gaining importance in the worldwide discussion mainly because of the large strategies that are currently being developed to govern the *Global Warming*.

In this sense, the CO_2 is considered one of the most important GHG (*Greenhouse Gas*) since it is also actually emitted in large quantities from anthropogenic sources. These emissions arise mainly from combustion of fossil fuels and biomass in power generation, gasification, industrial processes, natural gas processing, petroleum refining, building and transport sectors.

The deployment of the *Carbon Capture and Storage* (CCS) technique is currently under analysis as a mean of limiting these emissions and so the atmospheric concentration of the CO_2.

The CCS chain is subdivided into three main systems: the system of capture and compression, the transport system and the storage system. This technology therefore involves the handling of the CO_2 to store it in a reservoir, instead of allowing its release to the atmosphere, where it contributes to the Climate Change.

Therefore, an essential element of the CCS chain is the transportation of large amounts of captured CO_2 to the storage site. This is usually achieved by means of large infrastructures mainly consisting of pressurized pipelines that may typically be several hundred kilometers long.

Given the significant amounts of CO_2 involved and because of this substance at high concentrations is an asphyxiant, the safety of CO_2 pipelines is of primarily importance to the public acceptance of CCS as viable means for tackling the impact of the *Global Warming*.

This works moves therefore from the fact that central to QRA (*Quantitative Risk Assessment*) procedure of pressurized pipeline carrying CO_2 is the accurate prediction of the flow parameters concerning an accidental release induced by a rupture. From this point of view, there is naturally the possibility of pipeline rupture that may be driven by many factors like human errors, component failures, corrosion, earthquakes and many others external interferences.

In what concerning the CO_2 releases modeling, it should be underlined the lack of a comprehensive model able to manage all phenomena that are expected to take place during a rapid depressurization. In the case of CO_2 pipeline, the model must be capable of handling multiphase flows also at sonic conditions as well as the peculiar thermodynamic behavior that may invoke the occurrence of the solid phase.

The main target is to have a comprehensive, reliable and easy applicable (from a QRA perspective) model to be used in assessing hazard profiles related to a CO_2 pipeline rapid depressurization.

In this sense, available models lack the whole dynamics and the formation and sublimation of solid CO_2 expect for sophisticated and detailed CFD (*Computational Fluid Dynamic*) simulation that are substantially inappropriate to face the emergencies and the investigation of general scenarios.

The model availability is also still limited by the lack of experimental data that are used to drive the model formulation and its validation. The few accessible experimental series give contradictory results in what concerning the peculiar CO_2 behavior under transient pressure fields and in correspondence of choked flow conditions thus requiring further investigations.

Moving from these considerations, the present study has the aim of covering the existing gaps in what concerning the availability of a descriptive model.

The study is introduced by a detailed theoretical investigation of specific phenomena the CO_2 undergoes when subjected to a rapid depressurization. Examples of these may include the occurrence of multiple choked flow states depending on the established thermodynamic equilibrium (liquid-vapor, solid-vapor) and the investigation of specific thermodynamic pathways that are linked to the solid phase appearance.

A section pertaining to the experimental campaign follows. In this sense the data availability is enhanced by the collection of self-made data series especially linked to moderate pressures (up to 65-70 barg). The experimental arrangement allows for the investigation of different charging states, matching the operative CO_2 conditions. Collected data are then used to support the model development in the assessment of specific discharge and thermodynamic parameters that are needed to close the mathematical structure.

The proposed model, that is the main target of this investigation, is illustrated and discussed in a specific section with details on the adopted assumptions, the mathematical structure and the numerical approach. The structure covers all main mechanisms related to the rapid CO_2 depressurization including phase change mechanisms (boiling, solidification and sublimation), heat transfer and friction effects as well as a reliable thermodynamic description of the expansion pathway to atmospheric conditions.

Results are first checked against the collected laboratory scale experimental data especially in what concerning the prediction of the main depressurization variables requested by the QRA procedure (stagnation and orifice pressure and temperature profiles, mass flow rate evolution, total discharge time).

A model extension oriented to large scale geometries and different orifice sizes and operative conditions is then proposed. Main discharge parameters are analyzed and their sensitivity to variations in the domain and orifice sizes is assessed with specific light on the relative amounts of dense phase produced and the total discharge time.

The mathematical model is then supplemented of some features concerning non-equilibrium phenomena that do not allow for a mere thermodynamic description. Among these the behavior in the spinodal region, the structural entropy increase in the passage across the triple point and the irreversibilities in the phase change mechanisms are investigated. The target is to firstly check if the additional complication is reasonable from the QRA perspective to then move to variations in the release parameters that emerge because of this extended approach.

A final section is dedicated to the model application to some real existing CCS and EOR (*Ehnanced Oil Recovery*) projects worldwide making available the main discharge parameters and profiles for different pipeline lengths and orifice sizes. A specific investigation on the solid CO_2 is performed in addition to the collection of useful comprehensive parameters to be used in QRA studies.

Chapter 1

CCS and EOR QRA's Knowledge Gaps and Worldwide Projects

An overview of current knowledge gaps in the Quantitative Risk Assessment (QRA) studies applied to CO_2 handling operations at large scale is proposed. The implications of the uncertainties on the safety analysis results are therefore discussed with special focus on the modeling step.
The final section lists main worldwide CO_2-CCS (*Carbon Capture and Storage*) and CO_2-EOR (*Enhanced Oil Recovery*) projects.

1.1 Introduction

The CCS (*Carbon Capture and Storage*) technique is an option that is being developed to control CO_2 emissions from large stationary sources.
This solution is comprised of the capture, the transport of the CO_2 and the final storage operations. The intermediate step may involve different media like trucks, trains, ships or pipelines ([1]).
Among these, the transport by pipeline is considered one of the best solutions especially when dealing with large quantities of CO_2 over distances up to 800-1000 km.
The experience gained with transporting CO_2 on large scales is mainly derived by infrastructures located in the USA but it is directly applicable to other regions.
Most CO_2 pipelines, in fact, are situated in areas characterized by very low density population, this influencing the precaution measures taken.
The deployment of CO_2 pipelines in other regions, like in Europe, will be linked to large networks located in very densely populated areas.
IPPC on CCS has underlined the lack of safety experience in what concerning the operation of CO_2 pipelines in densely populated regions as a gap in the knowledge ([2]).

1.2 Safety Gaps in CO_2 Pipelines Management

Safety is one of the key aspects that should be assessed in the planning and operation phase of the CO_2 transport. Recently, several QRA (*Quantitative Risk Assessment*) studies for CO_2 pipelines have been proposed ([3,4,5]).

Their analysis allows for the identification of several gaps and uncertainties concerning especially the source modeling, the dispersion behavior as well as the establishment of CO_2 threshold values and possible effects at different distances from the infrastructure ([6]).

These uncertainties and gaps lead to controversies around the CO_2 transport hazards. For example, some authors claim the low (tolerable) risk in the CO_2 handling operations ([7,8]) while others suggest that risks associated are well understood ([9]). In addition, it is generally suggested that there is no enough experience in designing and operating CO_2 pipelines in highly populated areas and therefore CCS and EOR systems pose a risk at least comparable than pipelines carrying hydrocarbons ([1]).

A systematic evaluation of impacts of uncertainties in input parameters on the results of QRA has been performed in some studies ([1,2]) leading to the conclusion that following aspects need further knowledge to fill existing gaps:

- failure scenarios and their probability;
- CO_2 releases from pressurized domains;
- dispersion modeling.

Following sections are dedicated to the investigation of main knowledge gaps affecting these QRA aspects applied to CO_2 with a special focus on the CO_2 releases modeling.

1.2.1 Failure scenarios and probability

QRA procedures generally refer to two types of failure scenarios: puncture and full bore rupture.

In what concerning pipelines, failures are mainly due to corrosion, infrastructure defects, ground movement, operational errors and third party interferences. Recently, NaTech causes like those invoking earthquakes and floods have been included in safety reports.

Different failure distributions between the puncture and the full bore rupture are usually employed and some details are reported in Table 1.1.

Therefore, overall cumulative rates assumed are ranging from 0.7 to 6.1 per 10000 km per year. However, these data are often based on natural gas pipelines and may not be valid for CO_2 pipelines due to the peculiar properties of this substance. In addition, as discussed by some authors ([1]), historical failure rates for CO_2 infrastructures cannot be compared with those of natural gas being the gained experience limited.

Differences with pipelines carrying natural gas may arise because of the acidic behavior of the CO_2 in presence of impurities, like water, inducing higher failure rates ([10]). Other impurities are represented by SO_x, NO_x, O_2 and H_2S.

The effect of varying failure rates on the QRA results is represented by varied and unreliable risk contours that are strictly linked to the safety distances assessment. Some authors ([1,3]) underline that these uncertainties lead to safety distances derived from a pressurized CO_2 release varying from 37 to 117 m.

Table 1.1. *Failures frequencies used in QRA procedures applied to CO_2 pipelines ([1]).*

Cumulative failure rate $[10^{-4}\ km^{-1}yr^{-1}]$	Failure scenarios and distribution
6.1	Rupture: 25 %
	Puncture (20 mm): 75 %
3.4	Full bore: 25 %
	Large puncture (100 mm): 6 %
	Medium puncture (30 mm): 8 %
	Small puncture (7 mm): 41 %
1.55	Rupture: 50 %
	Puncture: 50 %
20	Rupture 25 %
	Puncture (20 mm): 75 %

1.2.2 Release and source modeling

The modeling of the CO_2 behavior subjected to a rapid depressurization is a critical step in QRA of CO_2 pipelines and it is the main topic of this research work. This step consists in the definition of the source term that it will contribute to the subsequent atmospheric dispersion through the investigation of the source aspects (geometry, direction), quantity, velocity and release duration.

In what concerning the CO_2 behavior, thermodynamic aspects are crucial in determining reliable results.

It is known that any release is specific to the substance released as its properties vary in time with the phenomenon evolution. Among these, the most important are the pressure, the volume and the temperature that define the instantaneous CO_2 state due to the depressurization. A first main issue of concern is the lack of comprehensive thermodynamic models able to describe all aggregation states pertaining to the CO_2 that may arise (supercritical, gaseous, liquid or solid) as represented in Figure 1.1.

Studies and experimental evidences give reason to state that main mechanisms involved in a rapid CO_2 depressurization are those listed below that are depending on the initial aggregation state:

- occurrence of a pressurized release that may be persistently gaseous or in form of a multi-phase mixture (vapor-liquid or vapor-solid);
- flashing phenomena that interest the liquid portion of the expanding jet;
- rainout and snow-out phenomena;
- atmospheric dispersion of a heavy-gas cloud and eventual sublimating dry-ice bank formation acting as a delayed dispersion hazard source ([11]).

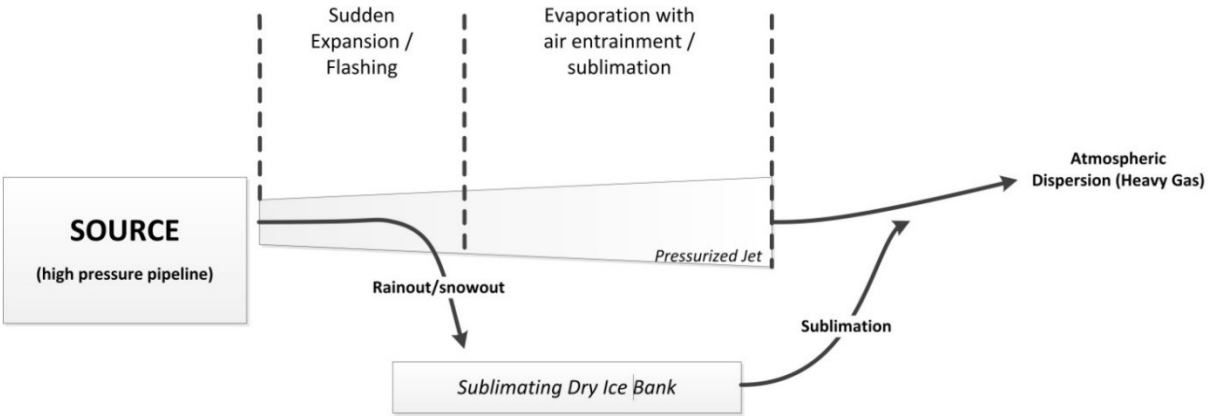

Figure 1.1. *Possible scenarios after a pressurized CO_2 release from CCS and EOR infrastructures ([11]).*

In the light of the listed features, the modeling of the outflow following a CO_2 pipeline failure is challenging given the large number of linked and complex phenomena that are governing the whole discharge process. Some of them, however, are characterized by uncertainties and gaps also derived by the lack of many supporting experimental data ([1,12]).

The dense release following a full bore rupture is calculated relying on transient two-phase models to take into account the discharge of vapor-liquid mixtures across the rupture plane. These models were originally applied for the LPG releases ([13]) but are usually generalized for other substances giving rise to uncertainties especially in the CO_2 case that is characterized by the peculiar thermodynamic behavior. In cases where the CO_2 is handled in its gaseous state, i.e. in EOR operations, a transient model for gas pipelines is instead used.

All these models lack a comprehensive approach able to manage all phenomena linked to the rapid depressurization including the prediction of the solid phase occurrence giving then rise to the snow-out.

Different model approaches are available and some of them are indicated below:

- simplified models made of algebraic equations (*AEs*) and ordinary differential equations (*ODEs*) resulting in scenarios differently conservative;
- general models based on conservation equations (*ODEs* and *PDEs*) and thermodynamic correlations (*AEs*) giving rise to mathematical structures usually handled through numerical approaches ([14,15]);
- detailed studies based on the Computational Fluid Dynamic (*CFD*) approaches characterized by a high degree of detail coupled with a relevant computational-burden demand usually not adoptable in emergency situations.

Uncertainties affecting these approaches are firstly linked to the thermodynamic expansion nature followed by the CO_2 during the rapid depressurization. Available experimental data do not actually give a unique interpretation of the occurring expansion that ranges between the (ideal) isentropic and the (ideal) isenthalpic pathway. Any accuracy affecting the supposed depressurization pathway will alter the thermal dynamic as well as the mixture nature resulting from the pressure gradients.

In addition, considerations must also be given to the effects of frictions and heat transfer which are both expected during the blowdown phenomena and are phase-dependent mechanisms.

To date, large part of the proposed outflow models relies on the HEM (Homogeneous Equilibrium Model) approach ([1,12,16,17]), thus imposing mechanical and thermal equilibrium during the decompression process. The gap is consequently linked to the absence of non-equilibrium phase transitions, phase-slip and delayed boiling mechanisms.

According to some authors ([1,17]), while ignoring phase-slip may be justified by experimental evidences, the same approach based on non-equilibrium vaporization is difficult to be a priori justified. The final part of the present work investigates the effects in neglecting these aspects on the release modeling.

All available models allow for important outcomes to be fed to the subsequent dispersion model. These outcomes are the release duration, the instantaneous discharged mass flow rate and the out coming mixture quality. The effect of varying assumptions may lead to the lack of these essential parameters especially in terms of number and nature of expected phases, these strictly linked to the thermal and fluid dynamic system behavior.

1.2.3 Atmospheric dispersion

The pressurized release of CO_2 gives usually rise to a dispersing heavy gas that is directly derived from the expanding jet and/or the sublimating dry-ice bank. Because of the CO_2

density field, this cloud moves close to the ground and its behavior is therefore influenced by local conditions and orography.

Features of a denser-than-air dispersion process are reported below ([1]):

- the behavior is deeply affected by local wind and temperature fields;
- the resulting cloud behaves dependently on the local terrain conditions;
- heat and mass transfer with surroundings and with the ground are expected to occur;
- the substance encounters gravity-induced spreading and density gradients reduce vertical mixing leading to stratification mechanisms.

These features apply to the CO_2 dispersion since common CCS and EOR operative conditions are likely to give rise to a heavy-gas dispersion following a rapid depressurization.

Limitations actually linked to heavy-gas models employed are due to the fact that they have not been specifically developed and addressed to the CO_2 dispersions. In addition, no modeling solutions involving the solid phase soil deposition ([18]) are available except for complicated CFD simulations whose runtimes are totally unsuitable for emergency responses.

In addition, important factors are affecting the CO_2 dispersion behavior.

The rupture of buried pipelines is linked to the ejection of the soil lying above causing the formation of a crater. Its shape and size is expected to induce modifications on the release features as well as the soil deposition of solid CO_2. The resulting jet will have an impinging behavior (75 % velocity reduction, ([8])) and the formation of a sublimating dry-ice bank is in fact usually linked to this occurrence ([11]). It is known that the soil type and the pipeline depth are crucial parameters in the determination of the crater size even if no models are available to give estimations.

In addition, the supposed expansion pathway will influence the subsequent dispersion step. This is mainly due to the appearance of the dense phase (initially liquid, finally solid) that may partially fall on the ground giving rise to the aforementioned dry-ice bank ([11]). In this case, the atmospheric dispersion experiences the additional delayed source represented by the sublimated CO_2 from the bank surface. Some authors highlighted some uncertainties related to flash calculations ([19]) that are inducing errors in the vapor quality estimation and therefore in the occurrence of rainout and snow-out processes.

The dispersion mechanism is also initially influenced by the direction and the momentum of the released CO_2. For example, different scenarios in terms of spatial CO_2 concentrations are expected depending on the occurrence or not of crater-release collisions ([8]).

In addition, meteorological conditions have a crucial role on the hazards related to the CO_2 dispersion. Actual debate is focused on the combination of release direction and meteorological stability class linked to the worst scenarios that may take place ([20]).

Finally, many gaps exist in what dealing with the effects on the human health. The expected impact estimation suffers some knowledge gaps. In fact, acute and chronic exposure to more vulnerable people still should be assessed. Current studies are based on full healthy subjects ([21]) and proposed threshold concentrations are derived from old investigations. In addition, only few Probit functions are available for QRA purposes indicating that no international standard for the CO_2 threshold exposure limit exists ([8]).

1.3 Final considerations

Moving from the conclusions of some works ([1,4]), the most important issues concerning the knowledge gaps in QRA's for CO_2 pipelines are listed below:

- it is not certain if natural gas failure rates are applicable to the CO_2 case. Supposed divergences may amount up to an order of magnitude;
- preliminary results show that the type of release is a crucial parameter affecting the hazard related to a rapid depressurization of a CO_2 pipeline and there is no consensus on the type of release that should be used in QRA's studies;
- methodological standards are required;
- the lack of experimental data prevents the development of reliable CO_2-specific models;
- no comprehensive release models are available and the predictions in what dealing with the mixture quality discharged from the pipeline deeply affect the subsequent dispersion process.

1.4 Current CCS and EOR projects worldwide ([22])

Globally there are more than 10 large-scale CCS projects in operation, with additional infrastructures under construction. The total expected CO_2 capture capacity of these projects is around 40 Mtpa.

Another 6 large-scale CCS projects are at the "concept definition" stage with a planned capacity of 6 Mtpa and further 12 projects are in earlier stages of development planning (25 Mtpa).

In 2015, two large-scale projects became operational: the Quest project (Alberta, Canada) involving hydrogen manufacture and deep saline formation storage and the Uthmaniyah CO_2-EOR Demonstration Project (Saudi Arabia) capable of 0.8 Mtpa of captured CO_2 from a LNG recovery plant.

In the early 2016, the Illinois Industrial CCS project (Decatur-IL, USA) was started in a corn-to-ethanol production facility representing the world's first bio-CCS project al large scale and the Abu Dhabi CCS project (Emirates) in the world's first iron and steel CCS applied project. Following Figure 1.2 and Table 1.2. lists current worldwide CCS projects ([22]).

Figure 1.2. *Worldwide diffusion of current CCS project ([22]).*

Table 1.2. *Details on the current CCS project ([22]).*

Project Name	Location	Project Lifecycle Stage	Operation Date	Industry	Capture Type	Capture Capacity (Mtpa)	Transport Type	Primary Storage Type
Val Verde Natural Gas Plants	United States	Operate	1972	Natural Gas Processing	Pre-combustion	1.3	Pipeline	Enhanced oil recovery
Enid Fertilizer CO2-EOR Project	United States	Operate	1982	Fertiliser Production	Industrial Separation	0.7	Pipeline	Enhanced oil recovery
Shute Creek Gas Processing Facility	United States	Operate	1986	Natural Gas Processing	Pre-combustion	7.0	Pipeline	Enhanced oil recovery
Sleipner CO2 Storage Project	Norway	Operate	1996	Natural Gas Processing	Pre-combustion (natural gas processing)	0.9	No transport required (direct injection)	Dedicated Geological Storage
Great Plains Synfuel Plant and Weyburn-Midale Project	Canada	Operate	2000	Synthetic Natural Gas	Pre-combustion (gasification)	3.0	Pipeline	Enhanced oil recovery
In Salah CO2 Storage	Algeria	Operate	2004	Natural Gas Processing	Pre-combustion (natural gas	0.0 (injection suspended	Pipeline	Dedicated Geological Storage

Project Name	Location	Project Lifecycle Stage	Operation Date	Industry	Capture Type	Capture Capacity (Mtpa)	Transport Type	Primary Storage Type
Snøhvit CO2 Storage Project	Norway	Operate	2008	Natural Gas Processing	Pre-combustion (natural gas processing)	0.7	Pipeline	Dedicated Geological Storage
Century Plant	United States	Operate	2010	Natural Gas Processing	Pre-combustion (natural gas processing)	8.4	Pipeline	Enhanced oil recovery
Air Products Steam Methane Reformer EOR Project	United States	Operate	2013	Hydrogen Production	Industrial Separation	1.0	Pipeline	Enhanced oil recovery
Coffeyville Gasification Plant	United States	Operate	2013	Fertiliser Production	Industrial Separation	1.0	Pipeline	Enhanced oil recovery
Lost Cabin Gas Plant	United States	Operate	2013	Natural Gas Processing	Pre-combustion (natural gas processing)	0.9	Pipeline	Enhanced oil recovery
Petrobras Santos Basin Pre-Salt Oil Field CCS Project	Brazil	Operate	2013	Natural Gas Processing	Pre-combustion (natural gas processing)	1.0	No transport required (direct injection)	Enhanced oil recovery
Boundary Dam Carbon Capture and Storage Pr.	Canada	Operate	2014	Power Generation	Post-combustion	1.0	Pipeline	Enhanced oil recovery
Quest	Canada	Operate	2015	Hydrogen Production	Industrial Separation	1.0	Pipeline	Dedicated Geological Storage
Uthmaniyah CO2 EOR Demonstration Project	Saudi Arabia	Operate	2015	Natural Gas Processing	Pre-combustion (natural gas processing)	0.8	Pipeline	Enhanced oil recovery
Abu Dhabi CCS Project (Phase 1 being Emirates Steel Industries (ESI) CCS Project)	United Arab Emirates	Execute	2016	Iron and Steel Production	Industrial Separation	0.8	Pipeline	Enhanced oil recovery
Kemper County Energy Facility	United States	Execute	2016	Power Generation	Pre-combustion (gasification)	3.0	Pipeline	Enhanced oil recovery
Petra Nova Carbon Capture Project	United States	Execute	2016	Power Generation	Post-combustion	1.4	Pipeline	Enhanced oil recovery
Alberta Carbon Trunk Line ("ACTL") with Agrium CO2 Stream	Canada	Execute	2016-17	Fertiliser Production	Industrial Separation	0.3 - 0.6	Pipeline	Enhanced oil recovery
Alberta Carbon Trunk Line ("ACTL") with North West Refinery CO2 Stream	Canada	Execute	2017	Oil Refining	Industrial Separation	1.2 - 1.4	Pipeline	Enhanced oil recovery

Project Name	Location	Project Lifecycle Stage	Operation Date	Industry	Capture Type	Capture Capacity (Mtpa)	Transport Type	Primary Storage Type
Illinois Industrial Carbon Capture and Storage Project	United States	Execute	2017	Chemical Production	Industrial Separation	1.0	Pipeline	Dedicated Geological Storage
Gorgon Carbon Dioxide Injection Project	Australia	Execute	2017 (Institute estimate)	Natural Gas Processing	Pre-combustion (natural gas processing)	3.4 - 4.0	Pipeline	Dedicated Geological Storage
Yanchang Integrated Carbon Capture and Storage Demonstration Project	China	Define	2018	Chemical Production	Pre-combustion (gasification)	0.4	Pipeline	Enhanced oil recovery
Rotterdam Opslag en Afvang Demonstratien	Netherlands	Define	2019-20	Power Generation	Post-combustion	1.1	Pipeline	Dedicated Geological Storage
Don Valley Power Project	United Kingdom	Evaluate	2020	Power Generation	Pre-combustion (gasification)	1.5	Pipeline	Dedicated Geological Storage
Korea-CCS 1	South Korea	Evaluate	2020	Power Generation	Post-combustion	1.0	Shipping	Dedicated Geological Storage
Riley Ridge Gas Plant	United States	Evaluate	2020	Natural Gas Processing	Pre-combustion (natural gas processing)	2.5	Pipeline	Enhanced oil recovery
CarbonNet Project	Australia	Evaluate	2020's	Under evaluation	Under evaluation	1.0 - 5.0	Pipeline	Dedicated Geological Storage
Teesside Collective Project	United Kingdom	Evaluate	2020's	Various	Various	2.8	Pipeline	Dedicated Geological Storage
Texas Clean Energy Project	United States	Define	2020/2021 (Institute estimate)	Power Generation	Pre-combustion (gasification)	2.4	Pipeline	Enhanced oil recovery
China Resources Power (Haifeng) Integrated Carbon Capture and Sequestration Demonstration Project	China	Identify	2020s	Power Generation	Post-combustion	1.0	Pipeline	Dedicated Geological Storage
Huaneng GreenGen IGCC Project (Phase 3)	China	Evaluate	2020s	Power Generation	Pre-combustion (gasification)	2.0	Pipeline	Enhanced oil recovery
Shanxi International Energy Group CCUS Project	China	Identify	2020s	Power Generation	Oxy-fuel combustion	2.0	Pipeline	Not specified
Shenhua Ningxia CTL Project	China	Identify	2020s	Coal-to-liquids (CTL)	Pre-combustion (gasification)	2.0	Pipeline	Not specified

Project Name	Location	Project Lifecycle Stage	Operation Date	Industry	Capture Type	Capture Capacity (Mtpa)	Transport Type	Primary Storage Type
Sinopec Shengli Power Plant CCS Project	China	Define	2020s	Power Generation	Post-combustion	1.0	Pipeline	Enhanced oil recovery
Caledonia Clean Energy Project	United Kingdom	Evaluate	2022	Power Generation	Pre-combustion (gasification)	3.8	Pipeline	Dedicated Geological Storage
Korea-CCS 2	South Korea	Evaluate	2023	Power Generation	Under evaluation	1.0	Shipping	Dedicated Geological Storage
South West Hub	Australia	Evaluate	2025	Fertiliser Production	Industrial Separation	2.5	Pipeline	Dedicated Geological Storage

In what concerning EOR (Enhanced Oil Recovery) projects, it should be underlined that the United States has been using CO_2-EOR for several decades. The U.S. Energy Department has estimated that the full use of this technique could make available additional 240 billion barrels of recoverable oil sources.

Despite the many CO_2-EOR projects in the United States, activity elsewhere in the world is very limited. Some projects are under development in Canada (EnCana's Weyburn and Midale field CO_2-EOR projects). Only a few CO_2-EOR projects are underway in the world like in Brazil, Turkey and China.

Table 1.3 gives a list of planned EOR project worldwide since 2008.

Table 1.3. *Details on the current EOR project* ([22]).

Operator	Field	Location	Pay zone	Size acres	Depth, ft.	Gravity °API	Start date
Anadarko	Sussex	Johnson Co., Wyo.	Tensleep	2,544	9,000	29	2010
ARC Energy Trust	Redwater	Redwater, Alta., T58 R21 W4M	Leduc D-3	160	3,000	36	7/08
Denbury	Cranfield	Adams Co., Miss.	Lower Tuscaloosa	7,754	10,250	39	5/08
Denbury	Heidelberg West	Jones & Jasper Co., Miss.	Eutaw	915	5,000	22	10/08
Core Energy	Chester 6	Otsego, Mich.	A1 Carbonate	100	5,700	43	6/09
Core Energy	Niagaran "A"	Otsego, Mich.	Brown Niagaran	120	5,700	43	12/09
Core Energy	Niagaran "B"	Otsego, Mich.	Brown Niagaran	140	5,700	43	12/10

Operator	Field	Location	Pay zone	Size acres	Depth, ft.	Gravity °API	Start date
Denbury	Delhi	Richland, Madison, Franklin Parishes,	L Holt-Bryant	8,000	3,300	42	1/09
Denbury	W. Lazy Creek	Pike Co., Miss.	Lower Tuscaloosa	600	10,250	39	10/09
Fasken	Abell	Crane Co., Tex. Blk 1C, H&TC RR Sur	Devonian	769	5,200	40	1/09
Fasken	River Bend	Crane Co., Tex. Blk 1C, H&TC RR Sur	Devonian	470	5,300	40	1/09
Fasken	Hanford ROZ	Gaines, Tex.	San Andres	340	5,700	32	1/09
Kinder Morgan	Katz	Stonewall County, Tex.	Strawn	5,483	4,800	40	5/09
Occidental	North Dollarhide	Andrews Co., Tex.	Clearfork	270	6,500	40	2008
Arizona Oil	Milnesand	Roosevelt County, NM	San Andres	40	4,600	27	2008

References to Chapter 1

1. Kornneef, J., Spruijt, M., Molag, M., Ramirez, A., Faaij, A., Turkenburg, W., 2009. Uncertainties in risk assessment of CO_2 pipelines. Energy Procedia, 1(1), 1587-1594.
2. IPPC. IPPC Special Report on Carbon Dioxide Capture and Storage, Cambridge University Press, Cambridge, UK, p. 442.
3. Witlox, H.W.M., Harper, M., Oke, A., 2009. Modelling of discharge and atmospheric dispersion for carbon dioxide releases, Journal of loss prevention in the process industries, 22, 795-502.
4. Kruse, H., Tekiela, M., 2005. Calculating the consequences of a CO_2 – pipeline rupture. Energy Conversion and Management, 37(6-8).
5. TetraTech, Final Risk Assessement Report for FutureGen Project Enviromental Impact statement, 2007. Lafayette CA, USA.
6. Koornneef, J., Spruijt, M., Molag, M., Ramirez, A., Turkenburg, W., Faaij, A., 2010. Quantitative Risk Assessment of CO_2 Transport by Pipelines-A review of Uncertainties and Their Impacts. Journal of Hazardous Materials, 117, 12-27.
7. Hooper, B., Murray, L., 2005. Latrobe Valley CO_2 Storage Assessment, CO_2CRC, Melbourne, Australia.

8. Turner, R., Hardy, N., Hooper, B., 2006. Quantifying the Risks to the Public Associated with a CO_2 Sequuestration Pipeline: a methodology and Case Study. Greenhouse Gas Control Technologies, 8, Trondheim, Norway.
9. Heinrich, J.J., Herzog, H.J., Reiner, D.M., 2004. Environmental Assessment of Geologic Storage of CO_2, MIT LFEE Report, 2004.
10. de Visser, E., Hendricks, C., Barrio, M., Molnvik, M.J., de Koeijer, G., Liljemark, S., le Gallo, Y., 2008. Dynamics CO_2 quality recommendations. Int. J. Greenhouse Gas Control, 2, 4, 478-484.
11. Mocellin, P., Vianello, C., Maschio, G., 2016. Hazard Investigation of Dry-Ice Bank Induced Risks Related to Rapid Depressurization of CCS Pipelines. Analysis of Different Numerical Modelling Approaches. Int. J. of Greenhouse Gas Control.
12. Mahgerefteh, H., Brown, S., Martynov, S., 2012. A study of the effects of friction, heat transfer and stream impurities on the decompression behavior in CO_2 pipelines. Greenhouse gases: science and technology 2, 369-379.
13. CPR, Yellow Book Methods for Calculation of Physical Effects-due to Releases of Hazardous Materials, VROM, TNO, The Hague, 2005.
14. Martynov, S., Brown, S., Mahgerefteh, H., Sundara, V., 2013. Modelling choked flow for CO_2 from the dense phase to below the triple point. International journal of Greenhouse Gas Control, 19, 552-558.
15. Witlox, H.W.M., Stene, A., Harper, M., Nilsen, S.H., 2011. Modelling of discharge and atmospheric dispersion for carbon dioxide releases including sensitivity analysis for wide range of scenarios. Energy procedia, 4, 2253-2260.
16. Witlox, H.W.M., Harper, M., Oke, A., Bowen, P.J., Kay, P., 2010. Sub-cooled and Flashing Liquid Jets and Droplet Dispersion II. Overview and Model Implementation/Validation. Journal of Loss Prevention in the Process Industries, 23, 831-842.
17. Benintendi, R., 2014. Non-equilibrium phenomena in carbon dioxide expansion, Process Safety and Environmental Protection, 92, 47 – 59.
18. CPR, Guidelines for quantitative Risk Assessment-The purple book. Committee for the Prevention of Disaster (CPR), RIVM, The Hague, Netherlands, 2005.
19. Calay, R.K., Holdo, A.E., 1996. Modeling the dispersion of flashing jets using CFD. J. Hazard. Mater., 154(1-3), 1198-1209.
20. Vendrig, M., Spouge, J., Bird, A., Daycock, J., Johnsen, 2003. Risk Analysis of the Geological Sequestration of Carbon Dioxide. Dept. of Trade and Industry, London, UK.

21. Rice, S.A., 2004. Health Effects of CO_2, EPRI.
22. Global CCS Institute, web portal (last check: October 2016).

Chapter 2

CO_2 Thermodynamic Behavior and dedicated EoS Models

The CO_2 state diagram and the peculiar thermodynamic properties of this substance are illustrated in this section. In addition, the Equation of State (EoS) models are investigated with special focus on the most used solutions to give a reliable description of the CO_2 behavior under pressure.
Details are given on a specific EoS model able to cover the CO_2 solid phase and the solid-vapor equilibrium usually occurring in the case of pressurized releases.

2.1 Introduction

The knowledge of the CO_2 thermodynamic behavior is essential in preliminary driving any model development. This covers the allowable aggregation states depending on the specific operative conditions as well as the investigation of the occurring phase equilibria.
The implementation of reliable descriptive and predictive models is essential for a robust depressurization dynamic description that is in turn essential in giving good estimations of the parameters used in the QRA procedures.

2.2 The CO_2 phase diagram

The phase diagram of a pure substance is the starting point of any analysis concerning pressurized releases from a high-pressure reservoir. In this diagram, all CO_2 phases are reported along with the respective ranges of existence. The phase diagram is resulting from a stability analysis based on the Gibbs potential. Its lower envelope surface of the different phases and the projection of the minima curves onto a pressure-temperature plane gives the phase diagram.
Following Figure 2.1 gives the CO_2 phase diagram.

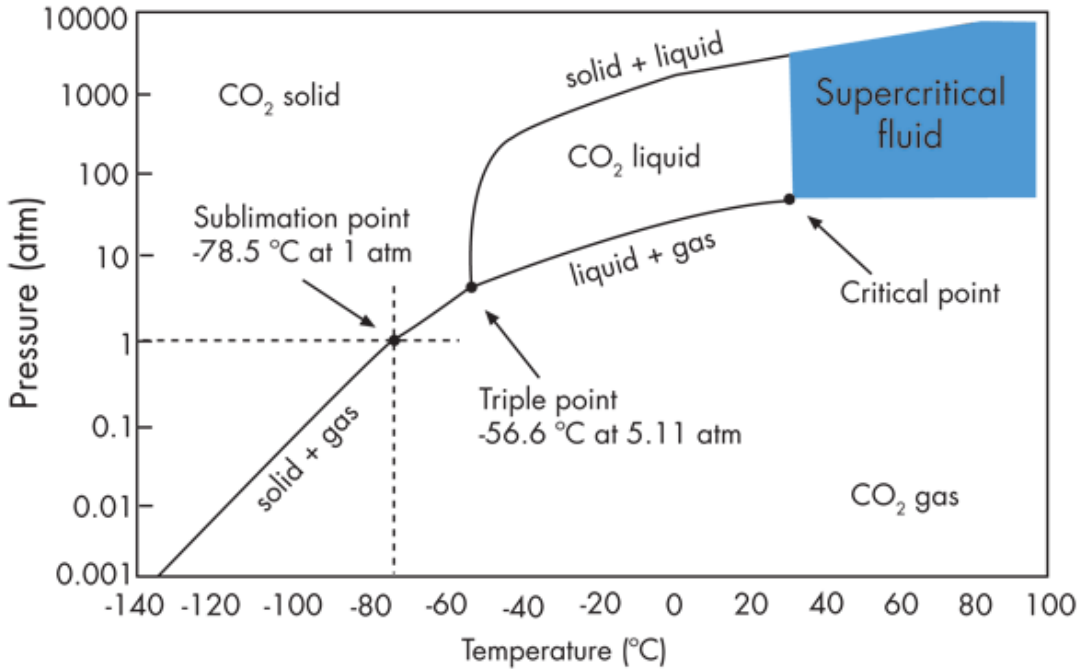

Figure 2.1. *CO_2 phase diagram. The triple point pressure is above the 1 atm giving rise to a solid-vapor equilibrium at atmospheric conditions.*

As shown in Figure 2.1 the domain is divided into several regions that are distinguishable in the number of expected phases as a function of a certain pair of temperature and pressure. Some of their values can identify a single-phase region or even a two-phase region along the saturation curves. The latter identifying the domain of existence of two phases at thermodynamic equilibrium.

The intersection of these saturation lines locates the triple point that is a unique point at which gaseous, liquid and solid phase coexist thus identifying a three-phase compatibility. In the case of the CO_2 this point lies at a pressure of 0.518 MPa and at a temperature equals to 216.58 K. The corresponding pressure value is the minimum to ensure the existence of the liquid phase.

2.3 The equation of state concept

The fundamental equation of thermodynamics expressing the total energy U of a system as a function of only extensive properties can be expressed as in (2.1):

$$U = U(S, V, N_1, \dots, N_r) \ . \tag{2.1}$$

When dealing with processes and associated changes of extensive parameters the (2.1) should be analyzed in the differential form (2.2):

$$dU = \left(\frac{\partial U}{\partial S}\right)_{V,N_1,\dots,N_r} dS + \left(\frac{\partial U}{\partial V}\right)_{S,N_1,\dots,N_r} dV + \sum_{j=1}^{r} \left(\frac{\partial U}{\partial N_j}\right)_{S,V,\dots,N_r} dN_j \ . \tag{2.2}$$

The various partial derivatives appearing in (2.2) can be expressed in terms of intensive parameters:

$$\left(\frac{\partial U}{\partial S}\right)_{V,N_1,\dots,N_r} \equiv T \quad (temperature)\,, \tag{2.3}$$

$$\left(\frac{\partial U}{\partial V}\right)_{S,N_1,\dots,N_r} \equiv P \quad (pressure)\,, \tag{2.4}$$

$$\left(\frac{\partial U}{\partial N_j}\right)_{S,V,\dots,N_r} \equiv \mu_j \quad (eletrochemical\ potential\ of\ jth\ component)\ . \tag{2.5}$$

The (2.3-2.5) states that the temperature, the pressure and electrochemical potential are partial derivatives of functions $S, V, N_1, \dots, N_r$ and consequently are also functions of $S, V, N_1, \dots, N_r$ identifying a set of functional relationships:

$$T = T(S, V, N_1, \dots, N_r)\,, \tag{2.6}$$

$$P = P(S, V, N_1, \dots, N_r)\,, \tag{2.7}$$

$$\mu_j = \mu_j(S, V, N_1, \dots, N_r)\ . \tag{2.8}$$

Such relationships express intensive parameters in terms of the independent extensive parameters and are called Equations of States (EoS).

2.4 CO_2 selected EoS models

2.4.1 Generalized CO_2 EoS

The generalized approach when dealing with EoS for pure fluids is beneficial since it allows to have an analytical formulation between thermodynamic variable that is presumed to be valid for a class of fluids. Its parameters have the property of not being fitted to a whole collection of experimental data but rather being obtained only from the fluid critical properties. Once the critical properties are known, the calculation of the substance thermodynamic behavior is straightforward.

Following Table 2.1 lists the critical CO_2 properties.

Table 2.1. *CO_2 properties at the critical point.*

Temperature	T_c	304.19 [K]
Pressure	P_c	7.376 [MPa]
Density	ρ_c	468 [kg/m^3]
Specific volume	v_c	0.094 [m^3/kmol]
Compressibility factor	Z_c	0.274

2.4.2 Peng-Robinson EoS (PREoS)

Equation ([1]) was presented in 1976 with some corrections made by the respective authors two years later. The complete generalized form of PREoS retains the character of the cubic equation of state as reported in (2.9):

$$P - \frac{RT}{v-b} + \frac{a(T)}{v(v+b)+b(v-b)} = 0 \ . \tag{2.9}$$

All (2.9) parameters are listed below:

$$a(T) = 0.45724\left(\frac{RT_c}{\sqrt{P_c}}\right)^2 \varepsilon(T)\,, \tag{2.10}$$

$$b = 0.0778\left(\frac{RT_c}{P_c}\right)^2 \ , \tag{2.11}$$

$$\varepsilon(T) = \left[1 + \varphi\left(1 - \sqrt{\frac{T}{T_c}}\right)\right]^2 \ . \tag{2.12}$$

In the (2.12), φ is expressed in terms of the acentric factor that for the CO_2 is equal to 0.239.
In addition, when dealing with residual properties, is also useful to evaluate the derivative (2.10) with respect to the temperature as in (2.13):

$$\frac{da(T)}{dT} = \frac{d}{dT}\left[1 + \varphi\left(1 - \sqrt{\frac{T}{T_c}}\right)\right]^2 = -0{,}45724\varphi\sqrt{\frac{\varepsilon(T)}{TT_c}}\left(\frac{RT_c}{\sqrt{P_c}}\right)^2 \ . \tag{2.13}$$

The PREoS equation, as often proved, can produce good predictions of the CO_2 data especially in the domain of both the liquid and the gas.
As for other relations, this EoS correctly predicts that various susceptibilities should diverge at the critical point but the analytic form of these divergences is not entirely correct.

This problem, as known, derives from the flattening of the minimum of the Gibbs potential in the critical region. For these reasons, the description of the system behavior near the critical point gets more difficult and so the PREoS should be carefully handled when approaching it. These observations are not inappropriate since the description of CO_2 pressurized releases is usually linked to thermodynamic paths that may give rise from the supercritical region.
In the present work, the PREoS relationship is primarily used to predict and describe the CO_2 behavior in the liquid and gaseous phase and also at the vapour-liquid equilibrium conditions. Supercritical properties are instead derived from the Span-Wagner EoS (SWEoS).

2.4.3 Span-Wagner EoS (SWEoS)

As reported in ([2]) this EoS is based on a huge amount of experimental CO_2 data covering the fluid region from the triple point temperature to 1100 K at pressures up to 800 MPa.
The SWEoS takes the form of a fundamental equation explicit in the Helmholtz free energy. More precisely several data concerning specific CO_2 properties have been used to fit the function for the residual part of the Helmholtz free energy thereby obtaining the SWEoS. Given the information provided by the authors, the estimated uncertainty following the application of SWEoS ranges from ±0.03 to ±0.05 % in the density, ±0.03 to ±1.00 % in the speed of sound and ±0.15 to ±1.50 % in the isobaric heat capacity. Moreover, this formulation yields a reasonable description even of the caloric properties in the immediate vicinity of the critical point.
The SWEoS is expressed in form of the Helmholtz energy A with the two independent variables namely the reduced density ρ_r and the reduced temperature T_r as reported in (2.14):

$$\frac{A(\rho_r, T_r^{-1})}{RT} = \frac{A^{IG}(\rho_r, T_r^{-1})}{RT} + \frac{A^{R}(\rho_r, T_r^{-1})}{RT} \ . \tag{2.14}$$

The (2.14) shows the splitting of the Helmholtz energy into a part depending on the ideal-gas behavior $A^{IG}(\rho_r, T_r^{-1})$ and a portion that considers the residual fluid behaviour $A^{R}(\rho_r, T_r^{-1})$. While the first is formulated as usual, the second part cannot be formulated from a theoretical approach and so should be determined empirically.
This approach has allowed the development of the SWEoS.
Since its mathematical shape is extremely demanding from a computational view, the SWEoS has been implemented in a polynomial form as proposed by some authors ([2,3]).
As an example, the CO_2 density is expressed in terms of the pressure and the temperature as in (2.15):

$$\rho = \sum_{i=0}^{4} A_i(T) P^i \ . \tag{2.15}$$

The $A_i(T)$ coefficients are function of the temperature as follows:

$$A_i(T) = \sum_{j=0}^{4} b_{ij} T^j \ . \tag{2.16}$$

The values of the parameters of (2.15-2.16) are listed in ([2]) to which the reader should refer for further information.

2.4.4 4th-degree polynomial EoS for the solid CO_2 and the solid-vapor equilibrium

As will be shown in next chapters, a pressurized release of CO_2 may lead to the formation of a bi-phase system mainly composed by mixture of liquid/solid and gaseous CO_2. At the triple point, in an even more complex way, the system involves the coexistence of all three phases.
The modelling of these situations is therefore strictly related to the possibility to give a description of CO_2 phase equilibrium as precise as possible.
Many methods have been proposed in literature for describing solid-fluid equilibrium, including also those already discussed here.
A non-exhaustive list has been collected by some authors to clarify the limitations associated with many ordinary models proposed in the past. This list collects the contributions provided for example in ([1,4]).
The Yokozeki EoS ([4]) is a polynomial in the 4th power of the specific volume and is considered as one of the most interesting literature models because it describes all three CO_2 phases via a single EoS. The authors also provide the EoS coefficients thus making it suitable for calculations.
The Yokozeki EoS (YEoS) has the pressure explicit form reported in (2.17):

$$P(T,v) = \frac{RT}{v-b}\left(\frac{v-d}{v-c}\right)^k - \frac{a}{v^2 + qbv + rb^2} \ , \tag{2.17}$$

where P is the pressure, R is the gas constant, T is the temperature, v the molar volume, c the liquid covolume, b the solid covolume, a the usual attractive term as in cubic EoS while d, k, q and r are parameters. To have a suitable behaviour in all regions of state variables, two important relations must be respected: $b < d < c$ and $k \in \mathcal{Z} - (-\infty, 0]$. $k = 1$ allows the Maxwell's equal area rule being the criterion for solid-liquid equilibrium.

Given the degree to which the (2.17) occurs, it can have up to 4 roots. If they were to be placed with increasing value, they would be those reported in Table 2.2.

Table 2.2. *Meaning of the (2.17) roots.*

$1^{st}\ root$	Volume of the solid phase v_S
$2^{nd}\ root$	Volume of the liquid phase v_L
$3^{rd}\ root$	Unphysical volume in the vapor-liquid region
$4^{th}\ root$	Volume of the vapor phase v_V

Depending on the value of k, the 2nd and the 3rd roots may assume different meanings. The qualitative Yokozoki EoS shape is straightforwardly constructed by use of analytical geometry knowledge. However, the choice of the appropriate values of a, b, c and d requires attention and criteria based on the numerical analyses.

Figure 2.2 gives a comprehensive chart of the numerical and analytical analysis for the proper choice of b (or equivalently of c) that is scaled on the P_c/RT_c group.

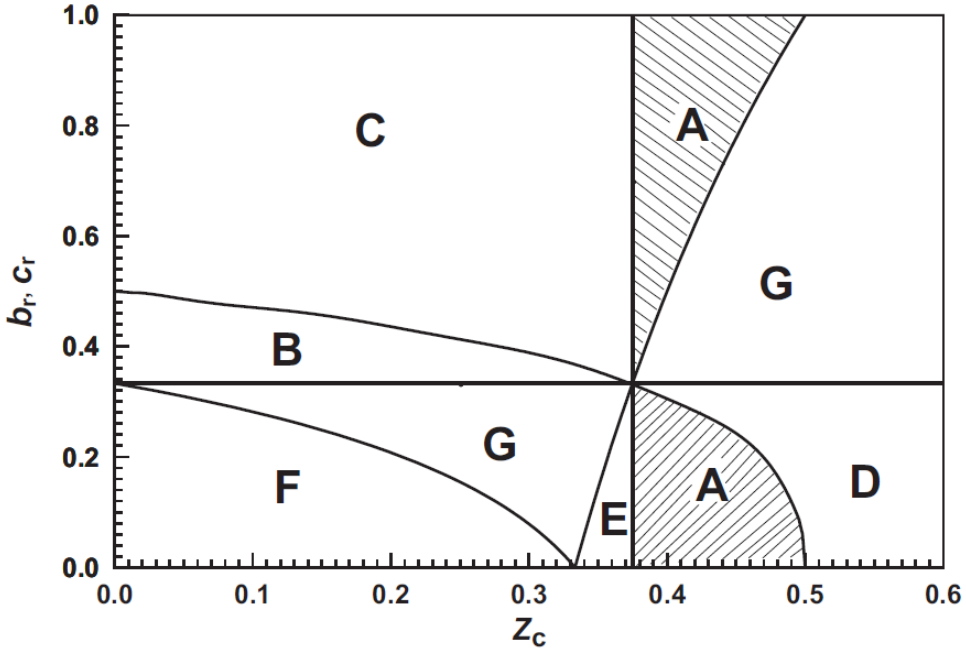

Figure 2.2. *Classification chart of various topological shapes of the (2.17) Area A-denoted is the proper EoS parameter region ([4]).*

A proper selection of parameters so they fall in region A corresponds to a physically stable solid phase branch and to the existence of the VLE critical point. Region B and D imply the occurrence of the critical point in the solid phase branch and the absence of a stable liquid

phase. Differently, region C outlines a critical point located in the fluid-phase branch but essentially no stable liquid phase exists. Region E has a proper fluid EoS type but without a physically meaningful solid-phase branch. Finally, region F and G give physically incorrect results.

When deriving thermodynamic properties from (2.17), its shape leads to serious difficulties although it can be written in analytically closed forms. These may be overcome considering a simplified form of the (2.17) as suggested in ([4]) and proposed in (2.18):

$$P(T,v) = \frac{RT}{v-b}\left(\frac{v-d}{v-c}\right) - \frac{a}{v^2} \ . \tag{2.18}$$

The (2.18) is derived by taking $k = 1$ and $q = r = 0$. Once expressed in terms of dimensionless parameters it takes the form reported in (2.19):

$$P_r = \frac{T_r}{Z_c(v_r - b_r)}\left(\frac{v_r - d_r}{v_r - c_r}\right) - \frac{a_r}{v_r^2 Z_c^2} \ . \tag{2.19}$$

Taking as reference the (2.19), the set of parameters for the CO_2 case are listed in Table 2.3.

Table 2.3. *Constants of (2.19) for the CO_2 case ([4]).*

c_r	d_r	Z_c	a_0	a_1	a_2
0.34017	0.32309	0.37510	0.28578	82.0637	6.40361
n	b_0	$b_1 \cdot 10^{-2}$	b_2	m	
0.424	0.31588	-4.90960	5.61866	6	

Constants reported in Table 2.3 also refers to the (2.20-2.21) that are useful in the estimation of parameters a_r and b_r of the (2.19):

$$a_r(T_r) = a_0 + a_1 T_r \exp(-a_2 T_r^n) \ , \tag{2.20}$$

$$b_r(T_r) = b_0 + b_1 T_r \exp(-b_2 T_r^m) \ . \tag{2.21}$$

where a_0, a_1, a_2 and n are positive. $a_r(0\ or\ \infty) = a_0$, $da_r/dT_r = a_1$ at $T_r = 0\ K$ and the maximum occurs at $T_r = (na_2)^{-1/n}$. In addition, b_0, b_2 and m are positive too and $b_r(0) = b_0 + b_1 > 0$. Finally, the relation $b_r(T_r) < d_r$ must hold.

When implemented, this EoS gives a reasonable description of the solid, liquid and vapor phases of the CO_2. The two phase branches are well outlined apart from the separation curve between the liquid and solid phase where significant errors arise. Figure 2.3 shows this situation.

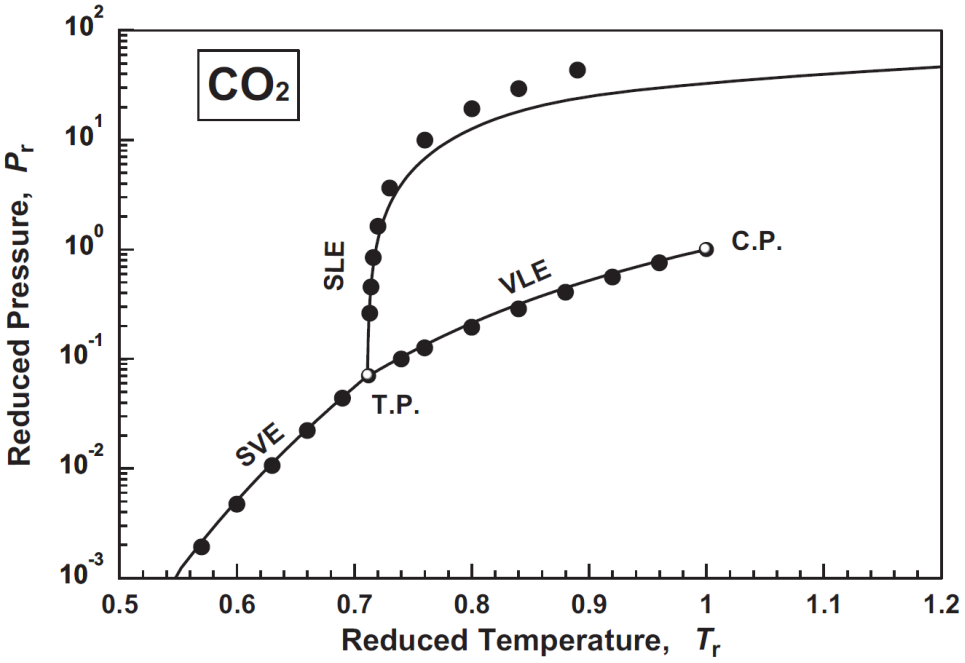

Figure 2.3. *CO_2 Phase diagram derived from the YEoS projected on the reduced temperature-reduced pressure plane. Dots refer to selected experimental data ([3]).*

It should be considered that the proposed EoS has an empirical basis and so its parameters derive from a correlation procedure. The uncertainties related to this aspect primarily emerges in the solid-liquid behavior description as seen above. The observed experimental data matching in the remaining domains is instead strong.

So, its strength is related to the fact that this EoS proposes a simple analytical form to describe the solid-liquid-vapor state in a unified way. Recent works ([3,4]) have shown the promising aspects related to this EoS. More accuracy may be achieved by using a larger quantity of experimental data.

Finally, it should be noted that this EoS, when applied to the solid state, omits its possibility to have multiple modifications with different crystal symmetries.

Using appropriate mixing rule, similarly to those applied to cubic EoS, this equation can describe also the mixture behavior. When dealing with pressurized releases of CO_2 and CCS procedure applied to infrastructure handling CO_2, the presence of impurities is usually neglected to simplify the system description to that of a pure fluid.

2.5 Evaluation of the CO_2 properties from the EoS model

Most of the main CO_2 properties are derived from the application of the EoS model.

These calculations firstly involve the formulation and the calculation of different derivatives of the state thermodynamic variable with respect to others. Generally, the pressure and the temperature are the variables with respect to which the derivation is required.

2.5.1 Relations involving 1st and 2nd derivatives from PREoS

To evaluate these derivatives may be helpful to reorder the (2.9) in the following equivalent formulation:

$$P - \frac{RT}{v-b} + \frac{a(T)}{(v+k_1 b)(v+k_2 b)} \ . \tag{2.22}$$

The application of the derivation rules to (2.22) gives the following relation (2.23) between the pressure and the specific volume:

$$\frac{\partial^n P}{\partial V^n} = (-1)^n n! \left[\frac{RT}{(v-b)^{n+1}} - \frac{a(T)}{b(k_2-k_1)} \left(\frac{1}{(v+k_1 b)^{n+1}} - \frac{1}{(v+k_2 b)^{n+1}} \right) \right] \ . \tag{2.23}$$

In relation to this work, main applications will involve the first and second derivatives of (2.23) giving respectively with $n = 1$ and $n = 2$:

$$\frac{\partial P}{\partial V} = -\left[\frac{RT}{(v-b)^2} - \frac{a(T)}{b(k_2-k_1)} \left(\frac{1}{(v+k_1 b)^2} - \frac{1}{(v+k_2 b)^2} \right) \right] \ , \tag{2.24}$$

$$\frac{\partial^2 P}{\partial V^2} = 2\left[\frac{RT}{(v-b)^3} - \frac{a(T)}{b(k_2-k_1)} \left(\frac{1}{(v+k_1 b)^3} - \frac{1}{(v+k_2 b)^3} \right) \right] \ . \tag{2.25}$$

In the same way, it is possible to obtain pressure derivatives of PREoS with respect to the temperature giving, for example, the relation (2.26):

$$\frac{\partial P}{\partial T} = \frac{R}{v-b} - \frac{da(T)/dT}{(v+k_1 b)(v+k_2 b)} \ . \tag{2.26}$$

In the (2.26), the derivative of the $a(T)$ term is directly given by the derivation of the (2.10)
On the contrary, the volume derivative with respect to the temperature can be handled in a more complicated way since the PREoS is not explicit in the specific volume.
From this consideration one can observe that the (2.27) holds:

$$\left(\frac{\partial v}{\partial T} \right)_P = \frac{RT}{P} \left(\frac{\partial z}{\partial T} \right)_P + \frac{Rz}{P} \ , \tag{2.27}$$

which is favorable since the compressibility factor derivative can be directly assessed starting from the cubic formulation of PREoS expressed as a function of the compressibility factor z.
In fact, neglecting the intermediate steps it can be shown that the (2.27) takes the following form:

$$\left(\frac{\partial v}{\partial T}\right)_P = \frac{\left(\frac{\partial A}{\partial T}\right)_P (B-z) + \left(\frac{\partial B}{\partial T}\right)_P (-z^2 + 2z + 6Bz - 3B^2 - 2B + A)}{3z^2 + 2(-1+B)z + (A - 2B - 3B^2)} \ . \tag{2.28}$$

For brevity, the original PREoS parameters have been collected in the group $A = aP/(RT)^2$ and $B = bP/RT$ thus leading to the (2.29-2.30):

$$\left(\frac{\partial A}{\partial T}\right)_P = \frac{P}{(RT)^2}\left(\frac{da(T)}{dT} - \frac{2a}{T}\right) , \tag{2.29}$$

$$\left(\frac{\partial B}{\partial T}\right)_P = -\frac{bP}{RT^2} \ . \tag{2.30}$$

These derivatives, along with many others, contribute to the calculation of the main CO_2 properties and their variation along a specific thermodynamic path. In addition, some of these derivatives appear in the residual contribution to the real behavior of the CO_2. Residual properties concern the deviation of CO_2 thermodynamic behaviour from that of ideal fluid whose internal energy and enthalpy are only temperature functions. Starting from PREoS and differentiating the expression with respect to the temperature and the pressure, the estimation of the deviations from the gas tendency is straightforward. When dealing with depressurization phenomena, quantities such as the enthalpy, the entropy and the internal energy need to be evaluated.

2.5.2 Residual internal energy from PREoS

Considering the relation between the residual internal energy U^R and the thermodynamic state variables, it can be shown that the following (2.31) holds:

$$u^R = \int_\infty^v \left[T\left(\frac{\partial P}{\partial T}\right)_v - P\right] dv \ . \tag{2.31}$$

Then making use of the (2.26), the (2.31) takes the form of (2.32):

$$u^R = \int_\infty^v \left[\frac{a - T(da/dT)}{v(v+b) + b(v-b)}\right] dv = \frac{T(da/dT) - a}{2\sqrt{2}b} \ln \frac{v + \left(1+\sqrt{2}\right)b}{v + \left(1-\sqrt{2}\right)b} \ . \tag{2.32}$$

2.5.3 Residual enthalpy from PREoS

Similarly to the (2.32), a similar relation can be obtained for the residual contribution to the enthalpy giving the following (2.33):

$$h^R = (z-1)RT + u^R = (z-1)RT + \frac{T(da/dT) - a}{2\sqrt{2}b} \ln \frac{v + \left(1+\sqrt{2}\right)b}{v + \left(1-\sqrt{2}\right)b} \ . \tag{2.33}$$

2.5.4 Residual entropy from PREoS

The residual entropy derives from the following relation (2.34):

$$s^R = R \ln z + \int_{\infty}^{v} \left[\left(\frac{\partial P}{\partial T} \right)_v - \frac{R}{v} \right] dv \ , \tag{2.34}$$

and the application of the PREoS then gives:

$$s^R = R \ln Z + R \ln \left(\frac{v-b}{v} \right) - \frac{da/dT}{2\sqrt{2}b} \ln \frac{v + \left(1-\sqrt{2}\right)b}{v + \left(1+\sqrt{2}\right)b} \ , \tag{2.35}$$

thus, finally leading to:

$$s^R = R \ln(Z-B) + \frac{da/dT}{2\sqrt{2}b} \ln \frac{v + \left(1+\sqrt{2}\right)b}{v + \left(1-\sqrt{2}\right)b} \ . \tag{2.36}$$

References to Chapter 2

1. O'Connell, J., Poling, B.E., Prausnitz, J., 2000. The properties of gases and liquids, Mc-Graw Hill Education, 5th ed.
2. Span, R., Wagner, W., 1996. A new equation of state for carbon dioxide covering the fluid region from the triple-point temperature to 1100 K at pressures up to 800 MPa. J. Phys. Chem. Ref. Data 1996, 25, 1509-1596.
3. Ouyang, L.B., 2011. New correlations for predicting the density and viscosity of supercritical carbon dioxide under conditions expected in carbon capture and sequestration operations. The Open Petroleum Engineering Journal, 4, 13-21.
4. Yokozeki, A., 2003. Analytical equation of state for solid-liquid-vapor phases. International Journal of Thermophysics, 24, 589-620.

Chapter 3

Theoretical Modeling of CO_2 Flows Subjected to Large Pressure Gradients

The theoretical investigation proposed in this chapter moves from the application of the conservation principles and thermodynamic concepts to the CO_2 flow description.
Special attention is given to the modeling of single-phase and multi-phase CO_2 flows induced by large pressure gradients as those arising from a pressurized release.
The establishment of the *choked* flow conditions is modeled and analyzed also with respect to the occurrence of CO_2 mixtures made of gaseous, liquid and solid CO_2.

3.1 Introduction

As discussed in Chapter 2, peculiar to the CO_2 is its thermodynamic behavior that allows for the establishment of an atmospheric equilibrium between the solid (dry ice) and the gaseous aggregation states given that $P_{tr} > P_{atm}$.
This occurrence has an incidence on the CO_2 pressurized releases especially in what concerning the compressibility-related effects linked to the appearance of the light phase and on the establishment of *sonic* flow conditions that are sensitive to the mixture nature and quality.
These aspects play a key role in determining the whole pressurized release dynamic and therefore the final estimated parameters to be used in the QRA studies.
A detailed and reliable description is therefore needed and this section is devoted to the development of suitable mathematical descriptive tools that are applied to the peculiar CO_2 behavior.

3.2 Conservation principles and balances

3.2.1 The mechanical energy balance

The modelling of a pressurized release of CO_2 invokes the description of its main properties (i.e. temperature, pressure and density) during the rapid depressurization to atmospheric conditions.

The description therefore requires a careful consideration of the instantaneous thermodynamic properties of CO_2 including all thermodynamic state variables, occurring phases, thermodynamic path and endpoint in addition to issues related to the hole size and shape as well as the leak duration.

The release phase is dependent on the release process and should be based on thermodynamic diagrams or data, equilibrium models and the thermodynamic path during the release. The initial point of the release process is defined by the initial condition of the CO_2 matching the normal CCS process conditions or abnormal states reached as a result of failures or external factors. The end point of the pathway, instead, will normally be at a final pressure corresponding to the atmospheric level.

In addition, the release modelling can not disregard the specification of the thermodynamic pathway used to reach the endpoint.

This aspect is strictly related on the formulation of the total energy balance since different assumptions on the pathway lead to significantly different results. The balance is reported in (3.1):

$$\frac{d}{dt}\left[U + m\left(\frac{u^2}{2} + \varphi\right)\right] = \sum_{n=1}^{N} \dot{m}_n \left(\widehat{U} + \frac{u^2}{2} + \varphi\right)_n + \dot{Q} + \dot{W}_s - P\frac{dP}{dt} + \sum_{n=1}^{N} \dot{m}_n \left(P\widehat{V}\right)_n . \tag{3.1}$$

The (3.1) collects all energy terms involved in the formulation of the conservation principle of energy of an open system with:

U: internal energy of the bordered system;

m: mass;

u: velocity;

φ: potential energy of the system bordered;

$\dot{m}_n$: mass flow rate across the system borders;

$\widehat{U}$: internal energy per unit of mass of the system bordered;

$\dot{Q}$: heat flow rate across the system borders;

$\dot{W}_s$: rate of shaft work;

P: pressure of the system bordered;

$\hat{V}$: volume per unit of mass of the system bordered.

The (3.1) can be written in a more compact form by combining the first and the last terms on the right side and introducing the definition of the specific enthalpic state function $\hat{H}$:

$$\frac{d}{dt}\left[U + m\left(\frac{u^2}{2} + \varphi\right)\right] = \sum_{n=1}^{N} \dot{m}_n \left(\hat{H} + \frac{u^2}{2} + \varphi\right)_n + \dot{Q} + \dot{W}_s - P\frac{dP}{dt} \ . \tag{3.2}$$

Table 3.1 shows the impact of the various assumptions on the thermodynamic path on the total energy balance as formulated in (3.2).

Table 3.1. *Implications of various thermodynamic assumptions on the (3.2).*
(*): evaluated from the remaining term of the Total Energy Balance.

	Term of (3.2)						
	Enthalpic	Kinetic	Potential	Heat	Shaft work	ΔT	ΔS
Isoenthalpic	Null	(*)	(*)	(*)	(*)	Null if Ideal Gas	Not null
Isentropic	(*)	(*)	(*)	Null	(*)	Not null	Null
Isothermal	Null if Ideal Gas	Not null	Not null	Not null	Not null	Null	Not null
Adiabatic	(*)	(*)	(*)	Null	(*)	Not null	Null if reversible

As shown in Table 3.1, various assumptions lead to very different results. In general, the adiabatic flow model predicts larger (i.e. conservative) flow rates, while the isothermal model predicts smaller amounts. The actual flow rate is somewhere in between these values.

For the isentropic release, instead, an equilibrium flash model should be used to determine the final temperature, the composition and the phase splits at ambient pressure. If a phase change is expected, as in the case of pressurized releases of CO_2, then two or three-phase flow may need consideration in the release description.

3.2.2 The HEM (Homogeneous Equilibrium Model) approach and the Euler's flow equation

In the HEM (Homogeneous Equilibrium Model) approach, the velocity, the temperature and the pressure among phases are assumed to be equal. In other words mass, momentum and energy are transferred between phases fast enough that equilibrium between them is reached.

The resulting equations resemble those for a pseudo-fluid with mixture properties linked by a suitable EoS (Equation of State).

This model is not able to accurately predict rapid accelerations or huge pressure changes and therefore assumption should be always checked.

Generally, the HEM model adopts three flow equations (3.3-3.5), matching respectively the conservation of the mass, the energy and the momentum:

$$\frac{\partial \rho}{\partial t} + \nabla \cdot (\rho \boldsymbol{u}) = 0 \ , \tag{3.3}$$

$$\frac{\partial (\rho \boldsymbol{u})}{\partial t} + \nabla \cdot (\rho \boldsymbol{u} \otimes \boldsymbol{u} + \ PI) = \rho \boldsymbol{g} \ , \tag{3.4}$$

$$\frac{\partial (\rho e)}{\partial t} + \nabla \cdot \big((\rho e + P)\boldsymbol{u}\big) = \rho \boldsymbol{g} \cdot \boldsymbol{u} \ . \tag{3.5}$$

The form taken by conservation equations in (3.3-3.5) is conservative since the conserved quantity is appearing under the time derivative. The convective form, instead, is reported in (3.6-3.8):

$$\frac{\partial \rho}{\partial t} + \boldsymbol{u} \nabla \rho + \rho \nabla \cdot \boldsymbol{u} = 0 \ , \tag{3.6}$$

$$\frac{\partial \boldsymbol{u}}{\partial t} + (\boldsymbol{u} \cdot \nabla \boldsymbol{u}) + \frac{\nabla P}{\rho} = \boldsymbol{g} \ , \tag{3.7}$$

$$\frac{\partial e}{\partial t} + \boldsymbol{u} \cdot \nabla e + \frac{P}{\rho} \nabla \cdot \boldsymbol{u} = 0 \ . \tag{3.8}$$

(3.3-3.5) and (3.6-3.8) are representative of non-linear hyperbolic *PDEs* (Partial Differential Equations). In detail, the convective formulation is a quasi-linear form being this mathematical typology expressible as in (3.9), that is all maximum derivative's orders linearly appear in all the equations:

$$\frac{\partial \theta}{\partial t} + L(x, t, \theta) \frac{\partial w}{\partial x} = 0 \ . \tag{3.9}$$

These *PDEs* are characterized by a scalar (mass and energy balance equation) and a vector nature (momentum balance equation).

Variables that appear are 4: the density ρ, the pressure P, the total internal energy e and the velocity vector u. Their (numerical) solvability is therefore asking for additional relations that are listed in (3.10-3.11):

$$P = P(e, \rho) \ , \tag{3.10}$$

$$T = T(e, \rho) \ . \tag{3.11}$$

Suitable initial and boundary conditions need to be supplemented. The first, given the transient behavior of the equations, require the initial variable ρ, e and u distributions that is $\rho(\boldsymbol{r},0)=\rho_0(r)$, $\boldsymbol{u}(\boldsymbol{r},0)=\boldsymbol{u_0}(\boldsymbol{r})$ and $e(\boldsymbol{r},0)=e_0(\boldsymbol{r})$, being $\rho_0(\boldsymbol{r}), \boldsymbol{u_0}(r)$ and $e_0(\boldsymbol{r})$ the respective initial given variable fields.

The boundary conditions supplementation is more complicated and is depending on the specific problem nature. It should be separately analyzed with respect to any rigid body or surface and the flowing fluid.

For example, on a rigid surface only the normal component of the velocity vector u must be imposed as reported in (3.12):

$$\widehat{\boldsymbol{n}}\cdot\boldsymbol{u}|_{s.s.}=\alpha \ , \tag{3.12}$$

with $\alpha=0$ if the solid body is at rest.

Therefore, none of the thermodynamic variables-related condition should be imposed (density and energy), these being part of the PDEs system solution.

Required boundary conditions on the external boundaries may vary from 0 to 4 (2-dimensional fields) or 5 (3-dimensional fields).

3.2.3 The additional entropy balance equation

Starting from the internal energy equation expressed in its convective form it is possible to derive that of the specific entropy $s=s(r,t)$.

By means of the relation $e=e(s,v)$ namely $e=e\big(s(r,t),v(r,t)\big)$, the internal energy equation finally takes the form indicated in (3.13):

$$\left(\frac{\partial e}{\partial s}\right)_v\frac{\partial s}{\partial t}+\left(\frac{\partial e}{\partial v}\right)_s\frac{\partial v}{\partial t}+\boldsymbol{u}\left[\left(\frac{\partial e}{\partial s}\right)_v\nabla s+\left(\frac{\partial e}{\partial v}\right)_s\nabla v\right]+\frac{P}{\rho}\nabla\cdot\boldsymbol{u}=0 \ . \tag{3.13}$$

By applying the Maxwell's relations following (3.14-3.15) are obtained:

$$T=\left(\frac{\partial e}{\partial s}\right)_v \ , \tag{3.14}$$

$$-P=\left(\frac{\partial e}{\partial v}\right)_s \ , \tag{3.15}$$

leading to (3.16):

$$\frac{\partial s}{\partial t}+\boldsymbol{u}\cdot\nabla s=0 \ . \tag{3.16}$$

The derivation of (3.16) is performed under negligible viscosity and thermal conductivity stating that flowing fluid particles of an inviscid substance preserve their specific entropy. In absence of discontinuities, the entropy equation may replace the energy conservation equation or that of the mass.

3.3 Stationary formulation of the flow equations.

The absence of time derivatives in the (3.3-3.5) leads to the following stationary problem (3.17):

$$\begin{cases} \nabla \cdot (\rho \boldsymbol{u}) = 0 \\ \nabla \cdot (\rho \boldsymbol{u} \otimes \boldsymbol{u} + PI) = \rho \boldsymbol{g} \\ \nabla \cdot \big((\rho e + P)\boldsymbol{u}\big) = \rho g \cdot \boldsymbol{u} \end{cases} . \tag{3.17}$$

In this case the energy conservation equation is redrafted by means of the specific enthalpy h once noted that:

$$h = e + \frac{P}{\rho} = e + Pv \ , \tag{3.18}$$

from which the total specific enthalpy h^t is defined as in (3.19):

$$h^t = e^t + \frac{P}{\rho} \ . \tag{3.19}$$

In terms of the total specific enthalpy h^t, the equation of the energy conservation takes the form reported in (3.20):

$$\begin{cases} \nabla \cdot (\rho \boldsymbol{u}) = 0 \\ (\boldsymbol{u} \cdot \nabla)\boldsymbol{u} + \dfrac{\nabla P}{\rho} = 0 \\ \boldsymbol{u} \cdot \nabla h^t = 0 \end{cases} . \tag{3.20}$$

The system (3.20) may involve also the specific entropy equation (3.16) in its stationary formulation.

In this it is clear how the vectors $\boldsymbol{u}$ and ∇h^t or ∇s lie on perpendicular spaces and that along a streamline the total enthalpy and the entropy are constant.

The possibility to derive all thermodynamic properties of the fluid is complicated by the fact that the total enthalpy has a hybrid nature being dependent on the velocity vector module $|u|$. As a result, the description of u along a streamline is required.

This can be accomplished by means, for example, of the balance equation for the tangential momentum component.

The imposition of a local cylindrical coordinate system (R, θ, z) with the assumption of a local circumferentially approximated streamline plane curvature, leads to the (3.21):

$$\hat{\tau} \cdot (\boldsymbol{u} \cdot \nabla)\boldsymbol{u} + \frac{\hat{\tau} \cdot \nabla P}{\rho} = \frac{u}{R}\frac{\partial u}{\partial \theta} + \frac{1}{\rho}\frac{\partial P}{\partial \theta} = \frac{u}{R}\frac{du}{d\theta} + \frac{1}{\rho}\frac{dP}{d\theta} = 0 \ . \tag{3.21}$$

The variable θ can be replaced with a curvilinear coordinate that can then in turn be skipped being the analysis addressed to a general streamline. The dependent variables relationship is therefore obtained as reported in (3.22):

$$udu + \frac{dP}{\rho} = 0 \ . \tag{3.22}$$

The (3.22) gives the link between the velocity and pressure variations with the density along a streamline. It should be noted that the pressure P is function of two thermodynamic variables, of which one, that is the entropy s, is constant along the streamline. It follows that:

$$dP = \frac{\partial P(s = const, \rho)}{\partial \rho} d\rho \ . \tag{3.23}$$

The (3.23) finally takes the form reported in (3.24):

$$udu + \frac{1}{\rho}\frac{\partial P(s = const, \rho)}{\partial \rho} d\rho = 0 \ . \tag{3.24}$$

A dimensional analysis applied to the pressure derivative with respect to the density shows that:

$$\left[\frac{\partial P(s, \rho)}{\partial \rho}\right] = \frac{[L^2]}{[t^2]} \ . \tag{3.25}$$

This derivative therefore is equivalent to $[u^2]$. The derivative sign can be assessed once observed that:

$$\frac{\partial P(s, \rho)}{\partial \rho} = \frac{1}{\rho^2}\frac{\partial^2 e(s, v)}{\partial v^2} > 0 \ . \tag{3.26}$$

The inequality comes from the second thermodynamics principles, that invokes the convexity of the $e(s,v)$ function. As known, the square root of this derivative is equivalent to the local fluid speed of sound c:

$$c \equiv \sqrt{\frac{\partial P(s,\rho)}{\partial \rho}} = \sqrt{\left(\frac{\partial P}{\partial \rho}\right)_s} \quad . \tag{3.27}$$

The introduction of the speed of sound c allows for a different formulation of the (3.24):

$$udu + \frac{1}{\rho}\frac{c^2(s = const,\rho)}{\partial \rho}d\rho = 0 \quad , \tag{3.28}$$

from which:

$$\frac{d\rho}{du} = -\frac{\rho u}{c^2} \quad . \tag{3.29}$$

In addition, considered that $d(\rho u) = \rho du + u d\rho$, (3.30) is obtained:

$$\frac{d(\rho u)}{du} = \rho\left[1 - \frac{u^2}{c^2(s = const,\rho)}\right] \quad . \tag{3.30}$$

The constancy in the entropy, that is derived along the streamline path, indicates that the (3.30) is a mathematical relation between the density ρ and the velocity u of the CO_2 once applied to a specific streamline.

3.4 Stationary behavior of the main CO_2 properties along a streamline

The energy conservation equation (3.17) can be reformulated once observed that the force field g is conservative giving a formulation depending on a (specific) potential energy γ:

$$\nabla \cdot (\rho \boldsymbol{u} h^t) = \rho \boldsymbol{u} \cdot \boldsymbol{g} = -\rho \boldsymbol{u} \cdot \nabla\gamma \quad , \tag{3.31}$$

that is

$$\boldsymbol{u} \cdot \nabla h^t = -\boldsymbol{u} \cdot \nabla\gamma \quad . \tag{3.32}$$

It is therefore proved that:

$$\boldsymbol{u} \cdot \nabla(h^t + \gamma) = 0 \ . \tag{3.33}$$

In other words vectors u and $\nabla(h^t + \gamma)$ are normal and streamlines are corresponding to the point locus marked by a constancy in $(h^t + \gamma)$ group.

The (3.34) follows with r moving in any point of the CO_2 flow field:

$$h^t(\boldsymbol{r}) + \gamma(\boldsymbol{r}) = h(\boldsymbol{r}) + \frac{1}{2}|\boldsymbol{u}(\boldsymbol{r})|^2 + \gamma(\boldsymbol{r}) = \alpha \ . \tag{3.34}$$

In absence of external forces, $\gamma(r) = 0$ and the (3.35) is obtained:

$$h(\boldsymbol{r}) + \frac{1}{2}|\boldsymbol{u}(\boldsymbol{r})|^2 = h(s = const, P) + \frac{1}{2}|\boldsymbol{u}|^2 = \alpha \ . \tag{3.35}$$

The (3.35) implicitly defines a relation between the pressure P and the velocity $\boldsymbol{u}$ along the streamline. Therefore the definition of a new function Π with the two independent variables (P, u) is performed obtaining (3.36):

$$\Pi(P, \boldsymbol{u}) = h(s = const, P) + \frac{1}{2}|\boldsymbol{u}|^2 - \alpha = 0 \ . \tag{3.36}$$

This definition is convenient since it allows for the determination of the main CO_2 properties derivatives along the streamline.

For instance, the variation of the CO_2 pressure with respect to the local velocity u is derived as follows:

$$\frac{dP}{d|\boldsymbol{u}|} = \frac{\frac{\partial \Pi(P, \boldsymbol{u})}{\partial |\boldsymbol{u}|}}{\frac{\partial \Pi(P, \boldsymbol{u})}{\partial P}} = -\frac{|\boldsymbol{u}|}{\left(\frac{\partial h}{\partial P}\right)_s} = -\rho|\boldsymbol{u}| \leq 0 \ . \tag{3.37}$$

In the derivation of (3.37), the Legendre transform-convolution property is applied.

The variation of the pressure with respect to the density is obtained as reported in (3.38):

$$\frac{dP}{d\rho} = \left(\frac{\partial P}{\partial \rho}\right)_s = c^2 > 0 \ . \tag{3.38}$$

Finally, the link between the CO_2 density and its local velocity is obtained by relying on the dependence of the CO_2 pressure with the velocity itself. In this way, the following (3.39) is derived:

$$\frac{d\rho}{d|\boldsymbol{u}|} = \left(\frac{\partial \rho}{\partial P}\right)_s \left(\frac{\partial P}{\partial |\boldsymbol{u}|}\right)_s = -\left(\frac{\partial \rho}{\partial P}\right)_s \rho|\boldsymbol{u}| = -\frac{\rho|\boldsymbol{u}|}{c^2} \leq 0 \ . \tag{3.39}$$

It should be noted that the constancy in the total enthalpy h^t means that whenever $|\boldsymbol{u}| = 0$ (stagnation points), the maximum value of the velocity is located at the respective minimum in the specific enthalpy. This because relation (3.40) applies:

$$h + \frac{1}{2}|\boldsymbol{u}|^2 = h_0 \ . \tag{3.40}$$

Fixed h_0 such that is the respective stagnation enthalpy, it is clear how the allowable maximum velocity along a selected streamline, once enforced a suitable enthalpy reference value (for example that at $T = 0\ K$), corresponds to:

$$|\boldsymbol{u}|_{max} = \sqrt{2h_0} \ . \tag{3.41}$$

The thermodynamic specific enthalpy comparing in (3.41) is a thermodynamic variable depending on the local CO_2 pressure and temperature (P, T) while the stagnation enthalpy $h_0(P_0, T_0)$ is defined with respect to any stagnation condition (P_0, T_0). Stagnation conditions may be assumed to match the internal domain subjected to the depressurization process.

The derivation, that is based on the isentropic path assumption, is therefore linked to a suitable constrain consequently related to the EoS model. This EoS model, under the imposed $ds = 0$ constraint, is essential to link the pressure P, the temperature T and the specific volume v of the CO_2 along the thermodynamic path to atmospheric conditions.

The constraint of constant entropy may be expressed in terms of differential dS as a function of the temperature and the pressure as indicated in (3.42):

$$dS = \left(\frac{\partial S}{\partial T}\right)_P dT + \left(\frac{\partial S}{\partial P}\right)_T dP = \frac{C_P}{T} dT - \left(\frac{\partial V}{\partial T}\right)_P dP = 0 \ . \tag{3.42}$$

The exactness test applied to (3.42) gives:

$$\left(\frac{\partial C_P}{\partial P}\right)_T = -T\left(\frac{\partial^2 V}{\partial T^2}\right)_P \ . \tag{3.43}$$

So the values of C_P can be obtained by numerical integration along an isothermal path giving:

$$C_P(T, P) = C_P^0(T) - T\int_0^P \left(\frac{\partial^2 V}{\partial T^2}\right)_P dP \ . \tag{3.44}$$

In (3.44), C_P^0 refers to the ideal gas property and its dependence on the temperature is determined by hyperbolic relations according to NIST chemistry WebBook ([1]).

When evaluating the (3.43-3.44) the links between the various thermodynamic state variables are required and, as previously seen, this implies the specification of the thermodynamic path. Once the nature of the transformation is specified, the relation between the state variables is obtained by means of the integration of the following relations (3.45-3.46):

$$\left(\frac{\partial V}{\partial P}\right)_S = \left(\frac{\partial P}{\partial V}\right)^{-1} + \frac{T}{C_P}\left(\frac{\partial P}{\partial T}\right)_V^2 \left(\frac{\partial P}{\partial V}\right)_T^{-2} , \tag{3.45}$$

$$\left(\frac{\partial V}{\partial P}\right)_H = \left[-C_p - T\left(\frac{\partial P}{\partial T}\right)_V^2 \left(\frac{\partial P}{\partial V}\right)_T^{-1} - V\left(\frac{\partial P}{\partial T}\right)_V\right]\left[-C_p\left(\frac{\partial P}{\partial V}\right)_T\right]^{-1} . \tag{3.46}$$

Various partial derivatives appearing in (3.45-3.46) can be computed using an appropriate EoS as proposed in Chapter 2.

The estimation of the system velocity is then directly derived from (3.40):

$$|\boldsymbol{u}| = \sqrt{2[h_0 - h(P,T)]} . \tag{3.47}$$

The (3.47) is extremely useful since it allows for the determination of the local and instantaneous CO_2 velocity $|\boldsymbol{u}|$ once fixed the stagnation reference conditions and the local specific enthalpy, i.e. the local thermodynamic conditions (P,T).

This derivation can be extended to multi-phase domains as proposed in some works ([2,3]).

This requires the description of the instantaneous CO_2 quality x_i that is mainly governing the mixture weighted properties. Subscript i ranges in the solid, liquid and vapour CO_2 domains.

In detail:

$$h_m = \sum_{i=s,l,v} x_i h_i = x_s h_s + x_l h_l + x_v h_v , \tag{3.48}$$

$$v_m = \frac{1}{\rho_m} = \sum_{i=s,l,v} x_i v_i = x_s v_s + x_l v_l + x_v v_v , \tag{3.49}$$

$$s_m = \sum_{i=s,l,v} x_i s_i = x_s s_s + x_l s_l + x_v s_v . \tag{3.50}$$

The following algebraic constraint on the mass fractions holds:

$$\sum_{i=s,l,v} x_i = x_s + x_l + x_v = 1 . \tag{3.51}$$

In this way variables groups used in the balances equations are related to the solid, liquid and vapour phase ratio values as in (3.52-3.53):

$$\rho_m h_m = \sum_{i=s,l,v} x_i(\rho_i h_i) = x_s(\rho_s h_s) + x_l(\rho_l h_l) + x_v(\rho_v h_v) \ , \tag{3.52}$$

$$\rho_m e_m = \sum_{i=s,l,v} x_i(\rho_i e_i) = x_s(\rho_s e_s) + x_l(\rho_l e_l) + x_v(\rho_v e_v) \ . \tag{3.53}$$

Once the depressurization mechanism is taking place, the instantaneous ratio among different phases is continuously changing in time having the total mixture entropy to be ideally conserved. Thus once established the instantaneous variation of thermodynamic state variables (T, P), the different mass fractions are directly derived from the application of the lever rule (3.54-3.56):

$$x_v = \frac{s - s_l}{s_v - s_l} \quad in\ vapor - liquid\ region \ , \tag{3.54}$$

$$x_v = \frac{s - s_s}{s_v - s_s} \quad in\ solid - vapor\ region \ , \tag{3.55}$$

$$x_v = \frac{s - s_l - (s_s - s_l)x_s}{s_v - s_l} \quad at\ the\ triple\ point \ . \tag{3.56}$$

In addition, at the triple points the *relation* $h_i - h_j = T_{tr}(s_i - s_j)$ holds, with T_{tr} corresponding to the CO_2 triple point temperature (216.6 K). This mathematical relationship derives from the equality of Gibbs free energies of the different phases at equilibrium.
The combination of these relations with (3.47) leads to different expressions of mixture velocity, which is finally expressed in terms of stagnation conditions and the instantaneous values of both enthalpy and entropy of phases at equilibrium as indicated in (3.57-3.59):

$$u_{l-v} = \sqrt{2[h_0 - h_l + T_{tr}(s_l - s)]} \quad in\ vapor - liquid\ region \ , \tag{3.57}$$

$$u_{s-v} = \sqrt{2[h_0 - h_s + T_{tr}(s_s - s)]} \quad in\ solid - vapor\ region \ , \tag{3.58}$$

$$u_{s-l-v} = \sqrt{2[h_0 - h_l + T_{tr}(s - s_l)]} \quad at\ the\ triple\ point \ . \tag{3.59}$$

The mixture velocity (3.57-3.59) can be grouped with the mixture density (or specific volume) to give a stream density J as defined in (3.60):

$$J \equiv \rho u = \frac{\rho}{v} \ . \tag{3.60}$$

The CO_2 specific volume v appearing in (3.60) is evaluated by means of an EoS model.
In detail, this quantity is strictly depending on the quality x, enthalpies and entropies of the interfacing phases:

$$v = \frac{s - s_l}{s_v - s_l}(v_v - v_l) + x_s\left[(v_s - v_l) + \frac{s_l - s_s}{s_v - s_l}(v_v - v_l)\right], \tag{3.61}$$

and thus, recalling the (3.30):

$$\frac{d(\rho u)}{du} = \frac{dJ}{du} = \rho\left[1 - \frac{u^2}{c^2(s = const, \rho)}\right]. \tag{3.62}$$

The optimum point of the function J is located at $u^2 = c^2$, i.e. the maximum stream density is achieved when the local CO_2 velocity is equal to that of the speed of sound along a streamline. As will be discussed later, it can be shown that many *choked* flow points exists with respect to P_{tr} when investigated with respect to the charging pressure P. This is mainly due to the transition from a vapor-liquid mixture to the solid-liquid domain passing through the triple point, where a discontinuity in J is observed.

The compressible behaviour is clear since the respective incompressibility-related trend complies a nearly straight line being the density ideally constant.

3.5 Modeling of CO_2 expansions

3.5.1 Constant enthalpy depressurizations

The prediction of the pressure and temperature trend along a characteristic thermodynamic path is derived from the EoS model application. Shapes concerning the constancy in the enthalpy or the entropy will be different and will lead to varying post-expanded states. It is clear how the real transformation followed by the CO_2 lies somewhere in the middle. Experimental trials will throw light on this aspect.

The starting point of the expansion is related to the initial conditions of the CO_2 or, in other words, to its transportation conditions when focusing on EOR and CCS operations. These are usually known since are driven by both economic and technical reasons and belong to fluid state (liquid or supercritical) but also to gaseous properties, for example in the case of EOR projects.

To better understand the CO_2 behaviour following a rapid depressurization, a list of expansion trends starting from 10 bar moving from an initial temperature of 0 °C to 20 °C are reported in Figure 3.1.

Isenthalpic trends reported show that data pairs (P, T) lie on a nearly straight line throughout the entire simulation domain. The constancy in the curves slope is therefore related to very

small variations of their local differential coefficient (first derivative). A local numerical derivation of the curves of Figure 3.1 is reported in Table 3.1.

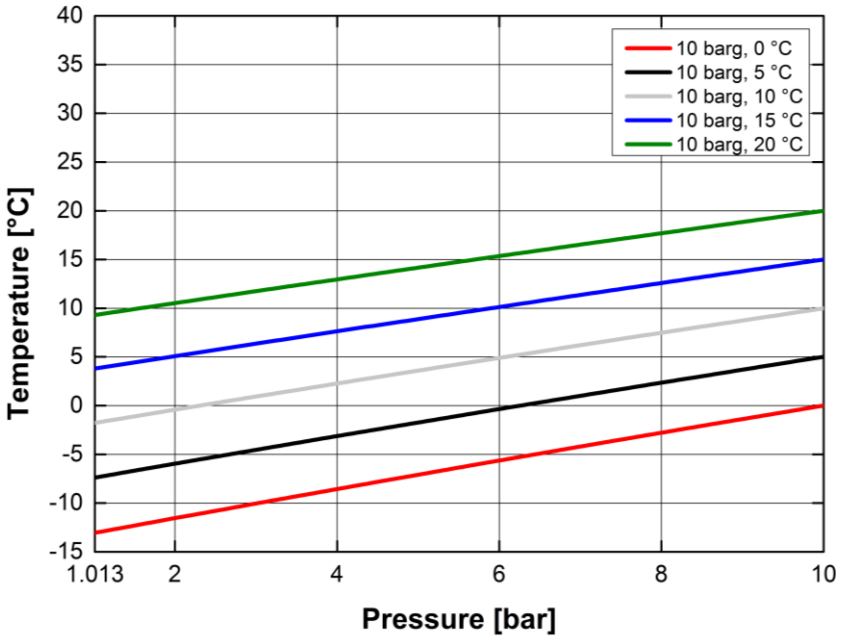

Figure 3.1. *Pressure-temperature evolution under the constant enthalpy condition. 10 barg expansions.*

Table 3.1. *Calculated first derivative of Figure 3.1 curves.*

Pressure (MPa)	First derivative (case 1)	First derivative (case 2)	First derivative (case 3)	First derivative (case 4)	First derivative (case 5)
1,0	13,70	13,01	12,38	14,46	15,29
2,0	13,56	12,89	12,27	14,30	15,12
3,0	13,42	12,76	12,16	14,15	14,94
4,0	13,29	12,64	12,05	13,99	14,77
5,0	13,15	12,52	11,94	13,84	14,60
6,0	13,02	12,40	11,83	13,69	14,42
7,0	12,88	12,28	11,72	13,54	14,25
8,0	12,75	12,16	11,62	13,39	14,09
9,0	12,62	12,05	11,52	13,25	13,92
10,0	12,50	11,93	11,41	13,10	13,76

Considering the isenthalpic nature of the expansion, this numerical first derivative may be related to the so called Joule-Thomson coefficient μ_{JT}. It invokes therefore the description of the CO_2 temperature change when subjected to a throttling process that is a free rapid expansion through a system kept insulated.

It should be noted that a process entirely performed at constant enthalpy is ideal since real conditions are characterized by heat-transfer mechanisms not always referable to the total enthalpy conservation.

By way of comparison, the μ_{JT} coefficient is estimated from CO_2 *P-v-T* data derived from the application of the EoS model as reported in (3.63):

$$\mu_{JT} = \left(\frac{\partial T}{\partial P}\right)_h = -\left(\frac{\partial T}{\partial h}\right)_P \left(\frac{\partial h}{\partial P}\right)_T = -\frac{1}{c_p}\left[v - T\left(\frac{\partial v}{\partial T}\right)_P\right] . \tag{3.63}$$

Setting the (3.63) equal to zero, that is:

$$v - T\left(\frac{\partial v}{\partial T}\right)_P = v\left(\frac{\partial z}{\partial v}\right)_T + T\left(\frac{\partial z}{\partial T}\right)_v = 0 \ , \tag{3.64}$$

one can get the inversion condition of μ_{JT} starting from CO_2 EoS data. This condition marks a boundary in the behaviour of the CO_2 since if $\mu_{JT} > 0$ the fluid cools down as it expands, otherwise, a temperature raise is observed.

Figure 3.2 shows the inversion curve of the CO_2 computed from the SWEoS with an indication of the region boundaries investigated in Figure 3.1.

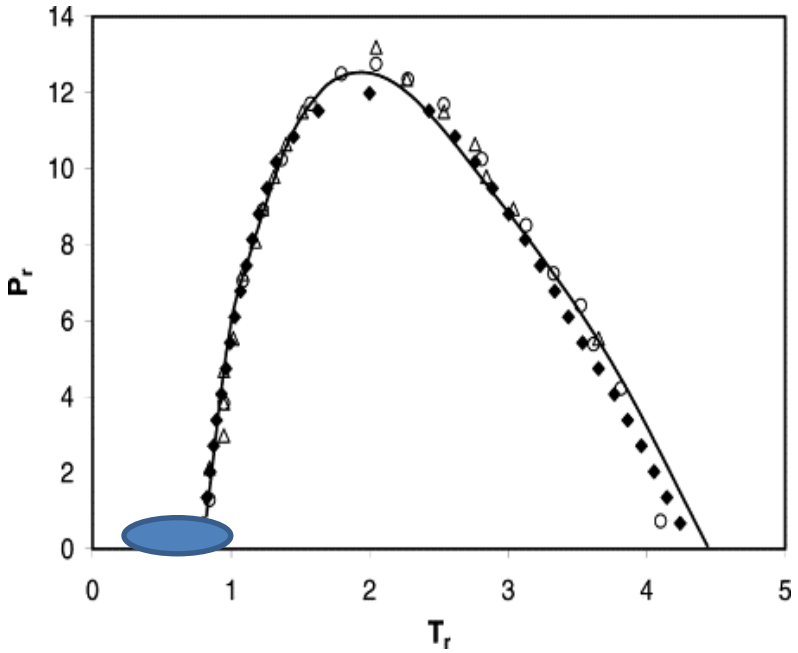

Figure 3.2. *Predicted CO_2 Joule – Thomson inversion curve by SWEoS.*

CO_2 conditions both before and after the isenthalpic expansions fall in the region characterized by $\mu_{JT} < 0$, this always involving the cooling of the CO_2 as a result of the depressurization. Therefore starting from a storage pressure of 10 bar, this expansion coefficient remains almost constant at around 11-15 K/Mpa in the temperature range investigated, i.e. a decrease of about 11 to 15 K with respect to the initial CO_2 temperature is to be generally expected.

The investigation of the CO_2 specific volume gives reason to assume that the isenthalpic expansion starting from 10 bar does not result in condensed phase appearance (liquid or solid). Figure 3.3 gives a representation of the specific volume trend with respect to pressures involved in the expansion.

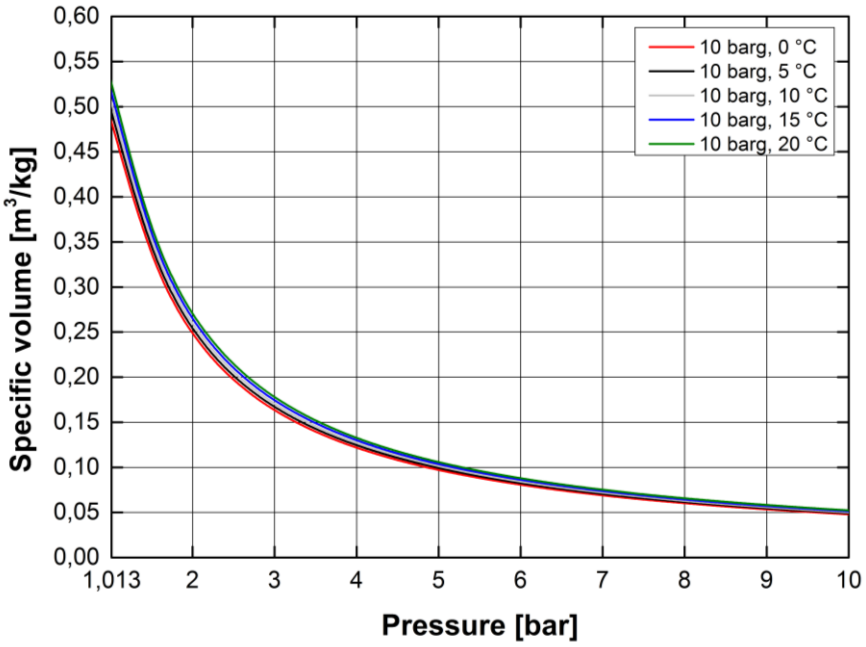

Figure 3.3. *Pressure-specific volume profiles under the constant enthalpy condition. 10 barg expansions.*

It is clear how the isenthalpic expansion leads to a gradual increase in the specific volume of the CO_2 with a variation from 0.05 to 0.5 m^3/kg, resulting in a scale factor equal to 10. This variation plays a key role in the assessment of the amount leaving the pressurized system since it is strictly affecting the massive load.

At the same time, the compressibility factor approaches the unity as the expansion occurs and therefore the pressure decreases together with the declining temperature profile leads to quasi-ideal gas conditions. The fully ideal state is not reached since it is pertaining to domains characterized by significantly higher temperatures.

The approximation of ideal-gas behaviour should be introduced with caution when dealing with depressurization from more severe initial conditions. In addition, any isenthalpic expansion cannot be predicted by an ideal-gas approach since it follows that $\mu_{JT} = 0$, this deriving from the fact that the ideal-gas enthalpy is not influenced by the pressure. In this sense, this kind of gas does not suffer temperature changes while subjected to a pressure variation (isothermal expansion).

It is observed that the isenthalpic expansion behaviour changes with increasing storage (initial) pressure.

Figure 3.4 illustrates the trend of the main CO_2 thermodynamic state variables following the isenthalpic path and starting from storage pressures of 30, 60 and 90 bar. The initial storage temperature is equal to 10 °C.

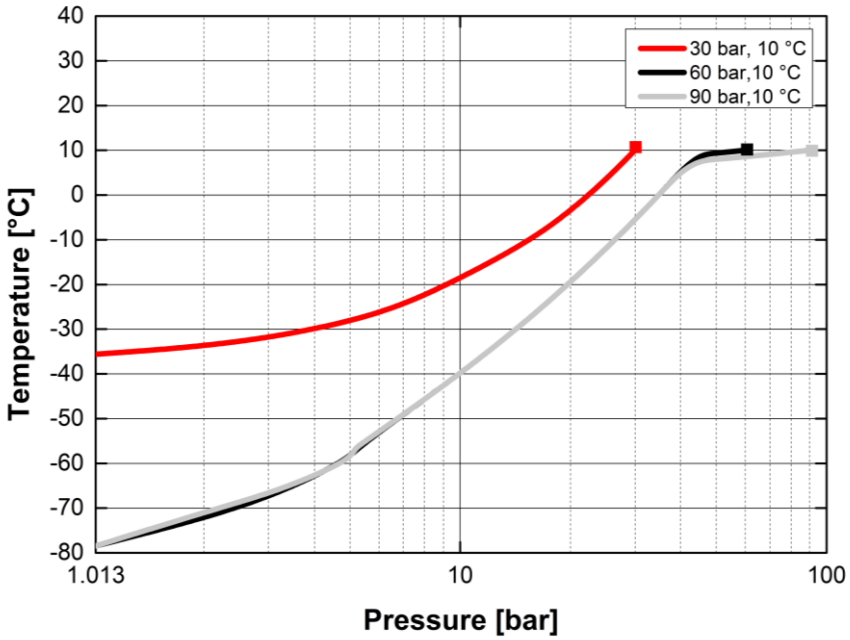

Figure 3.4. *Pressure-temperature profiles under the constant enthalpy condition. 30, 60, 90 barg, 10 °C expansions.*

Results presented in Figure 3.4 show very different trends than previously illustrated.

The (T, P) profile related to the CO_2 expanding from 30 bar preserves main features with a nearly constant μ_{JT} while staying in the single phase gaseous domain. Main difference is due to the final much lower expanded temperature (-35 vs -1.78 °C) mainly governed by different μ_{JT} values and by a wider pressure jump. As the storage pressure increases, a progressive decline of expanded temperature is to be expected at least until the final expanded point occurs within the gaseous domain.

Table 3.2 indicates the final expanded temperature depending on the initial storage pressure and temperature.

As previously indicated, an increase in the storage pressure leads to lower expanded temperature with values well below 0 °C while a corresponding increase in the storage temperature causes an opposite effect.

This observation is generally true just for isenthalpic paths leading to final thermodynamic states that belong to only gaseous phase. In other words all of the foregoing applies only to isenthalpic expansion paths whose thermodynamic state sequence occurs entirely in the gaseous or supercritical domain.

This, alternatively to sequences intersecting the vapour dome. Mathematically this corresponds to none or two different intersection points between the particular isenthalpic and the saturation curve.

Also the tangential situation belongs to this category representing the limiting mathematical case. Figure 3.5 sums up these topics on the CO_2 temperature-specific entropy diagram.

Table 3.2. *Predicted temperatures at atmospheric conditions following a constant enthalpy transformation.*

Initial pressure (bar)	Initial temperature (°C)	Final expanded temperature (°C)
5	0	-5.56
5	10	4.95
5	15	10.17
20	0	-30.52
20	10	-17.00
20	15	-10.50
30	0	-53.33
30	10	-35.62
30	15	-27.59

The case of a single intersection point is depicted in Figure 3.5 with a label and correctly represents the general situation belonging to phenomena of Figure 3.4 related to storage pressure of 60 and 90 bar.

Both the isenthalpic curves cut the saturation line only once and lead the CO_2 to a two-phase domain of liquid and vapour first and further to the final solid-vapour region.

Moving within the thermodynamics of equilibrium states, the final expansion temperature always matches the equilibrium one at atmospheric pressure that is 194.75 K. What differentiates expansions with altered initial conditions is the final quality of the solid-vapour mixture which then affects the released mass of CO_2 as a result of the process.

This can then influence the possibility of solid CO_2 soil deposition to form a dry ice bank and leading to further complexity in risk management of CCS infrastructures ([4,5]).

The trend of the mixture quality is depicted in Figure 3.6.

As shown an increase in pressure from 60 to 120 bar does not affect the qualitative trend of the vapour quality.

Above triple point pressure P_{tr} mathematical relation is almost linear indicating that during the depressurization the vapour CO_2 content of the liquid-vapour mixture increases up to 35-40 %.

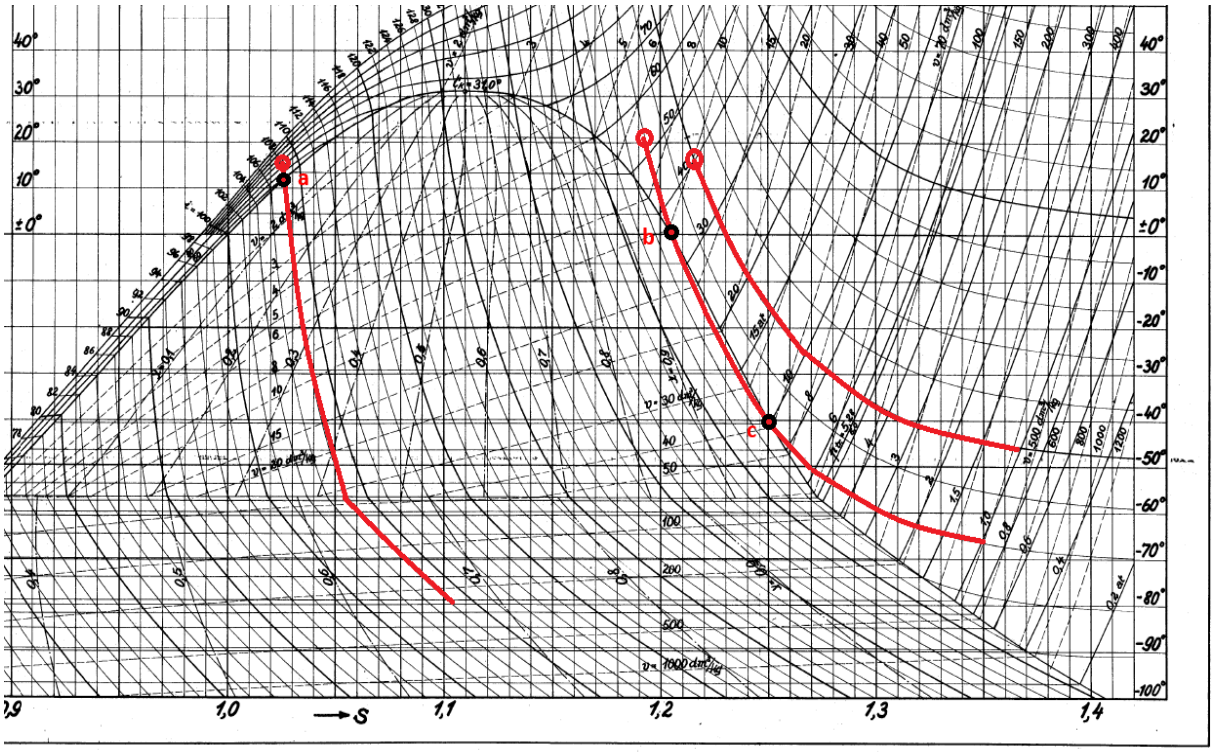

Figure 3.5. *Possible constant enthalpy pathways in CO_2 depressurizations. Point a: unique vapor-dome intersection point; points b and c: double intersection point.*

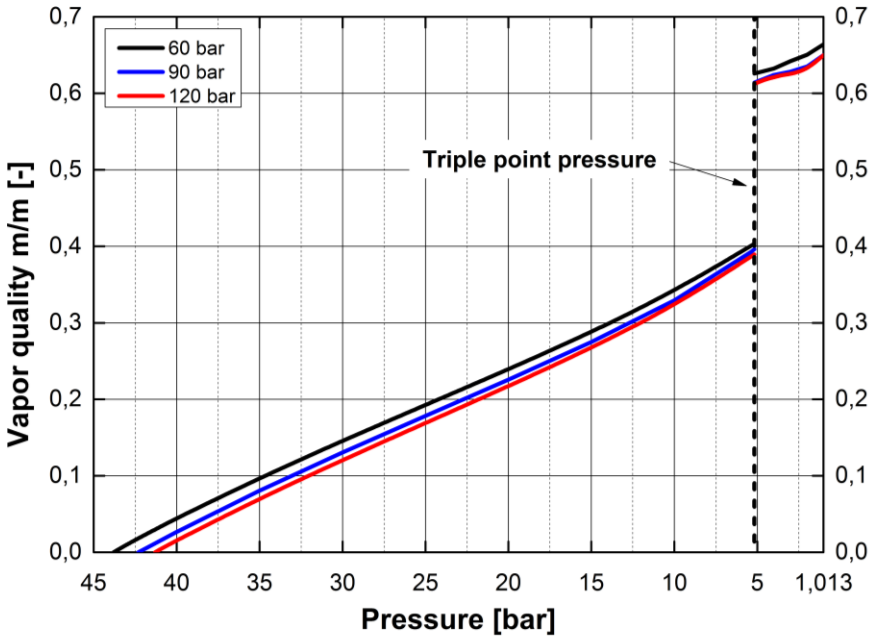

Figure 3.6. *Pressure-vapour quality profiles under the constant enthalpy condition. 30, 60, 90 barg, 10 °C expansions.*

Figure 3.6 shows also that the smallest value of pressure corresponding to the condition $x_v = 0$ (i.e. entry point to the two-phase LVE domain) is steadily located around 40-44 bar. These values mark the border between liquid and liquid-vapour domain. However passing from the LVE to the SVE domain the transition is not regular since it is characterized by a

sharp increase in the vapour content to 65 % at expansion occurred. This is mainly due to the difference between the properties of the gaseous and the solid phase of CO_2 especially for the specific volume and features along the saturation curves. In addition, the slope of the isenthalpic curves changes passing from LVE to SVE regions with an inclination closer to that pertaining to a constant vapour quality.

From a thermodynamic point of view this arises from the tendency of the thermodynamic system to restore its properties during the depressurization sharing them among the phases but keeping the overall enthalpy constant. The analysis has also shown that a variation in the storage temperature causes little alterations in the expansion dynamics and in the final value of the solid fraction. This is primarily due to the proximity of the different initial values in the thermodynamic plane since the corresponding steep isobaric curves are extremely close.

Table 3.3 shows the difference between the actual enthalpy at the initial point and that of the CO_2 at atmospheric pressure and 0 °C (assumed as the reference state).

Table 3.3. *Quantified enthalpy difference after the expansions from indicated conditions. Reference enthalpy state: 1,013 bar, 0 °C.*

Initial temperature [°C]	Initial pressure [barg]	Enthalpy difference [kJ/kg]
0	120	-302,56
	90	-301,39
	60	-299,61
	50	-298,82
	30	-55,24
	20	-37,27
	10	-23,21
10	120	-290,18
	90	-287,78
	60	-274,61
	50	-272,79
	30	-41,32
	20	-26,40
	10	-13,97
15	120	-269,41
	90	-266,07
	60	-260,33
	50	-77,53
	30	-34,93
	20	-21,13
	10	-9,37

Table 3.3 is useful to locate those thermodynamic state variable combinations that localize close initial points, i.e. those arranged along adjacent isenthalpic curves. For temperatures pertaining to Table 3.3, this applies to initial storage pressures higher than 60 bar. As pressure decreases the trend changes radically since a jump to the gaseous single-phase region takes place. In this area the dependency of the expansion dynamic from the pressure and temperature is stronger giving rise to paths with none, one or even two points of intersection with the two-phase region boundary. In practice, this implies that at low transportation pressures (less than 50-60 bar) a release may not give rise to solid deposition. This is especially true for all those points that lie above the isenthalpic tangent line to the vapour-dome that is reproduced in Figure 3.7.

The tangency condition should be evaluated searching via a numerical algorithm for the conditions of two identical intersection solutions between all isenthalpic lines and the saturation border line.

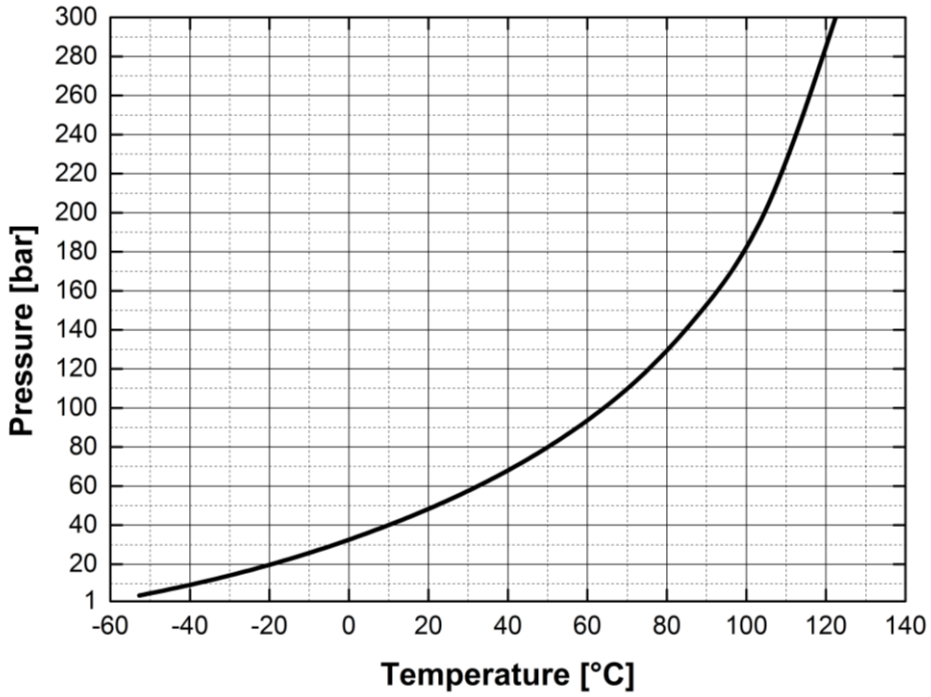

Figure 3.7. *Stagnation temperature-pressure couples giving rise to a constant enthalpy expansion tangents to the vapour-dome area.*

Usual transportation temperatures lie in the range from -10 °C to 35 °C ([2,4]) meaning that under these operative conditions, values for pressure over the range from 25 to 60 bar represent the limiting one for the dense phase formation.

In practice, these considerations should be linked to the best operational management of CCS infrastructures aimed at reducing both the costs and hazards related to safety. As will be

discussed in another chapter, it is also necessary to understand whether or not the formation of solid particulate contributes to increase the safety risks related to accidental CO_2 releases from CCS infrastructures.

From a merely thermodynamic point of view, it should be noted that after any expansion the CO_2 undergoes a process of rapid sublimation that reduces the size and the number of dry ice particles ([4]) thus increasing the forecasted vapour mass fraction.

Results of the detailed analysis of the theoretical relation between the final expected mass fraction and the initial storage temperature are reported in Figure 3.8.

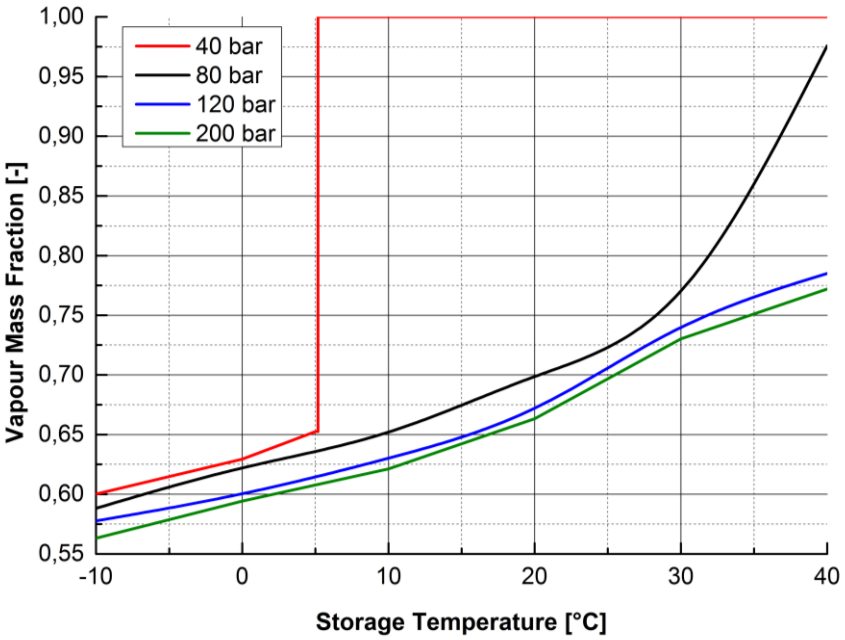

Figure 3.8. *Constant enthalpy post-expanded vapour mass fraction with respect to different initial storage conditions.*

The trend variability is very pronounced and is strictly depending on the storage pressure, this mainly governing the CO_2 aggregation state. An increase in the storage temperature involves higher vapour quality, i.e. a post-expanded mixture richer in gaseous CO_2. The growth trend is regular and continuous while maintaining the storage pressure over about 40 bar. An abrupt change is observed under this threshold. The jump is linked to the isobaric passage from the saturated liquid to the gaseous region and in this domain all isenthalpic curves are always concerning persisting gaseous CO_2.

The increase in the dense phase quality leads to deviations from the ideal behaviour and this is mainly observed in the specific volume departure. The single phase property gradually deteriorates while the dense phase quality increases.

It should be noted that during the expansion the specific volume can range through several orders of magnitude. EoS models suggest the following typical values for the pure CO_2 phases:

- liquid and supercritical 0.002-0.008 m^3/kg, much more dependent on the pressure that on the temperature;
- gaseous 0.01-0.5 m^3/kg, extremely dependent on the temperature, especially at low pressure;
- solid 0.0009-0.001 m^3/kg, with uncertainties related to the currently existing predictive models.

Multiphase CO_2 mixtures take intermediate values mainly driven by the relative content of each single phase. This content, in addition, is in turn forced by the preservation of the total system enthalpy.

Figure 3.9 gives the CO_2 mixture specific volume trend with respect to the pressure in the case of a constant-enthalpy expansion from 80 bar and 10 °C. The same graph is giving both trends of the saturated specific volume.

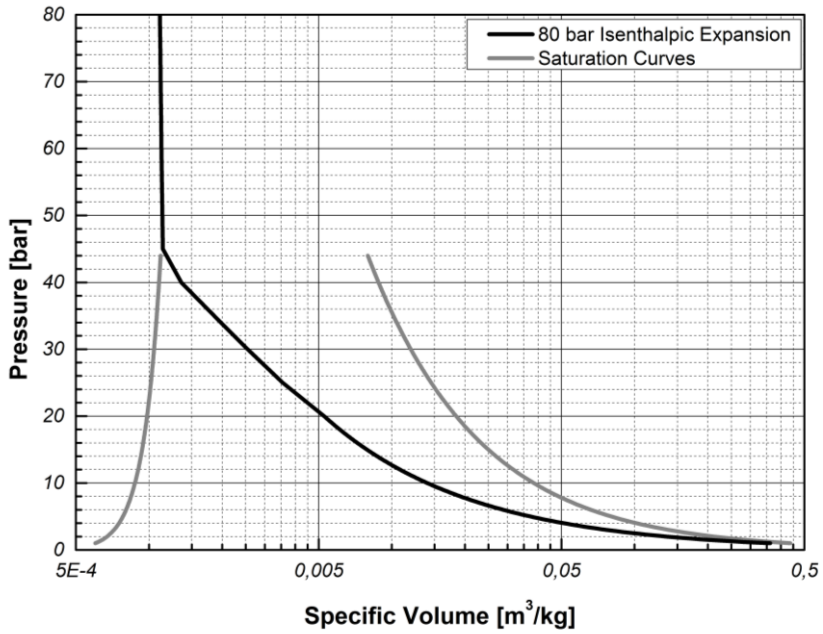

Figure 3.9. *Isenthalpic expansion from 80 bar, 10 °C. Specific volume trend with respect to gaseous, liquid and solid CO_2 saturated phases.*

While depressurizing, the CO_2 moves between the two saturation borders. The first stages down to a pressure of about 42 bar are involving a saturated liquid phase without any appreciable specific volume variations. At this pressure value, the isenthalpic expansion leads to the entrance in the vapour dome with a gradual vapour quality increase. The trend therefore moves towards the vapour saturation curve firstly passing in the liquid-vapour and then in the

solid-vapour equilibrium domain. The final mixture is composed by a 65.1 % by mass content of vapour and 34.9 % of dry ice. For QRA purposes, the solid portion will contribute to the dense gas dispersion following an atmospheric sublimation process.

The trend indicated in Figure 3.9 is almost preserved, at least qualitatively, varying the initial expansion pressure and maintaining the initial state in the dense domain (liquid or supercritical). But once the initial pressure crosses the critical value of 73.81 bar, the storage temperature turns out to be the main driver giving extremely variable trends. In this sense, for certain (P, T) pairs the expansion comes out exclusively with a decrease in the temperature coupled with an increase both in the specific volume and in the compressibility factor. In this case, the constancy maintenance of the total enthalpy does not imply the appearance of a different phase.

As an example, Figure 3.10 provides the specific volume tendency starting from a pressure of 50 bar and a temperature of 20 °C. The expansion is entirely occurring in the gaseous single-phase domain. The trend shows a strong increase in the CO_2 specific volume of two orders of magnitude with a final density approximately equal to 2.5 kg/m^3. This aspect is essential when assessing risks related to CO_2 releases since the main result of such these expansions is usually represented by the formation of a cold and very dense gaseous substance with respect to the surrounding air.

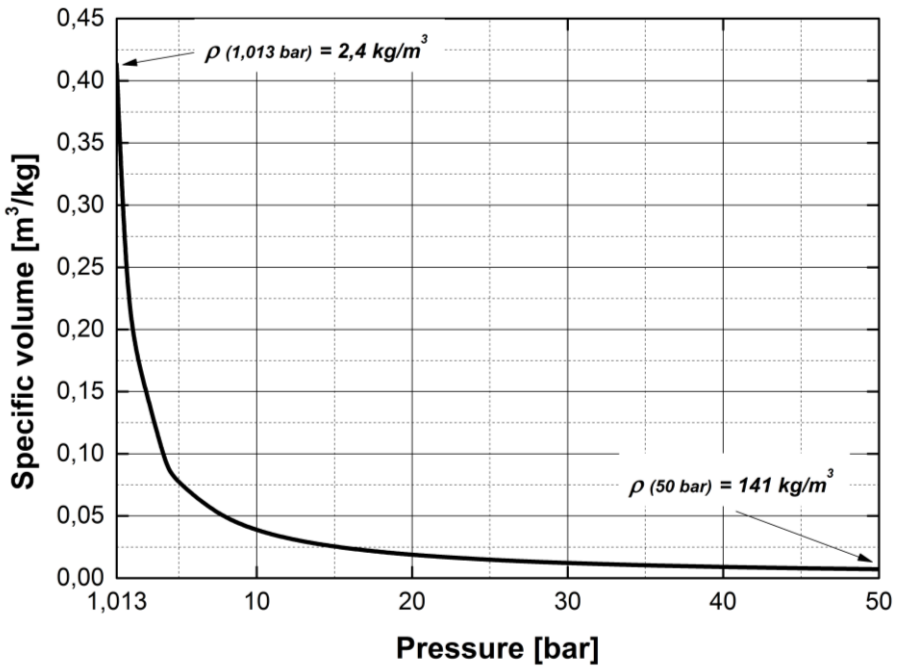

Figure 3.10. *Isenthalpic expansion from 50 bar, 20 °C. Specific volume trend with respect to the pressure. Initial and atmospheric expected densities are indicated.*

A more detailed investigation shows that a rough criterion to determine those conditions leading to an increase in the dense-phase fraction during depressurization can be formulated. This aspect along with a more strictly economic analysis can address the design of CCS infrastructures.

By applying the CO_2 EoS models, it can be proved that constant enthalpy lines satisfy following (3.65-3.67) conditions:

$$\left(\frac{\partial T}{\partial s}\right)_h < 0 \quad in\ the\ LVE, SVE\ and\ V\ domain\ , \tag{3.65}$$

$$\left(\frac{\partial T}{\partial s}\right)_h \geq 0 \quad in\ L\ domain\ for\ T \lesssim 263\ K\ and\ P > 250\ bar\ , \tag{3.66}$$

$$\left(\frac{\partial T}{\partial s}\right)_h < 0 \quad in\ SLE\ domain\ . \tag{3.67}$$

The discussion is valid for the temperature-specific entropy diagram but can be easily extended to any other domain with corresponding derivatives.

Therefore an isenthalpic line usually has a monotone descending character in almost the whole CO_2 existence domain if referred to the specific entropy, except for a portion of the saturated liquid phase domain that is not involved in CCS operations.

In addition the application of the EoS model gives reason to state that:

$$\left(\frac{\partial T}{\partial s}\right)_{h,LVE} > \left(\frac{\partial T}{\partial s}\right)_{h,SVE}\ . \tag{3.68}$$

meaning that an isenthalpic reduces its slope moving from the liquid-vapour dome to the solid-vapour coexistence domain.

The same behaviour is observed for the saturated vapour where in addition following (3.69) condition holds:

$$\lim_{P \to P_{amb}} \left(\frac{\partial T}{\partial s}\right)_h \to 0\ . \tag{3.69}$$

The previous equation applies only for non-intersecting curves (as previously defined) and basically shows that the gaseous CO_2 temperature tends to stabilize while expanding towards atmospheric conditions. In this sense, an isenthalpic expansion involving gaseous CO_2 will determine final temperatures well above than those detected in the case of multi-phase mixtures appearance.

In SLE domain a similar trend is observed with the addition that first derivative with respect to entropy is almost constant giving therefore rise to isenthalpic straight lines.

Moving to second derivatives, it can be proved that inflection points of isenthalpic curves are non-stationary points usually corresponding to slant inflections.

In the region of interest for CCS operations, these curves are always convex except for the saturated liquid domain where isenthalpic lines are convex upwards (concave). For the latter, the curve bordering the two-phase region is the locus of discontinuities of second derivatives. Therefore:

$$\left(\frac{\partial^2 T}{\partial s^2}\right)_h < 0 \quad in\ the\ saturated\ L\ domain\ , \tag{3.70}$$

$$\left(\frac{\partial^2 T}{\partial s^2}\right)_h > 0 \quad in\ LVE\ and\ SVE\ domain\ , \tag{3.71}$$

$$\left(\frac{\partial^2 T}{\partial s^2}\right)_h \sim 0 \quad in\ SLE\ domain\ . \tag{3.72}$$

Starting from these mathematical considerations it is possible to establish the conditions that maximize the solid content with respect to the storage conditions. This analysis applies only to curves having exactly one intersection point with the phase boundaries. Considering usual handling conditions, as discussed in Chapter 1, following considerations hold.

Firstly, the solid content of resulting CO_2 mixtures is characterized by a strong variability. CCS range of initial conditions may result in solid content up to 0.4-0.45 by mass achieved with lower temperatures and higher pressures. With an increase in the temperature this content decreases to give a final state characterized by only gaseous phase.

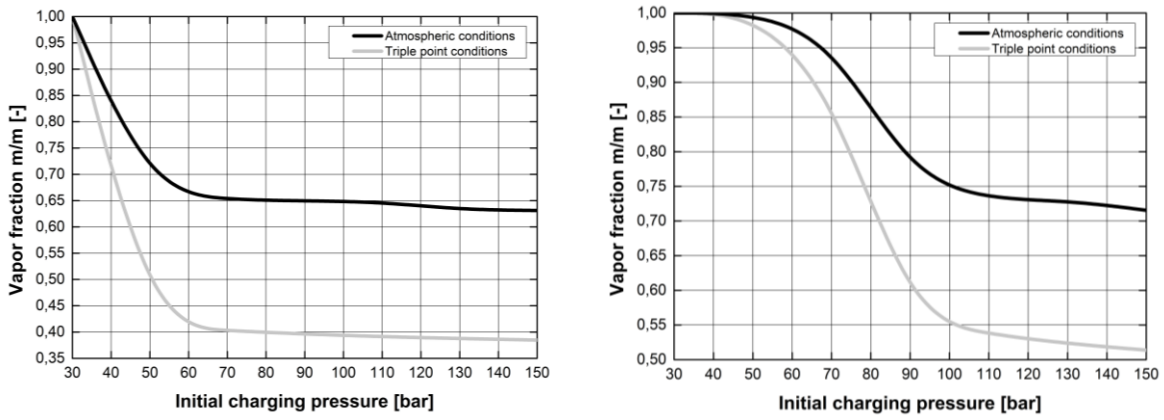

(a) *(b)*

Figure 3.11. *Expected vapor fractions at the triple point and at atmospheric conditions following constant enthalpy expansions from indicated storage pressures. Initial temperature: a- 10 °C; b- 30 °C.*

Larger solid contents are not consistent with CCS and EOR operations since are achieved for very high pressures and very low storage temperatures.

As an example, a sudden expansion from 300 bar and -50 °C gives rise to a mixture with 88 % by mass of solid content. In addition, the same isenthalpic line leads to the formation of a multi-phase mixture that is characterized by a liquid content greater than that of the solid expected at atmospheric conditions.

Figure 3.11a-3.11b give reason to this observation showing the vapour mass fraction trend with respect to different initial charging pressures. Two different trends are reported: the vapour content at the triple point pressure before entering the SVE domain and the final content expected at atmospheric conditions.

It may be observed that a growing storage pressure gives rise to mixtures characterized by an increased dense phase content. A stabilization in this dense phase appearance is observed above a threshold storage pressure and this is due to the closeness of isobaric curves in the dense domain in correspondence of temperatures below that of the critical point. Moving to lower pressures, the vapour content grows up to a completely saturated vapour mixture for pressure values depending on the storage temperature.

Table 3.4. *Expected CO_2 behavior once subjected to expansions at constant mixture enthalpy.*

Initial conditions	Post – expanded isenthalpic features
Gaseous saturated state	In the temperature operative range of CCS and EOR, the final state is gaseous, free from dense phase. Post expanded temperature is strictly depending on initial conditions. An increase in both storage pressure and temperature leads to higher post expanded temperatures. Some isenthalpic expansions for pressures in the range 40-60 bar match the appearance of a liquid phase that is subjected to phase-change mechanisms.
Liquid and supercritical saturated state	The post expanded temperature is no longer depending on the initial conditions being always equal to -78.4 °C. The expansion is always linked to the formation of a multi-phase mixture finally made of gaseous CO_2 and dry ice. An increase in the solid content is observed once the storage pressure is increased or the temperature is decreased. Concerning CCS and EOR operative conditions, maximum solid content theoretically expected is not greater than 40 % by mass. No liquid content is expected at post-expanded atmospheric conditions.

Moving from formulated considerations, a summary of the main features of the constant enthalpy CO_2 expansions are listed below:

- the (ideal) isenthalpic expansion may lead to the appearance of multi-phase CO_2 mixtures considering usual CCS and EOR operative conditions;
- an increase in the storage pressure leads to lower post-expanded temperatures but the relation is strictly depending on the initial CO_2 conditions.

In what concerning the latter, Table 3.4 is reported.

3.5.2 Constant entropy depressurizations

A rapid depressurization is also ideally bounded by an isentropic behaviour, that is the mixture during the expansion preserves its total specific entropy ([1,6]).

The isentropic trend is known to be a reversible and adiabatic transformation. This process is fictive since it is driven by frictionless work transfers, negligible heat transfer and is characterized by a putatively internal reversibility. In other words, the isentropic transformation is taking place in a thermally insulated system with respect to the environment. In real situations, the large domain dimensions do not ensure the adiabatic condition even if the expansion is taking place very rapidly ([6,7]).

This is to state that a real rapid depressurization is linked to an increase in the entropy mainly driven by 1st-species irreversibility. In fact any irreversibility contribution can be split in two different contributions:

$$dQ_{irr} = (dQ_{irr})_I + (dQ_{irr})_{II} \ . \tag{3.73}$$

Terms $(dQ_{irr})_I$ and $(dQ_{irr})_{II}$ refer respectively to first and second species irreversibility. $(dQ_{irr})_I$ is related to frictions linked to the CO_2 viscosity and the surface roughness as well as pressure and temperature gradients within the fluid while $(dQ_{irr})_{II}$ is only connected to the presence of chemical reactions.

Concerning CO_2 expansions, the rapid depressurization induced by an infrastructure failure is free from any chemical driving force and the corresponding term is thus neglected.

It should be noted that a gas with an ideal behaviour constrained to the conservation of the total specific entropy and subjected to the related hypothesis implies a Gibbs' equation with the structure of (3.74):

$$Tds = du + Pdv = c_v dT + Pdv = 0 \ . \tag{3.74}$$

The (3.74) is elaborated and integrated between two states 1 and 2 to give the (3.75):

$$P\,v^{c_p/c_v}\Big|_1 = P\,v^{c_p/c_v}\Big|_2 \ . \tag{3.75}$$

The ideal behaviour allows also for a different derivation that is based on the ideal-gas equation of state and leading to (3.76):

$$[Pv^k]_1^2 - e^{\Delta s/c_v} = 0 \ . \tag{3.76}$$

The (3.76) is matching (3.75) under the isentropic condition $\Delta s \to 0$.

This description applies only to moderately low pressures as to ensure and ideal gas behaviour with the compressibility factor $z \to 1$ and therefore expansions leading to the appearance of a dense phase are excluded. Considering usual CO_2 transportation conditions in terms of temperature, maximum initial storage pressures compliant with the imposed assumptions is equal to 10 bar.

So neglecting any dense-phase appearance in the system, the profile in terms of pressure and temperature is straightforwardly obtained by discretizing the thermodynamic reversible path in a series of successive states. However it should be noted that ideal gas specific heats change with the temperature therefore the analysis is carried out by tracing the thermodynamic pathway through small steps that are characterized by an arithmetical average value of the specific heats ratio, $\bar{k}$.

The scheme to be solved follows:

$$T_{i+1} = T_i \left(\frac{P_{i+1}}{P_i}\right)^{\bar{k}-1/\bar{k}} \ , \tag{3.77}$$

$$v_{i+1} = v_i \sqrt{\frac{P_i}{P_{i+1}}} \ . \tag{3.78}$$

Its application to gaseous CO_2 depressurizations from low pressures gives the results collected in Figure 3.12.

The main concern related to results obtained is related to the final post-expanded temperature at 1,013 bar. Temperatures reached appear to exceed that of equilibrium atmospheric condition (-78.5 °C). It is clear that the assumption taken leads to a deviation from the right thermodynamic behaviour that would instead always drive the system to a minimum temperature of -78.5 °C, if subjected to a theoretical isentropic expansion. While the expanded states lie in the low-pressure gaseous domain, the relation between the initial T_i and the expanded temperature T_f is well described by the following usual relation:

$$\frac{T_f}{T_i} \sim \left(\frac{P_f}{P_i}\right)^{\bar{k}-1/\bar{k}} . \tag{3.79}$$

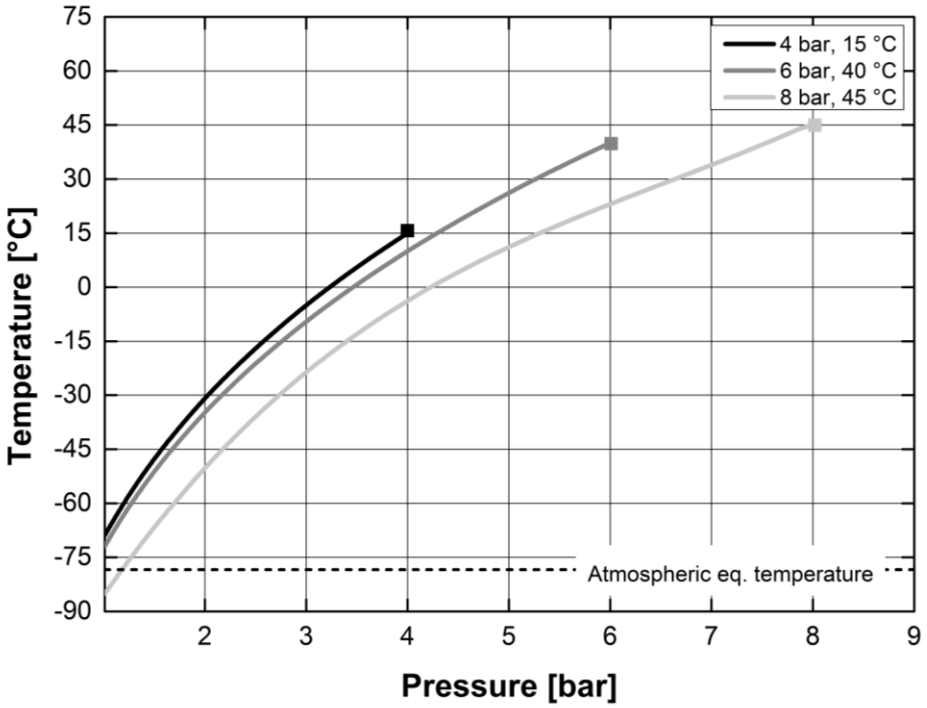

Figure 3.12. *Constant entropy expansion under the ideal-gas hypothesis from indicated initial conditions.*

So maintaining the initial temperature, an increase in the initial storage pressure determines lower expanded temperatures being the (3.79) exponent greater than 1. On the contrary taking a constant initial pressure value, an increase in the operative temperature determines higher final expanded temperatures. In addition, considered the relationship between the specific volume and the other thermodynamic state variables, an isentropic expansion may result in a significant specific volume increase. Still considering the initial domain of interest, specific volume may increase by 5 times up to 0.3-0.4 m^3/kg, this corresponding to a density three times higher than that of the air at atmospheric conditions.

To conclude, an approach based on the assumption of ideal gas behaviour seems to give approximated but reasonable results and this may help short-cut estimations when performing any preliminary QRA operation. However, the allowable application range is extremely limited (pressures up to 7.5-8 bar) and goes out from that of the CCS and EOR applications.

A more accurate and exhaustive description relies on the real gas approach and, under this hypothesis, the condition of constant specific entropy is formulated starting from the $ds = 0$ constraint as defined in (3.80):

$$ds = \frac{c_P}{T} dT - \left(\frac{\partial v}{\partial T}\right)_P dP = 0 \ . \tag{3.80}$$

In this way, the link between the pressure P and the temperature T under the imposed constraint is straightforwardly obtained as in (3.81):

$$\left(\frac{\partial T}{\partial P}\right)_s = \frac{T}{c_P}\left(\frac{\partial v}{\partial T}\right)_P \ . \tag{3.81}$$

The numerical integration of (3.81) firstly requires the analytical relation between the CO_2 specific volume v and the temperature T. At the same time, the constant pressure specific heat c_P, that is referred to the real gas state, is obtained from the ideal gas and residual contributions as follows:

$$c_P = {c_P}^{IG} + {c_P}^R = {c_v}^R - R + T\left(\frac{\partial P}{\partial T}\right)_v \left(\frac{\partial v}{\partial T}\right)_P \ . \tag{3.82}$$

The combination of (3.80-3.82) leads to (3.83):

$$\left(\frac{\partial T}{\partial P}\right)_s = \frac{T}{c_P}\left(\frac{\partial v}{\partial T}\right)_P = \frac{T\left(\frac{\partial v}{\partial T}\right)_P}{{c_v}^R - R + T\left(\frac{\partial P}{\partial T}\right)_v \left(\frac{\partial v}{\partial T}\right)_P} = \frac{\left(\frac{\partial v}{\partial T}\right)_P}{\frac{{c_v}^R}{T} - \frac{R}{T} + \left(\frac{\partial P}{\partial T}\right)_v \left(\frac{\partial v}{\partial T}\right)_P} \ . \tag{3.83}$$

The residual contribution ${c_v}^R$ and the partial derivative $(\partial P/\partial T)_v$ are directly assessed by means of a suitable EoS but some difficulties arise from the numerical evaluation of $(\partial v/\partial T)_P$. This is especially true when the EoS takes an implicit polynomial shape with respect to the specific volume.

In this sense, an explicit expression for the partial derivative with respect to the temperature cannot be obtained.

Any polynomial EoS up to 4th-degree (PREoS, YEoS) is formulated as follows:

$$\sum_{i=0}^{4} a_i(T,P) v^i = 0 \ . \tag{3.84}$$

It is not worth noting that an additional way to move around is by using the “cylindrical rule” of partial derivatives:

$$\left(\frac{\partial P}{\partial v}\right)_T \left(\frac{\partial T}{\partial P}\right)_v \left(\frac{\partial v}{\partial T}\right)_P = -1 \ . \tag{3.85}$$

In this way the unknown derivative is assessed from the other two once selected a suitable EoS model.

Then, by means of the Bridgeman's thermodynamic equation for $(\partial T/\partial P)_s$, the equivalent formulation of (3.85) is readily obtained:

$$\frac{(\partial T)_s}{(\partial P)_s} = \left(\frac{\partial T}{\partial P}\right)_s = -\frac{T}{c_P}\frac{\left(\frac{\partial P}{\partial T}\right)_v}{\left(\frac{\partial P}{\partial v}\right)_T} \ . \tag{3.86}$$

The use of (3.86) asks preferably for an explicit EoS in the pressure as well as a model for the estimation of the constant pressure specific heat.

Finally, a change in the temperature going from an initial to a final state through an isentropic path is given by the following (numerical) integration procedure:

$$\Delta T = T_2 - T_1 = \int_{P_1}^{P_2}\left(\frac{\partial T}{\partial P}\right)_s dP = -\int_{P_1}^{P_2}\left[\frac{T_{iso-s}}{c_P}\frac{\left(\frac{\partial P}{\partial T}\right)_v}{\left(\frac{\partial P}{\partial v}\right)_T}\right] dP \ . \tag{3.87}$$

In (3.87), T_{iso-s} is a dummy variable identifying the temperature that corresponds to the dummy integration variable P along the curve at constant entropy.

Results of the application of these concepts to the CO_2 case is explained below.

The modelling of suddenly isentropic expansion of CO_2 leads to the prediction of the temperature trend and phase fractions with respect to the pressure. As said, when dealing with CCS and EOR techniques, the final pressure is the atmospheric one since the CO_2 is intended to be then vented to atmosphere.

Modelling has firstly shown that the appearance of dense phase because of the isentropic depressurization is most common than the isenthalpic.

Figure 3.13 shows the limiting lower storage temperature, given the pressure, leading to dense phase appearance.

The curve should be read as follows: given a storage pressure, an initial temperature higher than that marked by the curve will lead to only gaseous CO_2. Below, the final atmospheric state will be characterized by the simultaneous presence of solid and gaseous phase.

Figure 3.13 is built on an array ending at 16 bar since higher values lead always to two-phase final states in the temperature range concerning CCS and EOR operations.

So moving to these situations, calculations point out that behaviours at constant enthalpy or entropy show similarities in the general trend even if different paths are observed in the SVE domain.

As an example, a rapid depressurization from 60 bar and 10 °C brings the CO_2 to results shown in Figure 3.14.

The VLE region exhibits a comparable tendency with the isenthalpic path driving the CO_2 towards higher vapour contents. The two curves tend to merge approaching the saturation line (Figure 3.14, bottom).

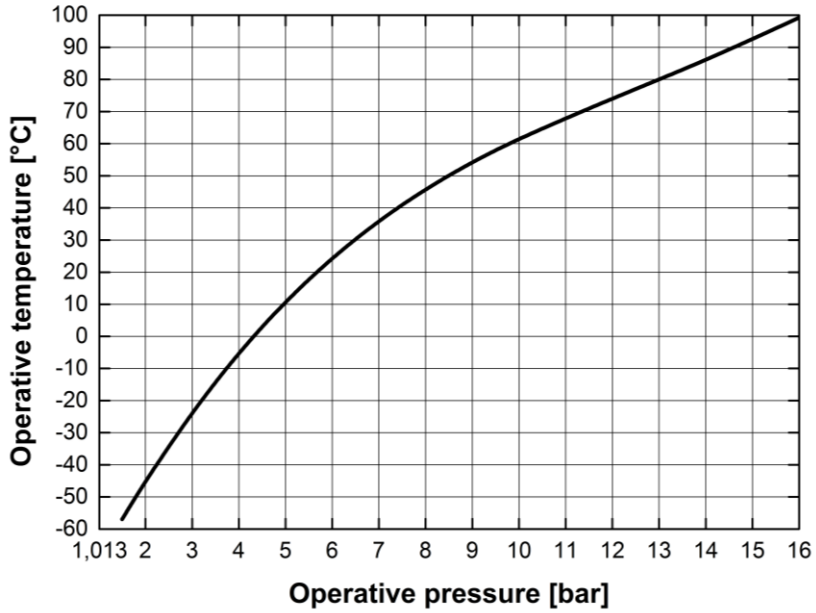

Figure 3.13. *Limiting (lower) storage temperature to dense-phase appearance during a constant entropy depressurization under different initial pressures.*

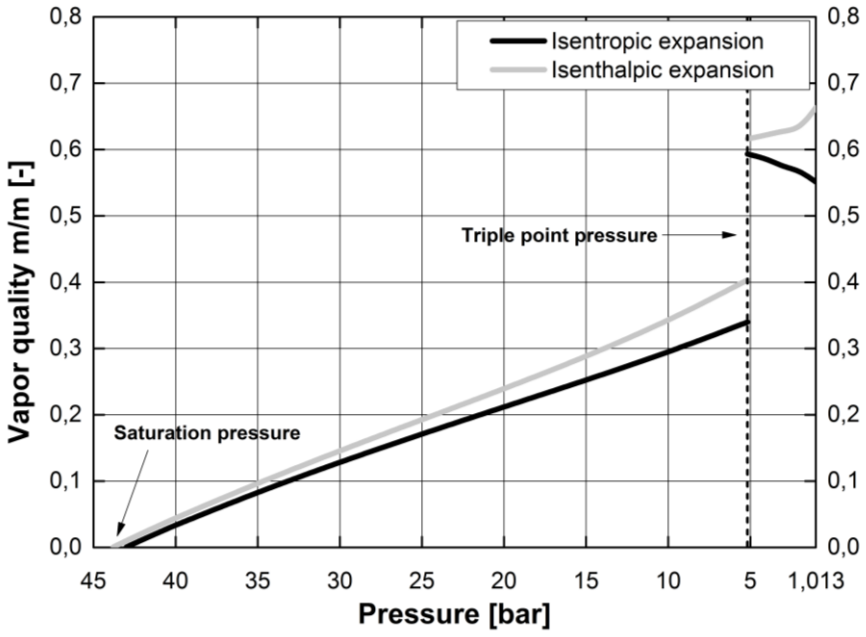

Figure 3.14. *Vapor quality trend with respect to the instantaneous pressure under constant enthalpy and entropy expansions. Initial conditions:60 barg, 10 °C. (The initial pathways in the liquid single-phase domain are not reported).*

As observed when dealing with isenthalpic depressurization, at the triple point pressure a discontinuity holds being sides limits different. However, main differences are observed with point belonging to SVE domain. Here quality derivatives with respect to the pressure are of opposite sign.

However, this behaviour is not general for isentropic depressurizations since a threshold vapour fraction value exists below which the trend described is exactly the opposite. Calculations shows that the threshold vapour quality value is approximately located along the constant-quality curve at 0.328 (32.8 % of vapour in the mixture). Anyhow, it should be noted that domains invoked by CCS and EOR specs always fall above the threshold value therefore giving a vapour content increase with decreasing pressure.

By using the proposed models, it is possible to depict isentropic depressurization paths below the triple point. As an example, an isentropic depressurization from 60 barg starting from different temperatures leads to varying vapour content. Figure 3.15 refers to this situation.

Calculations have not shown a general rule but it can be stated that under normal operating conditions this varies between 52 and 100 % in vapour content. Smaller values are obtained at higher transportation pressures coupled with lower temperatures. An isentropic expansion from 100 bar, instead, drives the CO_2 towards a solid content varying from 53.8 % with an initial temperature of 5 °C to 73.1 % at 50 °C.

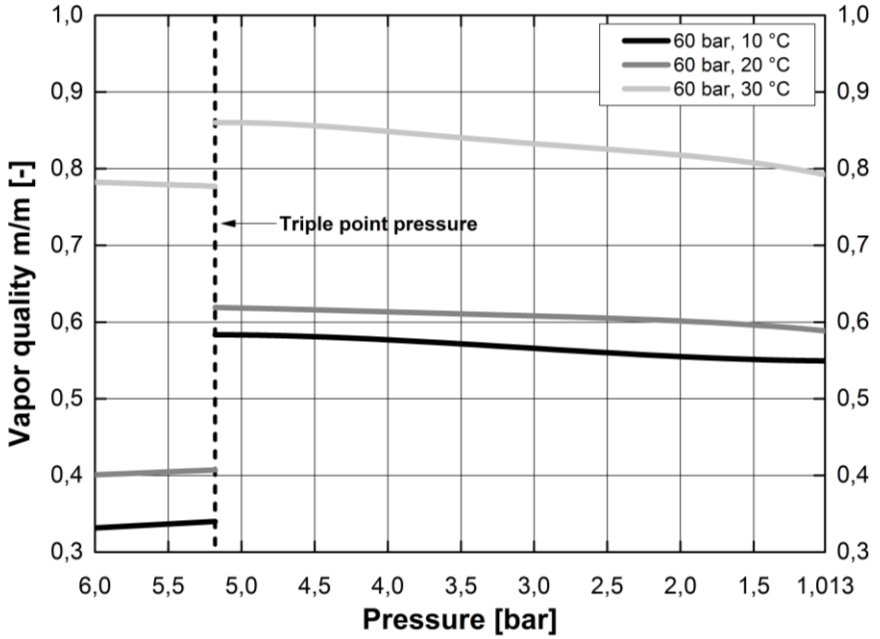

Figure 3.15. *Vapor quality trend with respect to the instantaneous pressure under constant enthalpy and entropy expansions. Initial conditions:60 barg, 10 °C. (The initial pathways in the liquid single-phase domain are not reported).*

Vapour fractions below 53 % are reached only for limited cases involving storage conditions characterized by very high pressure (> 150 bar) but very low temperatures (< -10 °C) that are not compatible with usual conditions. In addition, in the neighbourhood of the solid-liquid border region, the models lose accuracy with respect to the experimental reference points making them inappropriate.

A correct estimation of the vapour content is essential to a correct release modelling for two main reasons. Primarily a proper estimation of the vapour content allows for an acceptable estimation of the mixture specific volume and so of the overall amount released. Mixture properties are in fact based on weighted-average operations taking primarily into account the phase fractions.

The second reason is linked to the whole modelling activity and the possibility to lighten the calculations, especially when results should be urgently disclosed. From this point of view, the behaviour of mixtures with very high vapour content (i.e. greater than 90-92 %) below the triple point may be approximated to ideal gas. Such conditions are achieved for the initial pressure range 20-90 bar at ordinary operative temperatures. The usage of an ideal approach should always be checked.

Figure 3.16 gives a representation of the depressurization way using the real gas approach and the simplified ideal hypothesis. The expansion takes place starting from a storage pressure of 40 bar and a temperature of about 30 °C. The CO_2 comes to the triple point with a liquid mass fraction of about 12 % and ends at the atmospheric state with a solid fraction of 14.5 %.

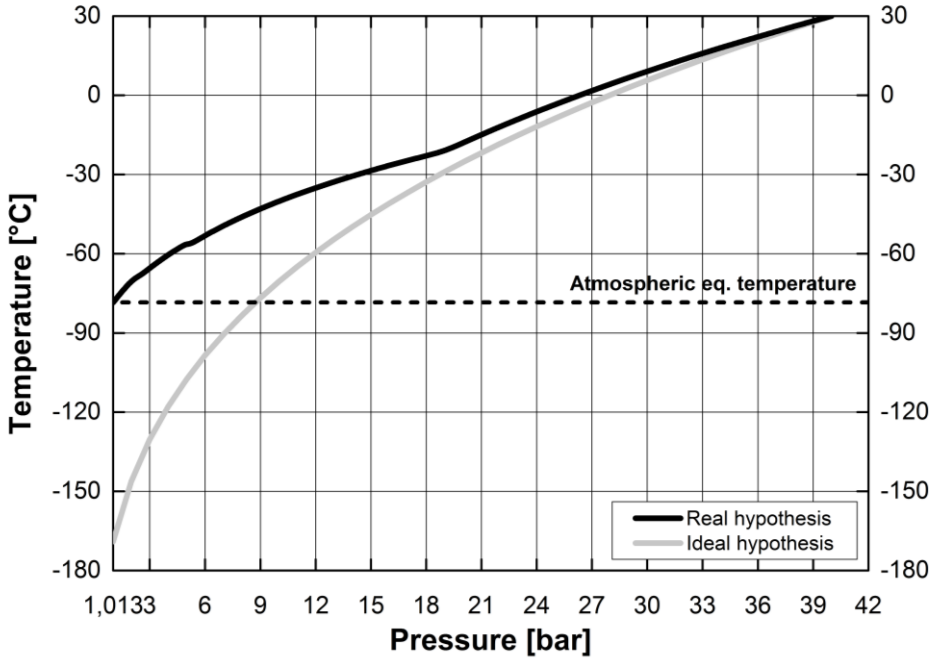

Figure 3.16. *Predicted pressure-temperature profiles under the ideal and real behaviour hypothesis. 40 bar, 30 °C expansion.*

When dealing with this type of expansions, it is clear from Figure 3.16 that the ideal expansion hypothesis leads to a deflected trend that is basically wrong. Once entered in the two-phase domain, the gap grows considerably resulting in meaningless states. Therefore the presence of a dense phase, even if limited in terms of mass quantity, greatly affects the whole behaviour making unsuitable the ideal assumption. This feature has been encountered in all the calculations related to mixtures at the triple point with a gaseous content greater than 88 %. This leads to the conclusion that an approach based on ideal considerations does not apply at all. A slight correspondence can be observed as long as the thermodynamic path lies in the single-phase domain where in general the description is sufficient. However it was observed that in this region ideal assumption fails when the pressure-temperature couple results in a compressibility factor differing from unity for more than 15 % ($0.85 < z < 1.15$).
Further attention must be paid since simplified conclusions based on the main driver of non-ideality, that is the compressibility factor, may mislead.
The investigated expansion outlines compressibility factor values set out in Figure 3.17.

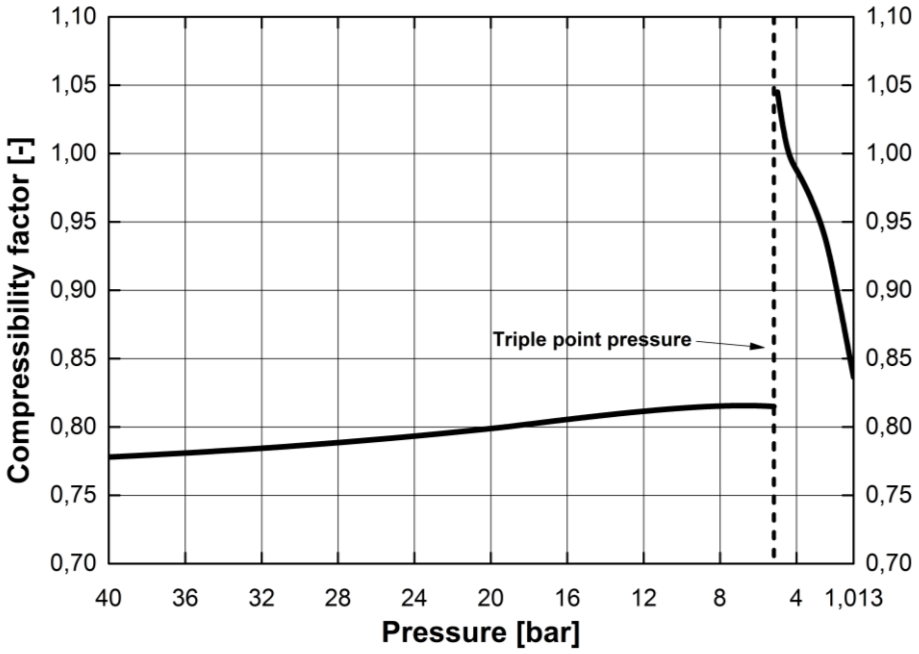

Figure 3.17. *Predicted mixture compressibility factor profile under the real behaviour hypothesis. 40 bar, 30 °C expansion.*

The region investigated falls in a domain characterized by compressibility factor values not far from unity. The criterion, also equivalently based on the fugacity, therefore suggests a quasi-ideal behaviour making apparently reasonable the use of the ideal-gas EoS. However, Figure 3.16 reveals a clear inaccuracy. Probably the main reason is inherent the approximations included in the ideal-gas specific heats.

It should be noted that usually ideal-gas heats requires only the knowledge of the temperature since they are given by empirical equations summarized under the following form:

$$\frac{C_p^0}{R} = A + BT + CT^2 + DT^{-2} \qquad T\ in\ [K]\ and\ T < 2000\ K\ . \tag{3.88}$$

The (3.88), however, cannot be extended in the SVE region since the lower limit of the temperature is located at 298 K. This reason drives the choice towards more useful links such as those based on hyperbolic functions ([1,7]).

Figure 3.18 depicts the constant-pressure and volume heat capacities under the ideal-gas approximation (saturated conditions) in comparison to those estimated from more complicated EoS model. Results refer to the 40 bar, 30 °C expansion under investigation.

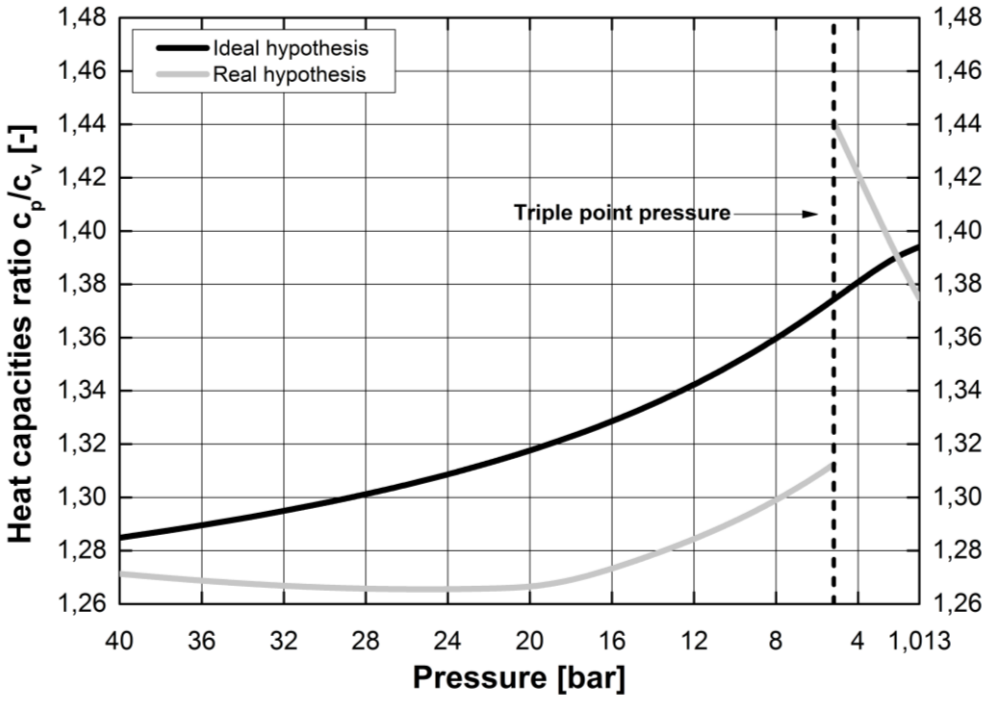

Figure 3.18. *Predicted mixture heat capacities ratio profile under the ideal and real behaviour hypothesis. 40 bar, 30 °C expansion.*

Figure 3.18 refers to the saturated vapour branch since ideal-gas model aims at describing solely the non-dense domain. It would be conceptually wrong the application of this approach to the description of the dense phases that occur during the depressurization. So the only feasible analysis should be applied to the gaseous phase during all the expansion path that is the single-phase gaseous CO_2, the CO_2 vapour in equilibrium with its liquid until the triple point and that in equilibrium with its solid dry ice going down to equilibrium atmospheric temperature.

The modelling of the expansion from 40 bar based on ideal assumptions is erroneous with respect to the more detailed analysis. The latter, in fact, reveals an irregular trend of specific heats ratio mainly driven by non-idealities. Taking as an ideality reference the trend depicted in Figure 3.18, the distance between the two behaviors is very wide. It is evident that neglecting the effects of pressure in the specific heats calculation, many errors are introduced leading to a constant overestimation of their ratio. The latter, appearing then as an exponent, further affects the estimation of pressure-temperature trend.
So even if the compressibility factor trend principle would claim a quasi-ideal behavior, when dealing with isentropic and isenthalpic expansions attention must be paid since this assumption may fall also for moderate pressures.
In other cases, it was found that these assumptions almost fail to describe the CO_2 behavior during depressurization so they will be omitted hereafter.

3.5.3 Prediction of choked flow conditions. Critical CO_2 mass flux

A natural consequence of risk assessment concerning a CO_2 transportation infrastructure is for sure the estimation of the mass of the released substance because of a rupture.
The amount released is driven by several factors. The most important are:

- storage conditions (mainly pressure and temperature);
- establishment of choked flow conditions;
- orifice size;
- presence of impurities.

Among these, storage and *choked* flow conditions may be handled using thermodynamics. As discussed by some authors ([1,3,6,7]) the modelling requires at least the following properties:

a. specific volume;
b. specific enthalpy;
c. specific entropy;
d. number and nature of the phase fractions.

All these properties should be readily obtained by reliable thermodynamic methods. The proposed EoS approach is one of the most convincing since it relies on mathematical formulations based on plentiful experimental data.
Thermodynamic properties are required for the actual multi-phase mixture as well as for the saturated phase conditions matching the actual one at every instant.
The analysis will therefore move to the prediction of choked flow conditions during rapid depressurization of CO_2 that may involve the occurrence of liquid-vapor and solid-vapor mixtures.

It should be underlined that the *choking* flow is essentially a compressible effect. Flows are typically considered compressible if the density of the fluid changes appreciably throughout the fluid field. These variations are usually driven by changes in the pressure and in the rate of change of density with pressure is closely connected to the velocity of propagation of small pressure disturbance (weak pressure wave but not shocks); that is, the velocity of sound in the fluid c. The sonic velocity is derived from a momentum balance based on the assumption that the compression induced by the pressure wave is adiabatic and frictionless, and therefore isentropic ([1,3,4]). So what has said concerning the isentropic behaviour is still valid.

To give a general expression of the sonic velocity let us consider a piston impulsively moving at a relatively small velocity. The sudden acceleration acts as a disturbance and in absence of viscosity and wall effects induces a planar pressure wave moving at the local medium speed of sound. As the pulse will be infinitesimally small, the continuity in the pressure and density fields may be assumed.

Now considering a control volume attached to a pressure pulse a mass balance yields (3.89):

$$(P + dP) - P = (\rho + d\rho)(c - du)^2 - \rho c^2 \ . \tag{3.89}$$

Neglecting higher order terms the (3.90) is obtained:

$$dP = (\rho + d\rho)c^2 - \rho c^2 \ , \tag{3.90}$$

and finally (3.90) yields:

$$c^2 = \left(\frac{dP}{d\rho}\right)_s \ . \tag{3.91}$$

The (3.91) is the fundamental expression of the speed of sound in any fluid medium and an expression is needed to represent its right hand side.

The speed of sound can be therefore evaluated through different strategies.

Firstly, it can be easily obtained for the EoS for an ideal gas (and perfect gas) because of a simple mathematical expression.

Considering the constancy in the entropy, the speed of sound is readily calculated from:

$$c = \sqrt{\left(\frac{dP}{d\rho}\right)_s} = \sqrt{\frac{c_p}{c_v}\Big|_{IG} \frac{P}{\rho}} = \sqrt{\frac{c_p}{c_v}\Big|_{IG} \tilde{R}T} \approx \sqrt{\left(\frac{\Delta P}{\Delta \rho}\right)_s} \ . \tag{3.92}$$

This approach, however, may induce large errors because of the aforementioned not ideal CO_2 behavior already at moderate pressures.

Secondly, the sound speed can be derived from CO_2 compressibility factor data, thus giving more reliable results especially under the real-behavior hypothesis. This approach, however, requires more mathematical expressions and, on this light, the (3.93) applies:

$$\frac{d\rho}{\rho} = \frac{c_v}{c_p}\left[\frac{z + T\left(\frac{\partial z}{\partial T}\right)_P}{z + T\left(\frac{\partial z}{\partial T}\right)_\rho}\right]\frac{dP}{P} \ . \tag{3.93}$$

The expansion transformation may be modelled through the following (3.94) integrated form:

$$\left(\frac{\rho_1}{\rho_2}\right)^\delta = \frac{P_1}{P_2} \ , \tag{3.94}$$

where δ, for convenience, is defined as follows:

$$\delta = \frac{c_p}{c_v}\left[\frac{z + T\left(\frac{\partial z}{\partial T}\right)_\rho}{z + T\left(\frac{\partial z}{\partial T}\right)_P}\right] \quad with \ \ \delta \to \frac{c_p}{c_v} \ \ if \ z \to 1 \ . \tag{3.95}$$

The (3.95) then gives a tool to determine δ starting from compressibility CO_2 factor data. It applies only for gaseous CO_2 since the derivation does not consider the dense phase existence. Once estimated δ by using a suitable EoS or experimental data, it is then possible to obtain the speed of sound estimation in the same way as for the ideal gas:

$$c = \left(\frac{dP}{d\rho}\right)_s = \sqrt{\delta Z \tilde{R} T} = \sqrt{\frac{c_p}{c_v}\left[\frac{Z + T\left(\frac{\partial Z}{\partial T}\right)_\rho}{Z + T\left(\frac{\partial Z}{\partial T}\right)_P}\right] Z \tilde{R} T} = \sqrt{\frac{c_p}{c_v}\vartheta \tilde{R} T} \ . \tag{3.96}$$

The (3.96) is similar to the (3.92) except for the correction of non-idealities.

However the (3.96) is used since changes in temperature may lead to huge variations in the speed of sound even at moderate pressures. The (3.96), in fact, shows that what is relevant to the calculation of c is not only the instantaneous value of z but also its velocity variation with temperature at constant density and pressure.

Once the EoS model is available and (3.96) is applied, the CO_2 choked flow states are then derived.

This limiting condition in the discharge dynamic is assessed with the evaluation of the expected specific mass flux G_{choked}.

As discussed by some authors ([1,3,4,6]), estimations are based on the knowledge of the stagnation state that are actually matching the CO_2 initial operative state and those following the release evolution.

The choked mass flux is therefore derived from an optimization that is corresponding to the imposition of the following mathematical constraint on the mass flux G:

$$\left.\frac{\partial G(P)}{\partial P}\right|_{P=P_{choked}} = 0 \ , \tag{3.97}$$

this matching the condition of maximum mass flux G_{choked} at the choked pressure P_{choked}:

$$G_{choked} = G(P_{choked}) = \max_{P} G(P) \ . \tag{3.98}$$

Starting from 10 bar and different initial temperatures, the predicted mass fluxes G_{choked} down to the triple point pressure (5.18 bar) is reported in Figure 3.19.

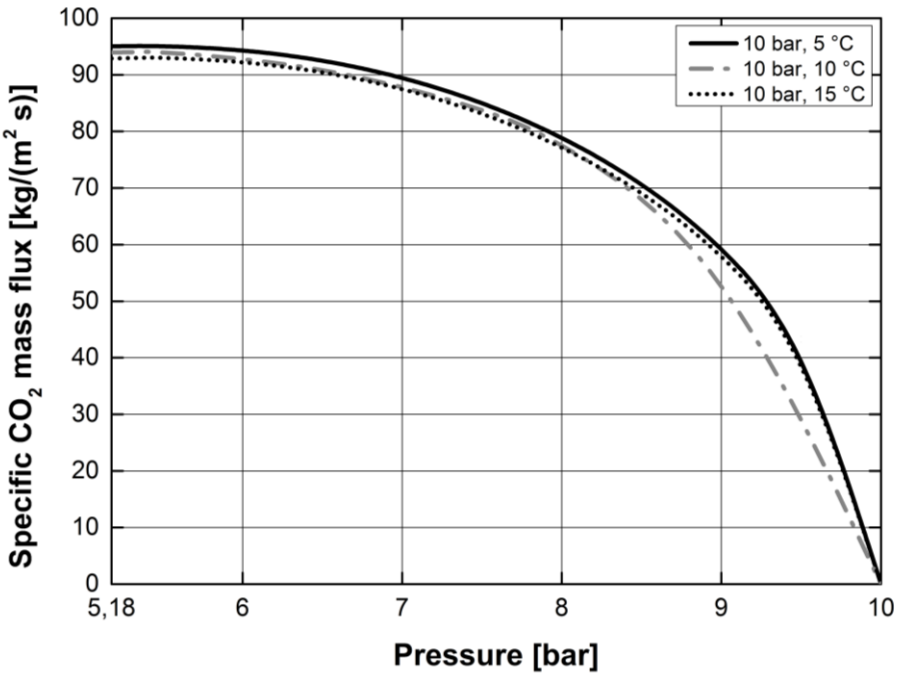

Figure 3.19. *Predicted CO_2 mass flux with respect to the instantaneous stagnation pressure down to the triple point. 10 bar release.*

Peculiar features of Figure 3.19 are firstly related to the increase in the specific mass flux with a decrease in the pressure with respect to the initial value. This behaviour is common to compressible substances and it is related to an increase in the pressure driving force inducing larger discharged flow rates. It should be noted that the mass flux increase is not progressive

and shows a stabilization around the triple point pressure because of the variations in the CO_2 specific volume and the substance instantaneous energy content.

In this sense, the resulting mass flux is driven by the combination of the instantaneous specific volume, specific enthalpy and entropy being these instantaneously affected by the local pressure and temperature.

On this regard, as it will be explained in the model illustration section, the following relation holds:

$$G\big(P,T(P)\big)=\frac{1}{v}\sqrt{2\big[h_0-h_{sat,L}+T_{tr}\big(s_{sat,L}-s\big)\big]}\ , \tag{3.99}$$

giving therefore indication of the dependency of the instantaneous mass flux G from the state variables through the enthalpic and entropic state functions as well as the instantaneous specific volume $v(P,T)$.

With respect to fig. Figure 3.19, no local maxima in G are observed indicating, in the range (5.18;10) bar, the lack of a choked state. This occurrence has also been observed by some authors ([2,3]) showing that in this range the choked pressure P_{choked} is almost matching P_{tr} with:

$$G_{choked}=\max_P G(P)=G(P_{tr}). \tag{3.100}$$

In the case of very low pressures (P $\lesssim$ 7 bar) a maximum in the the mass flux is observed in accordance to a pressure value $P<P_{tr}$ thus indicating the occurrence of a choked state in the SVE domain. The corresponding choked pressure value is well approximated by the ideal gas choked pressure ([3]). The applicability of the ideal gas approach in ensured by the very low amount of solid phase resulting from the isentropic expansion.

Results show that higher charging pressures determine the occurrence of two distinct choked states each pertaining respectively to the LVE and the SVE region. However, in the SVE region the determination of G_{choked} is also based on the instantaneous mixture solid mass fraction x_s being the respective mixture specific volume expressed as follows:

$$\begin{aligned} v=&\frac{s-s_{sat,L}}{s_{sat,V}-s_{sat,L}}\big(v_{sat,V}-v_{sat,L}\big)\\ &+x_s\left[\big(v_{sat,S}-s_{sat,L}\big)+\frac{s_{sat,L}-s_{sat,S}}{s_{sat,V}-s_{sat,L}}\big(v_{sat,V}-v_{sat,L}\big)\right]. \end{aligned} \tag{3.101}$$

This results in a different optimization criterion that is used in the model algorithm to give the G_{choked} estimation and that is reported in (3.102):

$$G_{choked} = \max_{x_S} G(x_S) = G_{choked}(x_S) \ . \tag{3.102}$$

The occurrence of one or two distinct choked states is strictly depending on the initial stagnation CO_2 conditions. However, no generally applicable criteria are observed being the choked states occurrence derived by the influence of the expansion path on the instantaneous determination of the mixture properties.

The estimations down to the triple point pressure, following a 30 bar release, are reported in Figure 3.20.

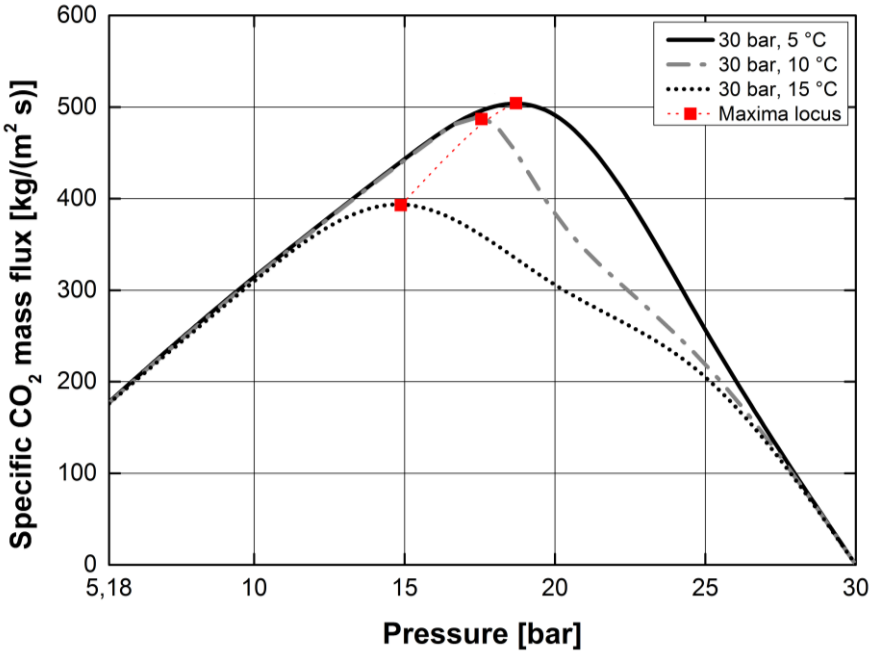

Figure 3.20. *Predicted CO_2 mass flux with respect to the instantaneous stagnation pressure down to the triple point. 30 bar release.*

Focusing on Figure 3.20, what makes the depressurization behaviour from a 10 bar expansion, is the discussed occurrence of the choked state for an intermediate pressure between the stagnation pressure P_0 and P_{tr}. Once the local maxima in G are linked, the resulting locus shows a dependency also on the initial stagnation temperature T_0 as reported in Figure 3.20.

The meaning of Figure 3.20 is that once the pressure decrease is taking place, the establishment of the choked state at the corresponding P_{choked} is observed. The resulting mass flux is the maximum and equal to G_{choked}. A 30 bar release is determining mass flux varying from 350 to 550 kg/(m^{2}s). Lower values are matching a higher initial thermal content. The respective P_{choked} is ranging from 15 to 20 bar.

The deviation from the ideal gas choked pressure is relevant with an increase in the stagnation pressure. Under the P_0 > 12 barg condition, the real behaviour induces positive deviations from the ideal gas P_{choked}.

Considering the CO_2 phase diagram, it should be noted that maxima of Figure 3.20 match different states that are pertaining to the VLE region. The marked difference in their locations is linked to the variations in the initial stagnation states that are altered because of the modification in the initial temperature.

The gaps are more limited once the charging pressure is increased for example up to 60 bar as reported in Figure 3.21.

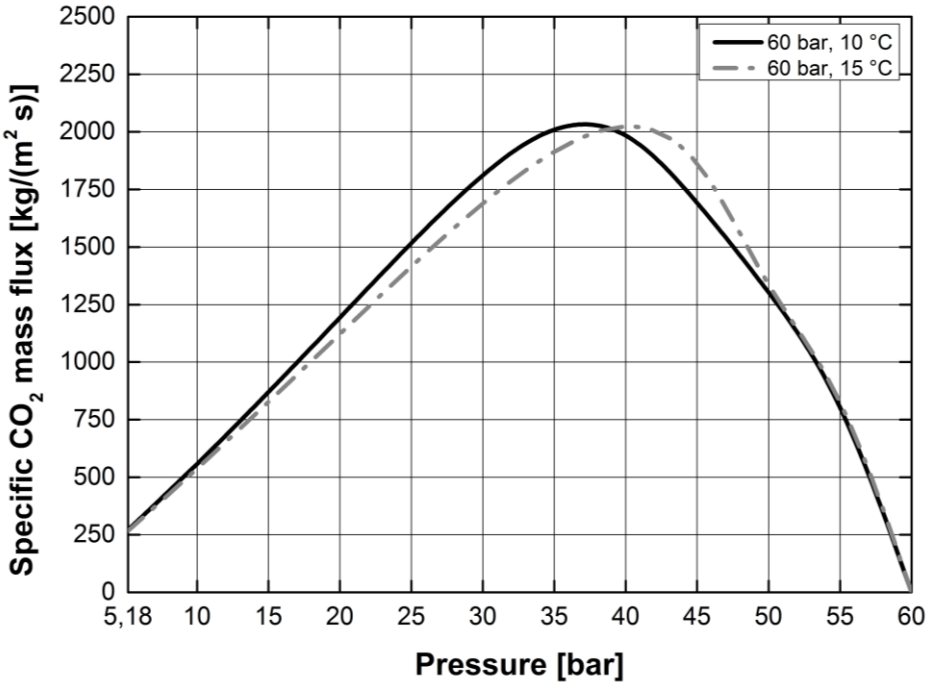

Figure 3.21. *Predicted CO_2 mass flux with respect to the instantaneous stagnation pressure down to the triple point. 60 bar release.*

In this sense, a variation in the initial temperature relatively alters the location of the stagnation state under moderate pressures. Resulting G_{choked} are comparable even under different initial states and an increase in the charging pressure leads to larger G_{choked} values. Isentropic curves departing from this region are almost comparable and this feature results in similar G_{choked} magnitudes. A sensitivity of P_{choked} with respect to initial conditions is observed thus requiring its evaluation in the model algorithm.

A gap of 30 bar increase the expected choked mass flux of 4 times and this value will match the discharged CO_2 during the related stationary sonic flow evolution.

Further pressure increases will modify the G_{choked} value as reported in Figure 3.22.

A variation of the pressure from 70 to 110 bar allows the G_{choked} to raise up to 3500 kg/(m^2 s). In this pressure range, P_{choked} tends to preserve its magnitude around 40 bar. Choked flow states quite always match a mixture of liquid and gaseous CO_2 with a vapor quality mainly depending on the initial conditions.

As highlighted by some authors ([2,3,6]), the pertaining vapour quality at the choked state, for a given P_{choked}, is increasing with the initial enthalpic content. From a practical point of view, the resulting mixture from an increase in the stagnation enthalpy h_0 will be characterized by larger vapor contents. Given the smaller magnitude of the vapor specific volume with respect to the dense phase, smaller mass fluxes are therefore expected.

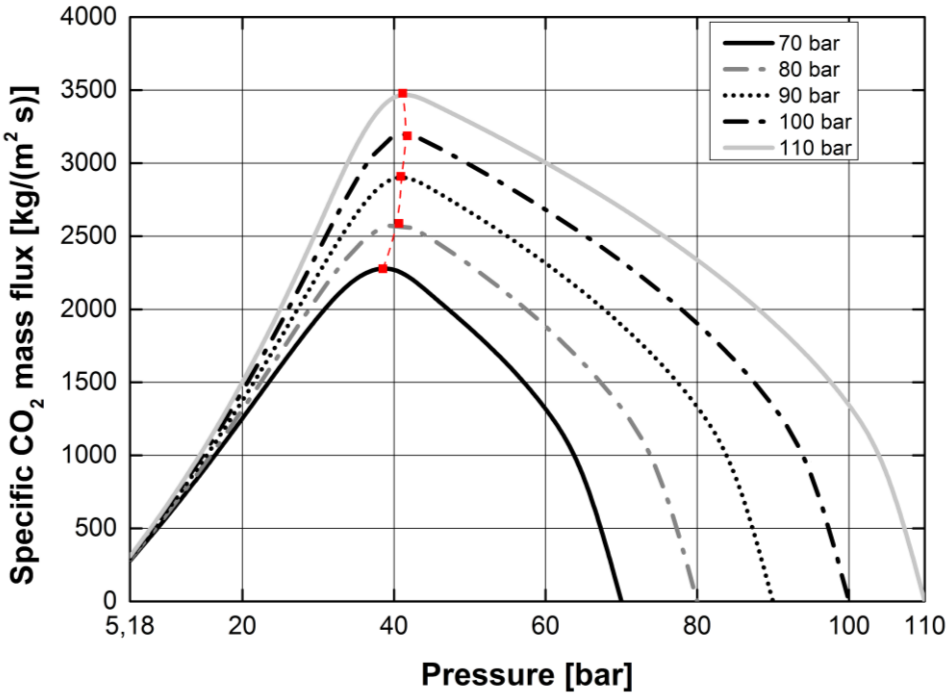

Figure 3.22. *Predicted CO_2 mass flux with respect to the instantaneous stagnation pressure down to the triple point. Charging pressures higher than 70 bar.*

Specific initial conditions are determining multiple choked flow states. The pressure domain may be divided into two ranges that are bounded by the triple point pressure P_{tr} = 5.18 bar. Situations corresponding to $P > P_{tr}$ have already been discussed in relation to the occurrence of a choked state characterized by G_{choked} depending on the specific initial conditions. All the states that are contemplating more than one phase result to be in the VLE domain.

Calculations show however that depending on the stagnation conditions, the mass flux may exhibit two maxima thus indicating the occurrence of two distinct choked states. No generalized indications can be provided regarding the initial conditions leading to this peculiar situation even if the second choked state is always located in the SVE region. The resulting mass flux for $P < P_{tr}$ is that characterizing a vapor flow carrying solid CO_2.

As a title of example, following Figure 3.23-3.24 give a detailed indication of the mass flux evolution under these specific features.

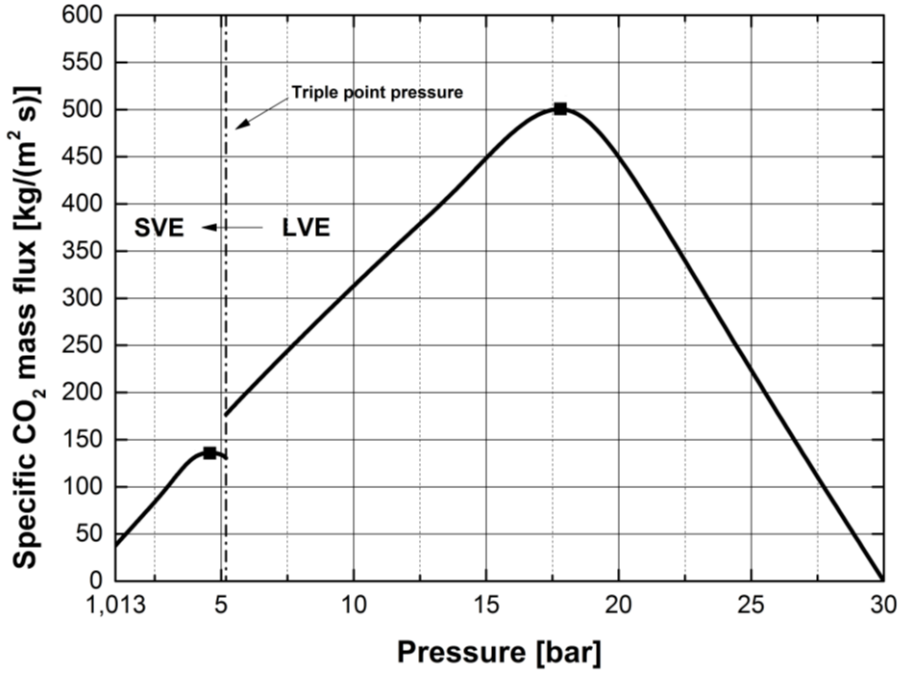

Figure 3.23. *Predicted CO_2 mass flux with respect to the instantaneous stagnation pressure down to atmospheric conditions. 30 bar, 10 °C release.*

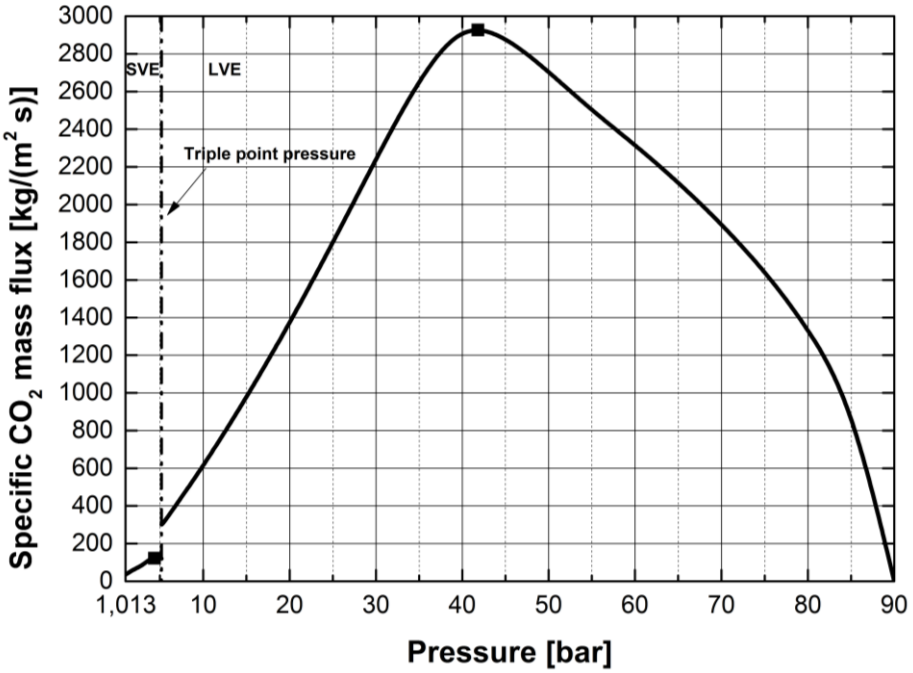

Figure 3.24. *Predicted CO_2 mass flux with respect to the instantaneous stagnation pressure down to atmospheric conditions. 90 bar, 10 °C release.*

In Figure 3.23-3.24, the investigated initial conditions lead to the appearance of the already discussed state for $P > P_{tr}$ and to an additional G local maximum for $P < P_{tr}$.

The pertaining P_{choked} value is approximately corresponding to a near ideal-gas behaviour and can be given by the usual (3.103) that is depending on the specific heat ratio γ:

$$\frac{P_{choked}}{P_0} = \left(\frac{2}{1+\gamma}\right)^{\gamma/\gamma-1} . \tag{3.103}$$

The quasi ideal-gas assumption holds because the solid-vapor mixture is mainly composed by vapor that is at low pressure ($P < P_{tp}$). In addition, results give reason to state that the choked mass flux is almost insensitive to the stagnation pressure P_0 if $P < P_{tp}$, consistently with this hypothesis. This is also shown in Figure 3.23-3.24 where G_{choked} in the SVE region is almost equal to 150 kg/(m^2 s) in both cases.

The discontinuity in the G profile for $P = P_{tp}$ is always observed and is due to the passage from VLE to SVE at the triple point. The latter is therefore a direct consequence of the jump in the thermodynamic state variables and functions of a mixture changing from VLE to SVE.

Additional observed discontinuities at $P = P_{tp}$ concern $x_V(P_{choked})$ that experiences a rapid increase in the passage to $P < P_{tp}$ that is directly linked to the peculiar CO_2 behaviour at the triple point. Further investigations show that the solid content in the SVE mixture can range from 2 % to more than 55 %.

It should be observed that once more than one choked state is forecasted, the depressurization will firstly drive the CO_2 to that pertaining to the higher pressure, i.e. that in the VLE domain.

This analysis, beyond the theoretical aspects, is useful to drive the model development and implementation.

In this sense, the logic algorithm will be structured to allow for:

- the evaluation of the establishment of choked flows;
- the calculation of related discharge parameters.

The latter consisting in the choked flow nature (number and type of expected thermodynamic facing phases), the mixture quality at choked conditions and the discharged mass flux that it is then linked to the orifice transversal section.

The procedure will be based on an iterative procedure since an instantaneous variation in the stagnation conditions following the release will change the nature of the choked flow accordingly.

References to Chapter 3

1. National Institute of Standards and Technology, NIST Chemistry WebBook, http://webbook.nist.gov/chemistry; 2014-12-02.
2. Mahgerefteh, H., Brown, S., Martynov, S., 2012. A study of the effects of friction, heat transfer and stream impurities on the decompression behavior in CO_2 pipelines. Greenhouse gases: science and technology 2, 369-379.
3. Martynov, S., Brown, S., Mahgerefteh, H., Sundara, V., Chen, S., Zhang, Y., 2014. Modelling three-phase releases of carbon dioxide from high-pressure pipelines. Process safety and environmental protection, 92, 36-46.
4. Kornneef, J., Spruijt, M., Molag, M., Ramirez, A., Faaij, A., Turkenburg, W., 2009. Uncertainties in risk assessment of CO2 pipelines. Energy Procedia, 1(1), 1587-1594.
5. Mocellin, P., Vianello, C., Maschio, G., 2015. Carbon capture and storage hazard investigation: Numerical analysis of hazards related to dry ice bank sublimation following accidental carbon dioxide releases. Chemical Engineering Transactions, 43, 1897-1902.
6. Benintendi, R., 2014. Non-equilibrium phenomena in carbon dioxide expansion, Process Safety and Environmental Protection, 92, 47-59.
7. Le Bellac, M., Mortessagne, F., Batrouni, G.G., 2010. Equilibrium and non-equilibrium statistical thermodynamics, Cambridge University Press, UK.

Chapter 4

Laboratory-scale Experimental Investigation of CO_2 Pressurized Releases

This section firstly illustrates the arranged experimental setup used to perform CO_2 pressurized releases under controlled conditions. Both mechanical and measurement components are described.
Secondly, the experimental results are collected and discussed with special focus on the transient pressure and temperature profiles and on the total discharge time.
The final part covers the discussion about the derivation of the required parameters for purpose of the model development.

4.1 Introduction

The description of the experimental setup used to perform pressurized releases of CO_2 and collected results is proposed.
The equipment is sized in order to bear operative pressures up to 110 barg while the initial CO_2 parameters are kept under controlled conditions.
It is mainly composed by the stainless steel storage tank and the discharging line and a set of measurement devices is arranged in order to investigate and record main release parameters at specific locations.

4.2 Aim of the experimental investigation

The proposed experimental investigation is planned to throw light on the evolution of the main CO_2 properties during a rapid depressurization from initial controlled conditions. The collection of these parameters is essential in any model development procedure since a completely predictive model may suffer inaccuracies or unreliable results.
The collected CO_2 parameters are listed below:

- internal temperature, i.e. inside the system, approximately matching the bulk conditions;

- external surface temperature;
- relative pressure to ambient conditions approximately matching the bulk conditions.

The analysis of these collected data allows for the investigation of the thermal and mechanical dynamic induced by the system depressurization.

In addition:

- the bulk recorded information, if suitably matched through a reliable EoS model, are enough to fully characterize the thermodynamic CO_2 behavior;
- the external surface temperature, if suitably linked to the bulk conditions, is able to give information on the heat amount locally transferred through the solid walls.

As it will be discussed later, measurement devices are arranged at suitable locations to follow the variables evolution in characteristic points where major pressure and temperature gradients are expected.

4.3 Experimental setup description

The experimental setup is mainly composed by the following components that are briefly described below: the CO_2 storage tank and the discharge system.

The charging line is not taking part at the experimental measurements since it is arranged for loading operations only.

4.3.1 Graphical overview of the experimental setup

The schematic representation of the experimental setup is reported Figure 4.1 with the indication of the main mechanical components and of the measurement devices.

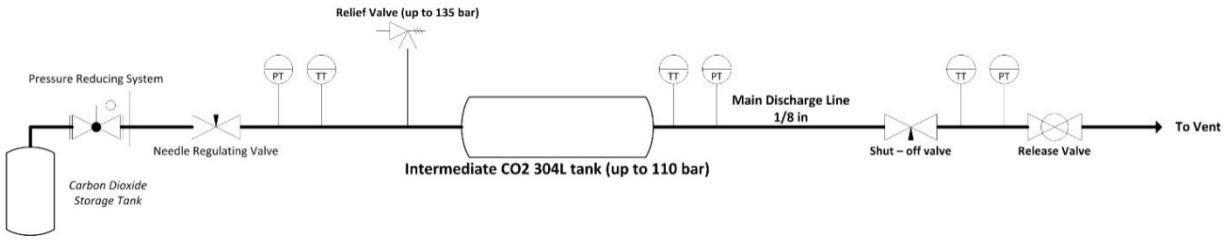

Figure 4.1. *Schematic representation of the experimental setup.*

Figure 4.2-4.3 gives further details on the experimental setup.

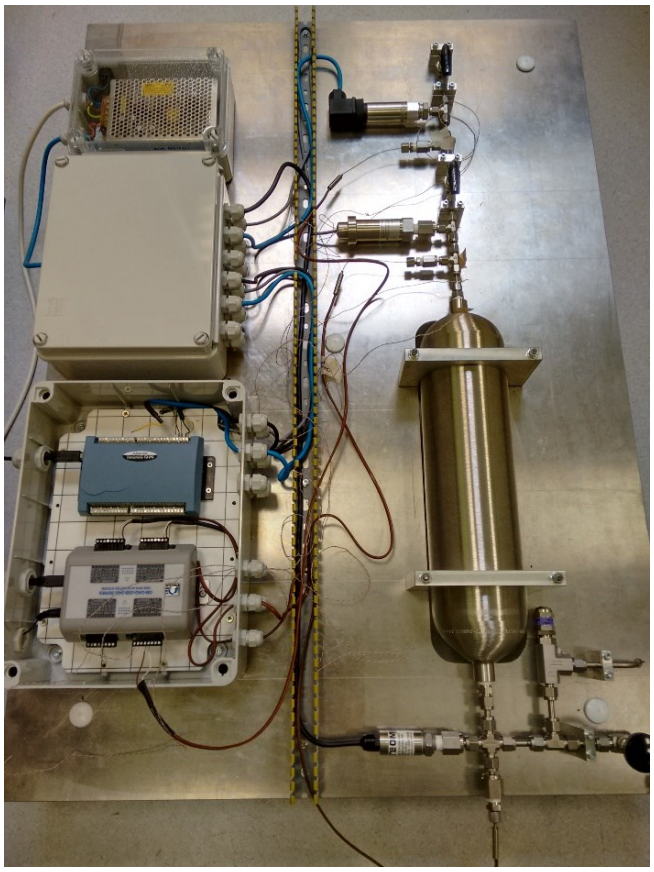

Figure 4.2. *Experimental setup overview.*

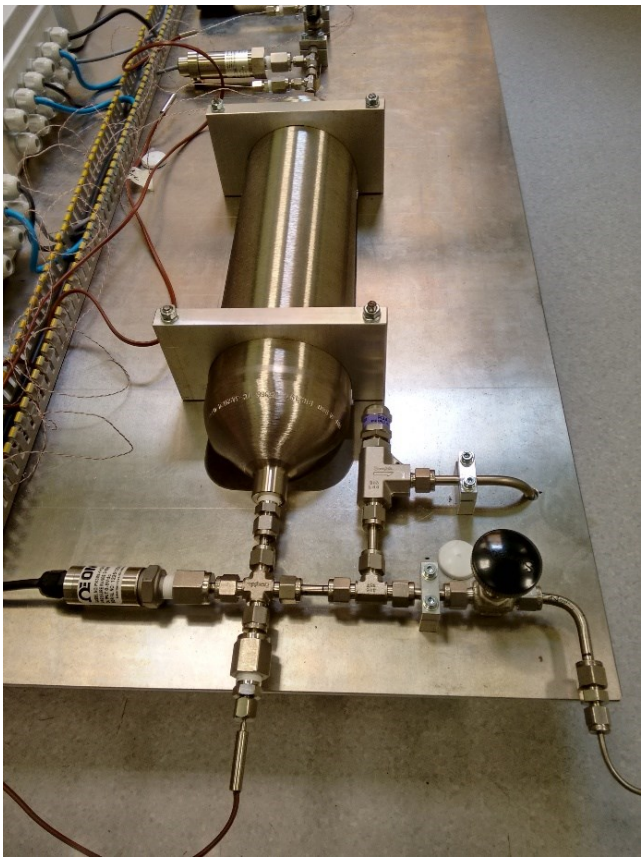

Figure 4.3. *Experimental setup. Vessel and charging system.*

4.3.2 Mechanical components

4.3.2.1 CO_2 storage tank

The CO_2 storage tank used during the experimental trials is discharged from a dedicated cylindrical vessel made of 304 L austenitic steel. The vessel material selection, as well as its sizing, has considered the occurrence of moderate temperature and pressure gradients.

In this sense, the capability to bear pressures up to 110 bar is ensured by a minimum wall thickness of 2.4 mm and the stainless steel ensured a good compatibility with the CO_2 that may exhibit acidic properties.

The tank has an external diameter of 102 mm and its internal volume amounts to 2.3 l.

As indicated in Figure 4.1, one end is connected to the charging line through which the CO_2 is conveyed prior to the release experiment. The other side, instead, is linked to the discharging line.

For safety reasons, the vessel is equipped with a safety calibrated spring-type valve to avoid uncontrolled pressure raises.

Main properties of arranged materials are reported in Table 4.1.

Table 4.1. *Main physical and chemical properties of the constituent stainless steels used in the experimental setup.*

Steel Type	C content [%]	Heat Capacity [kJ/(kg K)]	Density [kg/m^3]	Thermal Conductivity [W/(m K)]
Austenitic 304L	≤ 0.03	0.49 – 0.53	7.85 – 8.06	14 – 17
Austenitic 316L	≤ 0.03	0.49 – 0.53	7.87 – 8.07	13 – 17

4.3.2.2 Discharge line

A 316 L stainless steel line is dedicated to the discharging process of the CO_2 from the storage tank to the atmospheric environment. Main results are obtained with a pipe sector characterized by an external diameter of 3.175 mm and a constant wall thickness of 0.71 mm. An additional line section characterized by a doubled internal diameter has been used.

Its layout is perfectly straight in order to minimize and keep under control the pressure drops. The geometry of the discharge line is characterized by a ratio between its length and the internal diameter equal to about 150.

The discharge line is equipped with two ball valves of the same internal section of that of the pipe. No insulation is expected that is conductive and external convective heat transfer mechanisms are allowed respectively across the solid pipe walls and the surrounding stagnant air.

4.3.2.2 Charge line

The CO_2 is conveyed from a reservoir to the storage tank through a dedicated supplementary tube. The modeling procedure is not considering this section of the experimental setup since it is not involved in the release evolution.

Once the charging procedure is completed, the whole experimental part involved in the release is physically excluded from the load line through a dedicated valve.

It should be underlined that the vessel filling procedure is carried out very slowly meaning that small amounts of CO_2 are transferred to the storage tank in order to ensure the following results:

- the avoidance of heating mechanism related to the filling process;
- the retaining of thermal imbalances between the vessel bulk and the solid surface temperature.

These linked phenomena should be kept under control in order to facilitate the establishment of a thermal equilibrium between the CO_2 inventory and the storage vessel mass.

The alteration in the CO_2 transferred temperature is due to a mere thermodynamic reason that originates from the balance between the Joule-Thompson effect and the expected heating process linked to the compression mechanism induced by the charging process. In this sense, the CO_2 temperature tends to increase once the compression and the conversion of supply enthalpy energy to cylinder internal energy overcomes the Joule-Thompson cooling effect. The latter becoming progressively smaller as the tank pressure increases.

4.3.3 Measurement devices

Data concerning the release evolution are recorded by means of suitable measurement devices. These are arranged in specific locations as indicated in Figure 4.1 and consist of temperature and pressure sensors as detailed below.

4.3.3.1 Temperature measurement components

The temperature evolution is recorded with selected thermocouples.

It should be underlined that following expected features are governing the equipment choice:

- occurrence of instantaneous temperatures well below 0 °C because of the expansion mechanism;
- occurrence of rapid temperature variations that need to be accurately and rapidly recorded.

These aspects are strictly linked to the thermocouples features and translated in terms of device typology and size.

Considering the first required feature, thermocouple type-T are suitable for the indicated purposes because of their capability to work at very low temperatures as indicated in Table 4.2.

More precisely, thermocouples type-T are suitable for the expected application since the operative temperature range lies in the range between -250 and +400 °C in short term measurements and between -185 and +300 °C when used in continuous applications.

Table 4.2. *Main properties of arranged internal thermocouples.*

Temperature Range [°C]	Repeatability Temperature Range [°C]	Material	Sensibility [μV °C^{-1}]	Standard Error Limits [%]
-270 to 370 °C	-200 to 200 °C	Cu – Ni	48.2	1.0 °C / 0.75 % above 0 °C 1.0 °C / 1.5 % below 0 °C

The declared thermocouples accuracy is equal to ±1.0 °C above -67 °C and with a temperature dependence that can be expressed as in (4.1):

$$\Delta T = \pm 0.0015 \cdot |T_{measured}| \qquad T_{measured} \in [-67\,°C; 100\,°C] \quad . \tag{4.1}$$

Used thermocouples are arranged both inside and outside of the equipment, the latter on the stainless steel external surface. Because of this distinction, different type-T thermocouples are selected. Focusing on the internal measurement devices, thermocouples are characterized by varying diameters being these strictly related to the characteristic response time. In this sense, the diameter selection is mainly governed by the measurement location. Thinner thermocouples are required where expected thermal dynamics are faster and more fluctuating. On this basis, the devices specs are those reported in Table 4.3-4.4. Considering Table 4.3, the internal tank thermocouple is characterized by a greater external diameter since slower thermal dynamics are expected with respect to those forecasted along the discharge line. In addition, the size of the devices arranged on the line is taking also into account possible interferences with the flowing field that is predominantly perpendicular to the device setting.

Table 4.3. *Internal type-T thermocouples. Specifications ([1]).*

Location	Thermocouple type	External diameter [mm]	Response time at 63.2 % [s]	Coating material
Tank (inside)	T (Cu – Ni)	1.75	0.180	Stainless steel
Discharge line (inside)	T (Cu – Ni)	1.5	0.150	Stainless steel

Table 4.4. *External type-T thermocouples. Specifications ([1]).*

Location	Thermocouple type	External diameter [mm]	Response time at 63.2 % [s]	Coating material
External surface	T (Cu – Ni)	0.2 (exposed wires)	0.01	Polyimide

External thermocouples are consisting of sticky thermocouples with exposed wires because no specific problems are expected with respect to substance compatibility. These devices are characterized by an isolated thermocouple cable made of polymeric perfluoroethers and the measurable temperatures are ranging between -50 and +250 °C.

4.3.3.2 Pressure measurement components

Pressure sensors are arranged near the thermocouples and are such to ensure short response times and adequate accuracy, especially in the investigated pressure ranges. In addition, a large sampling rate is required during the blowdown phenomena in order to throw light on the instantaneous pressure variations.

Identified measurement devices for this purpose are characterized by a piezoresistive and silicon-based technology as indicated in Table 4.5.

Table 4.5. *Pressure sensors. Specifications.*

Pressure Sensor	Type	Location	Average Response Time [s]	(Declared) accuracy [% FS]	Temperature Compensation [°C]
Omega ([2])	Silicon type with SS diaphragm	Tank	< 1e-3	0.10	-70 to 100 °C
Schneider Technik ([3])	Thin film piezoresistive ceramic	Discharge line	< 5e-4	0.05	-60 to 150 °C
Druck EP ([4])	Micromachined silicon type	Discharge line	< 5e-4	0.04	-55 to 80 °C

Sensors, as indicated in Table 4.5, are characterized by different average response times that are strictly linked to the installed technology. More performing devices are installed along the discharge line where pressure drops are responsible for wide pressure variations and where the relative arrangement is more sensitive to pressure fluctuations.

Devices located in the discharge line offer a declared response time lower than $5e^{-4}$ s with stated accuracies down to 0.04 % FS. The tank pressure is instead investigated using a sensor with a sampling rate of 1 kHz and an accuracy of 0.10 % FS.
The temperature compensation is ensured in the sensor technology as well as in the adopted calibration procedure. Certified compensated temperature ranges are reported in the last column of Table 4.5 and are fully complying the experimental investigated temperature values. Therefore, no considerable temperature-related measurement errors are expected.
More details are demanded to the specific technical documentation ([2,3,4]).

4.3.3.3 Data acquisition devices (DAQs)

DAQs modules are devoted to the data acquisition and recording procedure of the electrical signal derived from the physical sensors. They allow for the interfacing between the sensor and the personal computer through specific software tools.
The logging procedure of data collected during the experimental trials is achieved by using two distinct DAQs that are respectively dedicated to the management of the temperature and the pressure measurements.
Each DAQ is characterized by suitable specification that are related to the measurement device properties (average response time, natural and resonant frequency, accuracy and measurement noise). From this point of view the selection of the DAQ sampling rate capability is accurately chosen and linked to the device specifications. For example, the specific frequency of the pressure sensors has been identified as the governing driver of the DAQ sampling rate choice while thermocouples specs are not representing a limiting condition.
For these reasons, in all the experimental trials, pressure signals are collected by using a sampling rate between 30 and 150 kS/(s ch) (kiloSamples per second per channel) with a resolution up to 14 bit that is the maximum provided by the composite channel DAQ. Temperature measures are instead recorded with a maximum sampling rate of 200 S / (s ch) at 24 bit of resolution.
Main DAQs specifications are collected in Table 4.6.

Table 4.6. *Data acquisition modules. Specifications.*

DAQ type	Input channel (SE: single ended; DIFF: differential)	Maximum cumulative sampling rate [kS s^{-1}]	Resolution [bit]
Omega® USB2401 ([5])	16 SE / 8 DIFF	1	24
MC® USB1208HS ([6])	8 SE / 4 DIFF	1000	14

The choice of the specific sampling rate is selected to keep the measurement noise under control that can dramatically increase once dealing with acquisition procedures at high sampling rates.

In addition, pressure measures acquisition rate is also based on the sensors characteristic frequency response in the sense that an appropriate DAQ acquisition rate should be at least 2.5 to 3 times larger.

For further details on the DAQ specs the reader should refer to the specific technical documentation ([5,6]).

Figure 4.4 shows the DAQs arrangement.

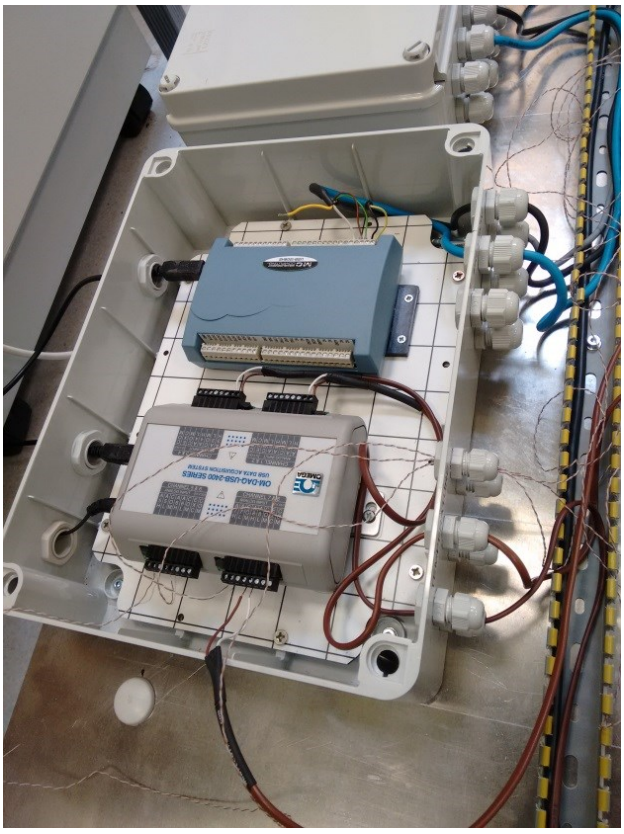

Figure 4.4. *Experimental setup. Pressure and temperature DAQs arrangement.*

4.3.3.4 Sensors calibration data

Calibration data of sensors used in the experimental campaign are reported in Table 4.7-4.9.

All sensors exhibit a linear behavior within the operative measurement range.

Calibration data are presented in the form of experimental pressure-excitation voltage couples or a values collection at zero and full signal scale.

Calibration procedures are therefore depending on the specific measurement device.

Table 4.7. *Pressure sensors. Calibration data.*

Sensor type	Pressure range [psig, barg]	Excitation range [Vdc]	Calibration method
Omega ®	0 – 1000 [psig]	28	5 points up and down
Schneider Technik ®	0 – 100 [barg]	14-30	Zero and span
Druck EP ®	0 – 100 [barg]	12-32	Zero and span

Table 4.8. *Omega® pressure sensor. Specific calibration data.*

Pressure [psig]	Measured excitation voltage [Vdc]
0.000	0.005
500.000	2.510
1000.000	4.991

Table 4.9. *Schneider® and Druck EP® pressure sensors. Specific calibration data.*

Sensor type	Measured range point	Measured voltage [Vdc]
Schneider Technik®	Zero	0.102
	Span	9.998
Druck EP®	Zero	-0.001
	Span	10.001

4.3.3.5 Data management and conditioning

The data management and conditioning is mainly oriented to pressure experimental series that are requiring more attention because of the possibility of measurement noise occurrence. In fact, large part of the experimental tests involves DAQ pressure sampling rate up to 35 kS s^{-1} $channel^{-1}$ and given the noise problems related to discrete data sampling, analytical filtering procedures are adopted. The declared noise occurrence is reported in the DAQs technical manual ([5,6]).

Inaccuracies are especially affecting measurements near the atmospheric levels that are always characterizing the final stages of the experimental trials.

Data filter approach used is in the form of a polynomial fitting procedure based on a least-square method moving over the data series. The method is known as that of Savitzky and Golay. The filtering function assumes the mathematical formulation indicated in (4.2):

$$F_{SG,j} = \sum_{i=-(N-1)/2}^{N-1/2} a_i y_{j+i} \qquad \frac{N+1}{2} \leq j \leq n - \frac{N-1}{2} \quad , \tag{4.2}$$

where n is the total number of points, N is the number of convolution coefficients a_i and y is an observed value. Coefficients are estimated solving a matrix equation and starting from the minimization of the differences between the value of the polynomial at a certain x_i and the actual y_i. The solution is therefore found when all partial derivatives of the residue with respect to any of the polynomials coefficients are equal to zero.

In this way, data result in a smoother distribution related to an increased signal-to-noise ratio, avoiding intolerable signal distortions.

4.4 Experimental campaign results

This section is dedicated to the collection of the experimental data obtained with the previously described setup. Main focus is oriented to pressure and temperature measurements that are derived from the arranged measurements devices. Because of the coupled collected measures, in the sense that measuring locations are close, any further data elaboration allows for the formulation of derived quantities such the density and other CO_2 properties that are useful to throw light on the release evolution.

4.4.1 Development of the experimental campaign

The experimental campaign is oriented toward the collection of profiles of specific physical quantities that are useful to give a description of the blowdown evolution from a pressurized tank involving CO_2.

Two quantities are measured and recorded:

- temperature (internal, external surface);
- pressure (internal).

Each of them is then elaborated in order to obtain the respective evolution in time both inside the tank and along the discharge line. In addition, their coupling gives the instantaneous and local CO_2 density value from which the released mass and an estimation of the discharge coefficient can be obtained.

Experimental trials involve the execution of different releases under controlled conditions that are expressed in terms of the initial CO_2 state inside the tank. Therefore the couple (P_0, T_0) is imposed and the profiles are concerning the variation in the release dynamics following an alteration in the initial variables. In detail following investigated ranges hold:

- initial CO_2 temperature in the range 5-50 °C;
- initial CO_2 pressure in the range 5-70 barg.

4.4.2 Pressure evolution

The instantaneous CO_2 pressure is recorded inside the tank and along the discharge line. The specific location of the tank pressure sensor is identified with the tank head on the opposite side with respect to the discharging throat and this location is supposed to be representative of the average pressure inside the tank matching the stagnation condition.

Figure 4.5 gives the time evolution of the pressure profiles inside the tank due to depressurizations from an initial pressure of 35, 20 and 10 barg performed starting from 298.15 K.

Corresponding dimensionless trends are reported in Figure 4.6.

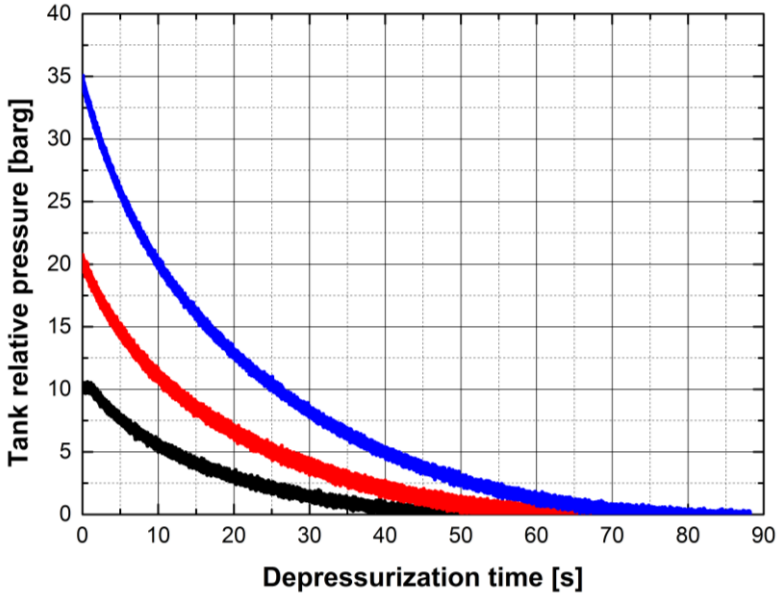

Figure 4.5. *Experimental tank pressure profiles for different initial charging pressures.*

Recorded profiles show some peculiar features that are described below.

Firstly, the different depressurization profiles show a qualitatively comparable trend that is mainly sensitive to the initial charging pressure. The shape similarity that is occurring in terms of a regular pressure decay is observed to charging pressures up to 45 barg.

The smooth shape of the transient profiles can be straightforwardly linked to the absence of phase change mechanisms inside the tank during the expansion. In fact, as observed by some authors ([7]) and as it will be explained later, the occurrence of boiling mechanisms is followed by a slope variation whose magnitude is linked to the intensity of these phenomena. The

experimental investigation shows no boiling occurrence for charging pressures up to 45 barg, independently on the initial and the environmental temperature.

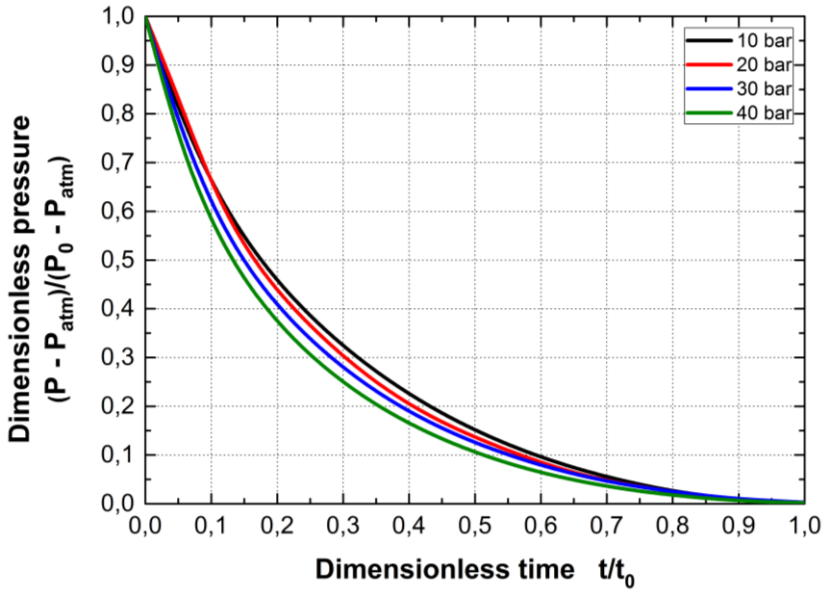

Figure 4.6. *Dimensionless tank pressure profiles for different initial charging pressures.*

Secondly, focusing on the dimensionless comparison, some differences arise and are concerning the dynamic in the dimensionless time range $0.1 < t^* < 0.5$. Different charging pressures are determining alterations in the depressurization path even if the initial conditions are similar. In fact, from this perspective, a variation in the pressure form 10 to 35 barg is not deeply influencing the initial density. The investigation shows that the observed discrepancy is mirrored on the different thermal dynamics that are induced by the pressure gradients.

A variation in the initial charging pressure is therefore affecting the depressurization evolution through the different induced expansion pathways that are resulting in different degrees of cooling as it will be reported later. At the same time, the CO_2 density is changing giving rise to observed differences in Figure 4.6. Results show that the final expansion pathway is never matching an ideal expansion and is strictly linked to the pressure-temperature relation that is occurring both in the bulk and at the orifice plane. The occurrence of heat transfer mechanisms between the CO_2 being discharged and pressure drops are effectively determining the expansion nature.

Recorded pressure drops across the constriction point are represented in Figure 4.7. Considered the experimental setup and the location of the measurement devices, these pressure drops are mainly related to:

- concentrated pressure drops across the abrupt flow area change between the tank and the discharging line;
- distributed pressure losses due to the flow to the atmospheric environment.

The mechanical effect related to the pressure decrease is then directly reflected on the CO_2 thermal state given the compressibility nature of the substance under the investigated conditions.

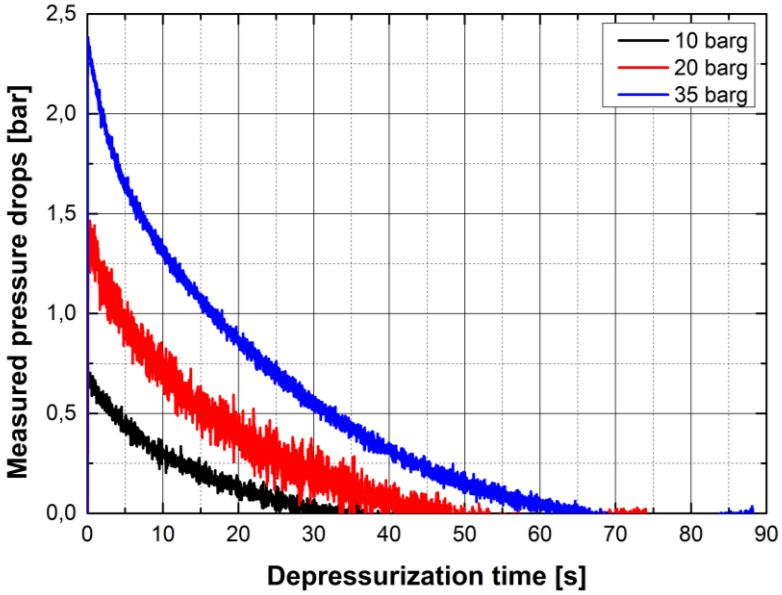

Figure 4.7. *Measured pressure drops in time across the constriction for different initial charging pressures.*

Constantly larger pressure drops are expected in correspondence of higher charging pressures because of two main reasons:

- larger density magnitudes related to the augmented absolute pressure that are linked to major friction effects;
- larger expected thermal variations (decreases) as a consequence of the pressure field.

It should be noted that the observed variations in Figure 4.6 are also due to the difference in the expected pressure drops these leading to lower instantaneous expected pressure levels with increasing charging values.

Resulting pressure profiles downstream of the constriction are reported in Figure 4.8.

Lower recorded pressure levels of Figure 4.8 are in agreement with the expected pressure drops of Figure 4.7 and an initial abrupt jump is displayed. It is depending on the initial charging pressure and is almost matching the initial observed pressure drops peak.

As of Figure 4.5, no noticeable variations in the slope are recorded therefore attesting the absence of phase-change mechanisms in close proximity of the constriction.

The respective dimensionless profiles are reported in Figure 4.9. It should be observed that the initial pressure magnitude decline remains almost unchanged under varying tank loading pressure. In percentage terms, the drop amount is equal to 6,8-7 % of the initial charging pressure.

In addition, for charging pressures higher than 20 barg, dimensionless profiles tend to overlap displaying a comparable effect of the pressure drops on the CO_2 depressurization evolution.

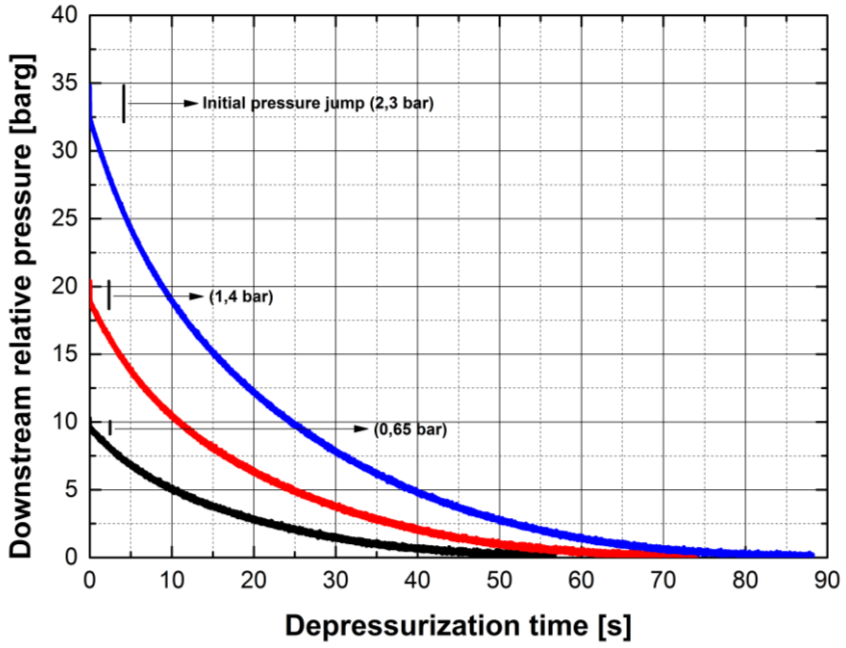

Figure 4.8. *Experimental pressure profiles downstream of the constriction for different initial charging pressures.*

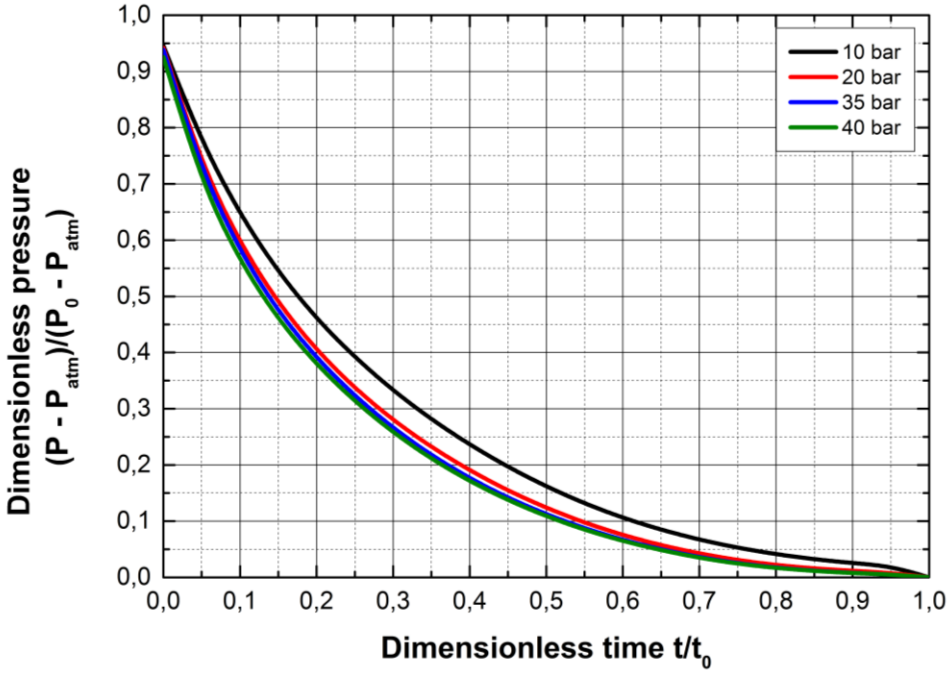

Figure 4.9. *Dimensionless pressure profiles downstream of the constriction point for different charging pressures.*

Once the charging pressure is increased, collected pressure profiles in the tank show substantial differences. Figure 4.10a-4.10b gives, as an example, the pressure tank evolution for releases from 60 barg.

A comparison with Figure 4.5 underlines the occurrence of a change in the pressure derivative somewhere along the depressurization path. Slope variations of Figure 4.10a-4.10b are pertaining to two distinct situations.

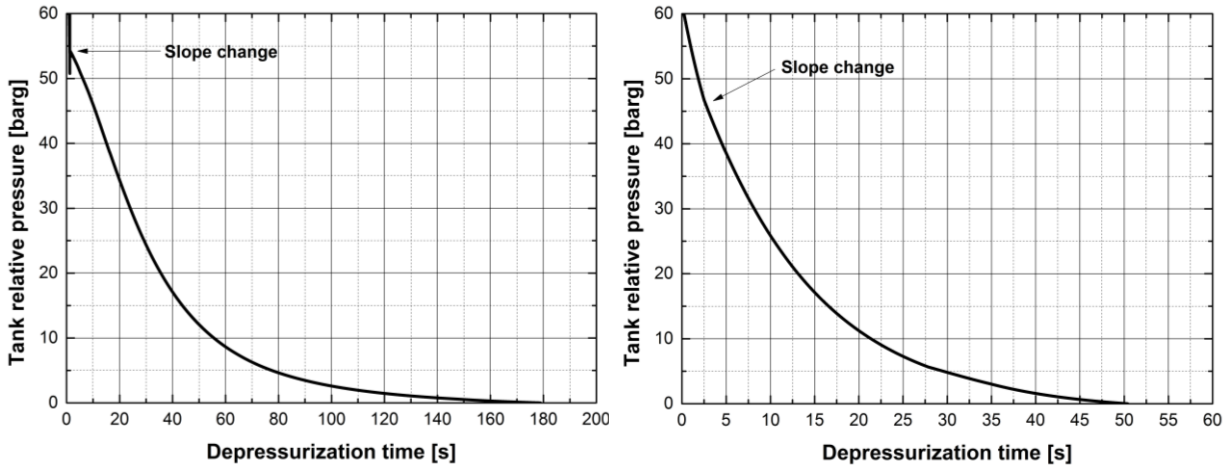

(a) *(b)*

Figure 4.10. *Experimental tank pressure profiles. a- 60 barg, 20 °C. b- 60 barg, 30 °C.*

The different situations are arising from diversified initial conditions with Figure 4.10a related to a charge at 20 °C and Figure 4.10b to 10 °C above whose pertinent initial aggregation state is respectively liquid and gaseous.

Thermodynamic considerations give reason to state that the slope change in Figure 4.10a is almost matching the local saturation pressure starting from which boiling inside the vessel occurs. The experimental apparatus does not allow further investigations but it is reasonable to assume that this value is depending on the initial CO_2 density and the transformation followed down to the vapor dome. As it will be discussed later, the expansion to saturated conditions is taking place with different degrees of reversibility strictly linked to the occurrence of friction and heat transfer mechanisms.

The slope change of Figure 4.10b is due instead to the appearance of the liquid phase inside the vessel bulk being the initial state gaseous. Its magnitude is not comparable to that of Figure 4.10a but it is again linked to the appearance of a dense phase and this statement is based on two experimental evidences:

- discharge of dense CO_2, neglecting condensed water vapor that would be immediately evaporated;
- instantaneous increase of the magnitude of heat transfer mechanisms across the vessel walls clearly showed by the external thermocouple.

Changes in the first derivative of the bulk pressure have been observed under different initial charging conditions.

In this respect, all releases performed from 60 and 65 barg are characterized by this feature. In addition only part of the discharges from lower pressures are involving the dense phase occurrence. In detail, only down to 50 barg this occurrence in the vessel is observed but for charging temperature below 8-10 °C and under external temperatures not higher than 15 °C.

4.4.3 Temperature evolution

Experimental trials show always a temperature dynamic linked to the rapid discharge. Both internal and external thermocouples are recording thermal variations whose trends and magnitudes are depending on the specific blowdown run and the measurement location.

Results concerning blowdowns from 10, 20 and 35 barg and 20 °C are reported in Figure 4.11a-4.11b.

Tank temperature profiles collected from the experimental trials show similar trends up to a charging pressure of 45 barg. This trend is characterized by two distinct behaviors:

- a first step linked to a temperature decline corresponding to the occurrence of cooling mechanisms inside the tank bulk;
- a final temperature increase indicative of heating phenomena.

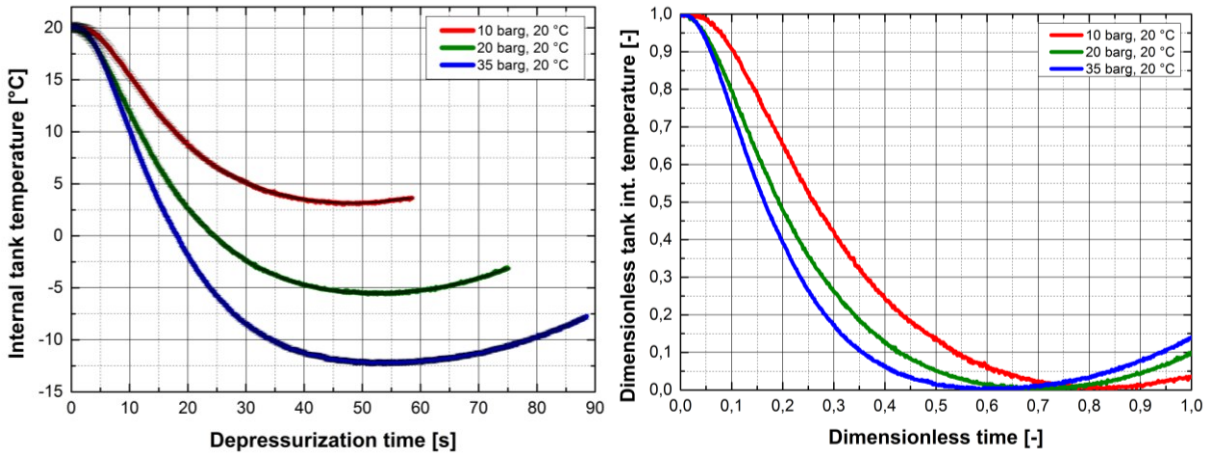

(a) *(b)*

Figure 4.11. *Experimental tank internal temperature profiles resulting from different charging conditions. a- time profiles; b- dimensionless profiles.*

These behaviors have always been observed once the tank is initially filled with gaseous CO_2 and no phase-changes are taking place. Because of this, the related thermal phenomena are expected to be linked to heat transfer mechanisms between the CO_2 that is being discharged and the vessel walls. This occurrence is testified by the recorded external vessel surface temperatures with major differences observed for the highest charging pressures. As a title of

example, the internal and the external representative tank temperature trends for the trial from 35 barg and 20 °C are reported in Figure 4.12.

It is clear from Figure 4.12 that once the internal vessel CO_2 temperature starts to decrease, an external surface dynamic is observed consisting in a less marked decline. For example, a 30 °C decrement in the internal temperature is corresponding to an external temperature gap of less than 5 °C. This behavior discrepancy is resulting from the difference both in the specific heat and the mass amount of the CO_2 with respect to that of the solid stainless steel. In this sense it should be noted that the operative conditions, even at higher pressures, are matching relative mass amount differences of some order of magnitude thus determining a relevant influence of the walls on the CO_2 expansion behavior.

For charging pressures up to 55 barg, the external wall temperature never drops below the CO_2 internal one indicating the persistence of a thermal driving force between the surrounding and the CO_2 being discharged. Figure 4.13 gives the instantaneous difference between the CO_2 temperature in the vessel bulk and that of the external surface.

The maximum difference is matching the minimum recorded bulk temperature being the external wall value almost constant. Experimental trials show that the widest external temperature variation is experienced once the CO_2 is charged at the highest operative investigated pressure, initially cooled down at 10-15 °C.

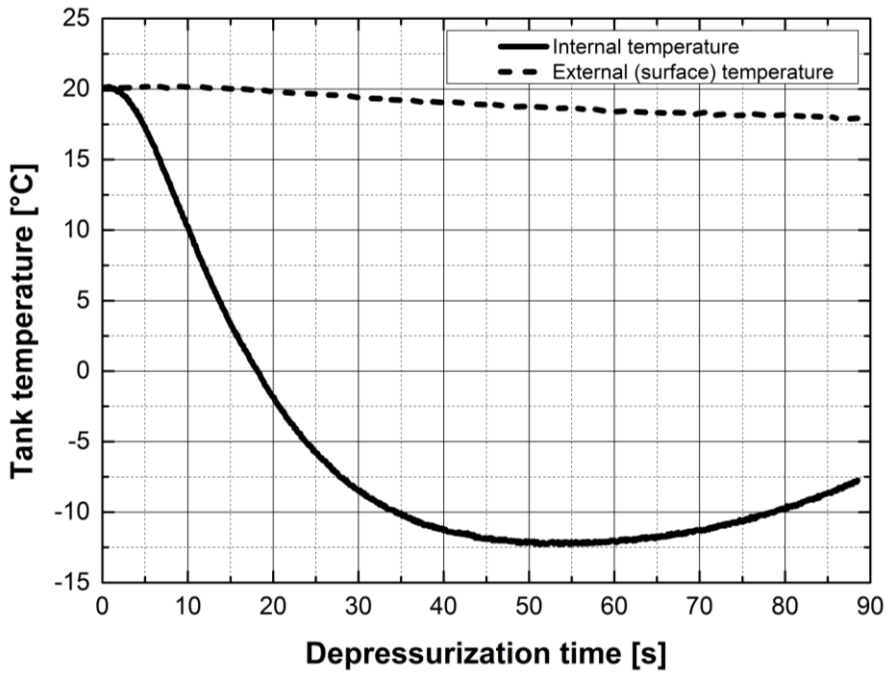

Figure 4.12. *Experimental internal and external (superficial) tank temperature profiles. 35 barg, 20 °C expansion.*

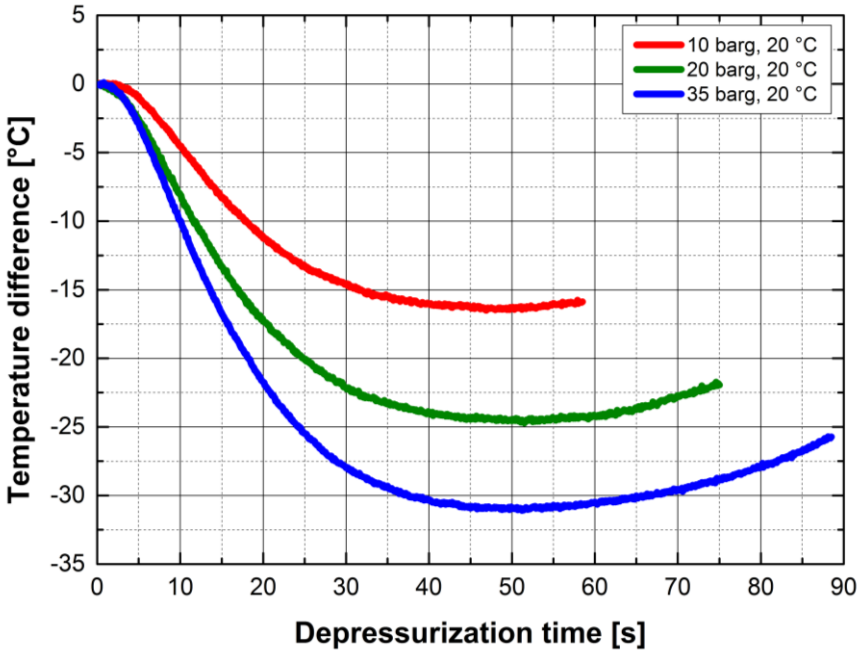

Figure 4.13. *Experimental instantaneous temperature differences between the CO_2 and the external wall temperature for different initial charging conditions.*

The maximum recorded external temperature variations are collected in Table 4.10 with data pertaining to pressures above 55 barg affected by the dense phase appearance inside the vessel.

With respect to the dimensionless profiles of Figure 4.11b, it should be underlined that the temperature behavior inside the tank is different depending on the initial conditions. In addition, it is also clear how the location in time of the bulk minimum temperature value is sensitive to these parameters.

Table 4.10. *Maximum recorded external vessel wall temperature excursions (absolute values).*

CO_2 pressure [barg]	CO_2 temperature [°C]	Maximum wall temperature variation [°C]
up to 35	any	< 5
40	10	10
40	20	7.5
40	30	< 5
50	10	12.5
50	20	10.1
50	30	7.5
60	10	15.1
60	20	12.4
60	30	10.5

A decrease in the initial CO_2 density is responsible for a delay in the achievement of this value being the influence of the warmer walls stronger.

The initial density value is governed by both a pressure and a temperature alteration and a variation in the latter induces different effects on the depressurization profiles.

Bulk thermal profiles following from different initial temperatures are reported in Figure 4.14a-4.14b respectively for a 20 and 35 barg expansions.

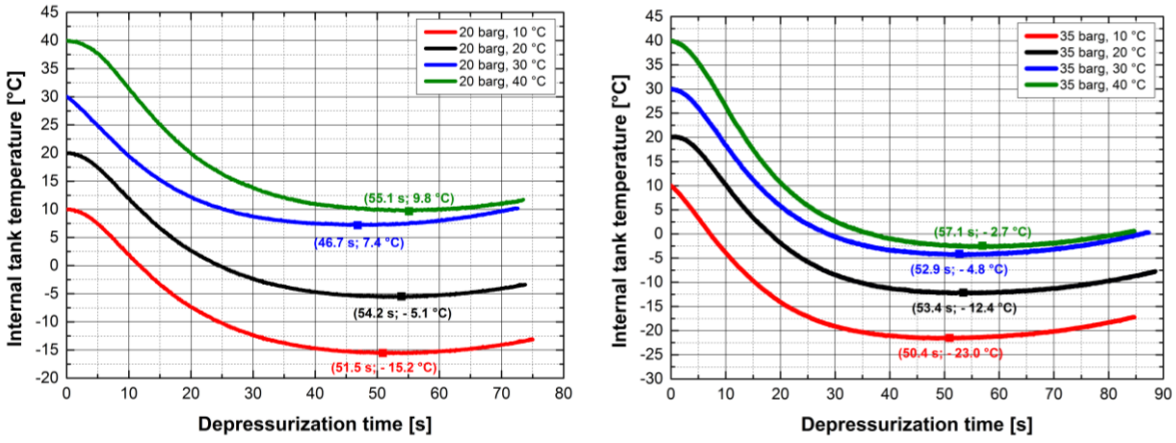

Figure 4.14. *Experimental tank internal temperature profiles resulting from different initial temperature conditions. a- 20 barg expansion; b- 35 barg expansion.*

The variation in the initial temperature alters the thermal profile shape and the minimum recorded bulk value. A decrease in the temperature, i.e. a rise in the initial CO_2 density, leads to lower minimum expected vessel bulk temperatures. Major gaps under different initial temperatures are observed for lower charging pressures and, as indicated in Figure 4.14a, the minimum observed temperature is ranging between 9.8 and -15.2 °C that are respectively corresponding to charging temperatures of 40 and 10 °C. The switch to 35 barg lets the minimum temperature ranging between -2.7 °C and -23 °C.

It is clear therefore that the initial imposed temperature variation is not conserved on the respective final vessel bulk value and this is due to two main reasons:

- the heat exchange related to the presence of the solid walls;
- the alteration of the expansion pathway induced by the different initial states.

These two features are not independent and, as it will be discussed later, the variation in the initial conditions leads to different expansion pathways that emerged to be quite always bounded by isenthalpic and isentropic transformations.

The minimum reached temperature inside the vessel is in some way the result of the balance between the effect induced by the expansion and the efficiency in the heat transfer

mechanisms. The proposed model in chapter 5 will therefore take into account these two competitive mechanisms in the description of the thermal dynamic inside the vessel.

With respect to Figure 4.14 it should also be noted that a variation in the initial temperature does not play a key role in determining the location in time of the minimum reached temperature especially at higher pressures (Figure 4.14b). This feature has been observed as long as the initial charge is gaseous. However, as reported in Figure 4.11b, the pressure effect on this parameter is larger because of the more relevant incidence on the initial density. The same negligible initial temperature effect on the minimum reached temperature inside the vessel has been observed for charging pressures up to 65 barg.

Minimum observed vessel bulk temperatures are reported in Figure 4.15. The 40 barg trend deviation observed for $T < 20$ °C and the separated 60 barg behavior are linked to the dense phase appearance inside the vessel.

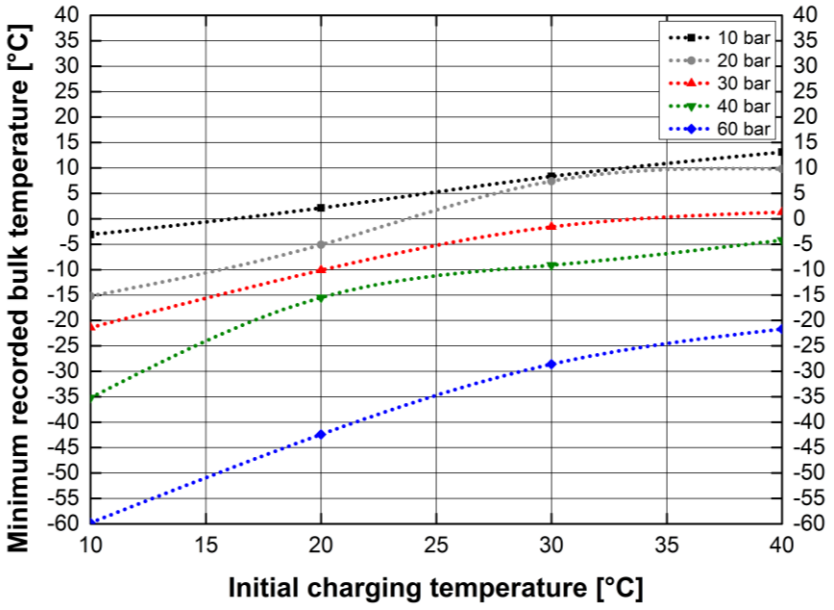

Figure 4.15. *Experimental minimum tank internal temperature profiles resulting from different initial conditions.*

Focusing on the constriction point, temperatures experienced by the expanding CO_2 are generally lower than those recorded inside the vessel. The pressure drops observed in Figure 4.7 are the main factor inducing the temperature decrease at this location.

The CO_2 recorded temperature at the constriction point is again depending on the initial conditions but some differences emerge in comparison to the bulk profile.

Firstly, the already mentioned lower recorded temperature that is linked to the pressure variations experienced by the CO_2 at the constriction location. However, experimental evidences show that the initial conditions do not show a univocal effect on the minimum temperature determination as it is instead observed for the vessel bulk value.

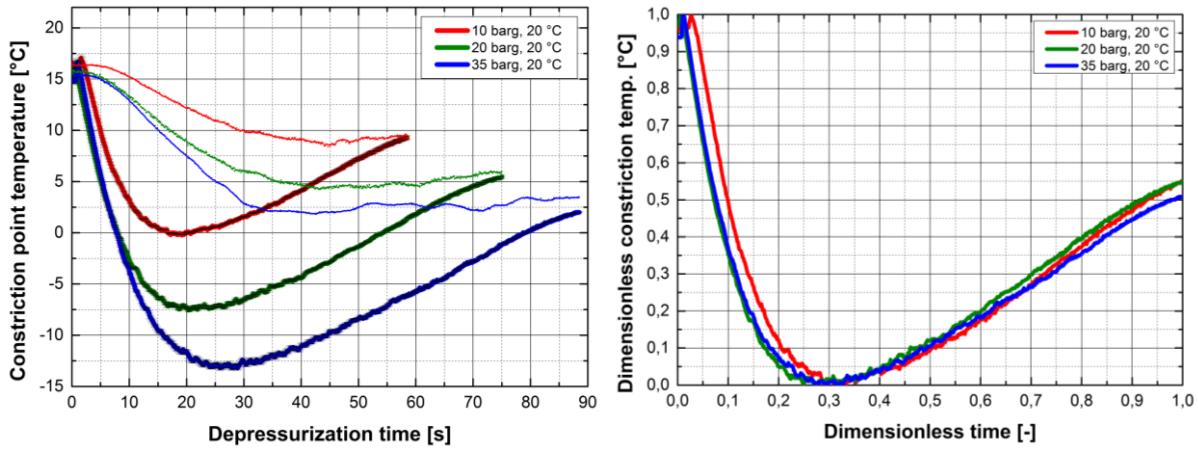

(a) *(b)*

Figure 4.16. *Experimental temperature profiles at the constriction point under different initial conditions. a- time evolution (dotted lines: external wall temperature); b- dimensionless trends.*

For example, the temperature drop for the 35 barg expansion performed from 20 °C is the same in the two locations while for lower pressures a minimum temperature difference is instead observed (Figure 4.16). In this sense, the role played by the heat transfer is crucial as reported in Figure 4.16a where a noticeable wall temperature decrease is recorded. In fact, at this location, a comparability in terms of heat capacities between the solid walls and the flowing CO_2 is expected.

Secondly, the comparison of Figure 4.16b with Figure 4.11b shows that, at the constriction point, the minimum CO_2 temperature is always achieved earlier in time ($t^* \cong 0.3$). In addition, it should be noted also that the temperature decrease is occurring earlier. On this regard, the instantaneous temperature difference in the pathway across the constriction point is reported in Figure 4.17 confirming that the expansion is actually taking place in this experimental section.

The increase in the charging pressure leads to larger temperature differences even if in the range 15-40 barg the profiles tend to overlap (Figure 4.17).

Experimental evidences show that higher charging pressures induce variations in the thermal profiles both in the vessel and at the constriction point. Figure 4.18 gives the recorded trends linked to a release from 60 barg and 20 °C.

Trends of Figure 4.18 have been qualitatively observed under the following experimental conditions:

- charging pressures in the range 50-65 barg;
- charging temperatures from 10 to 25 °C and external temperatures below 20 °C;
- initial charging states generally pertaining to the dense phase.

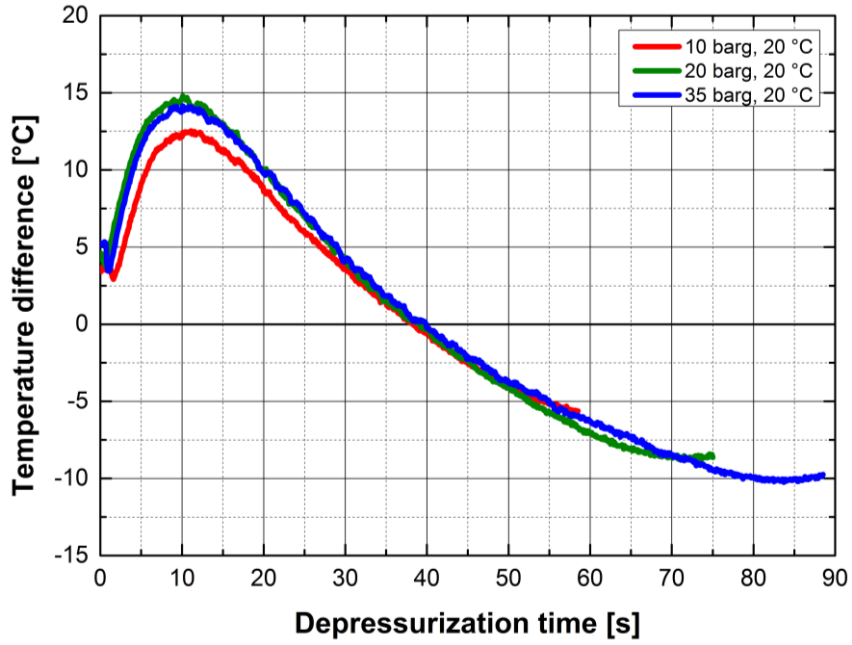

Figure 4.17. *Instantaneous temperature difference between the vessel bulk and the constriction locations for different initial conditions.*

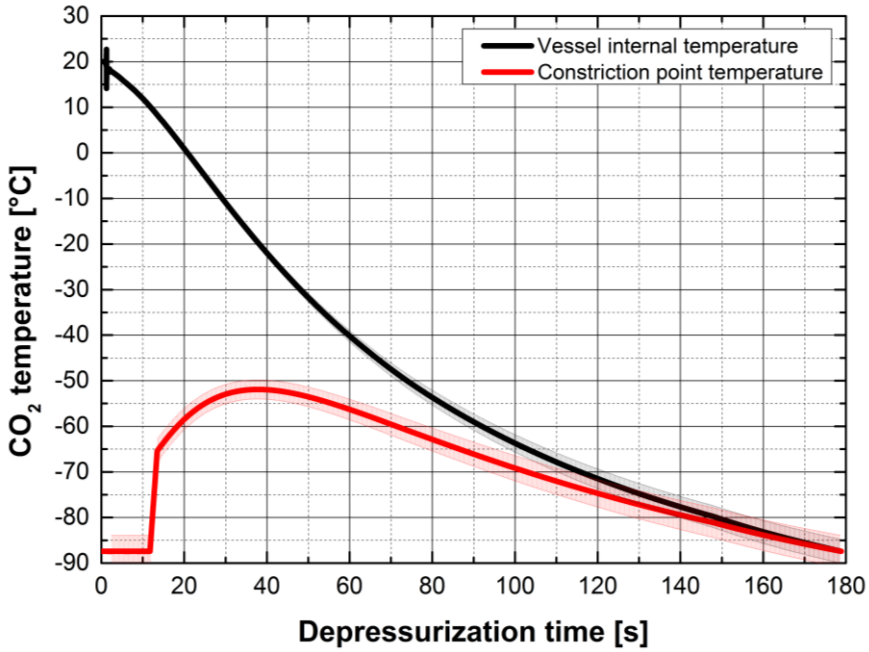

Figure 4.18. *Experimental temperature profiles in the vessel and at the constriction point during a 60 barg, 20 °C release.*

They are characterized by a progressive temperature decline inside the vessel bulk due probably to the already noted mechanical cooling effect. The lack of the final heating step induced by the solid walls is almost certainly due to the occurrence of latent heat-related effects linked to the liquid boiling. The additional phase change mechanisms that are taking place along the way to the discharge plane are responsible for lower temperatures observed at the constriction point and the rise in the temperature differences between the two locations.

As reported in Figure 4.18, the minimum temperature is observed in the early release stages, almost matching the equilibrium atmospheric temperature.

Qualitatively the temperature rise follows up to a value that is depending on the charging conditions and it is taking place while the bulk thermal content is declining and this fact is again linked to heat transfers mechanisms. However, the progressive cooling experienced by the walls then acts as a limiting condition allowing for the observed CO_2 temperature increase of Figure 4.18.

Another parameter that plays a key role in the determination of the thermal profiles is the orifice size.

Two distinct orifice sizes have been arranged: the already discussed base case with an orifice diameter of 1/8 in and additional runs with a doubled diameter.

Thermal profiles inside the vessel for different initial conditions are reported in Figure 4.19 with respect to the doubled orifice diameter situation.

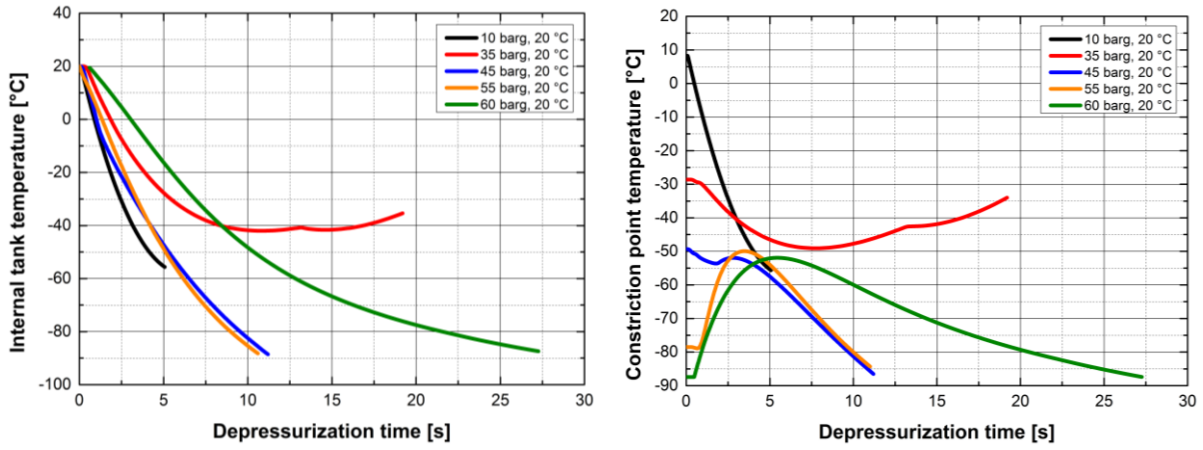

(a) *(b)*

Figure 4.19. *Experimental temperature profiles induced by a doubled orifice with respect to the base case. a- internal tank location; b- constriction point location.*

The increment in the orifice size significantly alters the thermal dynamic that results in different qualitative profiles depending on the initial conditions.

Results show that the orifice size increase firstly induces a persistent decrement in the bulk vessel temperature indicating that the solid wall heat capacity is not enough to sustain the previously observed CO_2 temperature rise.

Some trials, however, preserve the characteristic profile with a final heating step that is observed for charging pressures between 28 and 36 barg independently on the initial temperature. In this sense it follows that these conditions are determining a balance between the thermal capacity of the CO_2 and that of the stainless steel.

It should also be noted that the minimum temperature inside the vessel, in the rest of the cases, is always recorded in the final steps and for charging pressures higher than 40 barg this is matching a temperature ranging from -90 to -80 °C. Other authors recorded minimum temperatures in this range that is below the atmospheric equilibrium value ([10,11]). Further investigations on this aspect are reported in Chapter 7.

The final constriction point temperature is decreasing with a rise in the charging pressures as long as $P < 28$ barg. Over this threshold the same behavior of the vessel bulk is observed and for $P > 35$ barg the final temperature rapidly decreases down to the aforementioned range.

4.4.4 Total release time

The total release time has been experimentally recorded and it is here referred as the time interval to the complete vessel emptying. This variable takes a major role in the subsequent model development since the agreement with the experimental data is essential in assessing the model descriptive capability.

Experimental measurements are reported in Figure 4.20 with respect to different initial conditions.

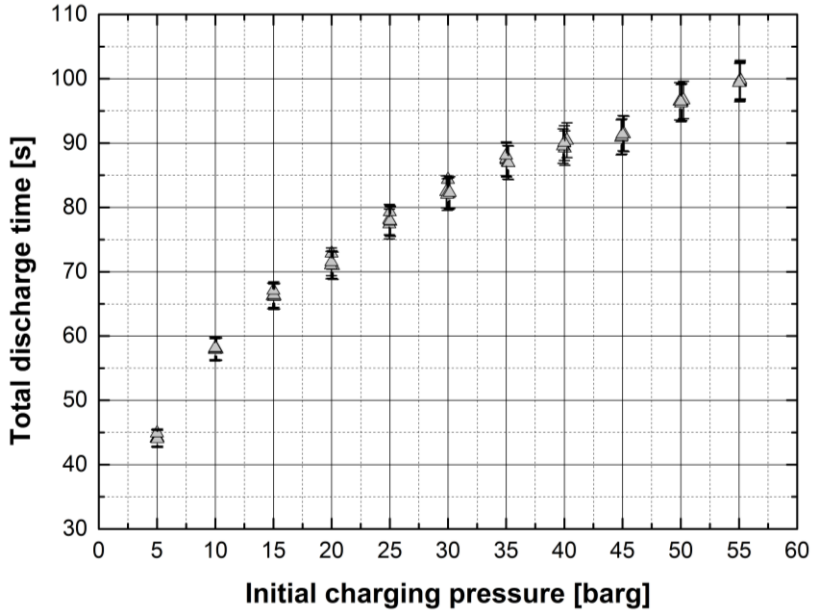

Figure 4.20. *Experimental measured total discharge time with respect to different initial conditions up to 55 barg. Base case.*

Collected data show that the total release time is strongly depending on the initial charging pressure but experiences a negligible influence of the initial temperature. The first parameter is actually governing the initial CO_2 density that is the total mass inventory to be discharged and therefore the time required to the vessel emptying.

At the same time the initial temperature, whose dependency is resulting in the different points of Figure 4.20, does not play a key role in determining the total discharge time. In fact its influence on the initial density, for pressures up to 55 barg, is negligible with respect to the pressure effect.

The investigated parameter trend reported in Figure 4.20 shows the dependency on the charging pressure for which the qualitative features are resulting from the influence of the orifice size and the actual expansion path followed by the CO_2 during the expansion, i.e. the instantaneous density variation.

The influence of the orifice size on the total discharge time is relevant as indicated in Figure 4.21.

While keeping the charging conditions unchanged, the expected decrease in the discharge time may amount up to an order of magnitude.

In the range 30-40 barg, a jump in the total discharge time is observed, this matching the conditions of the dense phase appearance in the vessel bulk. The time decrease is therefore due to the dense phase discharge that is characterized by much higher density values linked to the incompressible behavior.

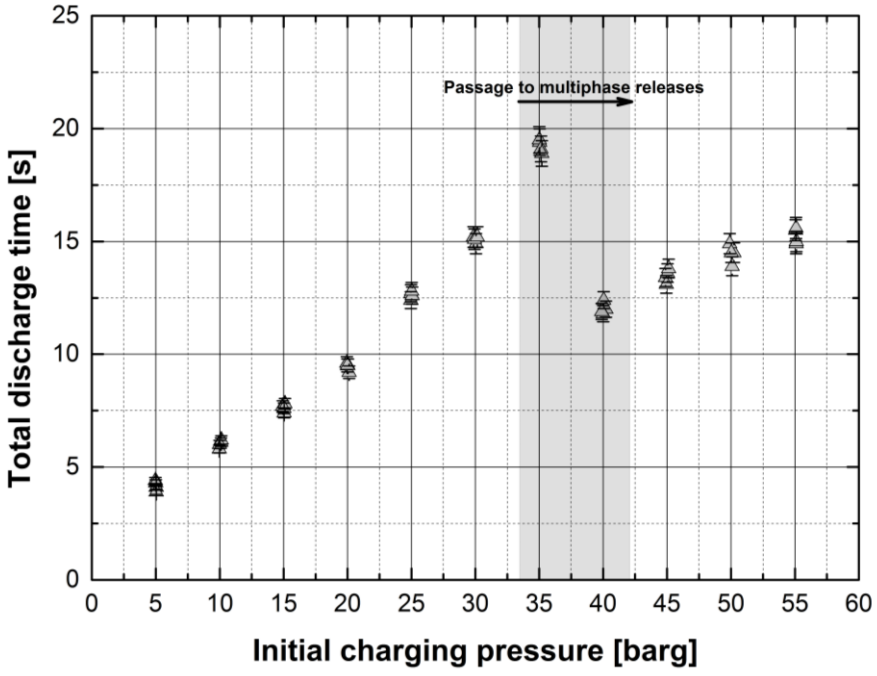

Figure 4.21. *Experimental measured total discharge time with respect to different initial conditions up to 55 barg. Doubled orifice size.*

Pressure levels higher than 55 barg (initial dense charge) unavoidably lead to an increase in the total discharge time because of the larger amounts of CO_2 to be discharged.

Considered the investigated initial charging pressures up to 70 barg, following experimental evidences are observed:

- the total discharge time recorded for the base case (orifice size of 1/8 in) is increasing with the charging pressure varying from 160 to 270 s respectively for 60 and 70 barg. The charging temperature value is relevant in determining this parameter being the CO_2 initial state sensitive to the thermal content. For example a 60 barg release subjected to an increase of 10 °C experiences a reduction in the discharge time from 160 to 55 s. As it will be discussed in the model development section, this is due to a mixed influence of the total amount being discharged and the nature of the thermodynamic expansion induced by pressure gradients. No experimental profile regularities are observed;
- the increased orifice size implies a general decrease in the total release time. However, because of the occurrence of phase change mechanisms both in the vessel and through the orifice that are altering the instantaneous amount of the light phase, the discharge time experience huge variations varying, for example, from 29 s in the case of 60 barg to 10 s with 70 barg. Experimental data do not show a peculiar trend with respect to the initial conditions and therefore specific features will be eventually predicted by the model.

4.4.5 Experimentally derived parameters

Collected experimental data allow for the estimation of two parameters of main interest in the model closure: the discharge coefficient and the nature of the expansion transformation.
Both are strictly derived from the model structure adopted in the description of the blowdown phenomenon.

4.4.5.1 Discharge coefficient

The introduction of the discharge coefficient is usual in QRA studies. It is intended as a correction factor that is introduced to face the known approximations adopted in the model formulation.
In what concerning the blowdown description, these approximations are mainly related to the evaluation of the viscous dissipations and the behavior of the CO_2 across the constriction point. In addition, because of the limited number of measurement locations, the adopted CO_2 velocity will certainly be affected by errors deriving from the average procedure that is actually not exactly matching the local value. Finally, the expansion pathway is surely affecting the model predictions and therefore its capability to match the experimental data.

In the case of a persistent gaseous release, the discharge coefficient γ_d is directly derived from the system of balance equations as reported in the chapter 3. In detail, the following (4.3) applies:

$$\frac{d\rho_1}{dt} = -\gamma_d \frac{\rho_2 S_2}{V} \sqrt{\frac{-2\int_1^2 \frac{1}{\rho} dP}{1 - \left(\frac{\rho_2 S_2}{\rho_1 S_1}\right)^2 + 8f\frac{L}{d}}} \quad . \tag{4.3}$$

The (4.3 relies on the experimental data in the sense that the value of γ_d requires the imposition of the expansion transformation through the numerical integral in the right term. The required $\rho(P)$ relation to be integrated is based on the experimental (P, T) couples collected between the stagnation conditions (subscript 1) and those pertaining to the constriction point (subscript 2). Remaining parameters in (4.3) are linked to geometric properties. The friction factor f is based on the estimated average Reynolds number Re and therefore on the expected velocity induced by the pressure difference and imposed by the local estimated density $\rho(P^{exp}, T^{exp})$. In this sense, the resulting γ_d is derived from the minimization procedure between the experimentally measured density $\rho(P^{exp}, T^{exp})$ and that obtained from the numerical integration of the balance equations.

The approach in the γ_d calculation invokes also the experimentally recorded pressure drops that represent a crucial parameter in the determination of the discharge coefficient. The apparent discharge coefficient is therefore based on the main friction sources that are mainly related to the geometrical configuration of the equipment at the constriction point. In addition, it includes the combined effects of surface shear and flow acceleration to which the CO_2 is subjected once going through the restriction.

Starting from this, the apparent discharge coefficient γ_d, is therefore linked to the measured pressure drops ΔP through (4.4):

$$\Delta P^* = 2\frac{\Delta P}{\rho u^2} = 4\gamma_d \frac{x}{d} \quad . \tag{4.4}$$

In (4.4), ΔP stands for the pressure difference across the loss element, ρ is the experimentally derived mean CO_2 density between the two pressure measuring locations, u is the corresponding mean velocity, x is the distance from the upstream measuring location and d is the internal pipe diameter.

Expressing (4.4) in terms of measurable quantities, the (4.5) is obtained:

$$\gamma_d = \frac{\Delta P d^5 \rho \pi^2}{32 \dot{m}^2 x} = \frac{\Delta P d^7 \rho \pi^2}{32 Re^2 \mu^2 x} \quad . \tag{4.5}$$

Therefore, in this way it is also possible to obtain a trend for the dimensionless group $\gamma_d Re^2 = \varphi(\Delta P, d, x, \mu, \rho)$ with respect to the listed experimentally derived parameters.

The apparent discharge coefficient obtained from the experimental data for different initial charging conditions is reported in Figure 4.22 superscripted *emp*. The same value obtained from the supposed model as of (4.3-4.5) is instead superscipted *semiemp*.

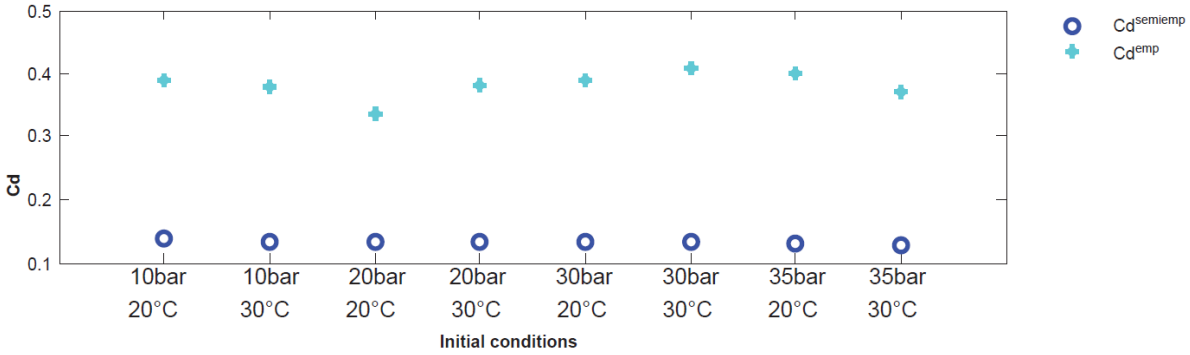

Figure 4.22. *Estimated apparent discharge coefficient with respect to different initial conditions and based on the experimentally measured expansion. Charging pressure below 40 barg. ([7]).*

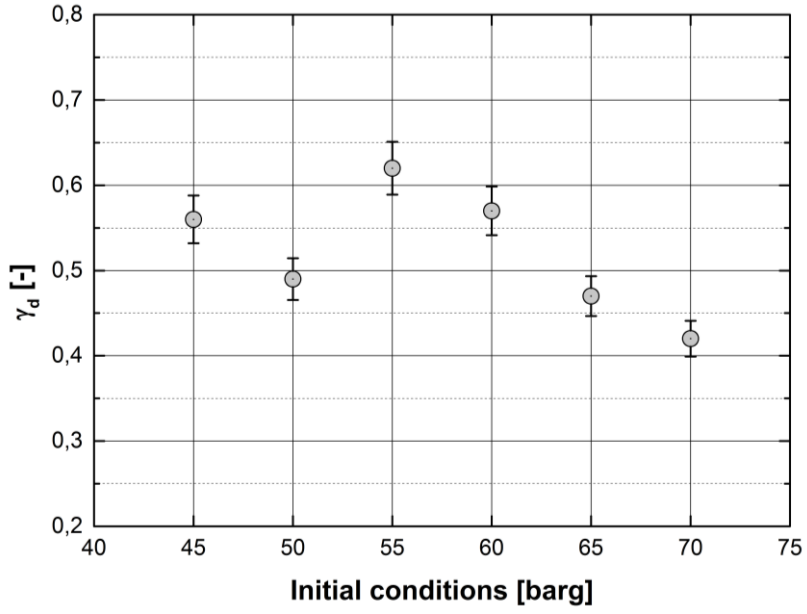

Figure 4.23. *Estimated apparent discharge coefficient with respect to different initial conditions and based on the experimentally measured expansion. Charging pressure above 40 barg.*

Referring to Figure 4.22, it should be noted that for charging conditions up to 35 bar the experimentally derived discharge coefficient is almost equal to 0.4 with minor variations. This value is not preserved once the initial conditions pertain to the dense phase or an initially

gaseous charging undergoes multiphase releases (Figure 4.23). Observed values are generally higher, ranging from 0.41 to 0.62.

In what concerning Figure 4.22, lower values (round marks) are obtained from the numerical integration of the balance equations indicating the large influence of the mathematical model formulation on the results. The latter are obtained starting from a density value calculated from the balance equations.

Similarly, the imposition of a specific thermodynamic transformation path in the integral of (4.3) leads to different γ_d estimates. As often is the case in QRA studies, the imposition of a specific expansion feature moves from ideal thermodynamic pathways that, strictly speaking, are never matching the real behavior. In this perspective, both the constant entropy and enthalpy transformations are considered. Different γ_d values are obtained moving through these expansion paths as indicated in Figure 4.24.

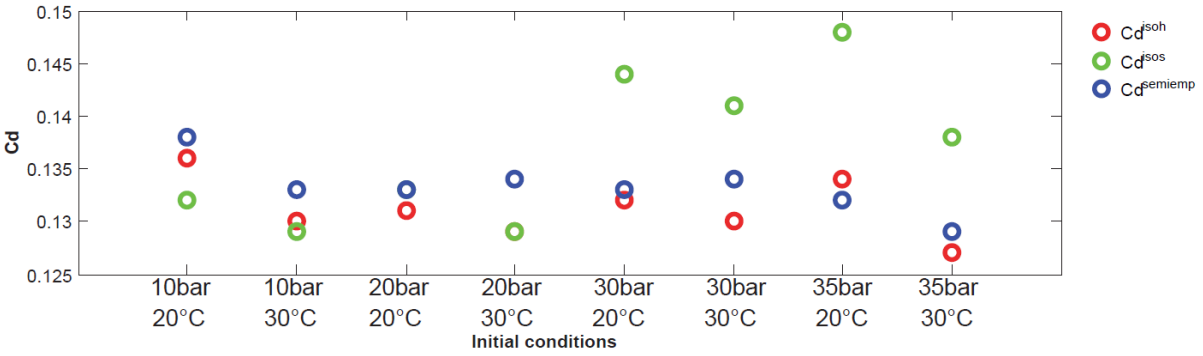

Figure 4.24. *Estimated apparent discharge coefficient with respect to different initial conditions and expansion pathways (red: constant enthalpy; green: constant entropy transformations). ([7]).*

The experimental data series are matched only in the proximity of a specific transformation nature depending on the initial conditions. At lower charging pressures, i.e. at a smaller initial CO_2 density, a good matching is ensured by both the supposed transformations. With increasing pressures, only the constant enthalpy transformation is giving a good data interpretation. In this sense, an increase in the friction dissipations induced by larger velocities are expected to give rise to a crucial enthalpic contribution on the whole transformation.

Once the release is involving also the dense phase, results show that the best match is quite always represented by an intermediate transformation. The resulting γ_d are larger than those pertaining to the persistent gaseous release with values up to 0.65-0.75. A deeper analysis of the expansion behavior is demanded to the model development chapter and to the following sections.

From a QRA perspective it should be underlined that the collected results are comparable with the usual adopted values for γ_d ([8]):

1. 0.64 for liquid discharges;
2. 0.8 for general liquid releases through short nozzles;
3. 0.61 for sharp-edged orifices with $Re > 30000$.

The discharge coefficient γ_d, when unavailable from self-collected data, is derived from experimental series both al laboratory and large scales. Main sources are made available elsewhere ([9,10,11]).

4.4.5.2 Expansion transformation

In this context, the expansion transformation is intended in terms of the (P,T) relation development in time, descriptive of the thermodynamic state sequence followed by the CO_2 in its way from the stagnation to the orifice conditions.

The resulting expansion path is derived from the already mentioned experimental data expressed in terms of local pressure and temperature data. However, given the uncertainties linked to data collection, an approach based also on the descriptive model is proposed. In this sense, the resulting expected transformation is compared to the ideal paths considering the best matching with the actual experimental data.

The two ideal mentioned transformations (isenthalpic and isentropic) are descriptive of pathways characterized by dissipation phenomena and different degrees of heat transfer whose relevance is giving the whole CO_2 expansion behavior.

In what concerning the transformation nature prediction, following Figure 4.25 is obtained.

Figure 4.25 gives the relative contributions to the resulting transformation that is obtained from a minimization procedure based on the statistical indicator as of (4.6):

$$\varsigma = \min_{\exp data} \frac{|\sigma_m(P)| + |\sigma_m(T)| + |\sigma_m(\rho)|}{3} \quad . \tag{4.6}$$

ς summarizes the error contribution, with respect to the experimental data, related to the three main predicted variables that are the pressure P, the temperature T and the CO_2 density ρ.

The minimization of ς corresponds to the best approximation (within the error) of the supposed transformation with respect to the expected value of the listed variables. Therefore, the resulting transformation, within the limits of its definition, is the one that best fits the experimentally observed expansion.

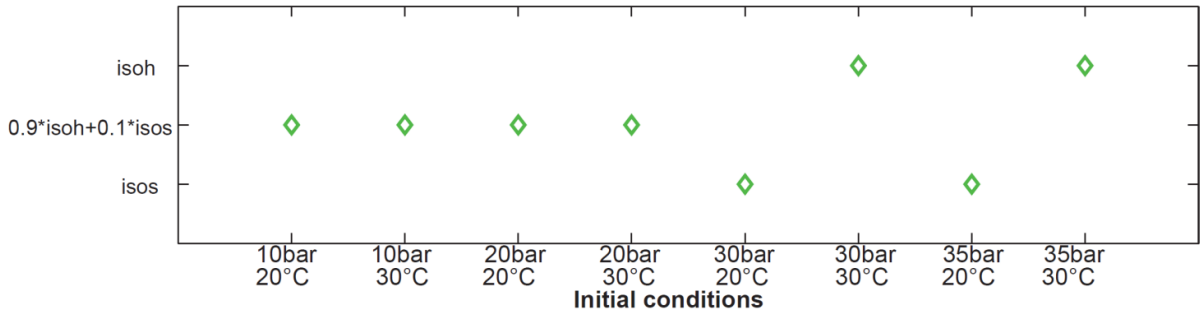

Figure 4.25. *Resulting CO_2 expansion nature from the minimization of ς with respect to collected experimental data. ([7]).*

It should be noted that, with a decrease in the charging pressure below to 20 barg and independently on the temperature, a transformation nearly taking place along a constant enthalpy path ensures a good approximation.

From a thermodynamic perspective, this is indicating a relevant contribution due to frictions and heat transfer mechanisms that therefore should be contemplated in the model formulation.

At higher pressures, approximately up to 40 barg, the minimized ς value is showing a decrease in the enthalpic term (*isoh*) with respect to a growing entropic contribution (*isos*).

As it will be better investigated, this is indicative of a varied balance between the frictions and the thermal effects that is occurring because of the pressure gradients induced by the blowdown phenomenon.

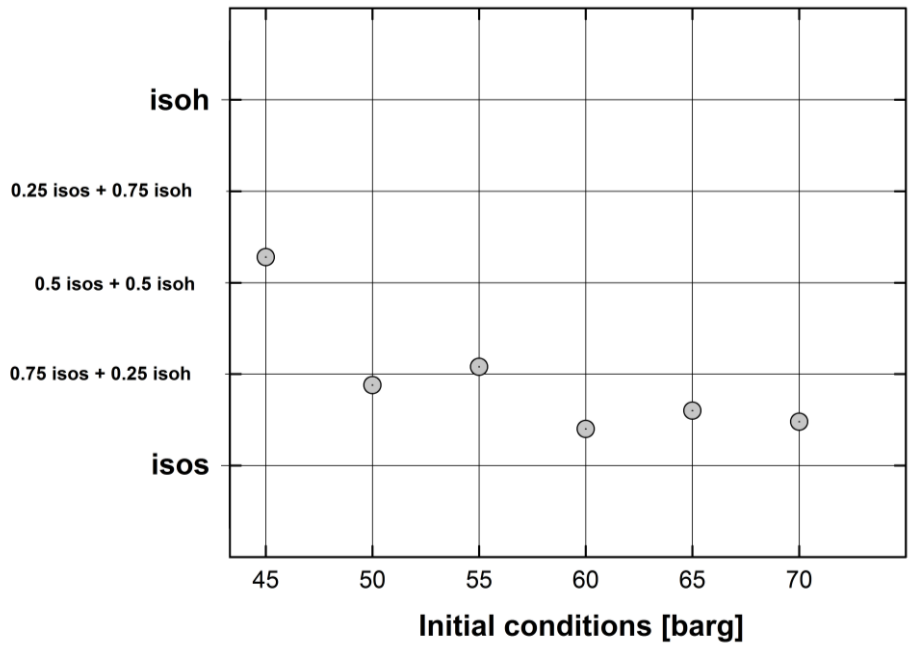

Figure 4.26. *Isenthalpic and isentropic estimated contributions to the real modeled expansion. Charging pressures above 45 barg.*

The minimization procedure applied to releases involving the dense phase shows that the enthalpic contribution is less significant in determining the whole expansion path. The larger thermal variations in addition to the occurrence of boiling mechanisms are linked to expansions that are quite always taking place along a constant entropy pathway.
For charging pressures in the range 50-65 barg, the transformation is nearly matching an isenthalpic contribution of 20 % that decreases down to 10 % for higher pressures.
Figure 4.26 gives further details.
The model development will consider the expansion nature that has been assessed starting from the experimental data but the description will be also improved by means of a specific parameter that is indicative of the transformation degree of reversibility.

4.4.6 Experimental results incorporation in the model structure

Data made available from the experimental campaign are used also to drive the model structure development. Main features that emerged from the experimental investigation are then used to propose a suitable framework primarily able to catch and describe all mechanisms that have been observed.
Main observed features are listed below:

1. pressure and temperature profiles are fully transient in time and therefore the instantaneous CO_2 properties are varying accordingly both at stagnation and the orifice plane;
2. initial conditions expressed in terms of pressure and temperature play a key role in determining the whole release dynamic;
3. stagnation pressure trends show slope alterations once the dense phase appears;
4. solid walls, depending on the relative mass amounts, transfer heat to the flowing CO_2 modifying its expansion to atmospheric conditions. Under specific conditions, thermal profiles show a peculiar behavior involving a passage through a local minimum;
5. lower temperatures are expected in accordance to the dense phase appearance. At the orifice observed temperatures are always lower;
6. the transformation nature from stagnation to orifice conditions is sensitive to the initial conditions and is never fully matching the ideal pathways.

Therefore, moving from these considerations, the descriptive model should match the following respective basic requirements:

1. the mathematical formulation is fully transient invoking balances that are depending on time both in the vessel and at the orifice. CO_2 properties sensitive to the pressure and the temperature are therefore updated at each time step;
2. the CO_2 properties descriptive models are carefully selected since any accuracy affecting the initial state will alter the whole release predictions. Robust equations of state (EoS) and reliable correlations are then required;
3. the model structure should be able to manage the appearance of different phases and therefore should invoke a multi-phase approach. In this sense, the mathematical formulation includes the description of the thermodynamic equilibriums and all expected phase-change mechanisms;
4. the model equations will also involve the description of occurring heat transfer mechanisms between the flowing CO_2 and the solid walls with respect to the resulting thermodynamic expansion nature;
5. point 5 is strictly linked to point 3 against which a robust prediction of the phase-change mechanisms will ensure a correct description of the thermal dynamic that will be surely affected by latent heat-related features;
6. the model should ensure, in addition to the main balance equations, a robust thermodynamic foundation that allows for a reliable description of the physics invoked by a rapid depressurization. This is mainly required for blowdown phenomena occurring with large compressibility effects like those pertaining to the gaseous CO_2 and mixtures that are rich in the light CO_2 phase.

References to Chapter 4

1. TC Direct, 2015. Compendio di Termometria, Termocoppie e Termoresistenze. Technical manual. Torino, IT.
2. Omega Engineering Sensors, Specific technical documentation-Silicon based sensor PX 409.
3. ICS Schneider Messtechnik, Prazisions-Druckmessumformer mit Kurzer Ansprechzeit, Tech. Datenblatt IMP 320 Drucksensor.
4. EPSAS, General-electric company, Pressure Sensor Technical Documentation, UNIK 5000 model.
5. Omega Engineering DAQs, Specific technical documentation-Multichannel DAQ 2401 USB.

6. Measurement Computing Electronics, Specific technical documentation-Multipurpose DAQ Acquisition Modules model USB-1208 HS.
7. Soccio, A., 2016. Fenomeni transitori di vessel blowdown applicati al caso della CO_2. Modellazione termoidraulica di dettaglio. Tesi di laurea, Padova.
8. Crowl, D.A., Louvar, J.F., 2002. Chemical process safety: fundamentals with applications, Prentice Hall PTR, New Jersey, U.S.A.
9. Mahgerefteh, H., Brown, S., Martynov, S., 2012. A study of the effects of friction, heat transfer and stream impurities on the decompression behavior in CO_2 pipelines. Greenhouse gases: science and technology 2, 369-379.
10. CO_2PipeHaz, 2009. Quantitative failure consequence hazard assessment for next generation CO_2 pipeline: the missing link. In: Description of Work of the Grant Agreement for FP7 Cooperation Work Programme 241346-2-CO2PipeHaz (CP), 1-83. www.co2pipehaz.eu.
11. CO_2PIPETRANS Project (DNV).

Chapter 5

CO_2 Release Modeling. Multi-phase 0-D Blowdown Model

This chapter covers the model structure development and illustration with focus on the constitutive equations, the adopted assumptions and the numerical method employed to ensure the problem solution. The model capability is then tested against the collected experimental data of chapter 4. QRA's required main parameters are obtained especially in what concerning transient pressure and temperature profiles, thermodynamic expansion nature, discharged mass flow rate and total release time.

5.1 Introduction

Central to QRA of pressurized CCS and EOR pipelines is the accurate prediction of the outflow of CO_2 in the case of a rupture. Main parameter to be assessed are the following: massive discharge rate, pressure and temperature. The appearance of a multi-phase release should also be contemplated.

In recent years, many scientific efforts have been oriented towards the formulation of suitable models despite the lack of experimental data ([1,2]) and many uncertainties related to the reliable description of the different phases appearing during the depressurization ([3]).

This section, moving from the actual state of the art, is dedicated to the formulation of a 0-D model concerning the CO_2 depressurization from a pressurized domain. Some of the constitutive parameters are derived from the available experimental data resulting in a semi-empirical model.

5.2 CO_2 blowdown modeling: state of the art

Actually, many studies concerning the investigation of the modeling of CO_2 expansions from a pressurized domain are being carried out. The description of a depressurizing system is a key step in any QRA Procedure aimed at proposing a comprehensive approach in the description of hazards related to emerging infrastructures.

The main problem, already outlined in the experimental section, is the lack of an adequate case history providing reliable experimental data series helpful in tuning the model parameters ([2]).

Different research groups are dealing with the formulation of suitable predictive and semi-empirical models. The most proposeful is that linked to the works of Sergey Martynov, Haroun Mahgerefteh and coauthors, based at the *London University College*.

The research roadmap started in 1999 ([4]) with a first study focused on numerical related issues concerning the full-bore rupture of hydrocarbons pipelines. The proposed 1D *CNGS-MOC* model that is based on the method of characteristics aims at solving the system of quasi-linear hyperbolic *PDEs* arising from the description of a full-bore depressurization of lines carrying two-phase hydrocarbons.

An improved outflow transient model was later proposed ([5]) but the applicability to CO_2 was restricted because of its peculiar thermodynamic behavior. Some years later the attention was focused on the investigation of puncture failures ([6]) that are characterized by a different dynamic with more contained gradients. The model was referred to the same lines handling mixtures of hydrocarbons.

The comprehensive numerical solution of highly transient flows appeared in a work of 2006 ([7]). The proposed model is able to cover the description of the transient fluid dynamics following a rupture of pipelines containing liquids, flashing liquids and permanent gases.

The need to extend the results to networks carrying CO_2 emerged in 2013 with a first work focused on the description of choked-flow conditions arising in a rapid depressurization of a domain filled with CO_2 ([8]). The proposed analysis offers the investigation of the link between the stagnation conditions relevant to CCS pipelines and the final mass flow rate, mixture composition and pressure. Most of the attention was addressed to the prediction of the solid content of the resulting mixture that is strictly linked to the soil deposition of a bank of sublimating dry ice ([9]). The following step concerned the prediction of the CO_2 behavior following a sudden release from a pipeline ([10]). In ([10]), outflow conditions match the choked flow occurrence and CO_2 properties are assessed by means of a suitable adapted Peng Robinson-based EoS. Following an experimental large-scale campaign as part of *the 7th Framework Programme* (*FP7-CO2PipeHaz*), the model has been validated with a positive outcome. The experimental setup was made of a 256 m long, 233 mm internal diameter pipeline completed with a flanged outflow orifice ([10]).

In 2016, a specific model was proposed with respect to the *ESDVs* (*Emergency Shutdown Valves*) activation in the case of an emergency pipeline isolation procedure ([11]).

All models proposed by the *University College* research group are characterized by following aspects:

- constitutive equations are *PDEs* with a hyperbolic-driven behavior needing a numerical solving procedure that is usually based on the method of characteristics;
- the degree of detail is deep since the modeling allows for the prediction of main phenomena related to a rapid depressurization (choked flows, pressure and temperature profiles, dry ice formation) but it may be not suitable for emergency quick hazard estimations since the solving procedure is not simple;
- some parameters are not clear derived and some boundary conditions are not indicated making the model availability limited.

Further investigations on CO_2 pressurized release have been developed by other authors usually relying on available commercial software tools.

Starting from DNV PHAST®, the work proposed by Witlox et al. ([12]) pays attention to the software capability to predict the CO_2 discharge and subsequent atmospheric dispersion. The need to an extension to the usual model employed emerges. The extension is carried out by completing the model with an approach considering also the occurrence of liquid to solid and vapor to solid transition both for the post-expansion modeling as well as for the thermodynamic description of CO_2 properties. The study led to the conclusion that the failure to account for solid effects in the discharge modelling results in a too low post-expansion temperature. The validation against experimental data has not been reported. An improved model completed with a sensitivity analysis was proposed by the same authors in 2011 ([13]). The work is related to the improvement that come with DNV PHAST® v. 6.6 including the description of the solid transition. The proposed method shows a certain degree of robustness even if some sensitivities analysis results show deficiencies when assessing near-critical events and convergence problems with high pressure releases. In addition, the capability of the long pipeline time-dependent release model requires substantial improvements as also highlighted in a subsequent work ([14]) dealing with the experimental validation.

Also D.M. Webber ([15]) in his work deals with the applicability of HEM models to the case of the CO_2. The study shows a generalization of the integral model to the solid phase with a partial analysis of the solidification mechanisms. The model extension works also in the case of pressurized releases of CO_2 even if the study conclusions are qualitative.

The modeling of the CO_2 discharge has also been assessed by means of more sophisticated approaches such as those based on *Computational Fluid Dynamics* (CFD). It should be primarily noted that such a detailed investigation may not be always justified when dealing with QRA. This because the computational burden related to any CFD simulation may be

incompatible with timing requested to front the emergencies. Concerning the CFD tool approach, the research group of Leeds University started facing the CCS hazards simulation in 2014 ([16]). The results come from a research project aimed at investigating all safety-related aspects concerning Carbon Sequestration (*COOLTRANS* project). ([16]) involves the development of a mathematical model for predicting the near-field dispersion of CO_2 from a puncture failure of a CCS pipeline. The sophisticated model is able to manage both shock-related phenomena as well as non-equilibrium situations between the different CO_2 phases and the accordance with the experimental data is good and verified. In ([17]) the attention is focused on the releases below the ground and the implementation of a suitable EoS allows for the description of the solid phase appearance. A more detailed investigation is presented in ([18]). The nature of the puncture is divided depending on its position on the pipeline. The idealized reproduced crater along with a Lagrangian tracking algorithm allow for the estimation of soil deposition of solid particles of CO_2. To conclude, a complete and robust method is described in ([19]) with some applications in ([20]). In ([19]) the attention is focused on the formulation of a novel, robust and thermodynamically accurate multi-phase source model able to support far – field dispersion calculations. The description relies on RANS equations and a PREoS modified as suggested by same authors. Its application in ([20]) to a 96 km pipeline with a nominal external diameter of 0.61 m shows good accordance with experimental data (*Don Valley CCS Project*) especially those concerning mass fluxes exiting the crater and solid CO2 soil deposition.

In this introductory section concerning the state of the art of CCS hazards modeling some main research lines have been outlined. It is clear how all models proposed suffer a lack in simplicity, that is an easy implementability on QRA procedures without the loss of the capability to identify and describe main phenomena involved in a rapid expansion. For example, a CFD approach may be invoked only in the design or planning activity and solely applied to the most critical situations On the other hand, commercial software suites are not always available to users and the capability to manage CO_2 is usually limited because of the appearance of a solid phase.

Focusing the attention on the modeling of a hazard source identified as a pressurized release of CO_2, it is essential to develop a model with the following specs:

- it should be easy enough and robust to be readily applied to the consequence modeling without the need of complicated numerical schemes;
- the calculation procedure should require a reasonable time also in relation to emergencies timing;

- the model is based on conservation principles and should be able to track the variation of main variables characterizing the source term (temperature, pressure, mass flux, heat rate);
- the model has to be completed with an appropriate EoS able to match all possible thermodynamic phases that may appear because of the rapid expansion (gaseous, liquid, solid and supercritical).

Next section is dedicated to the development and the discussion of a model aimed at the description of a pressurized release of CO_2 from a reservoir starting from the application to the experimental data already discussed and from which some parameters have been derived.

5.3 CO_2 release modeling

This paragraph deals with the description of the model employed to catch the rapid depressurization of the CO_2 from a reservoir kept under controlled conditions.
The first section is focused on the main features to be caught with a depressurization model with special attention to depressurization dynamics and the effects on the CO_2 behavior. A second section follows with a detailed investigation of the proposed model through its constitutive equations and relations. Finally, the model is tested against the self-collected laboratory scale experimental data and it will be extended to medium and large scales.

5.3.1 Real substance expansion modeling from pressurized domains

The QRA procedure requires the quantification of any source term. In the case of a release of CO_2, the source term need a deeper investigation since the occurrence of a multi-phase system may arise because of the expansion ([9,10,15]). In addition, one of the phases appearing during the depressurization path may be solid in the form of dry ice once passed the thermodynamic triple point that is located at a pressure equals to 5.17 bar. This is to say that from a mere thermodynamic (ideal) point of view, the atmospheric expansion may be characterized by the presence of some solid CO_2 that then tends to sublimate giving rise to an additional source to the gaseous plume ([21]). As discussed in the previous chapters, not all expansions give rise to a solid content being this extremely linked to the nature of the depressurization pathway and the initial storage CO_2 conditions. However, an exhaustive model should deal with this occurrence being suitable to predict the final content pertinent to each phase. As discussed in ([9]), the relative amount should be predicted and known in order to address a correct consequence modeling since, for example, the occurrence of a soil deposition of dry ice will act as a delayed hazard source changing the accident characteristic time scale.

At this step the first fundamental hypothesis employed is that related to the assumption of thermodynamic equilibrium (HEM Model, *Homogeneous Equilibrium Model*) between each phase that is appearing ([1,15]). This means that phases move together and at any given point in the flow have the same temperature and are at the saturation pressure. Any deviation from this assumption requires additional manipulations as the introduction of a suitable non-equilibrium approach as will be discussed later.

Under this assumption, as previously discussed, the initial storage conditions of the CO_2 as well as the nature of the expansion govern the final thermodynamic state. This is characterized by a specific value for the temperature T, the pressure P and the relative phase content and because the HEM hypothesis, no temperature and pressure gradients exist among phases.

During the rapid depressurization, the CO_2 will be subjected both to pressure and thermal gradients. As experimentally observed, these gradients are partially linked. The partial linkage is due to the fact that gradient origins are different. In fact, pressure gradients are related to the flow of the substance and therefore to the presence of pressure drop elements between the storage and the discharge orifice. The resulting drop in the pressure will subsequently govern the temperature with a tendency to decrease it. The decrease trend is connected with the local transformation that is taking place as the experimental trials have shown. These transformations are ideally bounded by a perfect heat transfer (isothermal expansion) and no heat exchange with the surrounding (adiabatic expansion) with the real depressurization located somehow in the middle. This because, in addition, the thermal dynamic is influenced by the presence of the solid walls of the reservoir and the discharge line acting as warmer source to heat transfer mechanisms.

A sketch of the investigated steps is reported in Figure 5.1.

As indicated in Figure 5.1, the model will deal with the description of the pressure dynamics, the thermal gradients that are taking place both inside the vessel and at the orifice and finally with the mass flow rate that is leaving the system. In addition, some information about the heat transfer mechanisms are modeled. Further details will be given hereafter.

The model provided as reported in Figure 5.1 is then completed by means of further improvements. First of all, the capability to manage impure CO_2 is provided being usually carried out along with CH_4, N_2, O_2 and C_2^+.

Finally, moving away from HEM hypothesis, a simplified non-equilibrium correction is proposed. The improvement is based on the concept of relaxation dynamics throwing light on the specific singularities affecting the CO_2 phase transitions once subjected to rapid phase changes resulting away from the equilibrium condition.

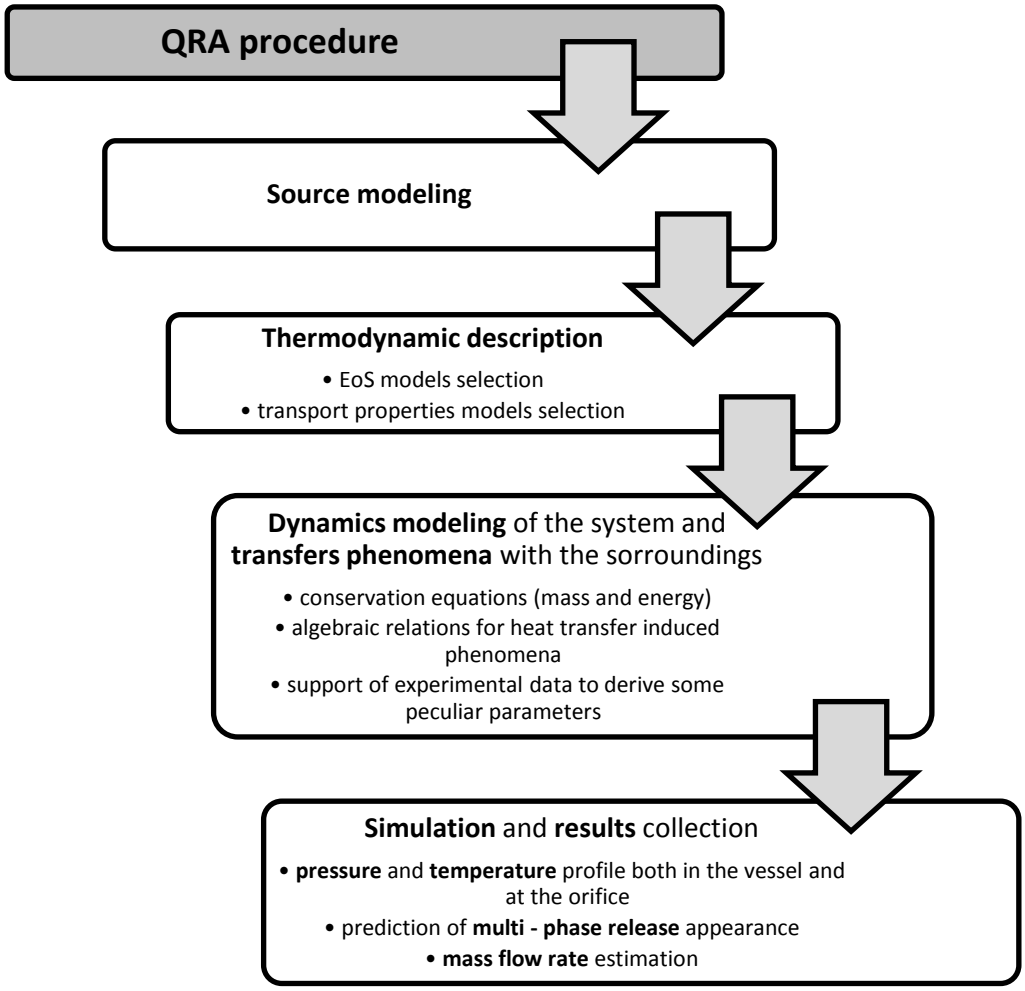

Figure 5.1. *Adopted approach in the CO_2 pressurized release modeling.*

5.3.2 CO_2 properties and expansion path description

Considered that the CO_2 is subjected to huge pressure and temperature gradients, a proper thermodynamic model is to be employed. The model should be able to correctly predict all properties of CO_2 in all possible phase domains as well as the thermodynamic transformations that are taking place because of the expansion.

Many models are actually available moving from the most simplified approaches to more complex Equations of State (EoS) and semi-predictive correlations ([22]). The accurate description of CO_2 behavior is essential since the physical phenomenon is essentially driven by the nature of the expansion that is taking place.

In addition, it should be noted that the thermodynamic model has to be characterized by the following aspects:

- it should be able to correctly predict solid, liquid, vapor and supercritical phase properties of CO_2;
- the transitions between distinct domain as well as vapor-liquid (VLE), solid-liquid (SLE) and solid-vapor (SVE) equilibria should be predicted with robustness;
- it should have an experimental basis or at least being validated against experimental data;
- it should be able to manage mixtures mainly composed of CO_2.

Among the available models, the most suitable are reported in Table 5.1.

Table 5.1. *Most suitable CO_2 EoS model.*

EOS MODEL	TYPOLOGY	NOTES	REFERENCES
PENG – ROBINSON (PREOS)	Predictive EoS	Suitable for liquid and vapor properties as well as for VLE	([23])
MODIFIED PENG – ROBINSON (MPREOS)	Semi predictive EoS	Reliable for the solid phase and in SVE description	([8,10])
SPAN – WAGNER (SWEOS)	Empirical correlation	Suitable for the supercritical domain	([24])
YOKOZEKI (YEOS)	Analytical EoS	Suitable for the description of the phase behavior of solid, liquid and vapor CO_2	([25])

As discussed in Chapter 2 and 3, among the illustrated models in Table 5.1, the YEoS is the most appropriate since it is able to match all CO_2 that may arise during the expansion and all parameters are available. However, when dealing with CO_2 mixtures, the PREoS is more suitable because of the lack of YEoS parameters concerning non pure compounds ([25]).

Briefly reiterating the main specs of the YEoS, it takes the formulation that follows in (5.1):

$$P(T,v) = \frac{RT}{v-b}\left(\frac{v-d}{v-c}\right)^{k} - \frac{a}{v^2 + qbv + rb^2} \quad . \tag{5.1}$$

In (5.1), P, T, v stand respectively for the pressure, the temperature and the specific volume while a, b, c, d, q and r are parameters whose meaning is illustrated in the dedicated section and in ([25]).

Solutions of (5.1) are strictly correlated to the function topology resulting from the parameters chosen combination.

The implementation of YEoS in the model will allow for the determination of the properties of liquid-vapor and solid-vapor equilibrium mixtures formed during the CO_2 vessel

decompression. At the same time the EoS model, that completes the conservation equations, is essential to give a description of the CO_2 thermodynamic path induced by the expansion.

As indicated in ([9,14,19]), the link between the thermodynamic state variables along the depressurization path needs to be assessed. However, a clear distinction between the ideal and the real framework should be highlighted. In this sense, when modeling any decompression phenomenon, the assessment of the specific sequence of thermodynamic states traveled by the CO_2 is usually based on assumptions ([1]). The most important concerns its nature being known that specific theoretical boundaries exist. These are mainly governed by the amount of heat exchanged with the domain boundaries. Therefore, the ideal limiting conditions corresponds on the one hand to a perfect heat exchange and on the other to negligible exchange with the vessel/pipeline walls. Corresponding transformations will be respectively isothermal and adiabatic. These conditions apply only to ideal transformations since neither a perfect heat transfer nor the adiabatic condition is ensured in a real system ([16,18,19]). Deviations arise since usual depressurization mechanisms are extremely rapid thus preventing an effective transfer of heat with the surroundings. Therefore, a certain amount of heat is exchanged especially with the vessel walls resulting in an intermediate transformation. Some details are reported in Figure 5.2.

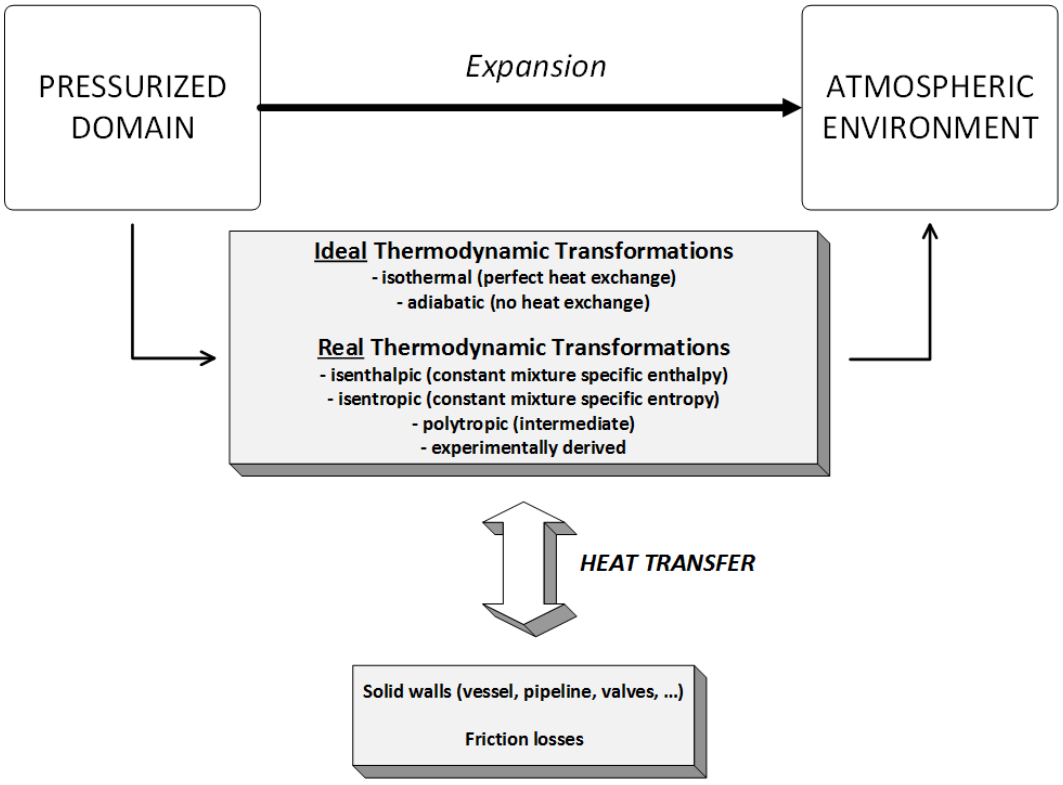

Figure 5.2. *Ideal and real expansions from a pressurized vessel. Heat transfer issues governing the transformations.*

As indicated in Figure 5.2 the presence of heat transfer mechanisms acts modifying the expansion nature and when modeling the expansion, the relative amount transferred cannot be known a priori. The quantity and the transfer efficiency will govern the transformation making it moving between the ideal limiting expansions (isothermal and totally adiabatic). Intermediate depressurizations can be identified as those performed at constant specific enthalpy and entropy (the specific conserved property is referred to the mixture).

The polytropic transformation can also be assumed when modeling the expansion once inserted a measure of the deviation from the ideal conditions and it is useful in characterizing the expansion and the compression processes which include heat transfer mechanisms. The insertion of an additional parameter represented by the polytropic index requires caution since only as long as the energy transfer ratio is constant it can be assumed to be a constant parameter. In addition, it should be noted however that a polytropic mechanism applies only for a transformation involving gaseous CO_2 ([22]) not subjected to a relevant kinetic energy contribution (i.e. with high-speed flow fields).

From a mathematical point of view, the selection of a certain thermodynamic pathway corresponds to the imposition of a constraint supplementing the discharge model. The formulation relies on the EoS model chosen because any constraint should be expressed in terms of the constancy of a specific differential. Focusing on the isentropic and isenthalpic expansions, the constraints are respectively $ds = 0$ and $dh = 0$, with s and h matching the specific entropy and enthalpy of the CO_2 mixture. The need of the EoS model arises when each differential is expressed in terms of the thermodynamic variables. In this sense, as already discussed, the manipulation leads to following (5.2-5.3):

$$ds = \left(\frac{\partial s}{\partial T}\right)_P dT + \left(\frac{\partial s}{\partial P}\right)_T dP = \frac{c_P}{T} dT - \left(\frac{\partial v}{\partial T}\right)_P dP = 0 \quad , \tag{5.2}$$

$$dh = \left(\frac{\partial h}{\partial T}\right)_P dT + \left(\frac{\partial h}{\partial P}\right)_T dP = c_P dT + \left[v - T\left(\frac{\partial v}{\partial T}\right)_P\right] dP = 0 \quad . \tag{5.3}$$

The derivation of (5.2-5.3) is essential since a numerical integration can lead straightforwardly to the link between two out of three state variables along a specified pathway.

If applied to (5.2-5.3), following (5.4-5.5) are obtained:

$$\left(\frac{\partial v}{\partial P}\right)_s = \left(\frac{\partial P}{\partial v}\right)^{-1} + \frac{T}{c_P}\left(\frac{\partial P}{\partial T}\right)_v^2 \left(\frac{\partial P}{\partial v}\right)_T^{-2} \quad , \tag{5.4}$$

$$\left(\frac{\partial v}{\partial P}\right)_h = \left[-c_P - T\left(\frac{\partial P}{\partial T}\right)_v^2 \left(\frac{\partial P}{\partial v}\right)_T^{-1} - v\left(\frac{\partial P}{\partial T}\right)_v\right]\left[-c_P\left(\frac{\partial P}{\partial v}\right)_T\right]^{-1} \quad . \tag{5.5}$$

The different partial derivatives are computed starting from an appropriate EoS model among those presented in Table 5.1 and the third thermodynamic state variable is derived from the application of the same EoS.

Strictly speaking, the transformation followed by the CO_2 and in general by any substance may not be known a priori. This because many phenomena are occurring ([8,26]) and because of the heat exchanged with the surroundings cannot be easily quantified. As discussed in the section dedicated to the experimental investigation, the laboratory scale investigation has allowed for the preliminary estimation of the near-wall heat exchanged as well as the thermodynamic expansion transformation followed by the CO_2. Trials involved the expansion of compressible CO_2 against which the model discussed in this section will be firstly tested.

5.4 The vessel blowdown model

The blowdown model, that is the system of equations describing the transient discharge rates following a vessel/pipeline rupture, is based both on conservation principles and appropriate correlations for predicting the CO_2 physical and hydrodynamic properties.

The model should be able to manage all the most important processes that are taking place because of the discharge phenomenon. These include the heat transfer between each fluid phase and the corresponding sections of the vessel walls, inter-phase fluxes due to evaporation, condensation and sublimation, the effects of sonic flow at the orifice as well as non-equilibrium effects that are discussed in a separate section.

The output includes the variations in time of the pressure, the temperature and all related variables both in the vessel and at the orifice, wall temperatures and the indication of the heat transfer coefficient.

The model can be run under different initial conditions, i.e. different CO_2 storage conditions. These ranging from the single-phase gaseous, liquid or supercritical state to a vessel filled with CO_2 at saturated conditions.

5.4.1 Pertinent modeled physical domain

Starting from the experimental setup, the physical domain is mainly represented by the pressurized vessel and the orifice discharge plane.

Figure 5.3 gives a schematic representation of the domain under investigation and required properties for the formulation of the outflow through the orifice.

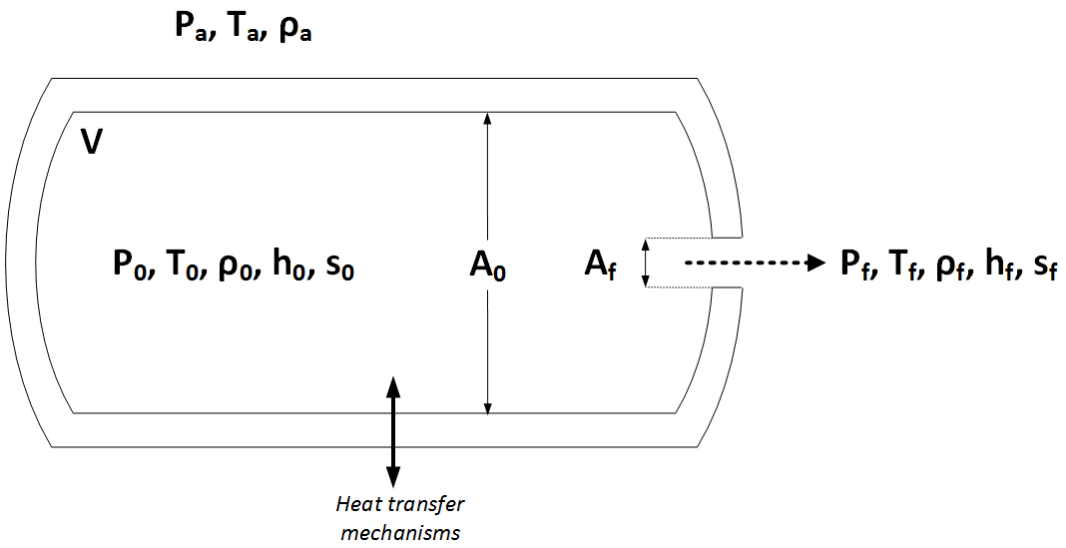

Figure 5.3. *Schematic representation of the discharging vessel with indication of the required properties.*

The physical system reported in Figure 5.3 shows that a distinction between the internal domain and the external environment is made. Each of them is characterized by the pertinent thermodynamic CO_2 properties that are evaluated both from the solving procedure of conservation equations and the algebraic constraints. Variables 0 subscripted refer to upstream (stagnation) conditions while f subscripted to downstream (post-expanded) conditions. The model makes a distinction between downstream choked and non-choked conditions applied at the discharge plane as discussed in chapter 3. As indicated in Figure 5.3, two distinct definitions of the atmospheric pressure P_a and that at the discharging throat P_f are employed ([27]).

The vessel is characterized by a constant volume V and the section driving the CO_2 to the orifice is assumed to have a negligible contribution to V. In addition, the thickness of the 316 austenitic stainless steel is considered when describing conduction-driven heat transfer phenomena as well as the ratio between the vessel internal section A_0 and that of the discharging orifice A_f.

The modeled domain as depicted in Figure 5.3 applies to a vessel filled with a single-phase vapour while a more general representation is given in Figure 5.4. Each phase is defined by means of proper thermodynamic properties while their pressure and temperature are initially assumed to be equal (homogeneous hypothesis). As discussed, non-equilibrium relaxation descriptive phenomena are considered later. In addition, the temperature of each phase is assumed to be uniformly distributed in space that is each portion is assumed to be well mixed.

The fluid prior to blowdown is assumed to be at equilibrium, i.e. each phase satisfies the equilibrium thermodynamic conditions. The fluid densities and phase equilibrium data at any

given pressure and temperature are determined using PREoS and YEoS. The number and the nature of the fluid phases existing at any given pressure and temperature are determined relying on the specified expansion pathway as well as on the Gibbs stability criterion.

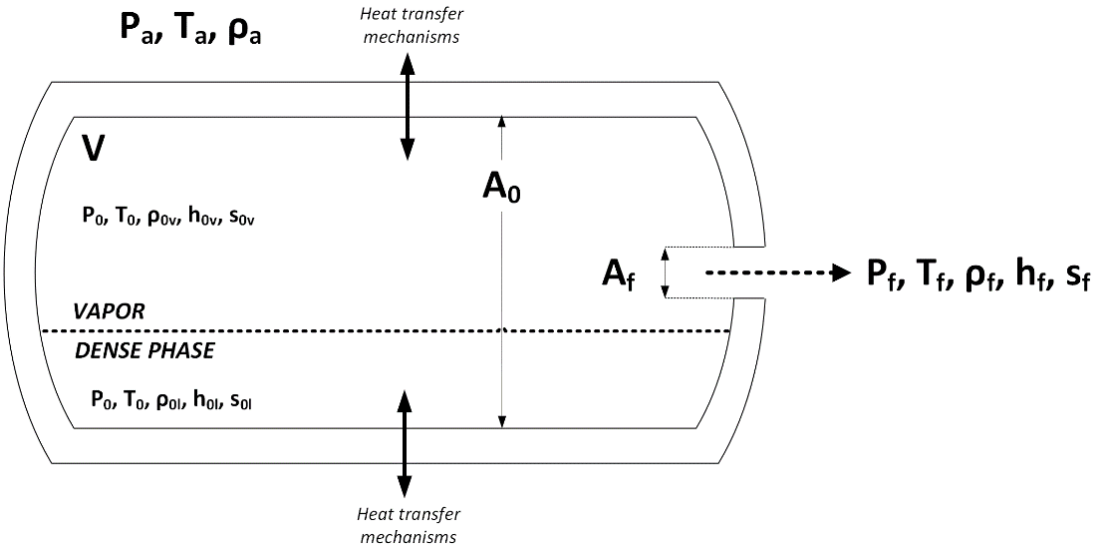

Figure 5.4. *Schematic representation of the discharging vessel with respect to a multi-phase release.*

5.4.2 The model structure

Two different approaches are followed depending on the initial state of the CO_2. Firstly, a model applied to only gaseous releases is illustrated in order to give reason to experimental data collected and parameters derived. A more complete approach follows, managing multi-phase releases.

5.4.2.1 Blowdown of vessels filled with gaseous CO_2

Considering Figure 5.3, two ideal sections are firstly marked. The position of section 0 is far enough from the discharge point to neglect the CO_2 velocity but allowing no reverse flow across it during the discharge. Section 1 corresponds instead to the discharge plane. The two portions so bounded are considered separately.

Relevant balances with respect to section 0 are the mass and the energy conservation equations as respectively formulated in (5.6-5.7):

$$\frac{d}{dt}(\rho_0 V) = V\frac{d\rho_0}{dt} = -\dot{m}_0 \quad , \tag{5.6}$$

$$\frac{d}{dt}(\rho_0 V\widetilde{u_0}) = V\left[\rho_0\frac{d\widetilde{u_0}}{dt} + \widetilde{u_0}\frac{d\rho_0}{dt}\right] = -\dot{m}_0\left(\widetilde{u_0} + \frac{P_0}{\rho_0}\right) + \dot{q}_v A_{int} \quad . \tag{5.7}$$

In (5.6), ρ_0 is the instantaneous CO_2 density, $\dot{m}_0$ is the mass flux of CO_2 leaving section *0* while in (5.7) $\widetilde{u_0}$ is the specific internal energy of the CO_2, P_0 the instantaneous pressure inside the vessel, $\dot{q}_v$ the heat flux at the vessel wall and A_{int} the internal vessel surface area.
The (5.7) takes the form reported in (5.8) once algebraically manipulated:

$$\rho_0 V \frac{d\widetilde{u_0}}{dt} = -\frac{\dot{m}_0 P_0}{\rho_0} + \dot{q}_v A_{int} \quad . \tag{5.8}$$

The differential of the real gas internal specific energy can be expressed as in (5.9) being the system at constant volume V:

$$d\widetilde{u_0} = \widetilde{c_v}(T_0)dT_0 + \left[T\frac{dP_0}{dT_0} - P_0\right]dV = \widetilde{c_v}(T_0)dT_0 \quad . \tag{5.9}$$

The mass flux $\dot{m}_0$ needs to be quantified to close the system of (5.6-5.8). It is strictly linked to both the pressure ratio P_0/P_f that is instantaneously changing because of the depressurization, the establishment of choked flow conditions and the expansion path followed by the CO_2 traveling from section *0* and *1*.
The description of the CO_2 flow between section *0* and *1* relies on the hypothesis that the mass flux at these two sections is almost the same, i.e. a *quasi-steady state assumption* (QSSA) is employed with no reverse flow. The application of the mass and mechanical energy conservation between section 0 and 1 allows for the $\dot{m}_0$ determination. They take the form indicated in (5.10-5.11):

$$\frac{d}{dt}(\rho v A) = 0 \quad , \tag{5.10}$$

$$\frac{\langle u_1\rangle^2}{2} - \frac{\langle u_0\rangle^2}{2} + \int_0^1 \rho^{-1} dP + \frac{1}{2}\langle v_1\rangle^2 \varphi = 0 \quad . \tag{5.11}$$

In the mechanical energy balance (5.11), $u_0 = 0$ because of the location of section *0* while the fourth term accounts for the viscous dissipation with φ that stands for the friction loss factor. φ can be directly to the obstacle geometry along the flow streamline. The case under investigation involves both a sudden section contraction as well as the discharging orifice whose contributions are respectively evaluated as follows ([28]):

$$\varphi = 0.45\left(1 - \frac{A_f}{A_0}\right) \quad , \tag{5.12}$$

$$\varphi = 2.71\left(1 - \frac{A_f}{A_0}\right)\left[1 - \left(\frac{A_f}{A_0}\right)^2\right]\left(\frac{A_f}{A_0}\right)^{-2} \quad . \tag{5.13}$$

The combination of (5.10-5.11) allows for the determination of $\dot{m}_0$ that takes the form indicated in (5.14):

$$\dot{m}_0 = \gamma_d \rho_1 A_f \sqrt{\left[-2\left(\int_0^1 \rho^{-1} dP + \frac{1}{2}\langle v_1\rangle^2 \sum_i \varphi_i\right)\right]\left[1 - \left(\frac{\rho_1 A_f}{\rho_0 A_0}\right)^2\right]} \quad . \tag{5.14}$$

The final descriptive model is therefore finally composed by following (5.15-5.16):

$$\rho_0 V \frac{d\widetilde{u_0}}{dt} = -\frac{\dot{m}_0 P_0}{\rho_0} + \dot{q_v} A_{int,v} \quad , \tag{5.15}$$

$$-V\frac{d\rho_0}{dt} = \gamma_d \rho_1 A_f \left[-2\left(\int_0^1 \rho^{-1} dP + \frac{1}{2}\langle u_1\rangle^2 \sum_i \varphi_i\right)\right]^{1/2}\left[1 - \left(\frac{\rho_1 A_f}{\rho_0 A_0}\right)^2\right]^{1/2} \quad . \tag{5.16}$$

The integral of (5.16) is evaluated along a streamline connecting section *0* and *1* by means of the appropriate EoS describing the occurring thermodynamic transformation. In this sense how T changes with P along a streamline is assessed selecting the suitable transformation as discussed in section 3.2 and the density ρ is derived from the relation $\rho = \rho(P,T)$.

The description of the heat transfer mechanism between the CO_2 and the vessel wall is relies on a 1-D semi-infinite modeling. In this sense the conduction in the walls is assumed to be mono dimensional and the approach consists in the description of the heat transfer in a semi-infinite homogenous medium with a front boundary condition related to the instantaneous CO_2 temperature.

Starting from these considerations, the model is therefore completed by the (5.17):

$$\rho_w C_w \frac{\partial T_w}{\partial t} = \lambda \frac{\partial^2 T_w}{\partial x^2} \quad . \tag{5.17}$$

In (5.17), ρ_w and C_w stand respectively for the wall density and heat capacity while λ is its thermal conductivity that is assumed to be temperature dependent. x instead is a space coordinate following the development of the wall.

The *PDE* comparing in (5.17) is therefore completed by following initial and boundary conditions (5.18-5.20):

$$T_w(x \to \infty) = T(t=0) \quad , \tag{5.18}$$

$$T_w(x, t=0) = T(t=0) \quad , \tag{5.19}$$

$$-\lambda \frac{\partial T_w}{\partial t}\bigg|_{x=0} = h_i A_{int}(T - T_w) \quad . \tag{5.20}$$

The heat flux that passes between the CO_2 and the solid wall is therefore computed from the Newton's law (5.21):

$$\dot{q_v}(t) = h_i A_{int}(T - T_w) \quad . \tag{5.21}$$

The transfer mechanism invoked by h_i in (5.20-5.21) is assumed to be represented by a heat flow resistance related to convection-driven phenomena.

Natural convection heat transfer individual coefficient is described by (5.22) as proposed in ([29]):

$$Nu_d = \left\{ 0.60 + \frac{0.387 {Ra_d}^{1/6}}{\left[1 + \left(\frac{0.559}{Pr}\right)^{9/16}\right]^{8/27}} \right\} \quad . \tag{5.22}$$

The (5.17) is valid for $Ra_d = Gr_d Pr < \sim 10^{12}$.

5.4.2.2 Blowdown of vessels filled with dense/supercritical CO_2

The description of the blowdown involving dense CO_2 should deal with boiling-related phenomena as well as the interphase heat exchange and the heat-induced phenomena with the vessel walls ([1,12]).

In fact, the dense CO_2 expansion will drive the system towards the appearance of a multi-phase release depending on the transformation that is taking place.

Therefore, being the heat transfer phenomena a key aspect in the release modeling, the description of both the boiling and condensation mechanisms should be taken into account. In addition, given the CO_2 thermodynamic behavior, also the solid phase appearance is to be included in the model especially at the final stages of the release where the pressure will fall below that of the triple point. In this case, the modeling of the solidification phenomenon with reference to the exchanged heat flux is expected.

The system description is dependent on the initial charging conditions and therefore on the number of phases initially present. The vessel can in fact be completely filled with dense CO_2 or under saturation conditions, i.e. partially filled with vapor. Each phase will contribute to the mass and energy balances because both matter and energy inter-phase exchanges are taking place.

In the case of liquid and vapor CO_2, the inter-phase mass and energy fluxes during the expansion are shown to be a consequence of:

- condensation in the sub-cooled vapor;

- evaporation in the boiling liquid.

Appropriate assumptions and the material balances need to be applied to each phase domain. Considering the domain pertaining to each phase, the material balance can be assumed as indicated in (5.23):

$$accumulation = (input - output) + (produced - consumed) \quad . \tag{5.23}$$

Therefore, the material balances on the domain occupied by the gas and the liquid are respectively described by the following (5.24 – 5.25):

$$\frac{dm_V}{dt} = \dot{m_{L\to V}} - \dot{m_{V\to L}} - \dot{m_{V,out}} \quad , \tag{5.24}$$

$$\frac{dm_L}{dt} = \dot{m_{V\to L}} - \dot{m_{L\to V}} - \dot{m_{L,out}} \quad . \tag{5.25}$$

In (5.24-5.25), m_V and m_L stand respectively for the instantaneous vapor and liquid mass contained in the vessel while $\dot{m_{i\to j}}$ has the aim of describing the mass flow rate leaving phase i and entering phase j. The relative mass flow rates are strictly depending on thermodynamic trajectory followed during the expansion.

In the case of solid phase appearance and considering only the solidification from the liquid phase and the sublimation phenomena to the vapor phase, the mass balance is as of (5.26):

$$\frac{dm_S}{dt} = \dot{m_{L\to S}} - \dot{m_{S\to V}} - \dot{m_{S,out}} \quad . \tag{5.26}$$

As discussed, the rates of mass and energy transfer in each fluid zone are governed by the transformation that is affecting each portion. In this sense, the application of the 1st and 2nd laws of thermodynamics allows to derive both the specific thermodynamic phase properties as well as the relative amounts.

Considering the vapor domain, the application of the 1st law of thermodynamic and the mass balance gives the (5.27):

$$s = \frac{T_V(m_V s_V + m_{L\to V} s_{L\to V}) + \dot{q_V}}{T_V(m_V + m_{L\to V})} \quad . \tag{5.27}$$

Instead, moving to the liquid phase domain and neglecting the mechanical work done by this CO_2 portion, the following (5.28-5.29) respectively applies for the specific enthalpy and entropy:

$$h = \frac{m_L h_L + m_{V\to L} h_{V\to L} + \dot{q_L}}{m_L + m_{V\to L}} \quad , \tag{5.28}$$

$$s = \frac{T_L(m_L s_L + m_{V\to L} s_{V\to L}) + \dot{q}_L}{T_L(m_L + m_{V\to L})} \quad , \tag{5.29}$$

while for the solid domain, the analogous (5.30-5.31) are used:

$$h = \frac{m_S h_S + m_{L\to S} h_{L\to S} - m_{S\to V} h_{S\to V} + \dot{q}_S}{m_L + m_{V\to L}} \quad , \tag{5.30}$$

$$s = \frac{T_S(m_S s_S + m_{L\to S} s_{L\to S} - m_{S\to V} s_{S\to V}) + \dot{q}_S}{T_S(m_S + m_{L\to S} - m_{S\to V})} \quad . \tag{5.31}$$

The presence of different phases requires also distinct approaches in the modeling of heat transfer phenomena between the phase domain and the contacting wall as well as the inter-phase transfer.

The application of the energy balance between each phase portion and the corresponding section of the vessel is determined by (5.32):

$$q_i = \left(T_{w,i} - T_i\right) U_i A_i \Delta t = m_w c_{P,w} \Delta T_{w,i} \quad . \tag{5.32}$$

In (5.32), $T_{w,i}$ is the average wall temperature adjacent to phase i at temperature T_i, U_i is the overall heat transfer coefficient between zone i and the corresponding wall portion with exposed area A_i. In addition, m_w is the mass of the vessel section in contact with the phase i and $c_{P,w}$ is its specific heat.

The definition of the heat transfer coefficient invokes all heat transfer mechanisms that are taking place between the vessel wall and each fluid domain.

In the vapor domain, it is assumed that both natural and forced convection may arise because of both density and pressure gradients. The heat transfer coefficient is weighted on the vessel geometry with a distinction between the vessel domes and the cylindrical section.

The (5.33) gives the formulation of the heat transfer coefficient U_i:

$$U_i = h_{i,END} \frac{A_{i,END}}{A_i} + h_{i,C} \frac{A_{i,C}}{A_i} \quad . \tag{5.33}$$

In (5.33), $h_{i,END}$ and $h_{i,C}$ stand respectively for the heat transfer coefficients referred to the end caps of the vessel and the cylindrical section. $A_{i,END}$ and $A_{i,C}$ correspond to exposed surfaces related to the end caps and the cylindrical section.

The heat transfer with $A_{i,C}$ can be adequately described by following relation (5.34) ([29]):

$$Nu_C = \left\{ 0.835 + \frac{0.387 {Ra_V}^{1/6}}{\left[1 + \left(\frac{0.559}{Pr_V}\right)^{9/16}\right]^{8/27}} \right\} \quad . \tag{5.34}$$

Considering the dimensionless groups presented in (5.34), the characteristic length to be used in the formulation is referred to the domed end of the vessel L_D and the exposed domed surface $A_{i,D}$ that is:

$$L_D = 2\left(\frac{A_{i,D}}{\pi}\right)^{1/2} \quad . \tag{5.35}$$

Moving to the dense phase domain, the heat transfer is mainly governed by the boiling heat transfer ([2,10,13]).

As known, many boiling regimes exist and are mainly driven by the excess temperature between the saturated liquid and the contacting surface as indicated in Figure 5.5.

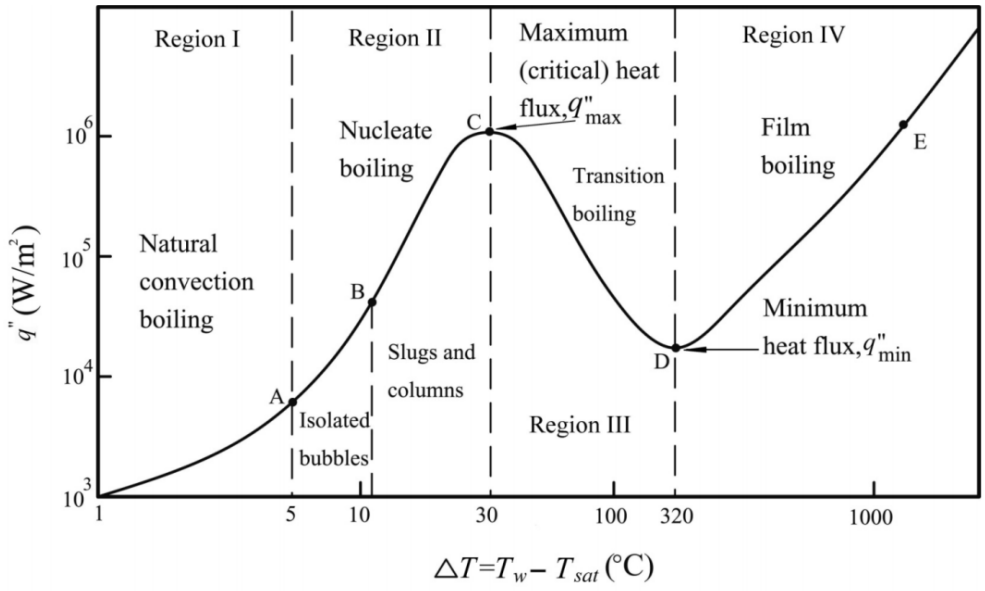

Figure 5.5. *Pool boiling curve of a saturated substance.*

The description of each boiling regime is widely discussed in technical references ([30]) with related correlations able to predict the excess temperatures at minimum and maximum heat fluxes.

Considering the conditions arising from the blowdown mechanism, it should be noted that the difference in the temperature between the wall and the liquid is usually small and leads to nucleate boiling effects. However, the domain should not be affected by external heat sources like that induced by fires.

The heat flux related to the nucleate boiling mechanism is estimated by means of a suitable correlation ([31]):

$$\dot{q} = \mu_L L_{ev} \frac{g\left(\rho_L - \rho_{L,ev}\right)}{\sigma} \left(\frac{c_{P,L} \Delta T_e}{\vartheta L_{ev} Pr_L^{\gamma}} \right)^3 \quad . \tag{5.36}$$

The (5.36) is applied for clean surfaces. L_{ev} stands for the latent heat of vaporization, $c_{P,L}$ for the liquid sensible heat, σ is the surface tension and $\rho_L - \rho_{L,ev}$ the difference between the liquid and the evaporated liquid density. ϑ and γ are two parameters related to the surface nature and are derived from ([31]).

Because of the absence of external relevant heat sources like fires, the transition to the film boiling mechanism is not considered since it is assumed to be extremely unlike. In fact, the transition to the film boiling regime occurs uniquely at very large excess temperatures that may only be induced by external heat sources.

The solidification mechanism that involves the unstable liquid region is modeled on the methodology proposed by some authors ([32]).

To confirm some hypothesis, a scaling procedure analysis is applied in order to establish the relative scales of both the convective u_{conv} and the solidification u_{sold} velocity. While u_{conv} is assessed starting from a balance between the buoyancy and the viscous effects, the solidification velocity is based on the two main fluxes arising during the solidification and related to the phase change. The first heat flux concerns the latent heat transfer while the second is linked to the flux across the solid layer. They are respectively modeled as reported in (5.37-5.38):

$$\dot{q_L} = \rho_{S,CO_2} L_{s,CO_2} \frac{dl}{dt} \quad , \tag{5.37}$$

$$\dot{q_S} = k_{S,CO_2} \frac{\partial T_s}{\partial x} \quad . \tag{5.38}$$

Therefore, considered the dimensional analysis applied to both u_{conv} and u_{sold}, it can be established that the following (5.39) holds:

$$\frac{u_{conv}}{u_{sold}} \gg 1 \quad , \tag{5.39}$$

thus allowing for the employment of a PSSA (*pseudo-steady state assumption)* relying on a corresponding correlation of the form $Nu = \varphi(Pr, Ra)$ as reported in (5.40) ([33]):

$$Nu = 0.069 \sqrt[3]{Ra} Pr^{0.074} \quad . \tag{5.40}$$

Moving to sublimation-related phenomena, it should be noted that this occurrence is related only to the solid phase appearance and this is not always the case in rapid depressurizations. In fact, the thermodynamic pathway may not lead to the solid phase domain that anyhow is located below the triple point pressure (5.17 bar). Conditions leading to the solid phase appearance depend on different expansion pathways and have been already discussed in Chapter 3.

The predicted solid content is upper bounded at 0.40 (m/m) at atmospheric conditions, that is when the vessel is almost empty. Therefore, the description of the solid phase is confined to the final blowdown stages and sublimation mechanisms may arise. In this sense the SVE that may be established because of the (P, T) conditions will lead to a relative increase of the vapor content of the mixture. However, experimental evidences ([34,35,36]) show that the sublimation mechanisms are almost entirely taking place downstream of the release orifice and therefore the description of this occurrence is not necessary when dealing with the vessel internal dynamics. Nevertheless, the formation of the solid domain cannot be neglected since it is actively involved in the thermal balance of the vessel interior. The presence of the solid content induces changes in the dynamics at the orifice especially with regard to the establishment of the choked flow conditions and the magnitude of the sonic velocity.

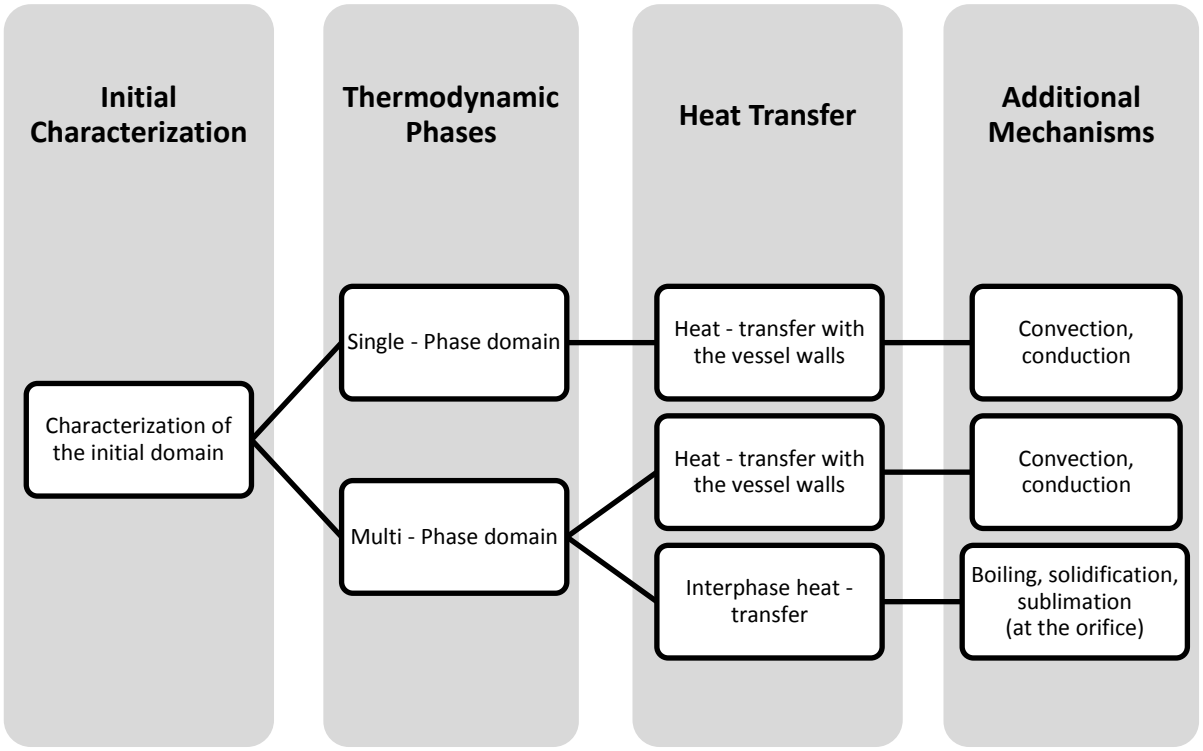

Figure 5.6. *Modelling approach with reference to heat-transfer mechanisms involved in the CO_2 vessel blowdown.*

As it will be explained in the following section, the solving algorithm checks the establishment of the choked flow conditions even with reference to the mixture solid amount and therefore the instantaneous relative quantity should be known. Figure 5.6 gives an overall representation of the main sections of the model employed for the description of the vessel blowdown with respect to heat-transfer mechanisms.
Heat-transfer mechanisms presented in Fig. 3.6 and related to the external and internal-driven temperature gradients, are coupled with the conservation principles applied to each appearing phase.
The solving algorithm is reported in the following section 5.4.3.

5.4.3 Solving algorithm

The proposed equations are not suitable to be directly solved and should be inserted in a solving procedure with the investigation of the choked flow occurrence, being a limiting condition on the discharge dynamics. From a theoretical point of view, the establishment of this limiting condition is always achieved since the charging pressure is well above the atmospheric threshold value. The discharged inventory is therefore connected to the sonic velocity at the orifice that is in turn strictly related to the mixture quality and the relative amount of dense phase.
Accordingly, the general logic diagram of the algorithm can be formulated as in Figure 5.7.
As of Figure 5.7, the model inputs concern both the initial CO_2 state and the vessel properties. The initial conditions of the substance are based on the EoS models of Table 5.1 while the phase coexistence description relies on the application of the Gibbs stability criterion. The assessment of the initial CO_2 conditions are directly derived from the EoS application with the initial phase distribution based on a flash calculation.
The algorithm involves the investigation of the occurrence of sonic conditions at the orifice, these representing a limiting stage of the CO_2 discharge. As already discussed, the limiting condition expresses itself as a local maximum with respect to the velocity along a streamline. In this sense, the mass flux exhibits different behaviors depending on its nature, i.e. the relative content of the different phases.
Figure 5.8 gives a general example of the dimensionless mass flux with respect to a dimensionless velocity based on the local speed of sound c.

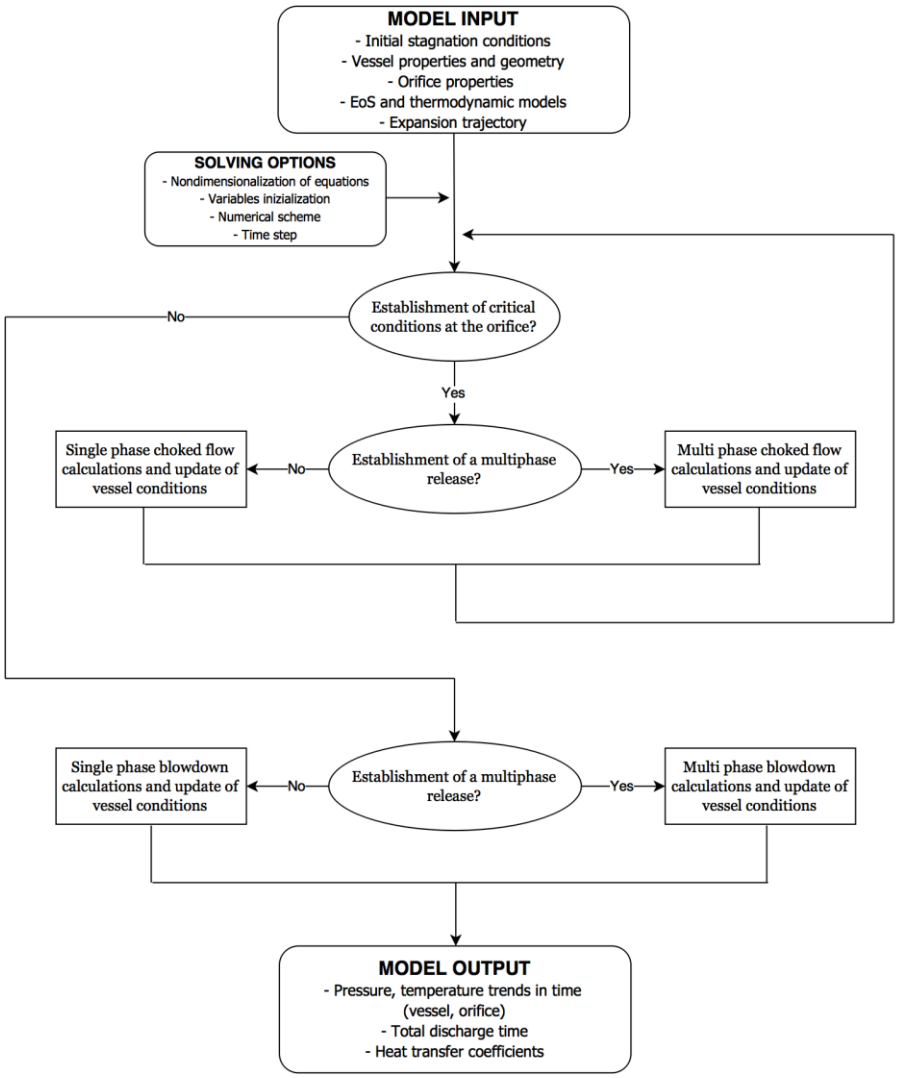

Figure 5.7. *Proposed logic diagram in the numerical model resolution.*

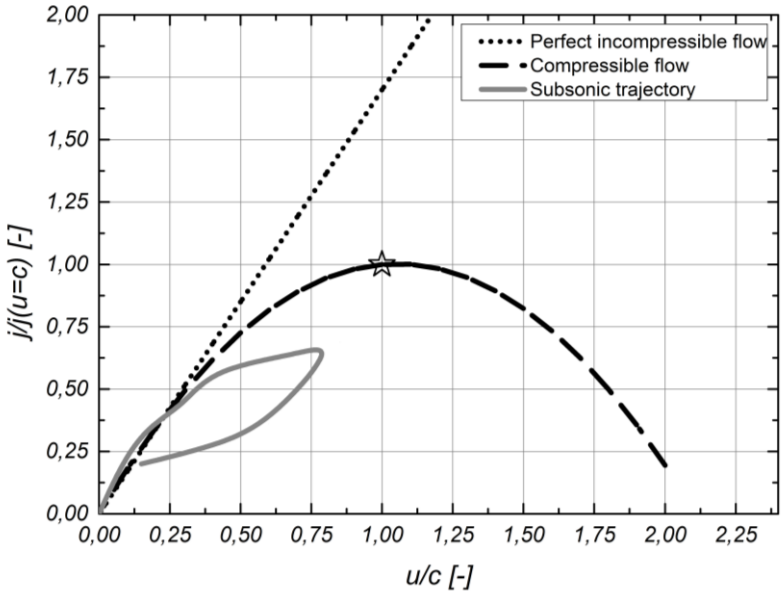

Figure 5.8. *Mass flux with respect to the streamline local velocity.*

The profiles indicated in Figure 5.8 derive from the direct application of the definition of the speed of sound c. This from a thermodynamic point of view can be expressed as indicated in (5.41):

$$c \equiv \sqrt{\left(\frac{\partial P}{\partial \rho}\right)_s} = v\sqrt{\frac{T}{c_V}\left(\frac{\partial P}{\partial T}\right)_s^2 - \left(\frac{\partial P}{\partial v}\right)_T} \quad . \tag{5.41}$$

The (5.41) and the following (5.42), that is derived from a local momentum balance along the streamline, gives reason to what indicated in Figure 5.8:

$$udu = -\frac{1}{\rho}\frac{\partial P}{\partial \rho}d\rho \quad . \tag{5.42}$$

Therefore, it is clear that if the substance density is uniform, an increase in the local velocity will always correspond to a parallel increase in the mass flux j. The constancy of the density as in the case of a perfect incompressible fluid, i.e. in its permanent liquid or supercritical state, will lead to a straight line as reported in fig. 3.8 without the appearance of limiting *choked* conditions.

However, the presence of a local multiphase system composed by a compressible fraction like that induced by the CO_2 vapor, leads to deviations from this behavior. The mass flux induced by a fully compressible flow behaves passing through a local maximum corresponding to the critical conditions ([37]). Once overcome, the flow assumes supersonic features.

From a qualitatively point of view, the nature of a subsonic compressible flow is similar to that of an incompressible substance but its quantification is complicated by the fact that the local density is instantaneously changing. At the same time, the local thermodynamic speed of sound c is affected by the evolution of the multiphase system. Therefore, referring to Figure 5.7, once assessed the occurrence of sonic conditions at the orifice, the algorithm should give an estimation of the local speed of sound c considering the instantaneous coexistence of different CO_2 phases.

For this purpose, as already discussed in Chapter 3, the mixture speed of sound is calculated as proposed by some authors ([37]). In this sense a general approach is followed with the aim to make the analysis feasible also in the case of solid phase appearance. Therefore, considered that from (5.42) follows (5.43):

$$c = \sqrt{-\frac{v^2}{MW\left(\frac{\partial v}{\partial P}\right)_{s,x}}} \quad , \tag{5.43}$$

the partial derivative comparing in (5.43) is derived making explicit its components. In (5.43), v stands for the molar volume and MW is the mixture molecular weight.

Numerical-related issues require the expressione of the partial derivatives in to easy-to-handle formulations especially with reference to the nature of the EoS model that may not be an explicit function of some thermodynamic state variables.

The general formulation suitable for the algorithm application is reported in (5.44):

$$\left(\frac{\partial v}{\partial P}\right)_{s,x} = -\left(\sum_{j=1}^{n_P} \frac{n_j (\partial P/\partial T)_{v_j,x_j}}{\left(\partial P/\partial v_j\right)_{T,x_j}}\right)\left(\frac{\partial T}{\partial P}\right)_{s,x} + \sum_{j=1}^{n_P} \frac{n_j}{\left(\partial P/\partial v_j\right)_{T,x_j}} - \sum_{j=1}^{n_P}\sum_{i=1}^{n_c}\left(\frac{\left(n_j\left(\partial P/\partial n_{ij}\right)_{T,v_j,n_{kj}\neq n_{ij}}\right)}{\left(\partial P/\partial v_j\right)_{T,x_j}}\right)\left(\frac{\partial x_{ij}}{\partial P}\right)_{s,n} \quad . \tag{5.44}$$

The derivation of the additional partial derivatives introduced in (5.44) are reported in Chapter 2. In addition, the same (5.44) is strictly linked to the phase balance since the changes in the relative amount, i.e. mass fraction, of each appearing phase is governed by the mass constraint.

In the case of a gas-liquid CO_2 flow, the algorithm refers alternatively to the (5.45) proposed by Minnaert (1933):

$$c^{-2} = [\rho_L(1-\beta) + \rho_G\beta]\left[\frac{\beta}{\gamma P} + \frac{(1-\beta)}{\rho_L c_L^2}\right] \quad , \tag{5.45}$$

In (5.45), the mixture speed of sound c is weighted on the instantaneous volume fraction β of the gas portion; γ stands for the heat capacities ratio and P the system pressure, assuming no local pressure gradients induced by the presence of the surface tension.

Moving back to Figure 5.7, the solving algorithm will therefore invoke the calculations reported in (5.41-5.45) giving an estimation of the local mixture speed of sound whenever the flow regime pertains to the *choked flow* case. This regime can be reached by a single phase (gaseous) or by a multiphase (mixture of liquid-vapor or solid-vapor) flow and this has implications on the mass flux prediction. As emerged by some works ([8,10,11]), the alteration in the mass flux related to the establishment of the sonic conditions is relevant when dealing with the liquid and solid phase appearance.

The mathematical relation involving the critical mass flux G_{choked} can be summed up as reported in (5.46) and is applicable to both single and multiphase domains:

$$G_{choked} = \left.\frac{\partial G}{\partial P}\right|_{P=P_{choked}} = 0 \quad , \tag{5.46}$$

The (5.46) is equivalent to state that the function $G(P)$, that is assumed to be continuous and smooth with respect to the pressure P, is analyzed with respect to the local maximum point $max\, G(P)$. This local maximum point defines the *choked state* for the flow under investigation.

As already discussed in Chapter 3, some conditions may lead to the appearance of multiple *choked flow* states in the sense that each phase coexistence domain (LVE or SVE) has its own critical point. The dividing pressure value is that corresponding to the CO_2 triple point.

Figure 5.9 qualitatively illustrates the above. Further details are demanded to Chapter 3.

Depending on the initial conditions, as shown in Figure 5.9, the expansion to the atmospheric condition can be characterized by one or two maxima. In the latter case, the first choked state is located above the triple point pressure while the second below and therefore are respectively characterized by the simultaneous presence of the liquid and solid CO_2 in the vapor flow ([8]).

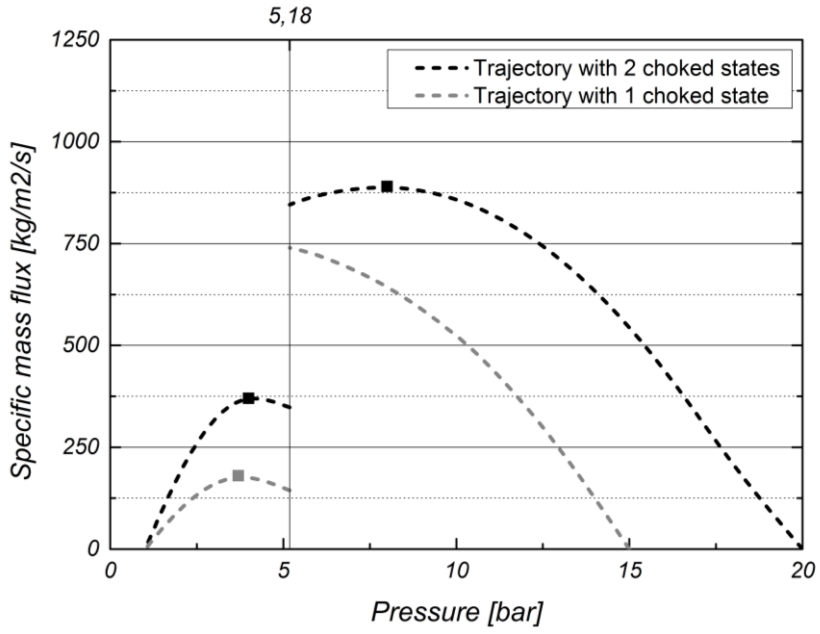

Figure 5.9. *Specific mass flux with respect to the pressure. Trajectory characterized by a single choked state (grey) and multiple choked states (black).*

When dealing with this occurrence, the algorithm philosophy will allow for the selection of the actual *choked* state since it should be noted that when the CO_2 is expanding and therefore its pressure is decreasing, only the *choked* state at the higher pressure will be matched, establishing a unique state. The corresponding mass flux will be therefore evaluated in order to assess the amount of fluid discharged from the system. Its evaluation can be translated in a

maximization of the mass flux with respect to the specific mass fraction of the dispersed phase ([8,11,38]).

The approach consists in the calculation of the corresponding mass flux under the hypothesis of local equilibrium between the facing phases be means of the continuity and the energy conservation equations ([8,38]).

In addition, considered that flow streams are in equilibrium (properties are evaluated along the saturation line), CO_2 features are only pressure dependent as indicated in (5.46).

However as observed by some authors ([8,11]), in the case of the SVE and SVLE (at the triple point), the functional relation is completed by the equation expressing the weighted general property φ with respect to the local vapor mass fraction x_v.

In this way the maximum mass flux G_{choked} can be expressed also in terms of the solid mass fraction x_s as reported in (5.47):

$$G_{choked}\left(P \leq P|_{t.p.}\right) = \max G(x_s) \quad . \tag{5.47}$$

This algorithm step is inserted in the specific procedure as indicated in Figure 5.10.

The specific procedure linked to Figure 5.7 is inserted in the general algorithm philosophy.

These calculations involve following main steps:

- numerical evaluation of the expansion path linking the orifice variables to the vessel behavior;
- numerical integration of mass balances for the single phase domain and the multiphase system;
- simultaneous integration of the energy conservation equations;
- determination of the wall temperatures and the heat transfers through a heat coefficient referred to each phase at equilibrium also considering the presence of thermal insulations.

Considering the numerical approach, conservation equation are integrated by means of a procedure based on an implicit *Runge-Kutta* scheme while the calculations concerning the *choked* flow are performed following iterative computations.

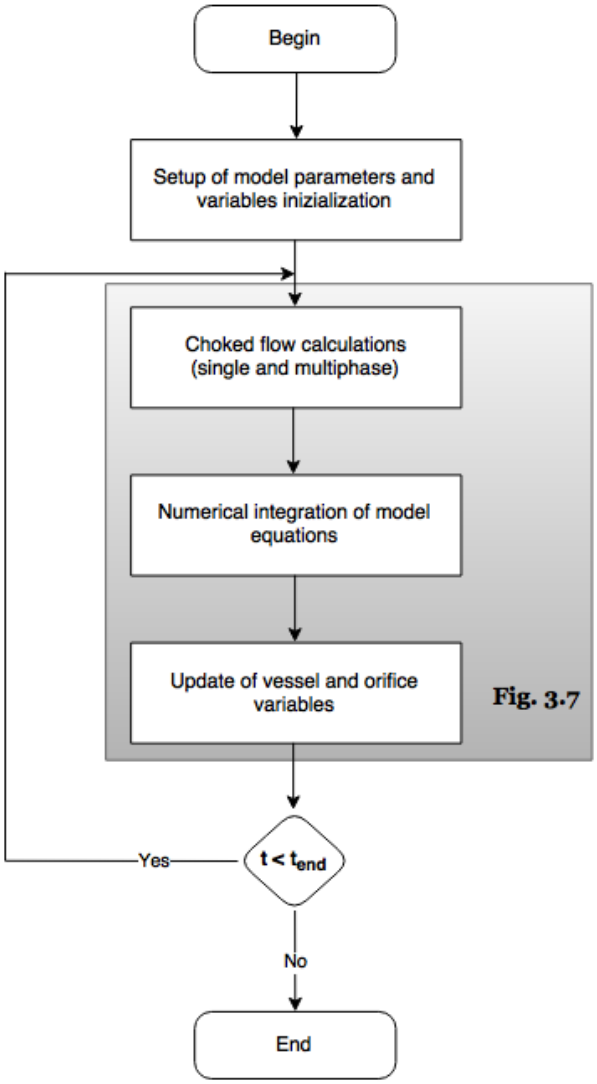

Figure 5.10. *Vessel blowdown solving algorithm.*

5.5 Model application and results

This section is devoted to the application of the proposed model to the experimental data in order to investigate the prediction capability. Transient pressure and temperature trends are firstly analyzed. The final part, instead, is focused on the discharged mass flow rate and the total discharge time.

5.5.1 Transient pressure profiles

Pressure profiles derived from 35, 20 and 10 barg depressurizations are firstly investigated. The initial temperature is 20 °C as reported in Table 5.2.

Table 5.2. *Examined experimental trials set.*

EXPERIMENTAL TRIAL	PRESSURE [BAR]	TEMPERATURE [°C]	INSULATION
A	10	20	No
B	20	20	No
C	35	20	No

Figure 5.11-5.13 gives a comparison between the experimental and the predicted pressure trends for depressurizations starting from an initial internal vessel temperature of 20 °C.

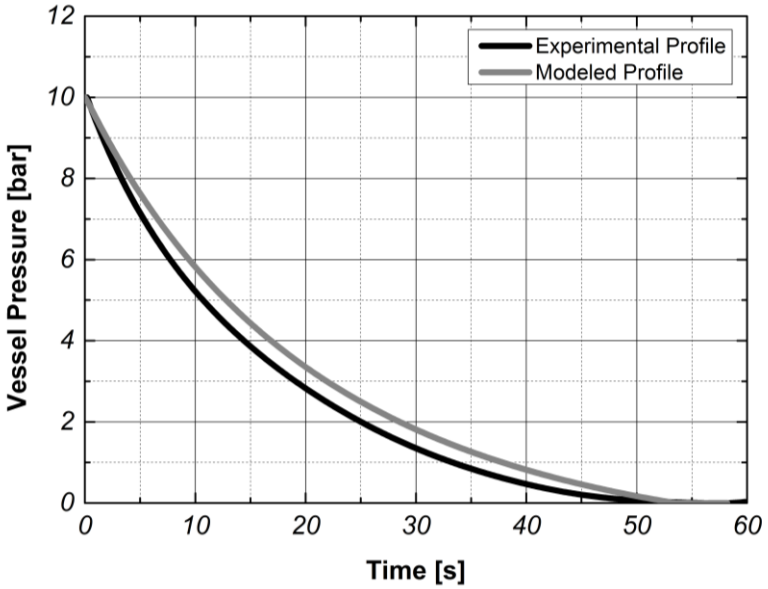

Figure 5.11. *Experimental and predicted transient pressure profiles. 10 barg expansion.*

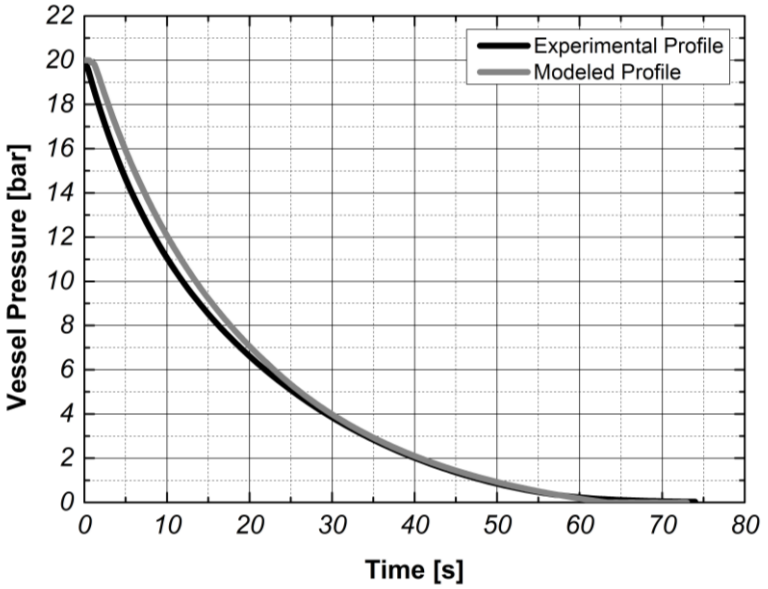

Figure 5.12. *Experimental and predicted transient pressure profiles. 20 barg expansion.*

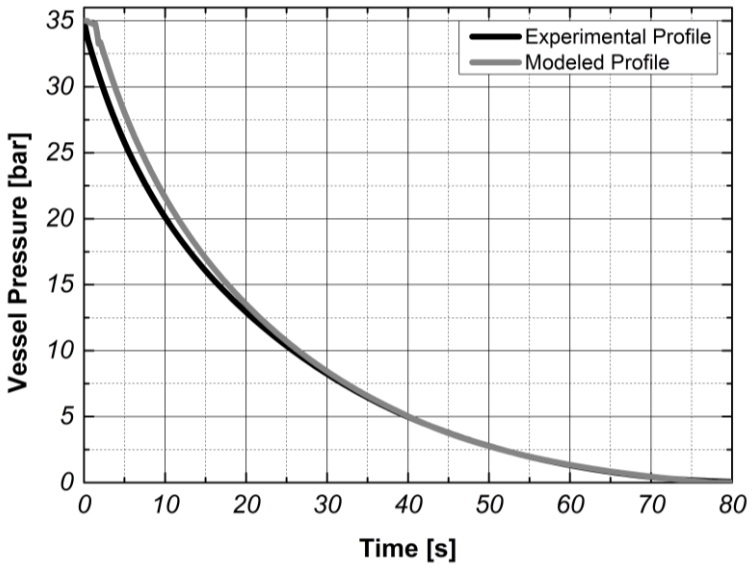

Figure 5.13. *Experimental and predicted transient pressure profiles. 35 barg expansion.*

Pressure profiles presented in Figure 5.11-5.13 are characterized by the absence of phase change mechanisms as attested by the monotonic decrease of the pressure to the atmospheric level. The persistence of the CO_2 in its gaseous phase, that is the charging state for the (P_0, T_0) couples investigated and that is experimentally observed, is matched by the model in all the investigated cases.

It should be noted that all simulated depressurizations are incorporating main features of the real system, first among everything the absence of external insulation. In this sense the boundaries are assumed to be not adiabatic therefore allowing heat transfers between them and the CO_2 and between the external stainless steel surface and the environment.

The pressure predicted by the model is in close agreement with the experimental data especially in the intermediate and final steps. Discrepancies arise in the initial release evolution where the pressures predicted are steadily higher than the measured data. The same deviation is observed for simulations involving charging pressures below 15 barg as indicated in Figure 5.11. In this case, the overestimation is extended to the entire simulated time domain.

Concerning the trial reported in Figure 5.11 it should be noted that a reason for this discrepancy may arise from a not perfect initial equilibrium conditions between the vessel walls and its content. The dimensionless pressure profiles with respect to the time coordinate allows for a comparison between different expansion behaviors. Figure 5.14 refers to the same depressurizations of Figure 5.11-5.13.

Model predictions are in accordance with experimental observation, indicating that any variation in the charging pressure is linked to a different expansion profile with greater

changes located in the range $0.1 < t/t_0 < 0.5$. This bounded interval matches the lowest recorded temperature that is when the enthalpic contribution is predominant. As will be discussed later, the location of the local minimum in the temperature is restricted to this dimensionless range.

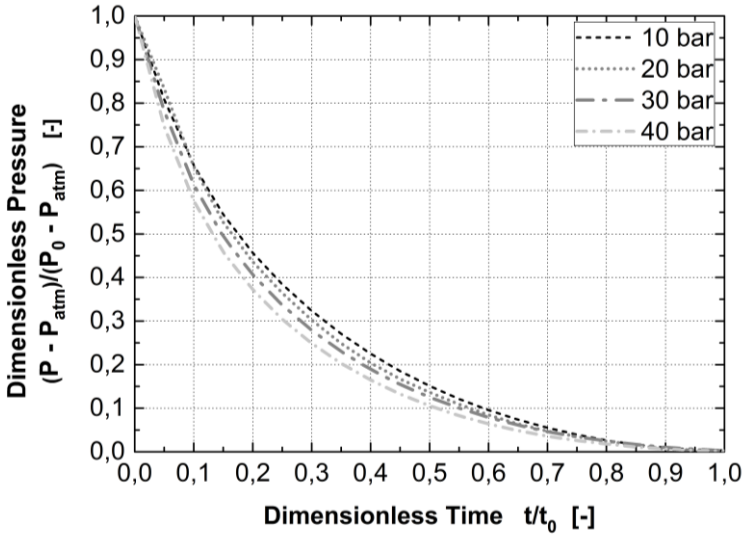

Figure 5.14. *Dimensionless depressurization profiles with initial vessel temperature of 20 °C.*

As far as the pressure profile at the orifice plane is concerned, the model capability is tested against the measured pressure drops. The friction losses are quantified in terms of the pressure difference between the value acquired by the internal vessel sensor and that recorded downstream of the constriction point. Figure 5.15-5.16 give the measured and modeled pressure differences in the case of a 35 barg expansion.

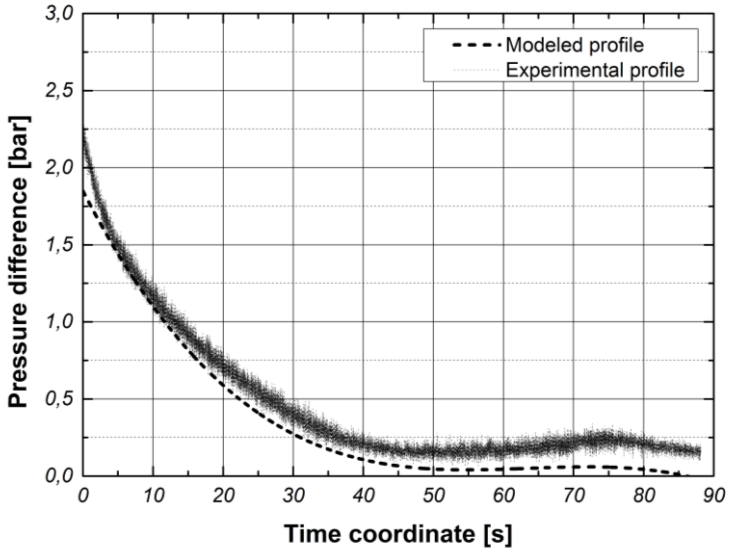

Figure 5.15. *Experimental and modeled time trends of the pressure difference between the stagnation and the downstream pressure control point. 35 barg expansion.*

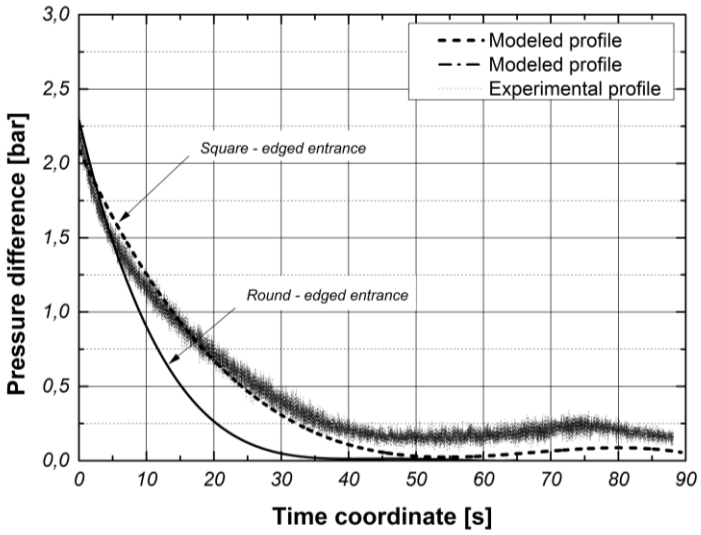

Figure 5.16. *Experimental and modeled time trends of the pressure difference between the stagnation and the downstream pressure control point. Distributed pressure losses incorporation.35 barg expansion.*

The observed decreasing trend of the pressure difference is mainly due to the CO_2 flow driven by the pressure gradient existing between the vessel and the discharging plane. The gradient, that is governing the discharge dynamic, is strictly linked to the velocity field assumed by the CO_2 and therefore to the measured pressure losses. The modeled profile as depicted in Figure 5.15 is predicting smaller pressure differences with respect to those experimentally observed. The theoretical profile that is derived from (5.12-5.13) can be justified considering that it is referring only to the presence of the sudden contraction and the discharging orifice while the experimental measuring point is located 7.1 cm downstream of the latter. The lower amount of pressure losses has the result of an internal vessel pressure decrease less marked than that experimentally observed as reported in fig. 3.11, initially delaying the discharge phenomenon. Results obtained by incorporating in the proposed model the contribution to distributed pressure losses induced by the discharge line section are reported in Figure 5.16. Two distinct cases are investigated diversifying the shape of the constriction point. The assumption of round-edged section reduction implies a pressure difference profile not matching the experimental evidences with too limited induced pressure losses. Higher pressure drops are observed in the case of sharp-edged profiles because of their geometrical shape.

It should be noted that while all simulations are predicting a vanishing pressure difference at each trail end, as is perfectly logical, the experimental measurements do not seem to agree with this. The main reason is related to inaccuracies that may arise during the measuring action. In this sense, measurements close to the sensor bottom scale limit give rise to errors not always manageable. Both sensors that are acquiring data are suitable to work on pressure signals up to 70 barg and therefore measurements close to atmospheric conditions may be

affected by inaccuracies. The same profile concerning the 20 barg depressurization is matching the experimental data but pressure differences predicted for the case of 10 barg show marked deviations especially in the early steps of the release as reported in Figure 5.17. The persistent underestimation of pressure differences throughout the whole experiment concerning 10 barg depressurization is consistent with the deviations obtained in the vessel pressure trend of Figure 5.11. The scattered behavior of the experimental profile is more marked than in the case of higher pressures indicating the appearance of uncertainties concerning the pressure measurements.

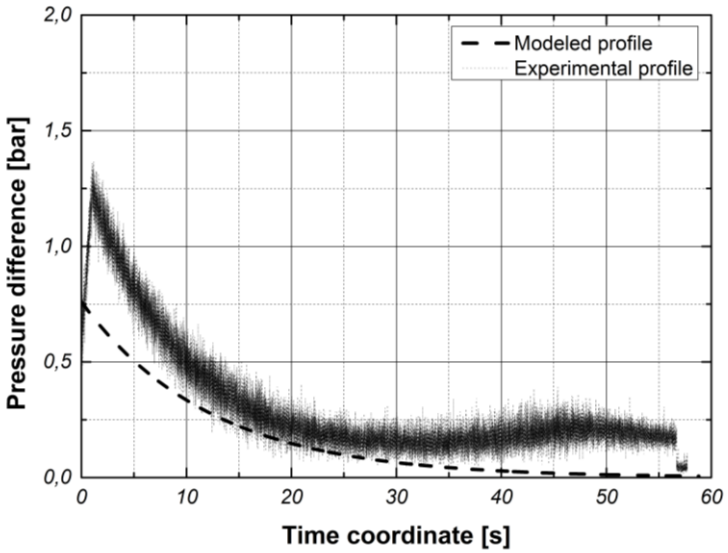

Figure 5.17. *Experimental and modeled time trends of the pressure difference between the stagnation and the downstream pressure control point. 10 barg expansion.*

To better investigate discrepancies arising in the modeling of 10 barg expansion, different experimental trials have been performed in order to throw light on the effect of a variation in the sampling rate on the pressure difference profile. It is in fact known that the sampling rate applied in the acquisition procedure with respect to the natural frequency offered by the sensor is one of the main parameters affecting the measurements quality. In this case, the quality is substantially expressed in terms of measurement noise affecting the recorded profile.

Results obtained show that a decrease in the sampling rate of the pressure sensors located downstream of the constriction point implies both a noise reduction and a variation in the collected pressure profile decreasing the gap between the modeled and the experimental profiles.

Table 3.2 gives the trend of the determination coefficient R^2 varying the sampling rate of the pressure sensor with respect to the unaltered modeled profile.

Table 5.3. *Determination coefficient with respect to different pressure sampling rates.*

Trial	Sampling rate	R^2	Trial	Sampling rate	R^2
5 bar 20 °C	2 kHz	0.965	10 bar 20 °C	2 kHz	0.985
	8 kHz	0.951		8 kHz	0.974
	15 kHz	0.864		15 kHz	0.841
5 bar 25 °C	2 kHz	0.954	10 bar 25 °C	2 kHz	0.988
	8 kHz	0.915		8 kHz	0.978
	15 kHz	0.904		15 kHz	0.894
5 bar 30 °C	2 kHz	0.969	10 bar 30 °C	2 kHz	0.990
	8 kHz	0.934		8 kHz	0.974
	15 kHz	0.885		15 kHz	0.914

It can be noted that halving the sampling rate, expressed in kS/s (kiloSamples/s), lowers the data variability increasing the R^2 over 0.96. Profiles indicated in Figure 5.16 apply to 10 barg, 20 °C depressurization with $R^2 = 0.841$. The sampling rate reduction to 2 kHz allows for a percentage increase of R^2 equal to 16 %.

Even if a further decrease of the sampling rate improves the R^2 value, the reduction goes against the need to investigate the dynamic system through an adequate sampling rate frequency.

5.5.2 Transient temperature profiles

Each experimental trial is characterized by a temperature dynamic that is depending both on the expansion nature and the amount of transferred heat with the surroundings, mainly represented by the solid stainless steel walls and the external environment.

The model predictions concerning the temperature trends are discussed below with respect to the model capability to match the experimental profiles as well as the location and the magnitude of the minimum temperature reached inside the vessel.

Temperature trends are derived from the thermal balance described by (5.15) in which two distinct competitive contributions have been included to give reason to the experimental behavior.

The first accounts for the gas expansion cooling through a numerical integration of the thermodynamic depressurization pathway and the second for the heat transfer induced by the presence of the walls and the instantaneous temperature gradient $(T - T_w)$.

Figure 5.18 gives details on both thermal balance contributions modeled by the (5.15).

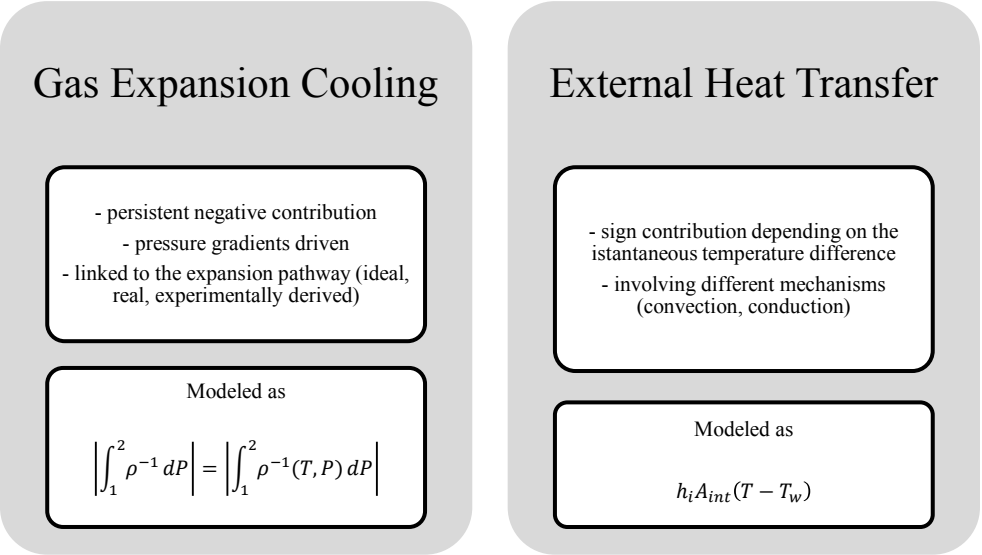

Figure 5.18. *Main features of the two contributions to energy balance: pressure-induced cooling mechanism and heat transfer with the surroundings.*

Starting from the expansions at 10 and 20 barg, both experimental and predicted vessel temperature profiles are respectively reported in Figure 5.19-5.20.

Predicted profiles are characterized by a passage through a local minimum as experimentally observed showing that the model structure as briefly explained in Figure 5.18 is qualitatively suitable to follow these trends.

In both cases, the location of the minimum temperature is predicted earlier in time even if its magnitude quantitatively matches the experimental observations.

The best match is found for the 20 barg trial but it is limited to the initial temperature drop with a deviation in the dominant final heating mechanism. Both the modeled profiles are in fact characterized by stronger heating mechanisms compared to those experimentally observed. Also in the case of a 35 barg depressurization, some differences persist even if more limited as reported in Figure 5.21.

Some considerations concerning the discrepancies are thus formulated.

It should be first noted the importance of the supposed expansion path with reference to (5.16) and therefore to the predicted time temperature trend.

As indicated in Figure 5.2 and 5.16, the thermodynamic description of the depressurization is included in the numerical integral of (5.16).

The description can rely both on supposed pathways as well as on experimental collected data. In that regard, profiles under discussion are derived from the experimental data meaning that the $P(T)$ relation is based on the measured instantaneous variations between the vessel and the orifice conditions.

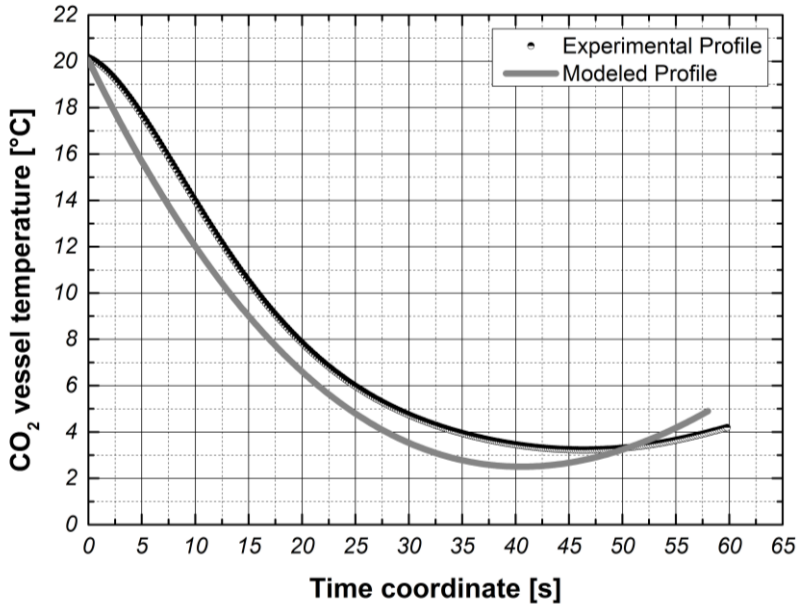

Figure 5.19. *Experimental and modeled profiles of CO_2 temperature in the vessel. 10 barg, 20 °C expansion.*

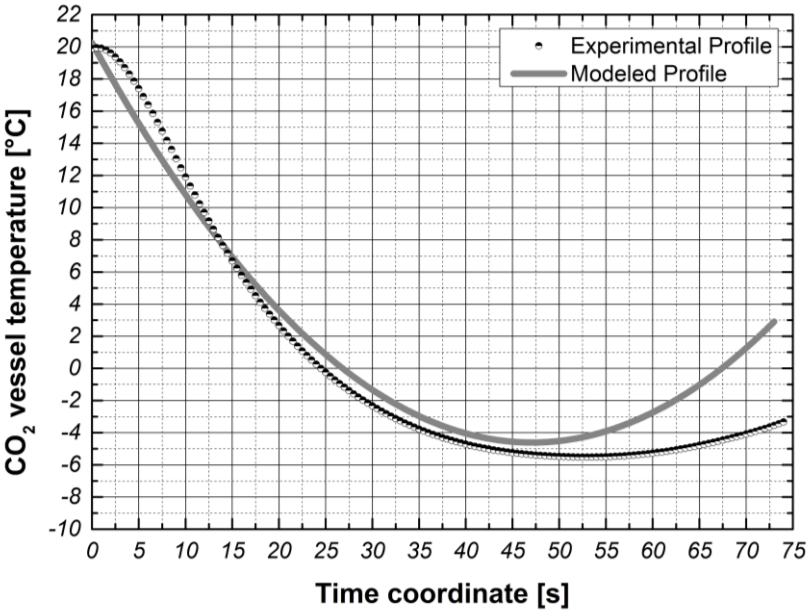

Figure 5.20. *Experimental and modeled profiles of CO_2 temperature in the vessel. 20 barg, 20 °C expansion.*

The integral of (5.16) is therefore approximated as reported in (5.48):

$$\int_0^1 \rho^{-1} dP \approx \sum_{i=0}^{n} \rho^{-1}(P_i)\xi_i \quad . \tag{5.48}$$

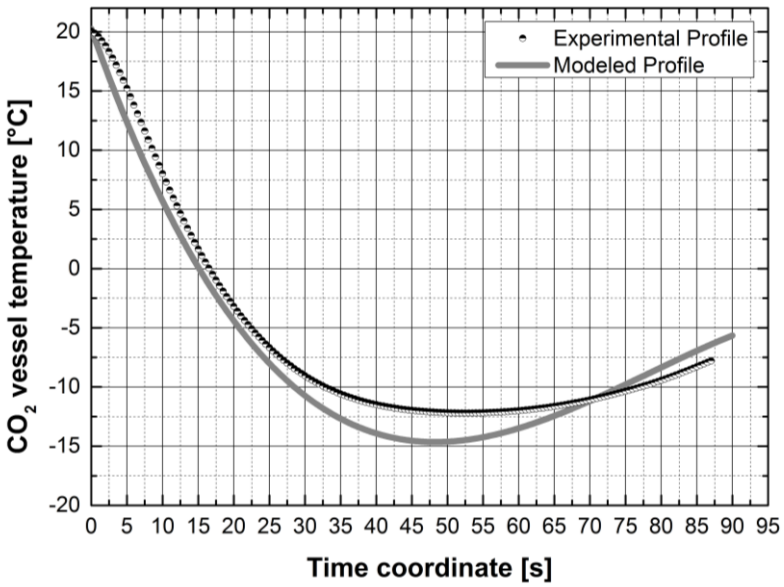

Figure 5.21. *Experimental and modeled profiles of CO_2 temperature in the vessel. 35 barg, 20 °C expansion.*

The (5.48) is based on n support nodes characterized by a certain value of the pressure P_i with ξ_i containing the numerical integral of the selected Lagrange base polynomial. The Simpson's rule has been employed with a polynomial degree equal to 2.

The instantaneous values of the function $\rho^{-1}(P_i)$ are derived from the measured couples (P_i, T_i) with the CO_2 density ρ that is obtained going through the EoS model.

Except for the heating step concerning the temperature trends, the first cooling stage is matching the experimental observations because of the use of collected data.

The analysis however should deal with usual assumed transformations in QRA procedures in order to give a term of comparison. More precisely, a merely thermodynamic approach is not directly applicable since its stationary perspective. In fact, being the blowdown a fully transient mechanism, a stationary description is not matching the real nature of the expansion even if a *quasi-steady state assumption* has been employed in facing the flow to the orifice ([4]). Therefore, the usual definitions of fully adiabatic and isenthalpic expansions, representing the limiting theoretical conditions to sudden discharges, should be differently formulated in order to match the transient phenomenon nature. The measure of the isentropic efficiency χ is introduced with respect to the general dynamic energy balance (5.49):

$$\dot{m}\tilde{c_p}(T_1)\left(T_1 - T_{ref}\right) + UA_{int}(T_0 - T_w) + \frac{d(Pv)}{dt} = \frac{d\left(m\tilde{c_p}T_0\right)}{dt} \quad . \tag{5.49}$$

In (5.49), the subscript 1 refers to outflow conditions while 0 to the internal vessel (stagnation) properties.

The term related to the definition of χ is that including the time variation of Pv.

As proposed by some authors ([10,11]), the instantaneous derivative can be computed as reported in (5.50):

$$\frac{d(Pv)}{dt} \approx \frac{P_0(t) - P_0(t - \Delta t)}{\rho_{CO_2,0}(t)} \chi \quad . \tag{5.50}$$

With respect to (5.49), the measure of the *efficiency* χ includes all mechanisms that prevent the complete reversibility of the transformation among which friction $(Pv)_{eq,f}$ and shock wave-related $(Pv)_{eq,sw}$ phenomena as indicated in (5.51):

$$\chi = \frac{(Pv)_{100\,\%} - \left[(Pv)_{td} + (Pv)_{eq,h} + (Pv)_{eq,f} + (Pv)_{eq,sw}\right]}{(Pv)_{100\,\%}} \quad . \tag{5.51}$$

Table 5.4 collects the different contributions to (5.50).

Table 5.4. *Contributions to (5.51).*

Term	Meaning
$(Pv)_{100\,\%}$	Value corresponding to fully reversible transformation
$(Pv)_{td}$	Thermodynamic transformation equivalent work
$(Pv)_{eq,sw}$	Shock waves formation equivalent work
$(Pv)_{eq,h}$	Heat transfer mechanisms equivalent work
$(Pv)_{eq,f}$	Irreversible friction mechanisms equivalent work

The meaning of (5.51) is that a value of χ corresponding to 1, or 100 %, stands for a completely reversible transformation basically equivalent to an expansion carried out along a constant-entropy curve. The presence of any phenomenon linked to irreversibility, i.e. dissipative mechanisms, tends to lower the magnitude of χ to the minimum value of 0. A decrease in the χ value, as defined by (5.51), implies therefore the fall of the hypothesis of complete adiabaticity, i.e. no heat transfer from the surroundings.

Therefore, starting from the meaning of (5.51), the experimental temperature profiles are compared with transformations corresponding to a χ value of 0 and 1.

Figure 5.22 gives the comparison between the temperature trends obtained through the experimental data and those corresponding to the limiting values of χ. Results are referred to the 35 barg, 20 °C expansion.

From Figure 5.22 it is clear the relevant reversible effect with respect to both the temperature dynamic and the minimum reached temperature inside the vessel. Considering the 35 barg depressurization, the recorded real process shows an intermediate behavior whose dynamic consists in a minimum temperature value between 2,6 °C and -24,4 °C that are respectively matching a fully irreversible and reversible expansion. The first one is characterized by the

highest temperature decrease that is driven by the weak heat transfer with the surrounding walls and the lack of relevant dissipative mechanisms.

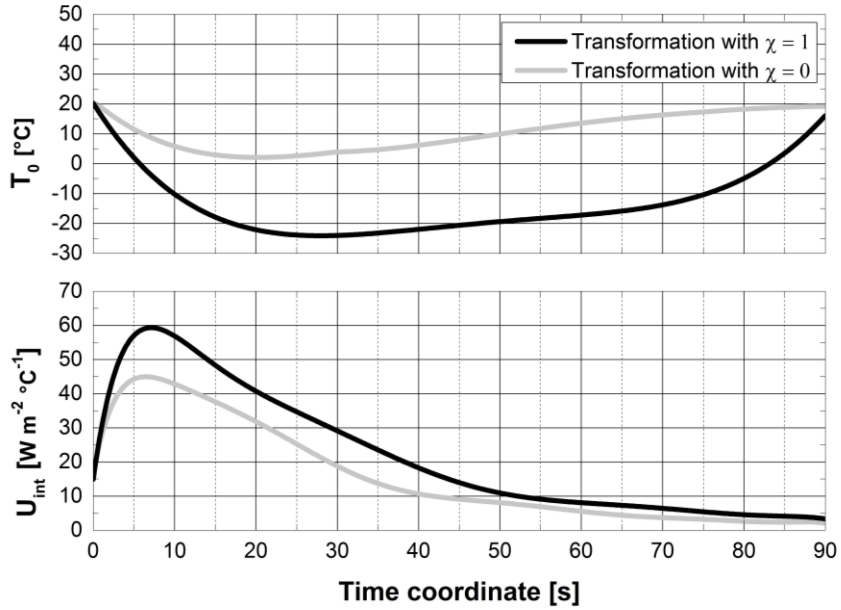

Figure 5.22. *Comparison between derived vessel temperature profiles assuming completely reversible ($\chi = 1$) and irreversible ($\chi = 0$) transformations. 35 barg, 20 °C expansion.*

The lowest decline is instead determined by an efficient exchange with the heat reservoir during the expansion.

It should be noted that with the defined limiting conditions, the thermodynamic isentropic temperature is never achieved even with $\chi = 1$ because of the presence of the warmer solid walls. This is also proved the internal overall heat transfer coefficient U_{int} variation in time with the highest values achieved during the expansion step as reported in Figure 5.22. The local maximum in U_{int} is never achieved at the corresponding inside minimum temperature vessel, i.e. at the maximum thermal driving force, pointing out that heat transfer is not the only source of irreversibility as contemplated in the (5.51).

Trends reported in Figure 5.22 are always observed under the investigated conditions. The irreversibility feature therefore should always be contemplated while discarding any pure thermodynamic approach.

Figure 5.23a-b give the trend representation of the internal overall heat transfer coefficient varying the initial expansion pressure in the vessel. The initial internal temperature is kept unchanged at 20 °C. They refer respectively to a χ value of 0 and 1.

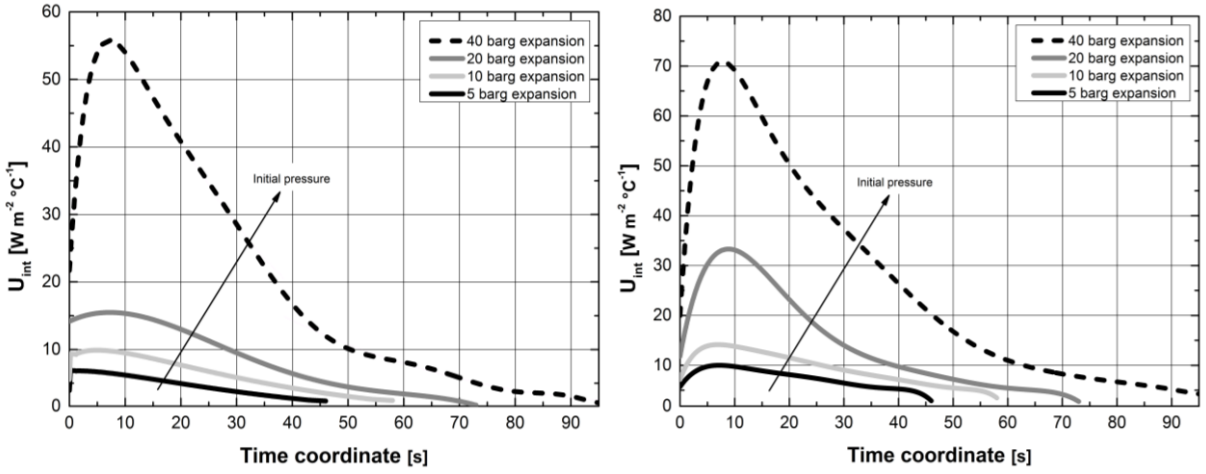

Figure 5.23. *Magnitude comparison of internal overall heat transfer coefficients with respect to different initial charging pressures. Initial temperature: 20 °C. a-* $\chi = 0$*; b-* $\chi = 1$.

The U_{int} behavior is strictly depending on the charging pressure and shows a monotonic decrease only for lower pressures (P < 7.3 barg). Higher pressures determine similar trends to that observed in Figure 5.22 with a local maximum located prior to the achievement of the minimum in the temperature. The reason for these U_{int} altered trends is related to the strength of the cooling effects induced by the mechanical pressure gradients with respect to the heating capability of the surrounding walls. In the case of higher charging pressure, the cooling effect is dominant to such an extent that the heating mechanism can be neglected. The peak in U_{int} is therefore the result of the mechanisms mainly induced by the initial higher pressure gradients and the lack of correspondence with the minimum in the temperature is linked to the resilience of the system. The decrease in the charging pressure as reported in Figure 5.23 lowers the effect of the mechanical pressure disequilibrium that becomes comparable to the walls heating contribution.

The effect induced by the charging temperature is different.

The experimental investigation covered initial charging temperatures varying from 15 to 50 °C as listed in the dedicated section. Modeling results with respect to observed trends for 35 barg expansions are reported in Figure 5.24.

Taking as reference the results concerning the 35 barg expansion, that is characterized by major temperature gradients, it may be noted that a variation in the charging temperature induces modifications with respect to the minimum reached values inside the vessel.

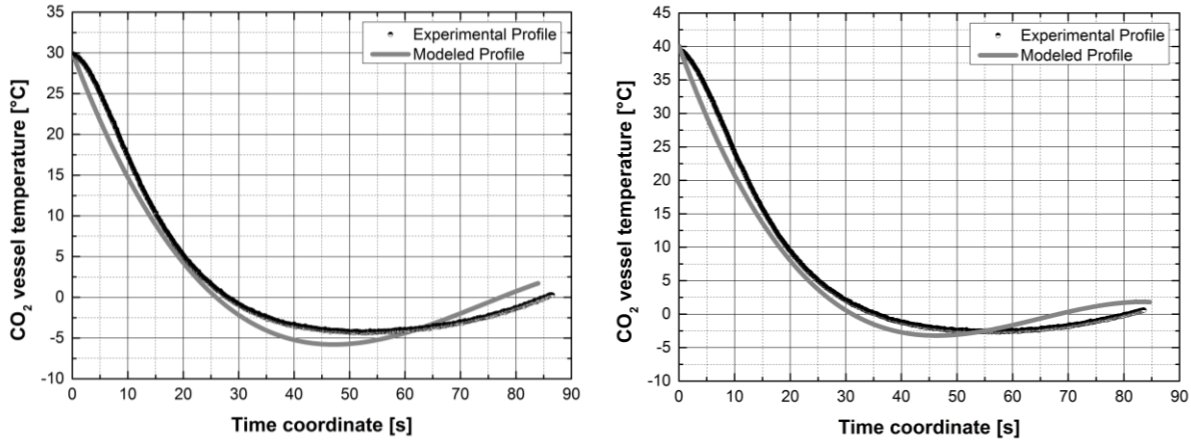

(a) *(b)*

Figure 5.24. *Experimental and modeled profiles of CO_2 vessel temperature. 35 barg expansion, a- 30 °C; b- 40 °C.*

The thermal dynamic is not strongly affected in contrast to what is observed for the pressure effect that is the main factor influencing the experimental and modeled profiles.

A decrease in the charging temperature always induces a parallel decrease in the minimum reached temperature even if the relative magnitude is not conserved. Results show that a variation in the charging temperature, keeping the others parameters unchanged, acts modifying the energy transfer magnitudes especially with reference to the initial stages as indicated in Figure 5.24. Less evident differences are observed in the later stages where curves tend to overlap effectively neglecting any initial temperature contribution. This is mainly due to the temperature effects on CO_2 properties, first among all the local density, viscosity and thermal conductivity being the pressure profile in time substantially insensitive to changes in the initial charging temperature as both experimentally and theoretically observed. In addition, main differences reported in fig. 3.21 are linked to the different paths followed by the CO_2 during the expansion. In fact, as of Figure 5.25, the corresponding variations in the internal vessel temperatures with respect to 35 barg expansions are characterized by different behaviors that are therefore strictly depending on the initial charging temperatures.

Figure 5.26 gives the different dimensionless profiles.

It may therefore be noted that a variation in the initial conditions acts modifying the internal vessel relation between the pressure P and the temperature T. Differences emerge from a change in the initial temperature increase once the initial pressure is raised because of the higher induces temperature gradients.

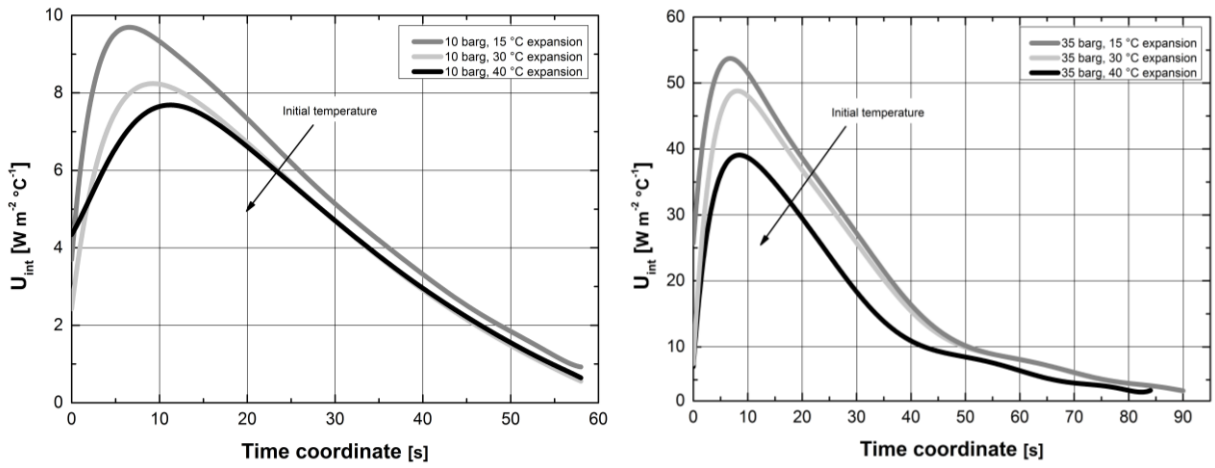

(a) *(b)*

Figure 5.25. *Overall heat transfer coefficient time trends with respect to a- 10 barg and b- 35 barg depressurization.*

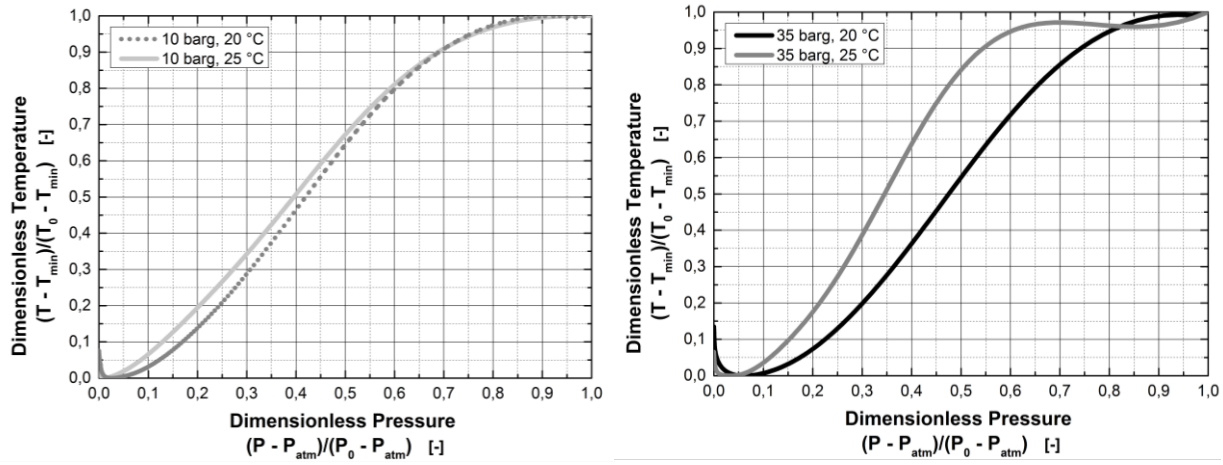

(a) *(b)*

Figure 5.26. *Internal vessel pressure-temperature dimensionless profiles. a- 10 barg, b- 35 barg expansion.*

Figure 5.26b gives a clear indication that while maintaining the charging pressure unaltered, a variation in the temperature gives rise to deviations in the expansion path with major changes found in the case of lower temperatures. For the same temperature variation, not relevant modifications are observed in the case of 10 barg expansions (Figure 5.26a) for which the two expansion trajectories are almost the same. The main reason is connected to variations in the thermodynamic and transport properties of the CO_2 during the change in the pressure and temperature. At higher pressures, temperature-induced variations especially in what concerning the density and the viscosity are more relevant leading to different (P, T) paths. Each of them is characterized by a different importance of frictions and heat transfer amounts and therefore by the degree of irreversibility.

In this sense it is interesting to give a measure of χ for the modeled transformations based on the experimental data. χ values that are best matching the experimental profiles are obtained from a minimization procedure that can basically formulated as follows:

$$\min_{\chi\in[0,1]} \|T(P,\chi) - T^{exp}(P^{exp})\| \quad . \tag{5.52}$$

The (5.52) indicates that the optimal value of $\chi \in [0,1]$ minimizes the distance between the modeled vector $T(P,\chi)$ and that experimentally observed $T^{exp}(P^{exp})$. The optimization procedure is therefore giving the magnitude of χ matching the experimental $T(P)$ profiles within a tolerance ε s.t. $R^2 \geq 0.90$. The reason for the R^2 threshold value selected in the optimization procedure relies on the very scattered nature of the experimental data under elaboration.

Optimization results are reported in Figure 5.27.

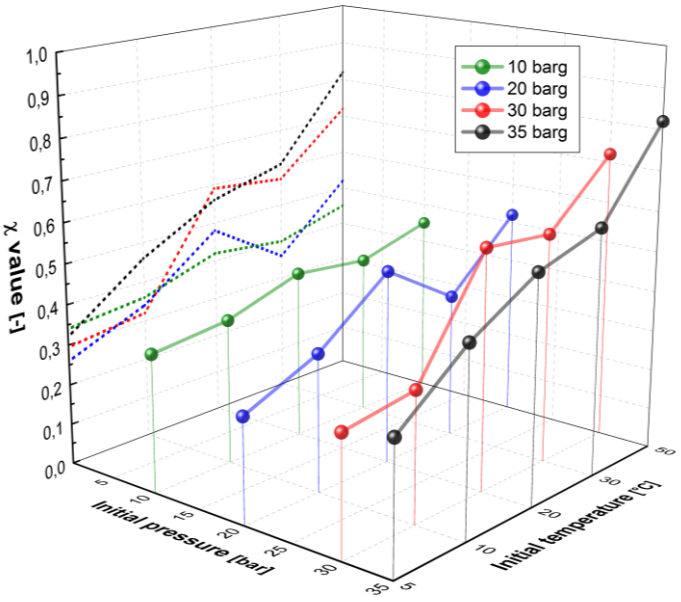

Figure 5.27. *Calculated χ value for different initial pressures and temperatures through the minimization procedure of (5.51).*

The analysis of Figure 5.27 shows that a variation in both the charging pressure and temperature acts sensibly modifying the calculated χ value. Fixed an initial pressure value, the trend is increasing with respect to the stagnation temperature up to a value equal to 0.82 that is a 82 % degree of reversibility with respect to the fully reversible transformation set at 100 %. Major differences as observed with higher stagnation pressures.

A rise in the charging pressure leads to a less sharp parallel increase of χ. It should be noted from Figure 5.27 that the minimum value of χ is located in the range (0.25;0.35) and is recorded for lower temperatures with the charging pressure that is not playing a key role.

Trends reported in Figure 5.27, that are derived from the experimental observations, show at least qualitatively an intermediate global behavior between a fully reversible and an irreversible transformation.

In this sense, considering the different contributions to (5.51), relative observed magnitudes that are determining the χ value are reported in Figure 5.28.

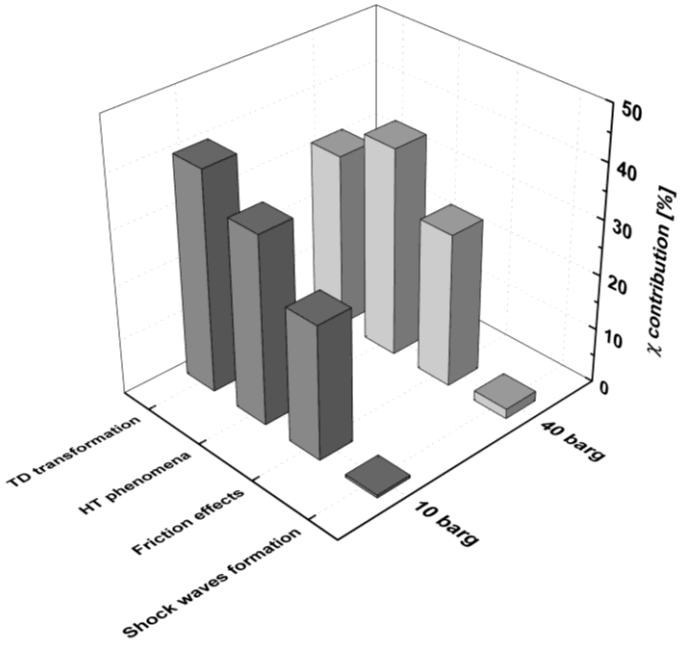

Figure 5.28. *Relative contributions to χ for different charging pressures. 20 °C expansion.*

Relative contributions to χ show that while the shock wave appearance-related irreversibility are negligible in both the 10 and 40 barg expansions, remaining amounts due to the CO_2 transformation, heat exchanges with surroundings and dissipative mechanisms are all relevant. Each of them contributes to χ according to various magnitudes strictly depending on specific established conditions.

Moving the initial pressure from 10 to 40 barg, friction effects increase their relative magnitude because of the enlarged mean velocity and related turbulence mechanisms at the discharge plane. Experimental observations give reason to state that on a 100 %-χ basis the contribution linked to friction is ranging from 22 to 30 % with higher values experienced with increasing pressures. A variation in the charging temperature is not significantly affecting the results.

Focusing the attention on both the transformation and the heat exchanges contributions, the behavior is less clearly detachable because of their mutual influence. It is clear that the nature of the expansion is determining the amount of heat transferred between the CO_2 and the walls but at the same time the relative mass amount of solid surface and CO_2 is driving the

effectiveness of this mechanisms. Referring to Figure 5.28 these two contributions amount to more than 70 % of the total, each of them allocated depending on the initial thermodynamic parameters. At lower pressures and temperatures, the thermal unbalances directly induced by the thermodynamic expansion are greater than those related to the presence of the warmer walls. On the contrary, an increase in the storage conditions gives a major role to the transfer with the surroundings walls even if the expected temperature gradients because of the expansion are wider.

These can be explained considering two distinct reasons:

- since the vessel wall temperature does not drop as low as the gas, an instantaneous and persistent temperature gradient between the vessel content and its walls exists (Figure 5.29). Being initially both at thermal equilibrium, an increase in the initial pressure with subsequent wider cooling effects enhances the gradient and thus the heat amount transferred to restore the equilibrium conditions. The decrease in the temperature, initially occurring at the internal energy expenses, is however not enough to monotonically lower the CO_2 temperature because of the intervention of the walls warmer surfaces transferring heat to the internal content;

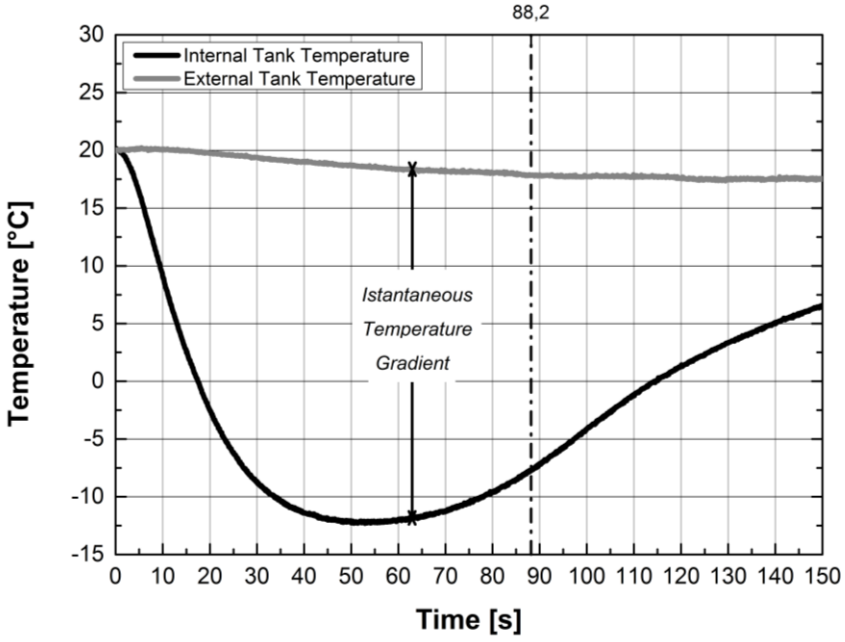

Figure 5.29. *Peculiar trends of the internal vessel and the external surface temperatures.*

- the relative amount of masses involved in the release mechanism (the total mass of stainless steel $m_{tot,SS}$ and that of the initial CO_2 m_{tot,CO_2}) plays a key role in determining both the most considerable contribution to χ and the value of the measure of the internal heat transfer factor U_{int}. With increasing pressures, the ratio

$m_{tot,CO_2}/m_{tot,SS}$ increases being the initial CO_2 density higher this thus leading to a predominant role of the heat exchange mechanisms with respect to the cooling effects induced by the expansion. This is also the reason why trends observed in Figure 5.25-5.26 show an increasing value of U_{int} with respect to the charging pressure.

All investigated transformations therefore imply heat transfer with the surroundings and a deeper analysis allows also for the investigation of the pathway followed by the CO_2 in the vessel because of the expansion mechanism. Experimental measurements as well as the predicted trends can be coupled to give the temperature (i.e. the density or the specific volume) development with respect to the pressure. The trajectory, that is extremely sensitive to the amount of heat exchanged as well as the total CO_2 instantaneously contained in the vessel, may give an indication of the CO_2 behavior during the depressurization ([6,10]). However, the knowledge of the pathway is not a sufficient condition to give complete description of the depressurizing domain being this steadily in direct contact with a heat source ([2]).

The specific volume-pressure diagrams are reported in Figure 5.30-5.32 with respect to different initial charging pressures and a temperature of 25 °C.

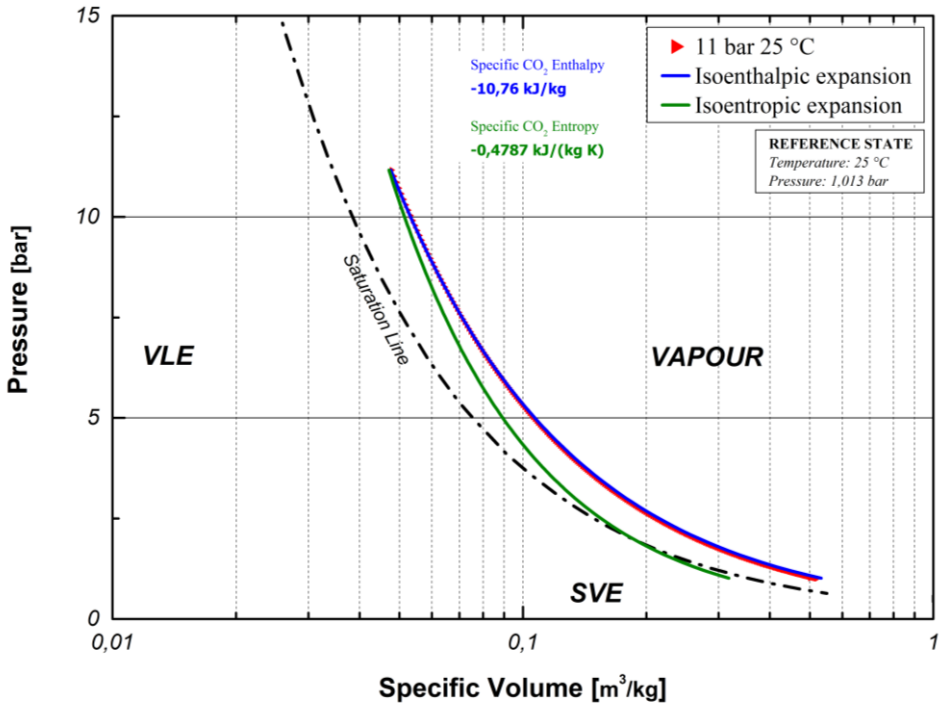

Figure 5.30. *Modeled specific volume-pressure pathway with respect to theoretical trajectories. 10 barg, 25 °C expansion.*

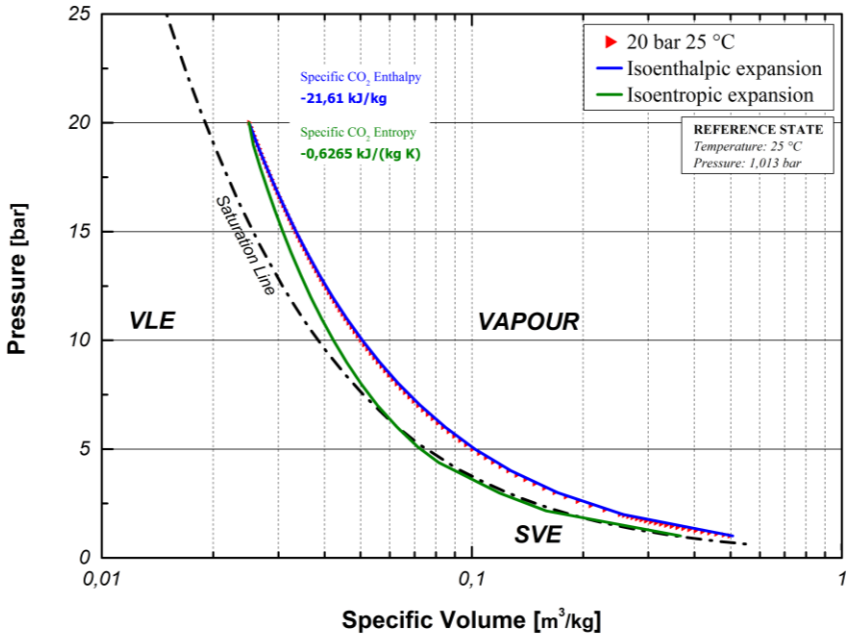

Figure 5.31. *Modeled specific volume-pressure pathway with respect to theoretical trajectories. 20 barg, 25 °C expansion.*

Diagrams reporting the trend of the specific volume (i.e. the density) with respect to the pressure inside the vessel show comparable behaviors even with varying initial conditions. Moving to charging pressures up to 35 barg, the link between these two state variables is nearly following a total constant specific enthalpy transformation till the complete vessel draining.

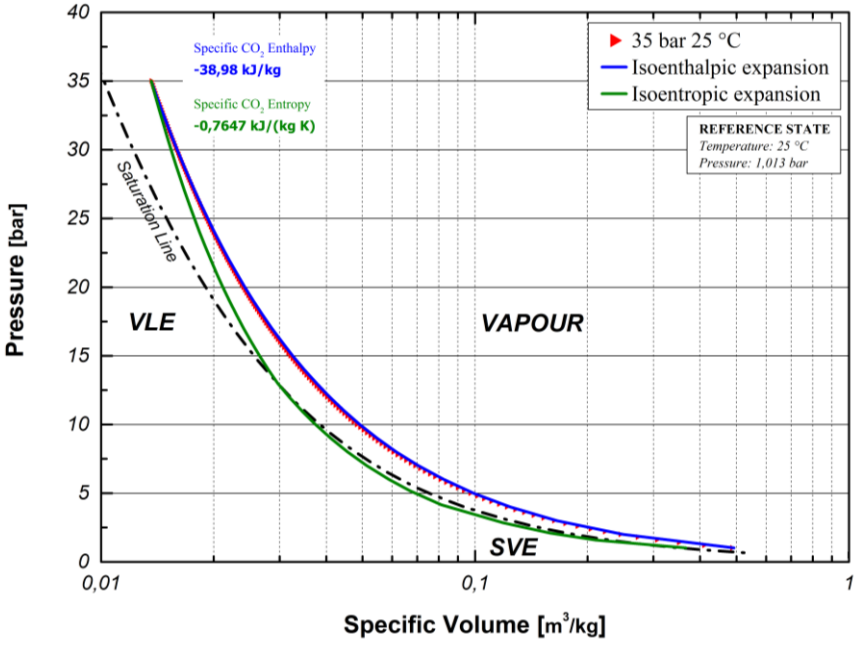

Figure 5.32. *Modeled specific volume-pressure pathway with respect to theoretical trajectories. 35 barg, 25 °C expansion.*

The expansion development along a constant enthalpy curve implies a theoretical vigorous exchange of heat with the walls in direct contact with the expanding gas. This occurrence has also been experimentally observed with a variation in the external stainless steel temperature (Figure 5.29) even if strictly depending on the heat capacity of the solid. In this sense, corresponding orifice sections are experiencing larger temperature drops because of the reduced amount of surroundings stainless steel.

Even in the presence of large CO_2 temperature variations, the vessel surfaces tend to preserve their initial temperature showing a marked capability to transfer heat to the CO_2.

In Figure 5.30-5.32, both expansions under constant specific enthalpy and entropy hypothesis are reported. Modeling procedure involved the imposition of a constant property constraint on the expansion development being clear the ideal character of these expansions. The matching of observed depressurizations with the one at constant enthalpy is clear even if attention should be paid being the meaning not strictly corresponding to that arising from a steady-state thermodynamic process ([16,18]). Stating that the CO_2 is expanding preserving its specific enthalpy implies only that the (P, T) or (P, v) trajectories inside the vessel develop according to a transient mechanism that can be modeled as a "black box" working on a series of states linked by the condition of the enthalpy conservation. The thermodynamic (steady-state) perspective loses part of its meaning being the whole expansion trend result due not only to heat exchange mechanisms but also to friction and appearance of shock waves under a transient system evolution.

The same isentropic condition leads to a completely different expansion path starting from the same initial conditions. The larger decrease in the temperature drives the CO_2 to the multi-phase domain firstly in the liquid phase domain and finally to a mixture of solid and vapor CO_2 also in the case of smaller charging pressures. These occurrences have never been observed during the experimental trials involving gaseous initial charges meaning that the gap with the isentropic expansion is reasonable. This is also testified by recorded and modeled temperature trends inside the vessel according to which the equilibrium isentropic temperature is never achieved ([11]).

All modeled profiles based on the experimental trials show this affinity for the isenthalpic transformation except for some modeled trials involving pressures higher than 55 barg that are characterized by a marked isenthalpic initial behavior then deviating toward isentropic features.

It is interesting to investigate the theoretical temperature development inside the vessel when subjected to a perfect (internal) insulation. In this sense, no heat transfer is allowed between

the vessel content and its walls apart from exchange mechanisms induced by temperature gradients in the CO_2 domain leading to convection-driven phenomena ([15]).

This occurrence may arise under the practical following conditions:

a. extremely rapid depressurization phenomena in which the characteristic time of pressure-induced temperature gradients are much smaller than that needed for the heat transfer by convection and conduction with the solid surfaces;
b. vessel geometries characterized by a very high initial $m_{tot,CO_2}/m_{tot,SS}$ ratio indicating a not negligible CO_2 overall heat capacity contribution with respect to that due to the solid body.

Condition a. is strictly related to the transportation pressure in the CCS pipeline while the latter to its size and the physical state of the conveyed CO_2.

Considering the experimental conditions under investigation, temperature trends for the internal adiabatic condition are reported in Figure 5.33-5.35.

Temperature trends corresponding to an internal adiabatic expansion are very different from a characteristic trend developed because of the presence of an external heat reservoir (Figure 5.29). The absence of local minima is due to the heat transfer contribution that is lacked while the whole expansion is taking place at internal energy expenses.

Therefore, considered the internal energy variations during the transient discharge phenomenon, the temperature shows always a monotone decreasing trend independently from the initial conditions.

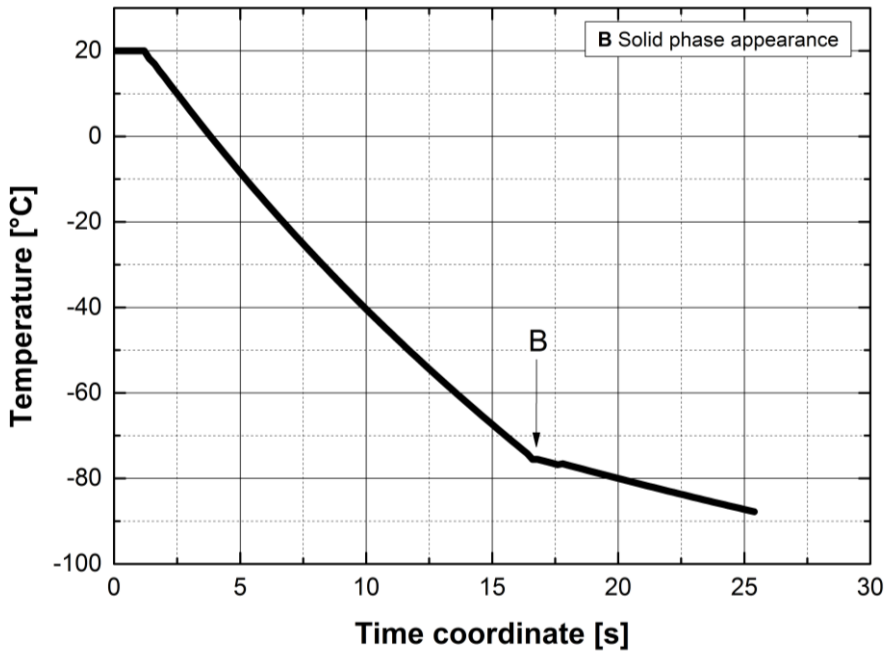

Figure 5.33. *Internal vessel temperature evolution under the hypothesis of internal adiabatic expansion. 10 barg, 20 °C expansion.*

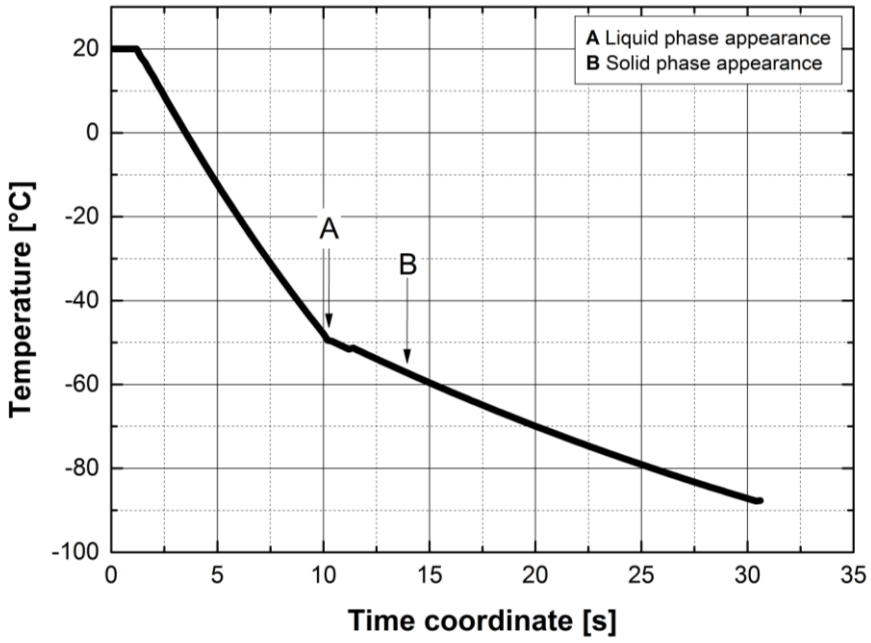

Figure 5.34. *Internal vessel temperature evolution under the hypothesis of internal adiabatic expansion. 20 barg, 20 °C expansion.*

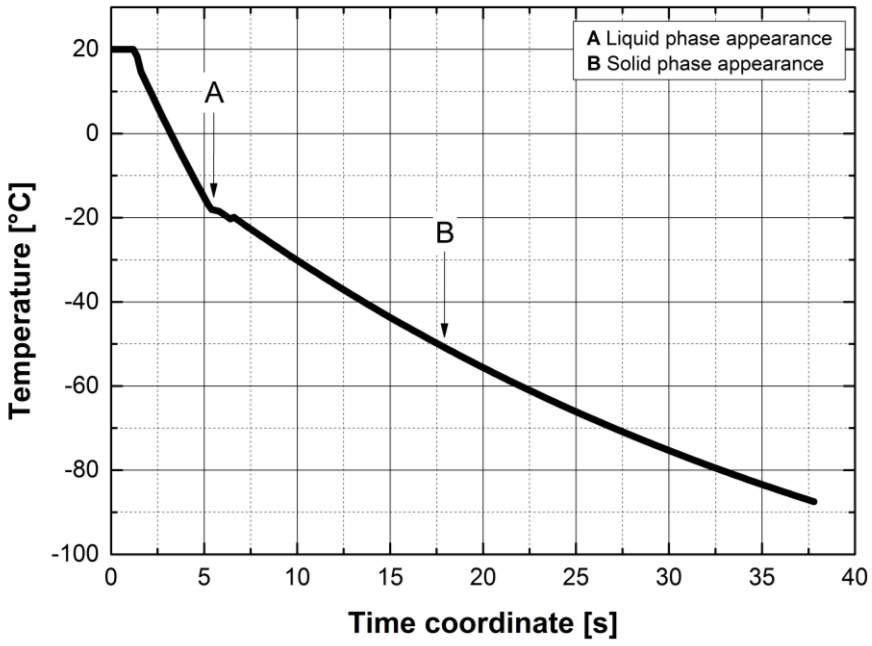

Figure 5.35. *Internal vessel temperature evolution under the hypothesis of internal adiabatic expansion. 35 barg, 20 °C expansion.*

However, the whole specific behavior, depending on initial charging conditions, is characterized by different characteristic portions.

These are separately identified with A and B markers and are outlined below:

- all modeled temperature profiles are characterized by one or more sudden changes in the first derivative highlighting a modification in the transient thermal dynamics;

- changes in the first derivatives are due to the appearance of an additional phase as in the case of the liquid (marker A) and solid phase (B) that in Figure 5.34-5.35 are coexisting with the vapor CO_2. The establishment of a multi-phase CO_2 mixture alters the temperature dynamics because of phase transition-related mechanisms.

More in detail, considering the expansions from 20 (Figure 5.34) and 35 barg (Figure 5.35), it may be noted that the depressurization path followed by the CO_2 implies the appearance of both the liquid and the solid phase that coexist with the gaseous CO_2 initially present in the vessel. The appearance time location is depending on the initial conditions as well as the relative amount of each of them. The latter is also depending on the (P,T) pathway induced by the internal adiabatic condition being the vapor quality of the developing mixture instantaneously changing with them. In fact, once the CO_2 is entering the vapor dome, the liquid phase starts appearing and then the passage through the triple point pressure leads to the solid phase appearance. These mechanisms and the specific mass evolution are however governed by two distinct opposite actions. While the decrease in the pressure plays a key role in governing the dense phases appearance, the phase change mechanisms works leading to a mass loss that migrates in the gaseous domain. Results concerning the mass time evolution are reported in Figure 5.36a-b.

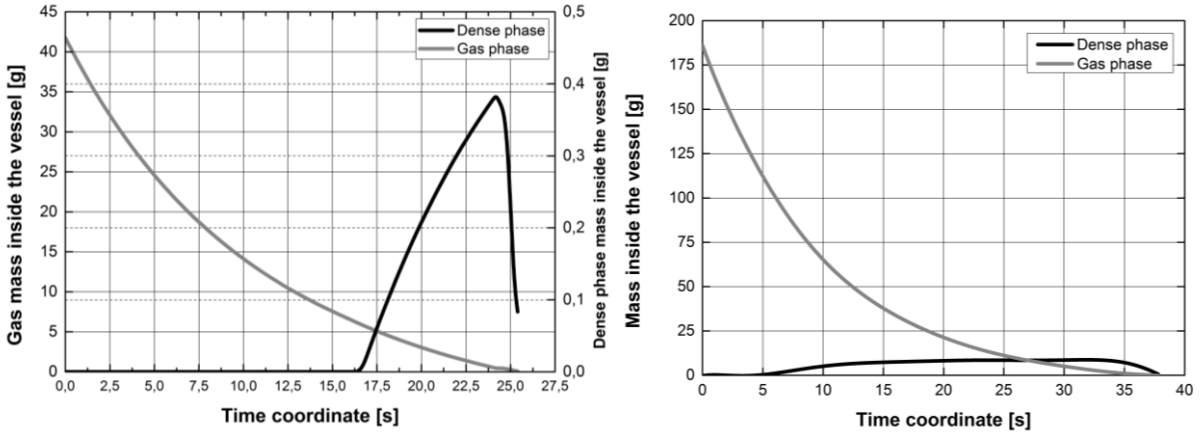

(a) *(b)*

Figure 5.36. *Mass evolution in time with respect to gaseous and dense phases inside the vessel. a- 10 barg; b- 35 barg expansion.*

Results show that the dense phase profiles, even if with different magnitudes, are similar with an initial time interval in which are not present. For example, in the case of the 10 barg expansion, the internal vessel conditions reach the saturation point after 16.6 s and with increasing charging pressure this parameter is lowered to 5.6 s as in the case of an initial pressure of 35 barg. This is due to the higher cooling effects induced by an increased charging

pressure as well as by the greater closeness of higher pressure states to the vapor dome keeping the initial temperature unchanged.

Once the saturation point is reached, profiles are characterized by a first growing step due to the gradual formation of the liquid phase leading to a mixture with growing dense phase fraction. At the same time, holding a VLE instantaneously changing with the pressure, part of this is boiling increasing the vapor amount. This incremented amount is not clearly detectable because of the small quantity of boiled liquid but a comparison with a pure vapor release shows the lowest value of vapor flow rates with respect to the multi-phase situation. Because of the competitive mechanisms represented by the growing in the dense fraction and the boiling occurrence, the mass profile reaches a local maximum. In addition, the trends in the case of 20 and 35 barg are also sensitive to the SVE established once the triple point pressure is reached respectively after 13.9 and 17.6 s. In the SVE region, giving the CO_2 properties, a sublimation process is modeled with a source term interesting the vapor phase.

The variations in the slope of the temperature trends are linked to the establishment of different thermodynamic equilibriums while the pressure is changing. It should be noted that all predictions lead to a minimum temperature which is less than the atmospheric equilibrium one (-78.4 °C). This is explained because of the occurrence of latent heat effects related to boiling and sublimation mechanisms that are taking place in the CO_2 domain.

Finally, the predicted (P, T) trends under adiabatic conditions are reported in comparison with the experimental observations. Results are collected in Figure 5.37-5.39.

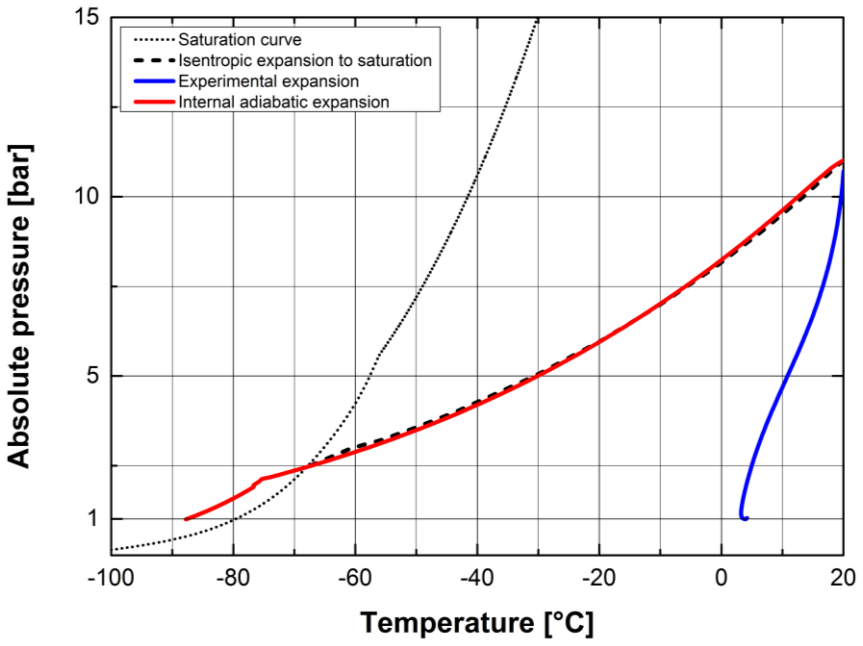

Figure 5.37. *10 barg expansion. Comparison between experimental and internal adiabatic profiles.*

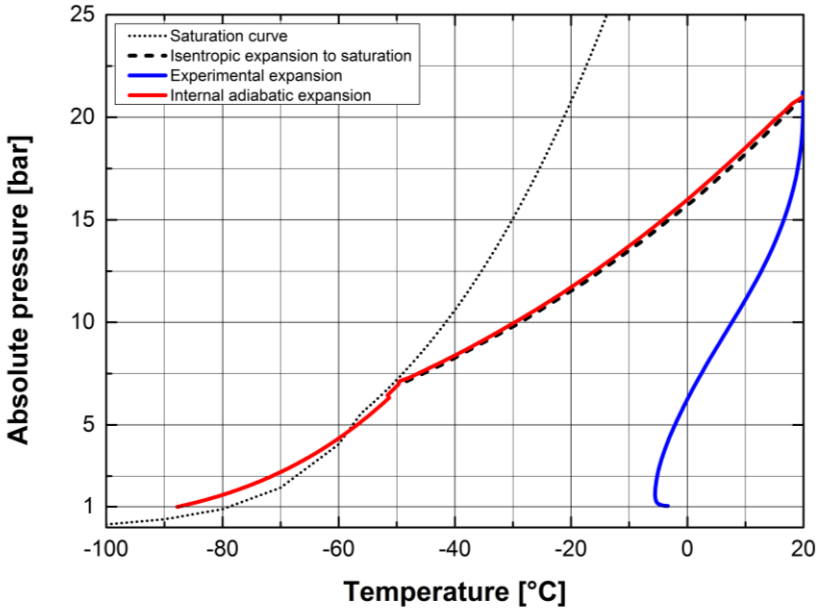

Figure 5.38. *20 barg expansion. Comparison between experimental and internal adiabatic profiles.*

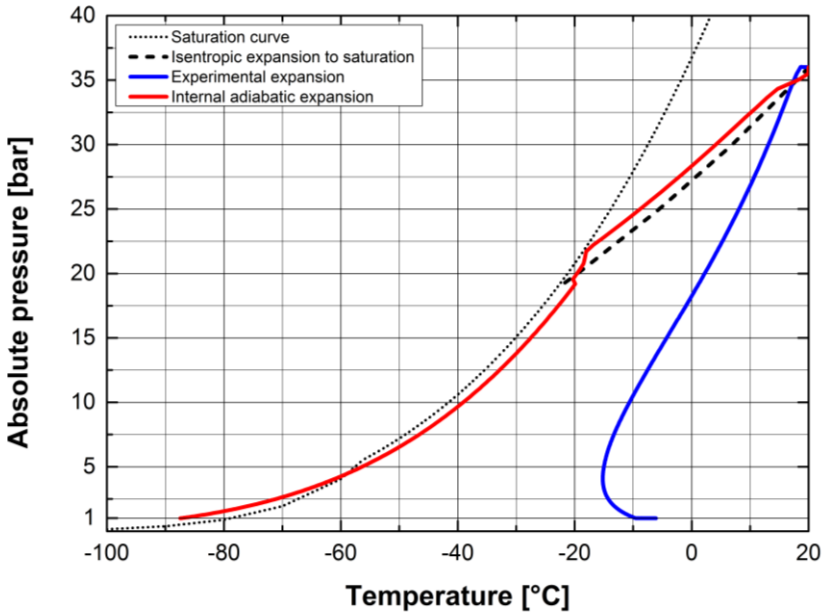

Figure 5.39. *35 barg expansion. Comparison between experimental and internal adiabatic profiles.*

Investigating the $P-T$ profiles it can be noted that the experimental trends are characterized by a pathway very far from being both isentropic and approaching the phase boundary. The pressure development with respect to the local temperature inside the tank, in fact, leads to a complete development inside the gaseous phase. These conclusions can be extended to all experimental concerning the initial charged vessel with gaseous CO_2.

The comparison with the (theoretical) isentropic trajectory, even if with varying initial conditions, show a good agreement in the case of the modeled internal adiabatic hypothesis

with growing deviations once the charging pressure is allowed to increase. The matching is preserved up to the saturation line where the occurrence of an additional phase is observed. Deviations are mainly due to the increasing friction effects leading to an alteration of the pressure profile that is therefore not uniquely determined by the thermodynamic expansion but also by irreversible mechanisms.

Once the vapor dome is reached, the trajectory is altered with the occurrence of the dense phase leading to a development very close to the saturation line. The match however is not always preserved because of the already outlined latent heat effects resulting in a colder CO_2 at a certain pressure value.

To conclude in what concerning modeled temperature profiles the following conclusions are formulated:

1. the agreement between experimental and predicted profiles is good both in the qualitative and quantitative perspective. Best matches are observed for higher initial charging pressures even if the model shows anyway the tendency to slightly overestimate the temperature value for a certain pressure level;
2. the definition of a factor including all contributions to irreversibility mechanisms, gives reason to state that an increase in both the initial charging pressure and the temperature determines its enhancement. Main contribution is due to the thermodynamic expansion effect and the heat transfer induced by the surroundings walls;
3. all expansions are characterized by absolutely not negligible heat transfer amount with the stainless steel walls even if are characterized by a rapid evolution;
4. the modeling of a (ideal) internal adiabatic depressurization, keeping unchanged the initial parameters, results in completely different profiles. These are initially characterized by an isentropic development down to the saturation boundary. The appearance of the dense phase (liquid and solid) then constraints the pathway along the right vapor dome boundary with local deviations induced by latent heat effects.

5.5.3 Transient mass flow rate profiles and total discharge time

The description of pressurized releases from a vessel, in what concerning the development of QRA tools, requires also the estimation of the temporal evolution of the mass flow rate and therefore the total release time. This information is relevant in assessing risks related to a rapid depressurization because are the main parameters governing the subsequent dispersion phenomenon as well as the influences on the planning of rescue and maintenance interventions ([1,12]).

The variation of the mass inside the tank in time, i.e. the outflowing CO_2 mass flow rate, is governed by the following main parameters ([6]):

- amount of pressure drops encountered by the CO_2 during the flow toward the orifice plane;
- local specific volume magnitude, strictly governed by both the pressure and the temperature fields that are instantaneously changing because of the transient nature of the discharge phenomenon;
- occurrence of phase change mechanisms.

The modeling procedure, based on the experimental data, returns the results collected below. Figure 5.40 gives the estimated CO_2 mass flow rate at the orifice plate, Figure 5.41 the CO_2 vessel mass and Fig. 5.42-5.43 the time evolution of the CO_2 density both inside the vessel and at the orifice. Results refer to depressurization performed starting from a temperature of 20 °C.

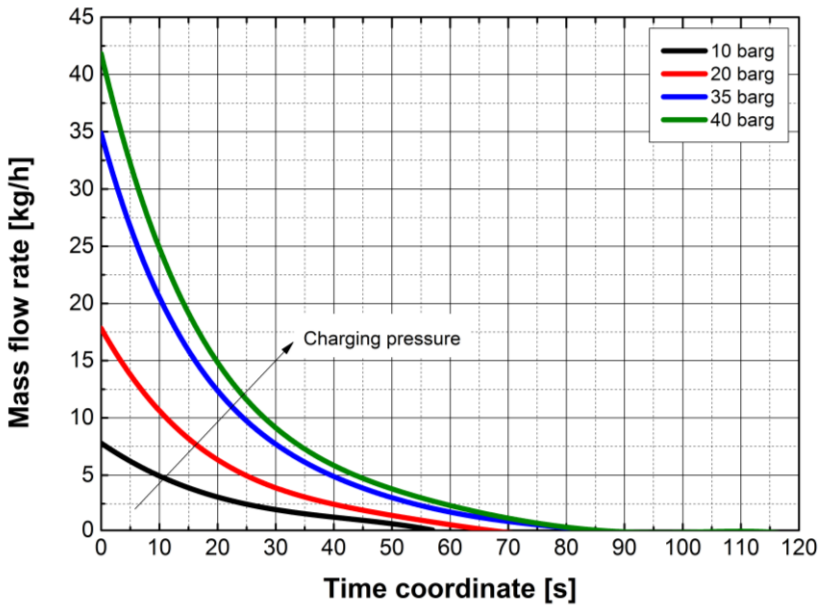

Figure 5.40. *Evolution of the discharged mass flow rate at the orifice plane for different initial charging pressures.*

Considering Figure 5.39-5.40, the trends concerning the evolution in time of the discharged mass flow rates and the remaining CO_2 mass inside the tank, show similar profiles also under varying initial charging conditions.

The characteristic decaying profile of the mass flow rate with the highest magnitude in the early stages is reasonable and observed by some authors ([26,34,39]).

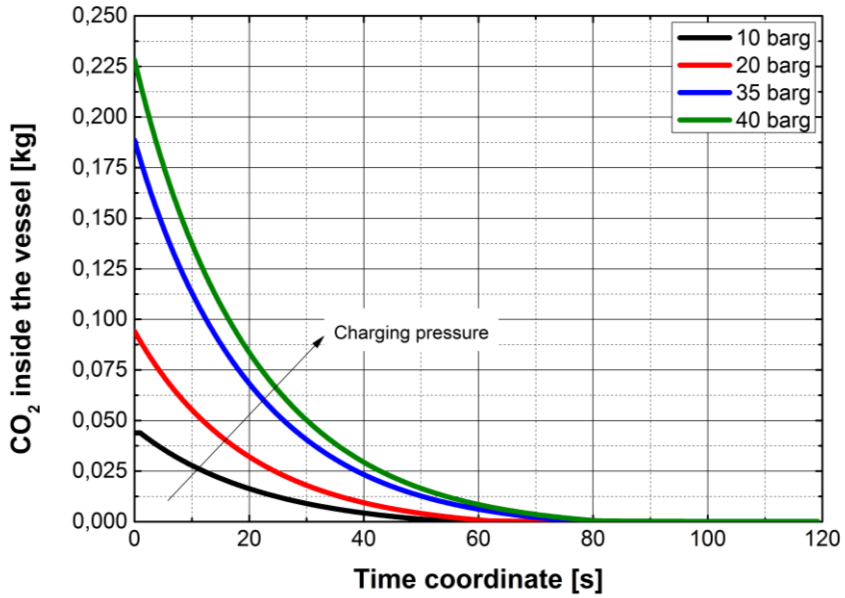

Figure 5.41. *Evolution of the CO_2 mass inside the vessel for different initial charging pressures.*

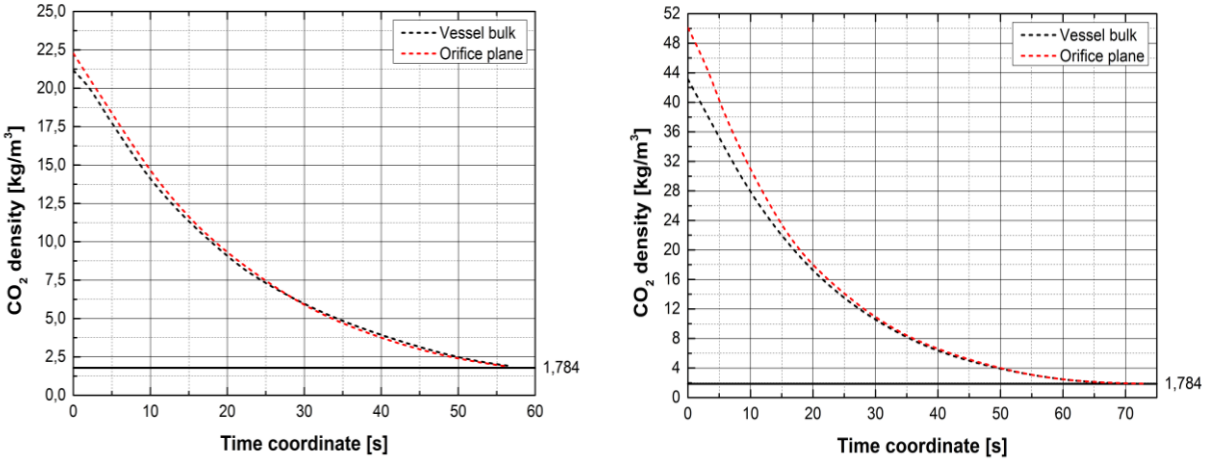

Figure 5.42. *CO_2 density evolution in the vessel and at the orifice plane. a- 10 barg. b- 20 barg. Indication of CO_2 density at SATP-Standard Atmospheric Temperature and Pressure (right axis).*

The main reason for this behavior lies in the higher CO_2 density values at the start of the experiment as observed in Figure 5.41-5.42.

The density variations are governed by the relatively low temperatures induced by the pressure gradients resulting in much larger CO_2 densities compared to that expected at SATP conditions that is anyway reached at the end of the experiment.

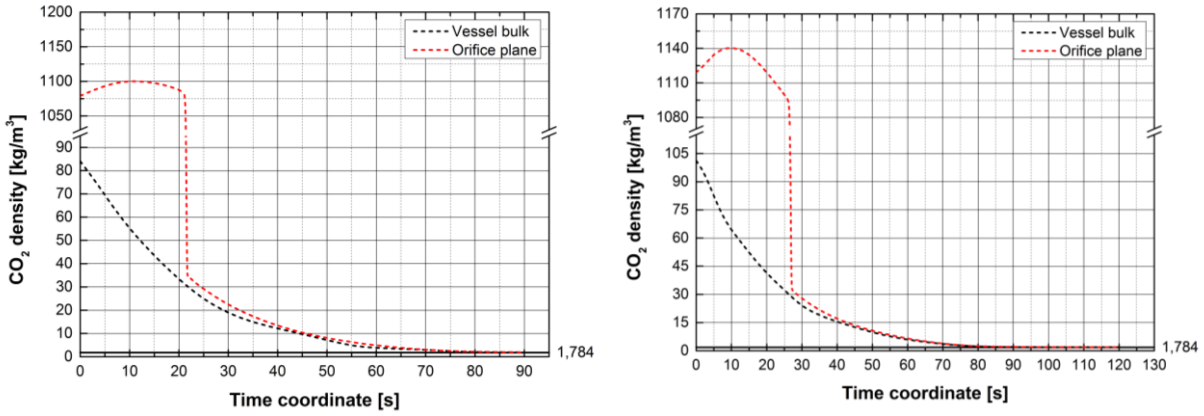

Figure 5.43. *CO_2 density evolution in the vessel and at the orifice plane. a- 35 barg. b- 40 barg. Indication of CO_2 density at SATP-Standard Atmospheric Temperature and Pressure (right axis).*

An instantaneous density difference between the bulk and the orifice condition persists because of both the pressure drops altering the depressurizing field and the lower temperatures predicted at the discharge plane that is directly facing the atmospheric conditions (Figure 5.42). The difference is amplified with increasing charging pressures but profiles tend to overlap along with the dropping pressure. Some specific initial conditions (Figure 5.43) may induce the dense phase appearance at the orifice plane because of the transformation that takes place between the bulk and the discharge location. Even if the dense phase formation inside the tank is never observed, as testified by the regular profiles of Figure 5.43, lower temperatures predicted at the discharge plane are suitable to drive the CO_2 inside the vapor dome. For example, in the case of 35 and 40 barg depressurizations, a certain initial period of time exists in which the thermodynamic conditions are those pertaining to the liquid domain. This lasts respectively for 22 and 28 s and after that the CO_2 recovers its gaseous state substantially following the development inside the vessel.

In the formulation of the QRA to CO_2 releases, also the total discharge time is essential in determining the timeframe of the whole phenomenon. This is strictly linked to discharged mass flow rate and therefore any inaccuracy pertaining to the discharge dynamics will affect also these predictions. In this sense, the right prediction of the physical state of the CO_2 at the orifice plane as well as the knowledge of the thermodynamic pathway traveled because of the expansion play a key role, especially in what concerning the discharge of a compressible substance ([4,14,18]).

In this context, the final discharge time should be intended as that to which the 99.9 % of any CO_2 phase has been ejected from the domain. This approach is essential since in the case of dense phase appearance this may significantly contribute to the whole mass amount of CO_2 instantaneously contained in the vessel.

Following Figure 5.44 gives the comparison between the observed and the predicted total discharge time.

The total discharge time, as already discussed in the section of the experimental data, is related to the initial CO_2 conditions. The dependence is clear since both the pressure and the temperature are acting on the CO_2 density that is the main parameter determining the discharge dynamic especially in terms of density ratio $\rho(t)/\rho_0$ ([13,18]). The growing trend with respect to the charging pressure is due to both the incremented initial mass to be unloaded and the induced thermal dynamic as previously observed. In addition, the ratio $P_{orifice}(t)/P_{vessel}(t)$ is representing a relevant parameter in driving the establishment of *choked* conditions and therefore in limiting the amount discharged per unit of time. The initial temperature influence is not so relevant since density induced variations are not so sensitive as much as to the pressure.

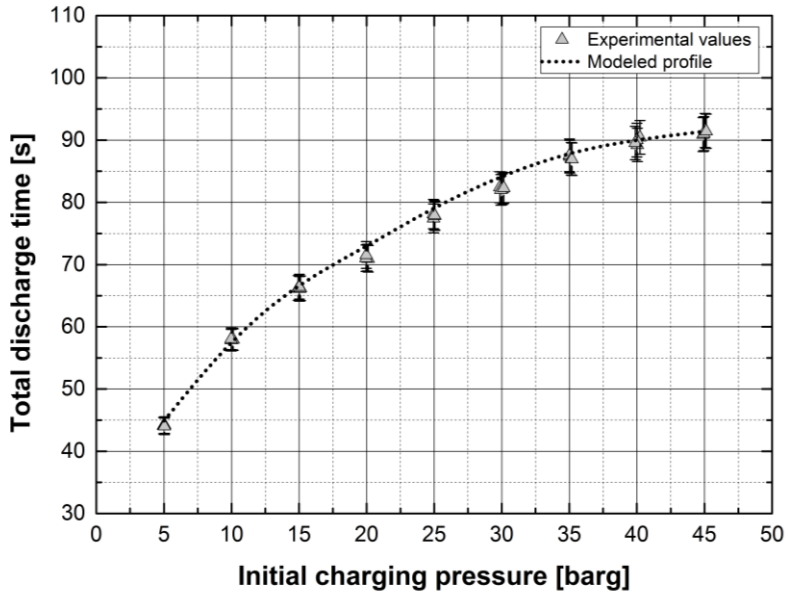

***Figure 5.44**. Measured and predicted total discharge time under different initial charging pressures.*

Modeled profile is well matching the observed data with a growth depending on the initial charging pressure. The growth intensity is not constant and is reduced with the increasing pressure also because the appearance of the dense phase at the orifice that alters the instantaneous discharged quantity of CO_2.

Relying on the fact that usual QRA may involve the assumption of ideal gas, some results have been produced under usual hypothesis of vessel blowdown of a non-condensable gas under choked adiabatic flow. This approach relies on the model proposed by some authors ([40]).

For this case, the authors give the following relation between the instantaneous pressure value $P(t)$ with respect to the time evolution coordinate t:

$$P(t) = P_0 \left[1 + \frac{\gamma - 1}{2} \frac{At}{V} \left(\frac{\gamma R T_0}{PM} \right)^{1/2} \left(\frac{2}{\gamma + 1} \right)^{(\gamma+1)/2(\gamma-1)} \right]^{-2\gamma/(\gamma-1)} . \quad (5.53)$$

In the (5.53), P_0 and T_0 refer to the initial CO_2 storage conditions, A is the cross-sectional area of the choke, V the tank volume, R the universal gas constant, PM the molecular weight of the CO_2 and γ the specific heats ratio. From the (5.53), the total discharge time t^* is derived as a function of the initial CO_2 conditions in the vessel and the required final pressure $P(t)$ from which the condition $P(t^*) = P_{amb}$ holds. The total discharge time is therefore given by (5.54):

$$t = \left[\left(\frac{P(t)}{P_0} \right)^{-(\gamma-1)/2\gamma} - 1 \right] \frac{2}{\gamma - 1} \frac{V}{A} \left(\frac{\gamma R T_0}{PM} \right)^{-1/2} \left(\frac{2}{\gamma + 1} \right)^{-(\gamma+1)/2(\gamma-1)} . \quad (5.54)$$

By using a mean value of γ evaluated between the condition at $t = 0$ and $t = t^*$ and neglecting any *vena contracta* phenomenon that is $A = S_2$, the predicted total discharge time t^* is plotted against the charging pressure P_0 in Figure 5.45. Results show how the ideal gas assumption dramatically alters the predictions concerning the total discharge time leading to strongly underestimated values. Experimental observations are never matched also in the case of the lowest pressures where the compressibility factor ranges from 0.94 to 0.96 even if the qualitative trend is correctly predicted. The ideal assumption, lacking the pressure-sensitivity of relevant CO_2 properties, primary among these the density and the heat capacities, leads to deviations that are incompatible with the description of the real phenomenon. Also the usually adopted hypothesis of adiabatic flow has a part in determining the results leading to unreal temperature trends not experimentally observed.

To conclude, the simplified approach usually invoked in QRA procedures may lack the whole discharge dynamics. Assumptions usually going with the application of ideal-gas based approaches introduce many errors primary among these:

a. the CO_2 key properties are not properly interpreted;
b. the adiabatic assumption almost never matches the real occurrence because neglecting the presence of the solid walls;
c. invoked equations contain a discharge coefficient that is usually assumed to be equal to 1 (conservative approach). In the case of multi-phase releases this may lead to serious inaccuracies because of the deviations induced by the appearance of a dense phase characterized by markedly different properties;

d. the time dependency is relegated to *AEs* while an *ODEs/PDEs*-based is the appropriate approach.

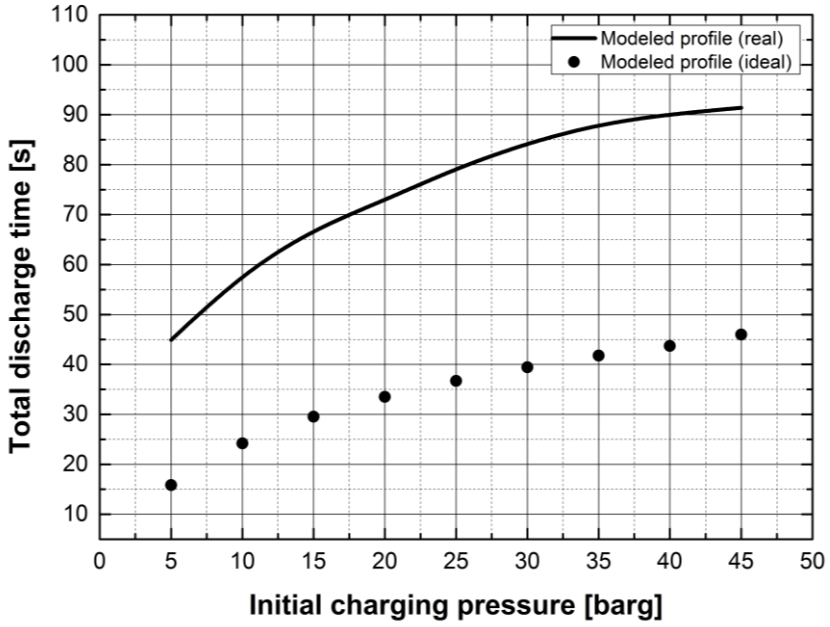

Figure 5.44. *Measured and predicted total discharge time under the real and ideal gas assumption (dotted profile).*

References to Chapter 5

1. Kornneef, J., Spruijt, M., Molag, M., Ramirez, A., Faaij, A., Turkenburg, W., 2009. Uncertainties in risk assessment of CO_2 pipelines. Energy Procedia, 1(1), 1587-1594.
2. Mahgerefteh, H., Brown, S., Martynov, S., 2012. A study of the effects of friction, heat transfer and stream impurities on the decompression behavior in CO_2 pipelines. Greenhouse gases: science and technology 2, 369-379.
3. Martynov, S., Brown, S., Mahgerefteh, 2013. An extended Peng-Robinson equation of state for carbon dioxide solid-vapor equilibrium. Greenhouse Gases: science and technology 3.
4. Mahgerefteh, H., Saha, P., Economou, I.G., 1999. Fast numerical simulation for full bore rupture of pressurized pipelines. Aiche journal 45, 1191-1201.
5. Mahgerefteh, H., Saha, P., Economou, I.G., 2000. Modeling phase transition effects on dynamic behavior of ESDV. Aiche journal 46, 997-1006.
6. Oke, A., Mahgerefteh, H., Economou, I., Rykov, Y., 2003. A transient outflow model for pipeline puncture. Chemical Engineering Science, 58, 4591-4694.
7. Mahgerefteh, H., Oke, A., Rykov, Y., 2006. Efficient numerical solution for highly transient flows. Chemical Engineering Science, 61(15), 5049-5056.

8. Martynov, S., Brown, S., Mahgerefteh, H., Sundara, V., 2013. Modelling choked flow for CO_2 from the dense phase to below the triple point. International journal of Greenhouse Gas Control, 19, 552-558.
9. Mocellin, P., Vianello, C., Maschio, G., 2015. Carbon capture and storage hazard investigation: Numerical analysis of hazards related to dry ice bank sublimation following accidental carbon dioxide releases. chemical engineering transactions, 43, 1897-1902.
10. Martynov, S., Brown, S., Mahgerefteh, H., Sundara, V., Chen, S., Zhang, Y., 2014. Modelling three-phase releases of carbon dioxide from high-pressure pipelines. Process safety and environmental protection, 92, 36-46.
11. Mahgerefteh, H., Sundara, V., Brown, S., Martynov, S., 2016. Modelling emergency isolation of carbon dioxide pipelines. International journal of greenhouse Gas Control, 44, 88-93.
12. Witlox, H.W.M., Harper, M., Oke, A., 2009. Modelling of discharge and atmospheric dispersion for carbon dioxide releases, Journal of loss prevention in the process industries, 22, 795-502.
13. Witlox, H.W.M., Stene, A., Harper, M., Nilsen, S.H., 2011. Modelling of discharge and atmospheric dispersion for carbon dioxide releases including sensitivity analysis for wide range of scenarios. Energy procedia, 4, 2253-2260.
14. Witlox, H.W.M., Harper, M., Oke, A., Stene, J., 2014. Validation of discharge and atmospheric dispersion for unpressurized and pressurized carbon dioxide releases. Process safety and environmental protection, 92, 3-16.
15. Webber, D.M., 2011. Generalizing two-phase homogeneous equilibrium pipeline and jet models to the case of carbon dioxide. Journal of loss prevention in the process industries, 24, 356-360.
16. Wareing, C.J., Fairweather, M., Falle, S.A.E.G., Woolley, R.M., 2014. Validation of a model of gas and dense phase CO_2 jet releases for carbon capture and storage application. International Journal of Greenhouse Gas Control, 20, 254-271.
17. Wareing, C.J., Fairweather, M., Woolley, R.M., Falle, S.A.E.G., 2014. Numerical simulation of CO_2 dispersion from punctures and ruptures of buried high-pressure dense phase CO_2 pipelines with experimental validation. Energy Procedia, 63, 2500-2509.
18. Wareing, C.J., Fairweather, M., Falle, S.A.E.G., Woolley, R.M., 2014. Modelling punctures of buried high-pressure dense phase CO_2 pipelines in CCS applications. International Journal of Greenhouse Gas Control, 29, 231-247.
19. Wareing, C.J., Fairweather, M., Falle, S.A.E.G., 2015. Modelling ruptures of buried high pressure dense phase CO_2 pipelines in carbon capture and storage applications-part I. Validation. International Journal of Greenhouse Gas Control, 42, 701-711.

20. Wareing, C.J., Fairweather, M., Falle, S.A.E.G., 2015. Modelling ruptures of buried high pressure dense phase CO_2 pipelines in carbon capture and storage applications-part II. A full-scale rupture. International Journal of Greenhouse Gas Control, 42, 712-728.
21. Vianello, C., Mocellin, P., Maschio, G., 2014. Study of formation, sublimation and deposition of dry ice from carbon capture and storage pipelines. Chemical Engineering transactions, 36, 613-618.
22. Poling, B.E., Prausnitz, J.M., O'Connell, J.P., 2001. The properties of gases and liquids. New York: McGraw-Hill.
23. Peng, D.Y., Robinson, D.B., 1976. A new two-constant Equation of state. Industrial Engineering chemistry, 15(1), 59-64.
24. Span, R., Wagner, W., 1994. A new equation of state for Carbon Dioxide covering the fluid region from the triple – point temperature to 1100 K at pressures up to 800 MPa. Journal of physical Chemistry, 25(6), 1509-1596.
25. Yokozeki, A., 2002. Analytical equation of state for solid-liquid-vapor phases. International journal of thermophysics, 24(3), 589-620.
26. Ahmad, M., Bogemann-van Osch, M., Buit, L., Florisson, O., Hulsbosch-Dam, C., Spruijt, M., Davolio, F., 2013. Study of the thermohydraulics of CO2 discharge from a high pressure reservoir. International journal of greenhouse gas control, 19, 63-73.
27. Haque, M.A., Richardson, S.M., Saville, G., 1992. Blowdown of Pressure Vessels. I. Computer Model. Trans IChemE Part B: Process Safety and Environmental Protection, 70, 10-17.
28. Darby, R., 2001. Chemical Engineering Fluid Mechanics, 2nd ed., marcel dekker inc., New York NY, USA.
29. Perry, R.H., Chilton, C.H., 2007. Perry's Chemical Engineers' Handbook, McGraw-Hill, New York, 8th edition.
30. Sun, K.H., Lienhard, J.H., 1970. The Peak Pool Boiling Heat Flux on Horizontal Cylinders. International Journal of Heat and Mass Transfer, 13, 1425-1439.
31. Burmeister, L. C., 1993. Convective Heat Transfer, John Wiley and Sons, INC., 1st ed.
32. Hanumanth, G. S., 1990. Solidification in the Presence of Natural Convection. Int. Comm. Heat Mass Transfer, 17, 283-292.
33. Globe, S., Dropkin, D., 1959. Natural Convection Heat Transfer in Liquids Confined between Two Horizontal Plates. J. of Heat Transfer, 81, 24.
34. Ahmad, M., Bogemann-van Osch, M., Buit, L., Florisson, O., Hulsbosch-Dam, C., Sruijt, M., Davolio, F., 2013. Study of Thermohydraulics of CO_2 Discharge from a High Pressure Reservoir, Int. J. of Greenhouse Gas Control, 19, 63-73.

35. Ahmad, M., Bogemann-van Osch, M., Buit, L., Florisson, O., Hulsbosch-Dam, C., Sruijt, M., Davolio, F., 2013. Experimental Investigation of CO_2 Outflow from a High Pressure Reservoir, Energy Procedia, 37, 3005-3017.
36. Zhang, Z.R., Yamaguchi, H., 2011. An Experimental Study on Heat Transfer of CO_2 solid-gas Two Phase Flow with Dry Ice Sublimation. Int. J. of Thermal Science, 50, 2228-2234.
37. Castier, M., 2011. Thermodynamic Speed of Sound in Multiphase Systems. Fluid Phase Equilibria, 306, 204-211.
38. Moody, F.j., 1965. Maximum Flow Rate of a Single Component, two-phase Mixture. Journal of Heat Transfer, 87, 134-142.
39. Vree, B., Ahmad, M., Buit, L., Florisson, O., 2015. Rapid Depressurization of a CO_2 pipeline-an Experimental Study, Int. J. of Greenhouse Gas Control, 41, 41-49.
40. Haque, M.A., Richardson, S.M., Saville, G., 1992. Blowdown of Pressure Vessels-I: Computer Model. Trans. I. Chem. E. part B, 70, 3-9.

Chapter 6

Model Extension to Real Scale Operations

In this section, the model developed in Chapter 5 is extended to real scale operations. In this sense, the model is applied to geometries that are matching the existing infrastructures.
Different parameters are investigated such as the orifice size, the pipeline length and the operative conditions. Model runs allow for the collection of the most relevant parameter to be used in QRA studies.

6.1 Introduction

The previous chapter was focused on the model validation involving gaseous pressurized release of CO_2. This section is dedicated to the investigation of the model capabilities when the vessel is filled with dense CO_2 both at saturation conditions or in the single phase domain.
Significant differences are expected since the dense physical state acts firstly modifying the amount subjected to the release and also the thermal dynamic because of the altered CO_2 properties. In addition, the presence of the pressurized domain certainly leads to phase-change mechanisms.
The first part of this section however is focused on the analysis of the system concerning only gaseous CO_2 subjected to a variation in the external parameters (environmental temperature, insulation) to then move to different geometries and length scales..

6.2 Gaseous CO_2 charge. Effect of the external temperature, insulation and different orifice sizes

Every pressurized release is influenced both by internal and external factors. While the internal aspects are linked to the substance thermodynamic state and the geometry, the external parameters concern the environmental conditions as well as the presence of external obstacles to the heat exchange ([1,2]). The presence of insulation structures may be linked to design and economic drivers as well as the burial of the transportation structures while the weather conditions are depending on the geographical location of the infrastructure.

The influence on the main release parameters of both a variation in the external temperature as well as the presence of an insulation thickness is thus investigated.

6.2.1 External temperature

The incidence of a variation in the external temperature on the release features has been investigated by applying the model proposed in Chapter 5. As suggested by some authors ([3,4]), the external temperature acts affecting heat transfer mechanisms between the external solid surface and the environment. The heat is transferred in a convective way and is driven by the temperature gradient existing between the mean bulk stainless steel temperature and that of the atmospheric environment ([5]). It is however expected that the magnitude of the external convective phenomena is negligible when compared to the effects induced by the expansion of the CO_2.

In this sense, the external domain is modeled as a solid cylindrical vessel exposed to a large quiescent volume of surrounding air. The heat is transferred according to an approximated relation of the type $Nu = f(Ra, Pr)$ as indicated in Chapter 5.

A variation in the external temperature is therefore investigated in order to throw light on the effects on the main release parameters. In actual situations, this variation is mainly induced by daily environmental temperature fluctuations and is therefore strictly linked to weather conditions as well as the geographical location of the infrastructure.

The investigation involves therefore the analysis of the release features varying the external temperature in the range 0-40 °C. Keeping the remaining parameters unchanged, the expected variations in the internal vessel temperature are firstly analyzed.

Figure 6.1 gives the variation in the minimum internal expected temperature inside the vessel and at the orifice plate in the case of 35 barg depressurizations.

Results show clearly how the minimum reached temperatures show a certain degree of sensitivity with respect to a variation in the environmental temperature. The dependence is not strong because, for example, an increase of 40 °C of the external temperature leads to a parallel variation of 5 °C of the expected internal one. The same variation is recorded at the orifice plate except for the expansion from 35 barg and 10 °C. In this case both trends show discrepancies. The calculated vessel internal temperature is much lower than the expected if compared to the other reported trends: for example, given the 35 barg and 20 °C trend, expected values should be less than 7 °C.

However, the difference in this behavior is due to the appearance of the dense phase that induces a wider decrease in the temperature if compared to the permanent single-phase case.

All trials concerning an initial temperature of 10 °C are characterized by the appearance of liquid CO_2 independently from the external temperature.

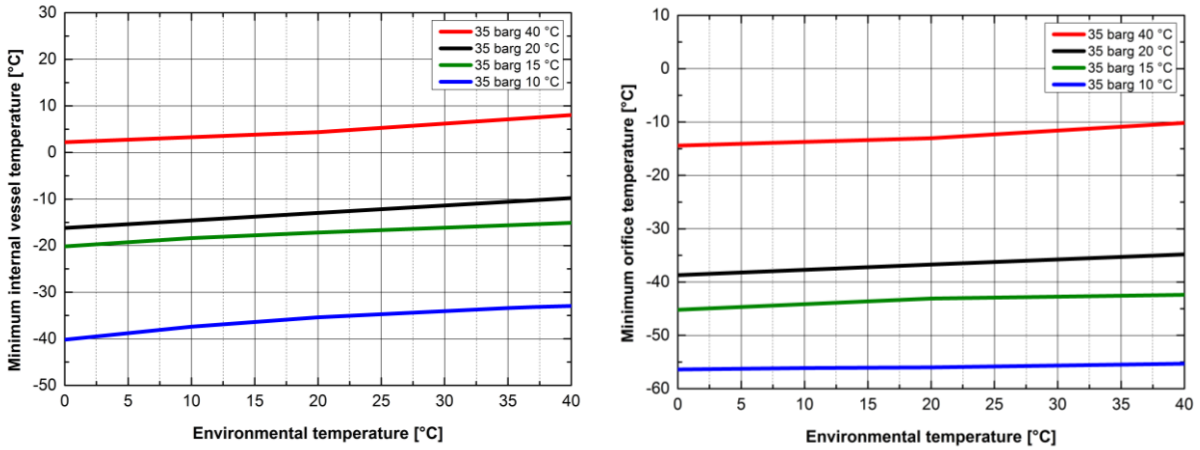

(a) *(b)*

Figure 6.1. *35 barg expansions. Effect of the environmental temperature with respect to different initial conditions on a- the minimum predicted vessel internal temperature; b- the minimum predicted orifice temperature.*

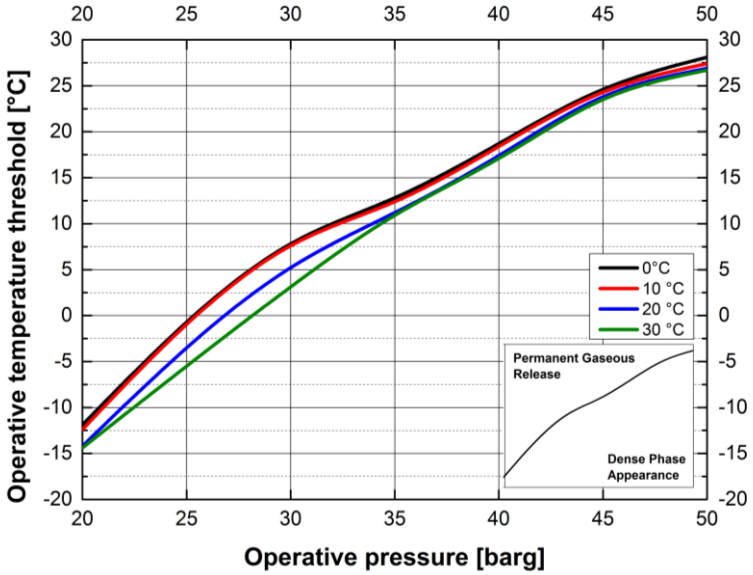

Figure 6.2. *Threshold operative conditions to dense phase appearance under different environmental temperatures.*

This is testified also by Figure 6.1b in which the discharge temperature is almost insensitive from this variation. In the case of only gaseous discharge, also the temperature at the orifice is sensitive to the external value with a tendency nearly comparable to that observed inside the vessel.

Therefore, under some circumstances a decrease in the environmental temperature may induce dramatic changes in the release features because of the establishment of favorable conditions to the dense phase appearance inside the tank. Simulations show that, fixed the

internal charging conditions, a minimum external temperature exists below which a gaseous charge turns out to be multiphase because of the expansion. Figure 6.2 gives the operative threshold conditions leading to a release with dense phase appearance depending on the external environmental temperature.

As indicated a variation in the external temperature that may induced both by variables weather conditions as well as other external causes (fires, explosions, …), is responsible also for a variation in the release nature and mechanism. This influence will be reflected on the critical operative conditions leading to the dense phase appearance because of the depressurization. In this sense, gaseous CO_2 handling operations are characterized by a threshold internal operative temperature below which liquid CO_2 is expected once the operative pressure is fixed (fig. 4.2). For this reason, as an example, gaseous CO_2 pipelines operated in the pressure range of 35-45 barg when planned at temperatures equal to 12-25 °C require a modeling procedure involving the occurrence of a multi-phase release. This is essential when facing risks through a dedicate QRA procedure since the lack of the dense phase alters the accident characteristic time as well as the consequences related to the depressurization.

In addition, a decrease in the external temperature acts raising this operative temperature threshold with an external variation of 30 °C leading to a parallel increase of 5 °C in the investigated parameter.

6.2.2 External heat source

The presence of external sources of heat may induce modifications in the CO_2 release parameters. Among the most relevant, an external fire occurrence is definitely the most critical because of the huge fire load that can be transmitted to the CO_2 system. From this point of view, the proximity to natural gas pipelines need to be considered in QRA since it may represent a serious source of hazards, especially in what concerning fires ([6]). This because many actual investigations are throwing light on the economic convenience of using existing O&G (Oil and Gas) corridors to arrange also the CCS infrastructures ([7]).

The modeling of a fire event concerning natural gas pipelines is based on both the estimation of the flow rate released as well as the heat release rate that is transferred to the CO_2 containment. Not being the detailed fire investigation the aim of the study, simplified approaches have been implemented.

The release rate from the gas pipeline is modeled as proposed by some authors ([8]) and based on the verified hypothesis that heat transfer to the moving gas through the pipe walls maintains an almost isothermal condition throughout the length of the pipe. Only the last 200

diameters are modeled as an adiabatic flow induced by a rapid acceleration of the discharging gas.

More sophisticated models are available and concern the description of the unsteady discharge from a long pipeline as proposed in some works ([9]). For example, the work of Fanneløp and coauthors is based on the nonlinear *PDEs* expressing the balance between friction and pressure forces. The application of the integral method with supposed boundary functions allows for the formulation of the variation in time of the group $Pu = I$ at the discharging plane as indicated in (6.1):

$$I_L(t) = \left[\omega L\left(3 - \frac{8}{\pi}\right)\right]^{-1/2} [P_0^2(t) - P_L^2]^{1/2} \quad , \tag{6.1}$$

where ω is a parameter depending on friction effects, L is the pipeline length, $P_0 = P(0,t)$ and $P_L = P(L,t)$ the pressure evaluated at the boundary pipeline sections. The pressure inside the pipeline is instead supposed to be described by a cosine profile:

$$P(x,t) = P_L + [P_0(t) - P_L]\cos\left(\frac{\pi x}{2L}\right) \quad . \tag{6.2}$$

The modeling of the discharging rate $\dot{m_{out}}$ is then useful to assess the thermal radiation emitted from a jet flame that is supposed to be the most likely consequence induced by a gas pipeline failure with ignition. In that respect, the estimation of the thermal radiation relies on the model proposed by Carter (1991) ([10]). The flame is treated as a multiple source radiator and the thermal radiation is given by the (6.3):

$$q = \frac{\vartheta(-\Delta H_{comb})\dot{m_{out}}\tau_{atm}}{4\pi x^2} \quad . \tag{6.3}$$

In (6.3), ϑ is the fraction of heat radiated that is linked to the combustion power ([11]), ΔH_{comb} is the heat of combustion, $\dot{m_{out}}$ the mass flow leaving the pipeline and τ_{atm} is the atmospheric transmissivity that should be corrected depending on the target distance.

In order to investigate the effects on the CO_2 release, an external jet fire originated from a gas pipeline of the same internal diameter as that of the vessel is simulated. The length of the pipeline is assumed to be equal to 1000 m to ensure the development of a pipe geometry able to sustain a pressurized release. The CO_2 vessel is supposed not to be insulated.

Different investigations have been performed exposing the CO_2 vessel to external equivalent heat fluxes induced by the natural gas fire. Different heat flux magnitudes are investigated: 10, 5, 2 and 1 kWm^{-2}.

Results concerning the variation in the internal CO_2 vessel temperature and pressure are reported in Figure 6.3a-6.3b with reference to 10 barg expansions.

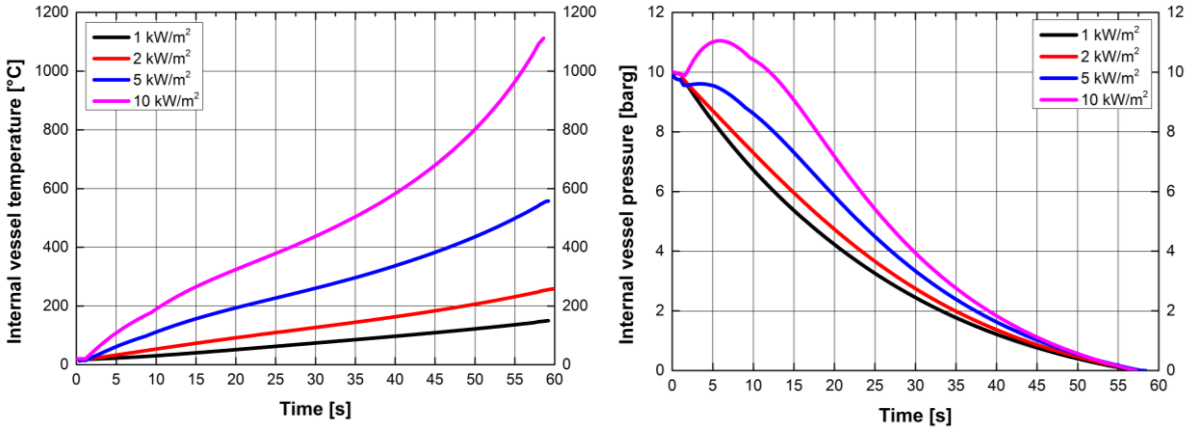

(a) *(b)*

Figure 6.3. *CO_2 vessel exposed to fire-induced heat fluxes. Charging conditions: 10 barg; 20 °C. a- internal vessel temperature profiles; b- internal vessel pressure profiles.*

Internal temperature profiles modeled show for each applied heat flux a not bounded growth. The increase in the temperature, that is obviously major for higher applied external fluxes, is not bounded and the CO_2 is therefore subjected to a heating process helped also by the conductive features of the steel walls. The final temperature is depending on the external conditions as well as the dynamics leading to the end state. It should be noted that the thermal dynamics is not preserving the characteristic trends previously observed since the rapid experienced expansion is not resulting in a satisfactory cooling effect. In this sense, the initial temperature gradients induced by pressure variations are overwhelmed by those resulting from the fire effect: the early decrease in the temperature is not observed and the initial storage temperature is also the minimum one.

Moving to pressure developments, a more complicated behavior is observed. In fact, given the CO_2 compressibility under the investigated conditions, the imposition of a heat flux may lead to different depressurization paths. This is observed above a threshold value (3.5 kW/m^2) in the case of 10 barg expansions) where the relevant increase in the temperature induces a certain pressure increment on the CO_2 even if subjected to a discharge. For example, in the case of 10 kW/m^2, the maximum recorded pressure is equal to 11.3 barg, 6.2 s after the release start. Also in the case of 5 kW/m^2 a deviation in the native pressure trend is observed but with a certain balance between the pressure increase induced by thermal effects and the decrease driven by the discharge. Lowering the heat flux results in no relevant pressurization phenomena because of the main contribution derived by the depressurization-induced by the orifice discharge.

Higher charging pressures involve more complex consequences because of the possible occurrence of dense phase CO_2 with implications on the variated thermal capacity, heat transfer to the liquid domain and the thermal-induced acceleration of boiling mechanisms.
Pressure and temperature profiles obtained under an initial charging pressure of 45 barg are reported respectively in Figure 6.4-6.5.

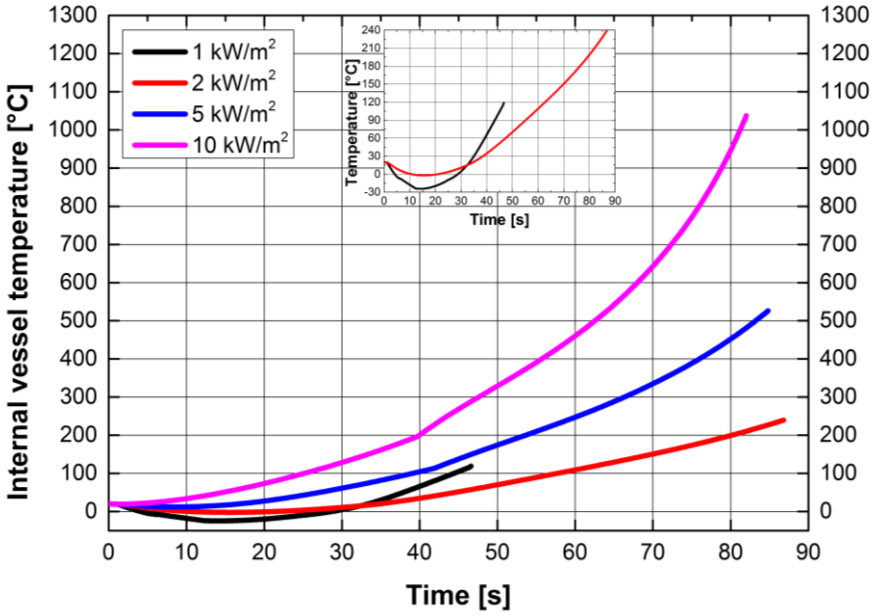

Figure 6.4. *Vessel exposed to fire-induced heat fluxes. Internal CO_2 temperature profiles. 45 barg, 20 °C expansion.*

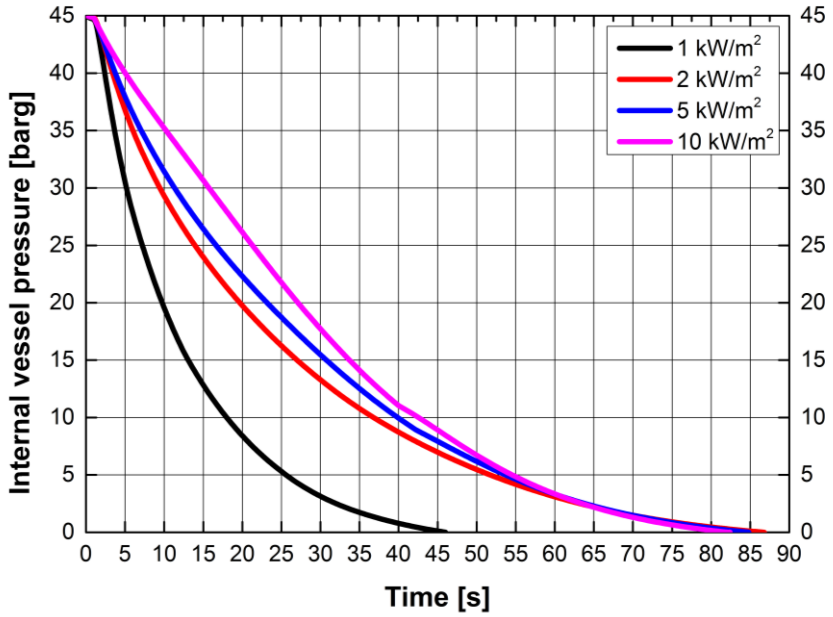

Figure 6.5. *Vessel exposed to fire-induced heat fluxes. Internal CO_2 pressure profiles. 45 barg, 20 °C expansion.*

Differences are relevant even if initial charging conditions are kept unchanged. A CO_2 initially filled at 45 barg may undergo a completely different evolution depending on the external radiation degree. Considering Figure 6.4-6.5, a heat flux greater than 2 kW/m^2

induces similar consequences with the CO_2 subjected to qualitatively comparable temperature and pressure trends. However, focusing on the pressure evolutions (Figure 6.5), some differences arise in terms of quantitative development with higher fluxes determining greater instantaneous internal pressures with respect to weaker fires. Nevertheless, none of them is able to significantly alter the decreasing pressure trends in contrast to what observed in Figure 6.3b. The expansion mechanical effect is in fact vigorous to cause also the usual initial CO_2 temperature decrease as depicted in Figure 6.3a even if of more moderate magnitude and only in the case of 1 and 2 kW/m^2. It should be considered that without the external contributions, the minimum observed vessel internal temperature is equal to -41.5 °C while in the case of additional heat flux injection, this is increased respectively to -24.3 and -2.0 °C with a heat flux of 1 and 2 kW/m^2.

A further investigation of Figure 6.4-6.5 shows a relevant discrepancy in the total discharge time as clearly indicated. The deviations between the 45 barg expansion subjected to 1 kW/m^2 and to other investigated fluxes is mainly due to the appearance of the dense phase. In fact, the applied heat flux is not able to give a persistent gaseous phase and during the release, exactly 6.1 s after the start of the release the liquid phase occurs as reported in Figure 6.6a.

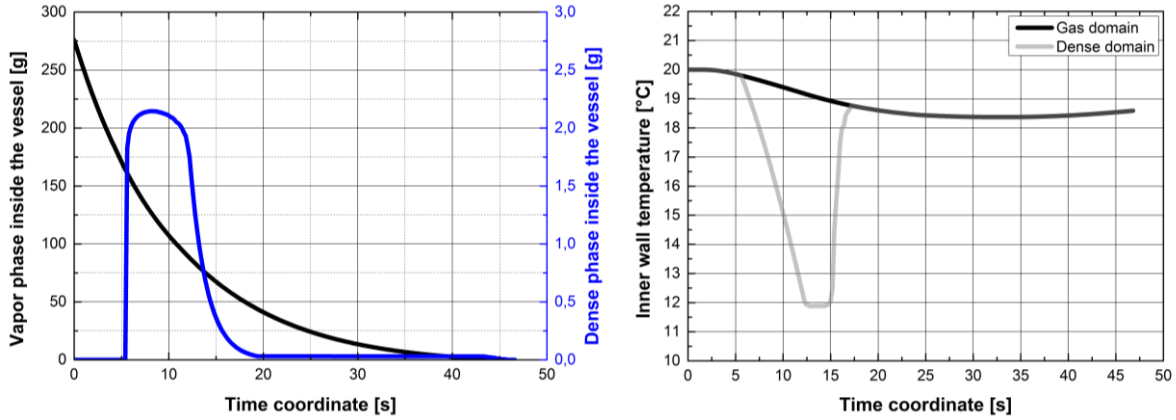

(a) *(b)*

Figure 6.6. a- *mass time evolution inside the vessel for a 45 barg expansion subjected to an external heat flux of 1 kW/m^2; b- inner wall temperatures pertaining to gas and liquid phase.*

Thermodynamic conditions allowing for the solid phase appearance are not ensured and only the liquid phase is therefore observed, contributing to the gaseous phase because of the boiling mechanisms. The amount of produced dense phase is not so relevant but detectable effects are observed with regard to the temperature dynamics. In fact, the initial cooling step is relevant not only for the weak radiative fire contribution but also because of the heat effects related to the liquid appearance and boiling. Considering Figure 6.4, it may be noted that the decrease in the temperature is almost corresponding to the time existence domain of the liquid

phase. During this step, strong heat transfer mechanisms are observed and differences in those taking place with the vessel walls in contact with the liquid or the gas. Portions facing the liquid phase are in fact experiencing a temperature drop induced by the diversified heat capacity and the latent heat-related phenomena that is not observed with the gaseous phase. Inner wall temperatures observed in the investigated 45 barg case are reported in Figure 6.6b with the clear variation explained above. With respect to Figure 6.6a, once the liquefaction is taking place, an almost linear decrease in the inner wall temperature is observed down to the minimum value of 11.94 °C. The temperature readjustment starts before the completion of the phase transition with a faster dynamic because of the vanishing latent heat effect and the additional external heat flux.

As observed in Figure 6.6b, the overall inner wall temperature trend is decreasing during the release because the relevance of the mechanically-induced cooling is overwhelming the fire contribution supply. Even if this difference in the exposed wall sections, it is essential to highlight that facing phases are always in thermal equilibrium because of the hypothesis employed in this model development stage. This to say that the modeled inside temperature trend is characteristic of both phases and the difference expected in the surface values are effectively resulting from the change in the peculiar phase thermal properties.

To conclude, the presence of an external heat source, depending on its magnitude, is primarily acting on the following aspects:

a) alteration of both the internal bulk and inner wall surface temperature, especially in what concerning the dense phase;
b) modification in the depressurization profiles with peculiar compression stages in the initial release steps driven by the external-induced temperature gradient;
c) relevant change in the total discharge time because of the occurrence of phase-redistribution mechanisms.

6.2.3 External insulation

The modeling of the presence of the insulation is needed wherever the domain under investigation is coated with specific materials or even though if the equipment is accommodated in the soil.

Actual design procedures may require the application of an external coating thickness to preserve the pipe material from the external corrosion. As reported in some technical sources ([12,13]), typical pipe coatings are represented by fusion bounded epoxy (FBE coating) supplemented with polyolefin layer (PE or PP).

In addition, the presence of the soil acts as a heat transfer medium considered its capacity to allow for a certain amount of energy transfer ([14]). A deeper analysis shows that the conduction is the primary mode of heat transfer in soil with three main parameters influencing its thermal conductivity: mineral composition of the solid phase, voids proportion and spatial arrangement and finally water content, with a distinction between frozen and unfrozen soils. The heat capacity of the soil as well as its thermal conductivity have been derived as proposed by some authors ([14]).

Performed simulations involve the presence of the external FBE insulation whose properties are reported in Table 6.1.

Table 6.1. *Details on the current CCS project ([22]).*

Material	Density [kg m^{-3}]	Thermal Conductivity [W m^{-1} K^{-1}]	Heat Capacity [J kg^{-1} K^{-1}]
Steel Pipe	7850	Temperature dependent	Temperature dependent
FBE coating	1200	0.3	2000
PTFE insulation	2200	0.24	1050

The amount of external coating is expressed in terms of the ratio β between its thickness and that of the vessel that is made of stainless steel and is equal to 5.4 mm. Following β are investigated: 0.10, 0.25, 0.5, 1 and 2.

Figure 6.7 gives the trend of the outside overall heat loss with respect to the release development in time which is depending on the selected value of β.

As a general result, it may be noted that an increase in the value of β leads to a decrease in the overall heat loss as can be expected making up the insulation a barrier to external heat transfers. The $\beta = 0$ line is linked to the case of directly exposed vessel surface with major heat losses. The magnitudes of the heat exchanges with the surroundings are an order of magnitude lower than those internally recorded indicating that main thermal phenomena are taking place in the vessel and at the internal surface. Under the investigated conditions of initial pressure equals to 35 barg and a temperature of 20 °C, no relevant variations in the internal pressure and temperature trends are observed due to a variation in the insulation thickness. Only little discrepancies are recorded with respect to the internal wall vessel temperature as appearing in Figure 6.8. Differences are negligible and reflect the absence of substantial variations in the internal thermal dynamic that is not affected by the insulation.

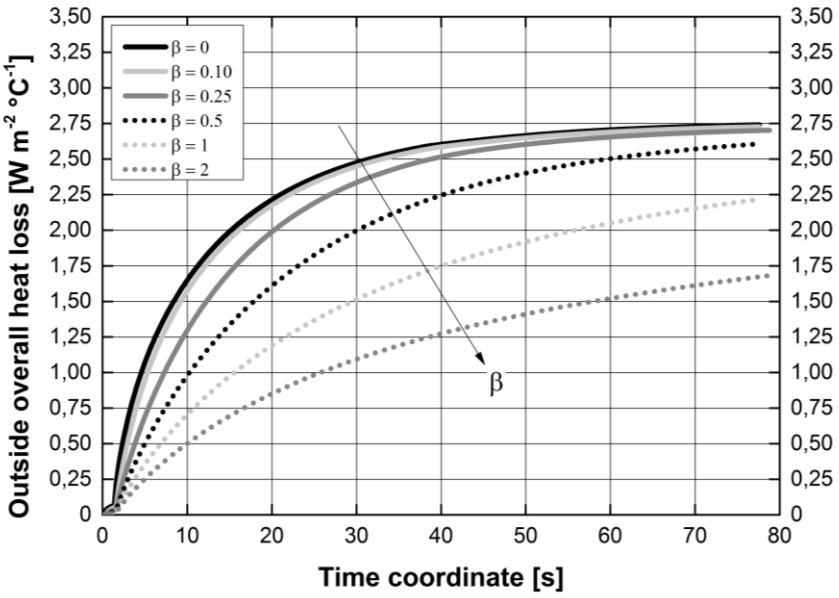

Figure 6.7. *Outside overall heat loss time evolution with respect to the ratio between the insulation and the vessel wall thickness.*

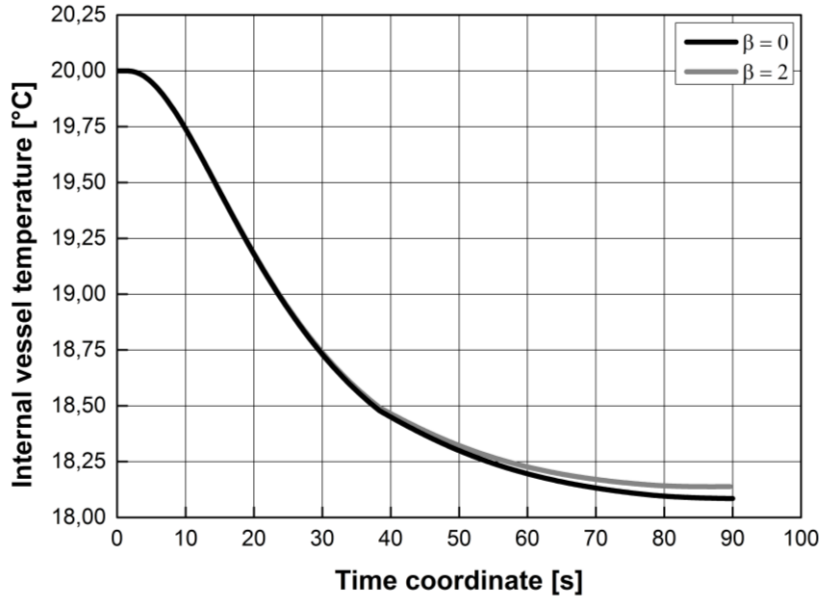

Figure 6.8. *Time evolution of the internal wall vessel temperature with respect to the presence of the external insulation.*

The main reason for this insensitivity to the insulation is that the CO_2 is entirely interacting with the solid walls and, under the investigated conditions, its heat capacity is so reduced with respect to that of the vessel that, in relation, the latter may be intended as an infinite-capacity thermal reservoir.

Further investigations give reason to state that some differences arise when the external temperature is altered with respect to the initial charging CO_2 temperature. The presence of the insulation allows for an initial temperature difference between the surroundings and the internal wall surface that is not observed in the previous cases.

With respect to this occurrence, a survey has been performed lowering the ambient temperature down to 0 °C while keeping unchanged the initial CO_2 parameters (35 barg, 20 °C). The analysis concerning the insulation is restricted to $\beta = 0$ and $\beta = 2$ (Figure 6.9) The whole investigation is then extended to a charging pressure of 45 and 10 barg to throw light on the two limiting experimentally investigated initial pressures.

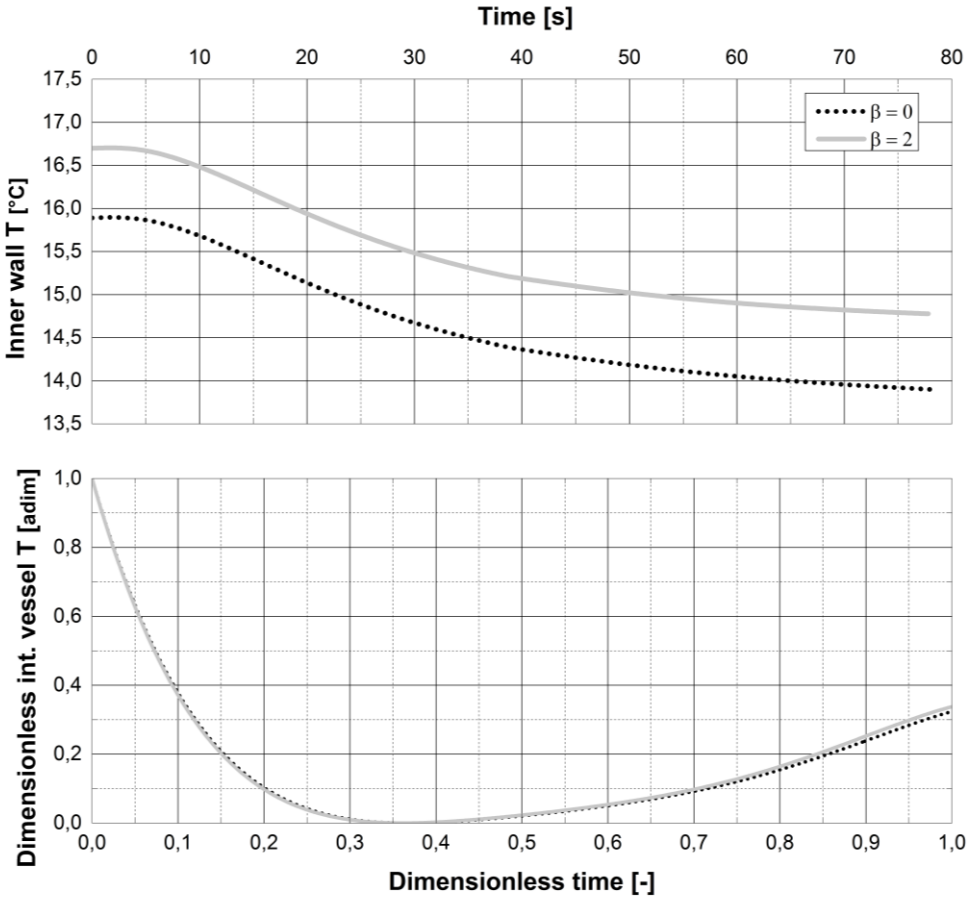

Figure 6.9. *Internal wall vessel and CO_2 bulk temperature trend with respect to β . 35 bar, 20 °C expansion. External temperature: 0 °C.*

As reported in Figure 6.9, the fall of the hypothesis of the same initial temperature between the vessel inside and the surroundings leads to a different inner wall temperature dynamic with an initial value depending on the external temperature. However, it should be noted that, despite these differences, the dimensionless trend of the internal bulk CO_2 temperature is not noticeably sensitive to variations in the external temperature once the insulation is arranged. Also a variation in the charging CO_2 temperature, under the investigated conditions, does not imply variations in the discharge dynamic once different values of β are inspected. Results show that, for example, while preserving a charging pressure of 35 barg, a variation in the initial temperature in the range 0-40 °C does not lead to significant alterations in the main discharge parameters. In addition, also with the appearance of the dense phase observed under

the specific conditions of fig. 4.2, the presence of an insulation of different thickness does not act modifying the internal CO_2 variables.

The investigation extension to lower charging pressures down to 10 barg, gives similar results with differences much less discernible.

Moving to higher pressures, the case of the 45 barg expansions modeled supposing the same initial temperature inside and outside the vessel give no substantial differences in the CO_2 parameters as already previously observed. However, once the external temperature is altered down to 0 °C, alterations are observed in both the internal CO_2 temperature evolution as well as in the internal surface temperatures. Results are collected in Figure 6.10a-6.10b. in what concerning the internal temperature of the discharging CO_2.

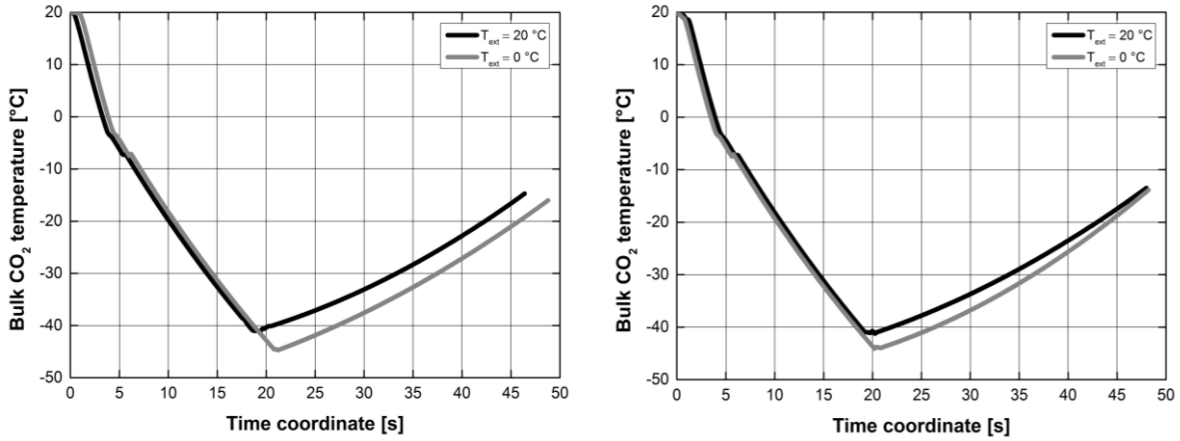

Figure 6.10. *Bulk CO_2 temperature evolution. a- $\beta = 0$; b- $\beta = 2$. 45 barg, 20 °C expansion.*

Figure 6.10b refers to an external insulation thickness corresponding to $\beta = 2$ while Figure 6.10a to no external insulation. The analysis of the CO_2 temperature evolution firstly shows that a variation in the external temperature induces some discrepancies in the trends with main differences concerning the minimum reached temperature and the subsequent heating process to the equilibrium reestablishment. A decrease of 20 °C in the environmental parameter is related to a parallel decrease of the minimum bulk CO_2 temperature of 3.5 and 2.6 °C respectively for the case of $\beta = 0$ and $\beta = 2$. The presence of the insulation thickness tends to bring the two profiles closer as reported in Figure 6.10a-6.10b and this is resulting from the insulating character of the extra thickness. No differences are observed in the initial cooling step because mainly driven by the pressure drop that is keeping almost unchanged. In addition, a deeper investigation of the interphase heat transfer reported in Figure 6.11a-6.11b throws light on the negligible differences in the amount of heat transferred under different external conditions.

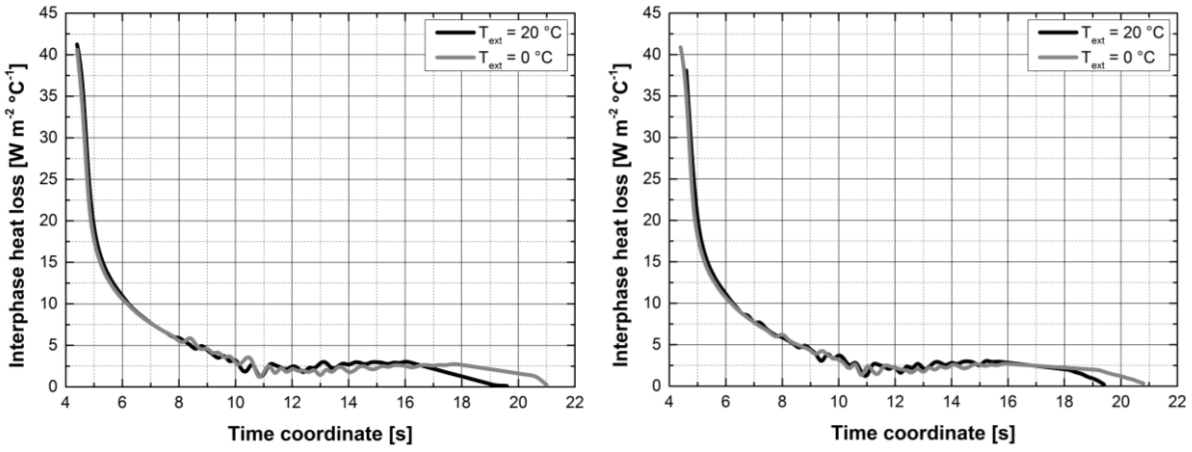

Figure 6.11. *Interphase heat transfer coefficient. a- $\beta = 0$; b- $\beta = 2$. 45 barg, 20 °C expansion.*

The graphical representation of the interphase heat loss is restricted to the phase-coexistence time domain that is slightly different with a variation in the external temperature. A lower external temperature yields to higher dense phase contents and therefore to a longer time-to-complete evaporation. However, no relevant variation in the amount of heat exchanged between the vapor and liquid phase are observed as reported in Figure 6.11 to indicate the relative constancy in the generated dense phase during the expansion with the highest value involving dense mass fractions in the range 3.8-4 %. The existence time domain of the dense phase is narrower for higher external temperatures and the same parameter is responsible for the observed lower bulk CO_2 temperatures observed in Figure 6.10 being the latent heat effects almost the same for the unchanged amount of dense phase.

In this sense, a decrease in the external temperature is reflected on a lower internal surface temperature contributing to a decrease in that of the bulk CO_2 without relevant variations in the expansion pathway.

The substitution of the experimentally used insulation with that characterized by the properties in Table 6.1, does not alter markedly the results already listed. This means that, under the investigated conditions, only the insulation thickness (and in a small extent) plays a role in determining the internal thermal dynamic as well as the external temperature. However, as observed, the geometrical size of the experimental setup gives reason to state that, for QRA purposes, the effects of the presence of the external insulation can be neglected without making any substantial mistakes. These observations held as long as the CO_2 initial charge is gaseous.

6.2.4 Orifice size and initial operative conditions

This part of the analysis is dedicated to the investigation of the effects related to both a variation in the initial CO_2 state as well as the implications derived from a change in the vessel geometry. The latter is faced according to two different parameters: the ratio between the length of the vessel and its diameter δ and the orifice size.

Both will influence the whole release phenomenon because of the variation in the physical properties of the CO_2 and the total discharged inventory. The total released inventory is also sensitive to the vessel volume while the discharge rate is somehow affected by the orifice size ([1]).

Starting from the experimental setup used, the analysis has been carried out by varying the characteristic size of the orifice, expressed in terms of internal diameter, while keeping the vessel dimensions unchanged. In this sense, two additional situations are investigated with a doubled and fourfold orifice discharge diameter with respect to that used in the previous analysis.

Firstly, considering a release from 35 barg and 20 °C, the thermal dynamic is investigated in terms of bulk CO_2 temperature. The base case is represented by the experimental reproduced conditions. Figure 6.12a-6.12b give respectively the time and the dimensionless trends.

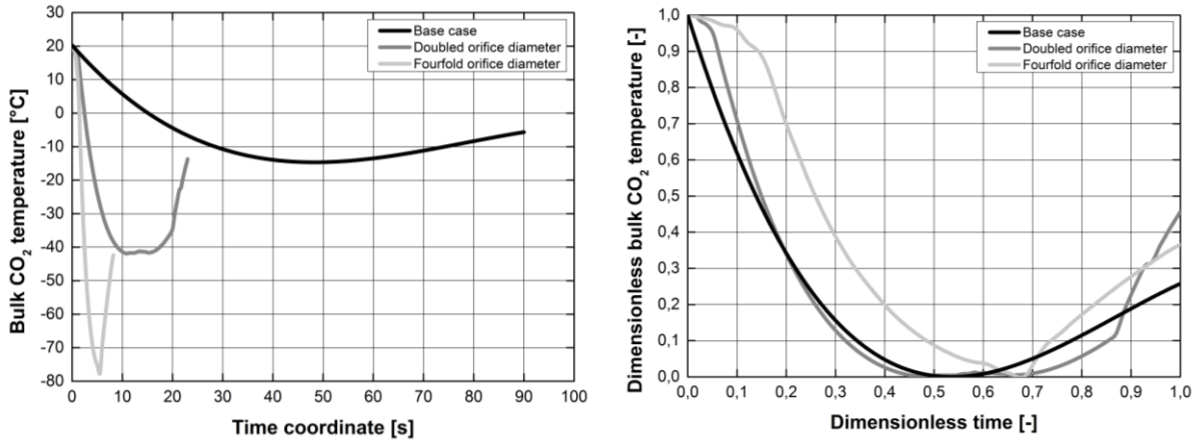

(a) *(b)*

Figure 6.12. *Investigation of the thermal dynamic induced by a variation in the orifice size. a- bulk CO_2 temperature time trend; b- dimensionless profiles. 35 barg, 20 °C expansion.*

As indicated in Figure 6.12a, the variation in the orifice size is essential in determining the whole discharge dynamic. Starting from the base case, an increase in the discharge section involves larger and faster temperature variations inside the vessel. Trends observed are extremely sensitive to the orifice size with an overall observed reduction in the total release time.

The increase in the discharge section, aside from determining larger release rates, is responsible for extremely lower bulk temperatures and the dynamic followed to achieve them. For example, under the investigated conditions, the base case lowest recorded temperature (-12.2 °C) is further reduced to respectively -42 and -78.3 °C with increasing orifice size. It should be noted that, despite this huge variation in the minimum forecasted temperature, it is achieved in a relative time (with respect to the total release evolution) that is comparable in the base case and in that with a doubled orifice diameter as reported in Figure 6.12b. A further increase in the orifice leads to a different dimensionless trend that is not fully comparable.

It may be interesting to throw light on the depressurization path and on the implications following from a different release intensity driven by the discharging orifice size, also with respect to saturation conditions, i.e. the appearance of different CO_2 phases. The temperature-pressure profiles concerning both the bulk and the orifice locations are respectively reported in Figure 6.13a-6.13b.

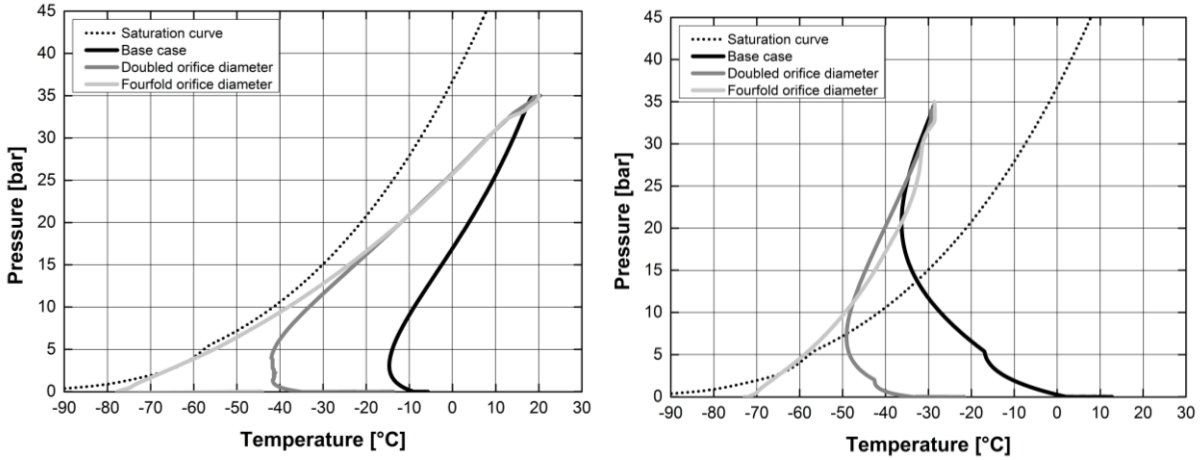

Figure 6.12. *Temperature-pressure evolution in the vessel bulk (a) and at the orifice plane (b) for different orifice sizes. 35 barg, 20 °C.*

It is clear how an alteration of the discharging orifice leads to completely different temperature-pressure trajectories even if the initial conditions are identical. The bulk progress is characterized by the completely development in the single gaseous phase domain with a certain degree of comparability of the new expansion trends with respects to the base case at least down to -15 °C. This bulk temperature is reached respectively after 3.9 and 1.7 s. No dense phase is therefore forecasted in the vessel bulk under the investigated conditions.

Substantial differences are also observed at the orifice plane where the orifice size variations are determining huge alterations. It is not worth to mention that despite these variations, the initial post-expanded state (the initial trajectory point above the saturation line) remains

almost the same with an instantaneous drop of 48.5 °C down to a temperature of -28 °C. Starting then from this point, each trajectory is different. Each of them is driving the CO_2 inside the vapor dome indicating that the dense phase is expected in all the analyzed expansions. However, what makes them different, in addition to the actual trajectory, is the minimum reached temperature and also the state matching the dense phase appearance. An increase in the orifice size leads to a variation in the intersection state with the vapor dome that is taking place respectively at the conditions reported in Table 6.2.

So each combination drives the CO_2 far from the fully (ideal) isentropic conditions, with the release involving the smaller orifice that tends to be closer. Once the orifice size is increased, the degree of reversibility χ goes down indicating the occurrence of irreversible mechanisms especially linked to frictions and heat transfer induced by more extended temperature gradients.

Table 6.2. *Saturated states (vapor dome intersection points) pertaining to different orifice sizes. 35 barg, 20 °C.*

Orifice diameter	Saturated conditions			χ
	Observed	Isentropic	Isenthalpic	
Base case	(14.3 bar; -32.1 °C)	(21 bar; -18.4 °C)	no dense phase appearance	0.74
Doubled	(7.2 bar; -48.9 °C)			0.42
Fourfold	(3.3 bar; -64.4 °C)			0.39

In addition, a deeper investigation of the instantaneous conditions affecting the discharging CO_2, shows that the base case and that with the doubled orifice imply the disappearance of the liquid phase without a passage in the SVE domain. Only the largest investigated orifice is able to drive the CO_2 firstly in the LVE domain and after inside the SVE region as indicated by the intersection pressure value equal to 3.3 bar that is lower than that pertaining to the triple point. In any case, under these initial conditions, a variation in the orifice diameter is not determining the appearance of the dense phase in the vessel bulk.

The persistence of the liquid phase, which is increasing with the orifice size, is also responsible for the difference in the total recorded discharge time. In addition, huge variations are recorded with respect to the total CO_2 mass instantaneously contained in the vessel as reported in Figure 6.14 and, as expected, highest flow rates are observed with larger orifice sizes. No relevant variations in the discharge profiles are observed testifying again the absence of phase changes inside the vessel.

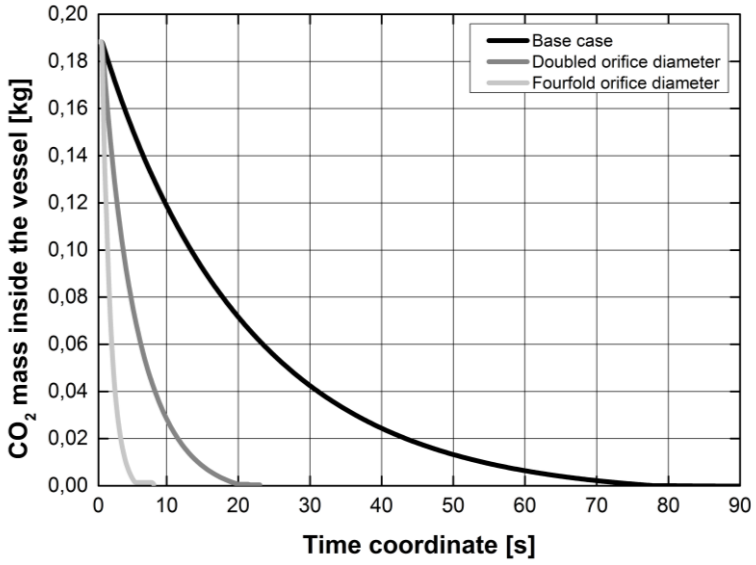

Figure 6.14. *Time evolution of the vessel CO_2 mass. Incidence of different orifice sizes.*

Moving to higher charging pressures, the situation is extremely different and sensitive to initial charging conditions that may lead also to initial dense states. Starting from an initial temperature of 20 °C, 45, 55 and 60 barg charging pressures are investigated. The thermal dynamic and the bulk dense CO_2 fraction are reported in Figure 6.15 with reference to the base case.

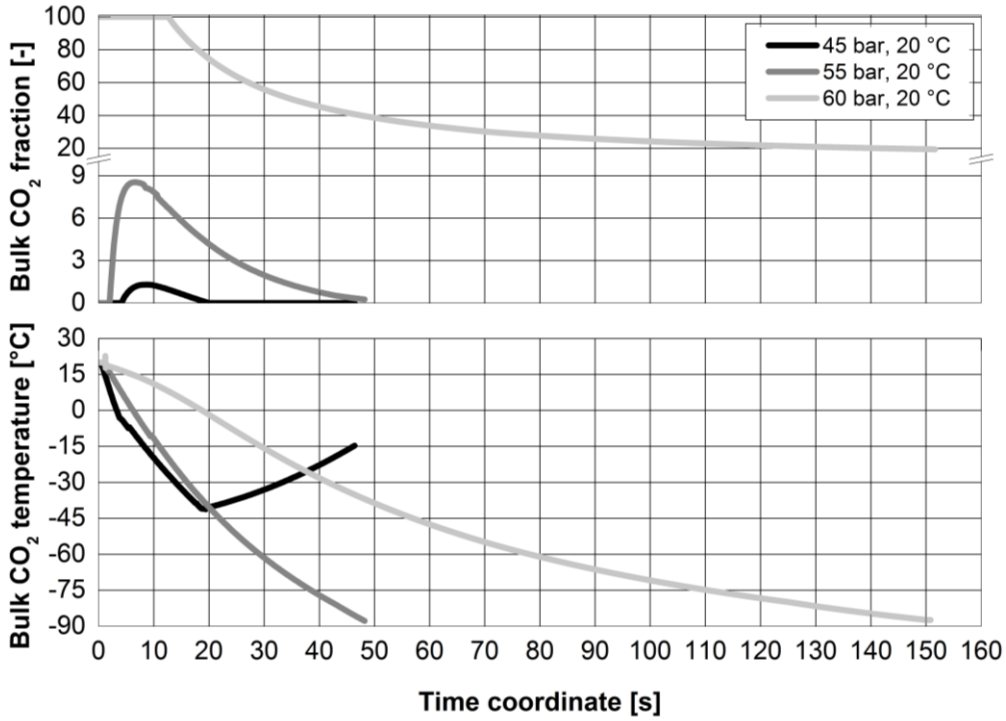

Figure 6.15. P*ercentage vessel dense CO_2 fraction and temperature evolution under different charging conditions.*

A first comparison shows that the temperature dynamics is sensitive to the initial charging pressure as already demonstrated with reached minimum temperatures ranging down to -88 °C. Both the 55 and 60 barg releases show a tendency to approximately reach this degree of cooling without any heating effect that is instead observed for a 45 barg release because of the intervention of the warmer vessel walls. The forecasted temperature profiles alteration with respect to Figure 6.12 is due to the dense phase appearance in the vessel bulk that is taking place as demonstrated in fig. 4.15. The trial at the lowest charging pressure gives rise to a mixture composed by 1.8-2 % of liquid CO_2 without any solid trace because of the unfavorable thermodynamic conditions under the triple point pressure (that is reached after 24.2 s). Instead both for the 55 and 60 barg, the solid phase is expected. Therefore, in their final stages, what is characterizing the vessel bulk is a mixture of solid and vapor CO_2 whose sublimation heat is responsible for the further temperature decrease observed in Figure 6.15. It should be noted that some authors have experimentally observed this behavior ([16,17]).

As it can be highlighted, the 60 barg release is involving a liquid initial charge that is subjected to a decreasing liquid content that tends to a stabilization on a mixture composed of a 20 % of dense phase. It can be proved, in fact, that these final stages are characterized by a pathway evolution substantially matching a transformation characterized by a constancy in the mixture quality. Neither the instantaneous specific enthalpy nor the entropy are conserved: the recorded χ value is almost equal to 0.44.

Larger orifices lead to substantial variations in all the investigated parameters. In detail, considering the 55 barg release and moving to larger orifices, the minimum reached temperature is almost the same and below the atmospheric equilibrium value. It should be highlighted that both releases depicted in Figure 6.15 are concerning the appearance of dense phase both in the bulk and at the orifice. The trial characterized by a doubled orifice involves mixtures with a dense content up to 9.5 % (on a mass basis) that goes up to 12 % with a larger configuration as reported in Figure 6.16.

The same picture is giving reason to the fact that, for the intermediate orifice size, the dense phase is observed at this location relatively late, about 5 s after the dense phase appearance in the vessel bulk (red dotted line). This trend finds its reason in the fact that all the dense phase formed in the vessel bulk is exhausted by sublimating phenomena in its way to the discharge plane. The occurrence of sublimation mechanisms is justified since the establishment of the characteristic transition conditions from VLE to SVE domain is actually taking place as indicated in Figure 6.17.

Also in the case of the larger orifice, this state occurs but during the unloading of the CO_2 mixture. The result is an instantaneous variation (decrease) in the dense CO_2 mass fraction

both in the bulk and at the orifice, that is driven by its thermodynamic behavior across the triple point.

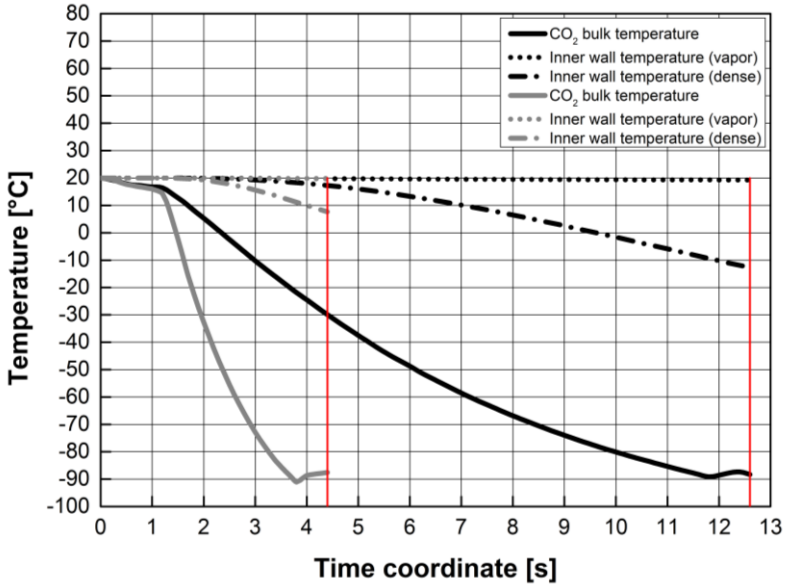

Figure 6.16. *Characteristic temperature evolution. 55 bar, 20 °C release. Doubled (black) and fourfold (grey) orifice size.*

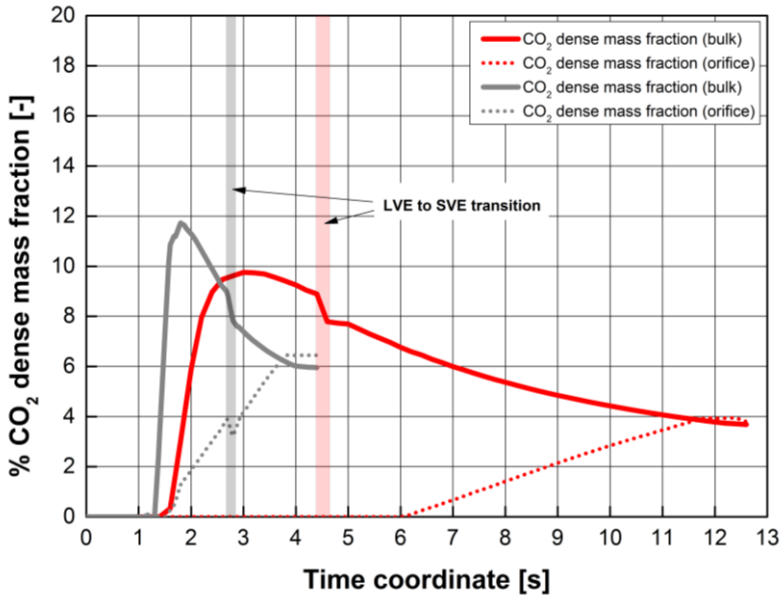

Figure 6.17. *Mass fraction time trends in the vessel bulk and at the orifice plane. 55 barg, 20 °C release. Orifice size: doubled (red profiles), fourfold (grey profiles).*

Some experimental works ([16,17,18]) involving dense phase discharges from pressurized vessels have shown some characteristic variables profiles during the blowdown mechanism.

Some discrepancies arise in what concerning the bulk vessel pressure trends especially when the system is experiencing multiphase discharges. While some authors have observed a

certain degree of pressure stabilization in the time domain ([16]), others have still recorded decreasing trends with no discernible *plateaux* ([18]).

Within the trials ran so far, present work is matching the latter with only some changes in the local slope not to be treated as a stabilization. This arise from the fact that boiling / sublimating mechanisms, that involve the formation of the light phase, are not enough to sustain the pressure decrease induced by the discharge phenomenon. It should be highlighted that these aspects are related also to the relative amount of light phase produced as well as the rapidity involving the phase change mechanisms. The latter being sensitive to the nucleate boiling mechanisms that are supposed to take place because the vessel internal surface is always hotter than the saturated temperature of the fluid.

Differences arise when the charging pressure is moved up to 60 barg therefore involving a liquid initial charge at 20 °C. Figure 6.18 gives some details concerning the pressure evolution inside the vessel and the instantaneous mixture density ratio based on the initial value following a release across a fourfold orifice size with respect to the base case (Figure 6.19).

Dealing with the dynamic pressure profiles, it should be noted that a release starting from a saturated CO_2 liquid is characterized by different phases, not observed in the previously analyzed situations concerning gaseous charges.

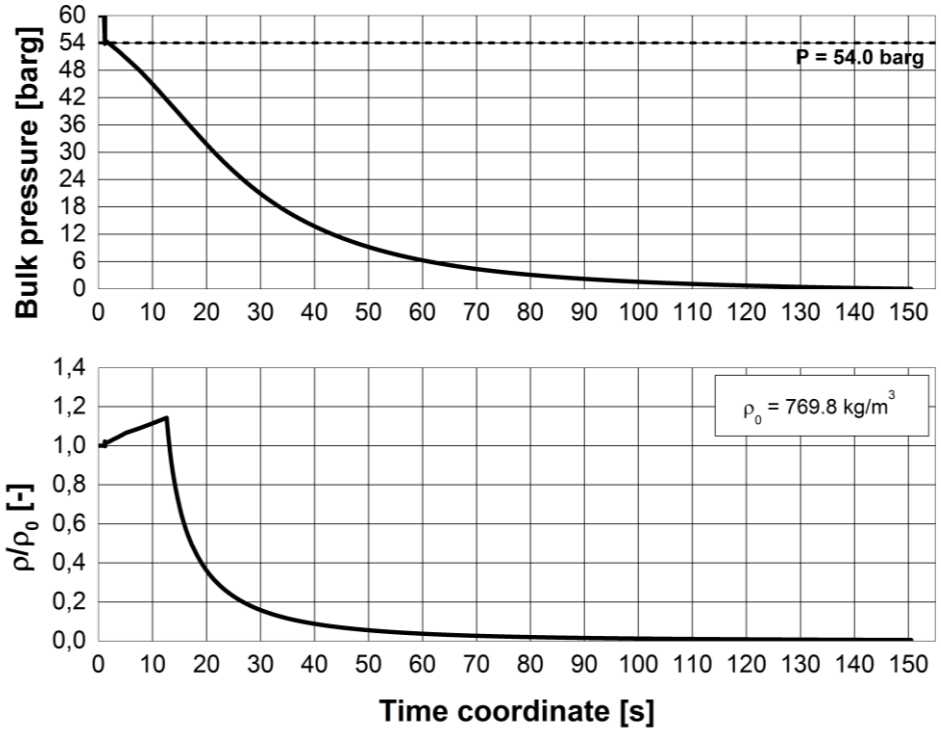

Figure 6.18. *Time profiles of the vessel bulk pressure and of the ratio between the instantaneous mixture density and that pertaining to the initial state. 60 barg, 20 °C expansion. Base case.*

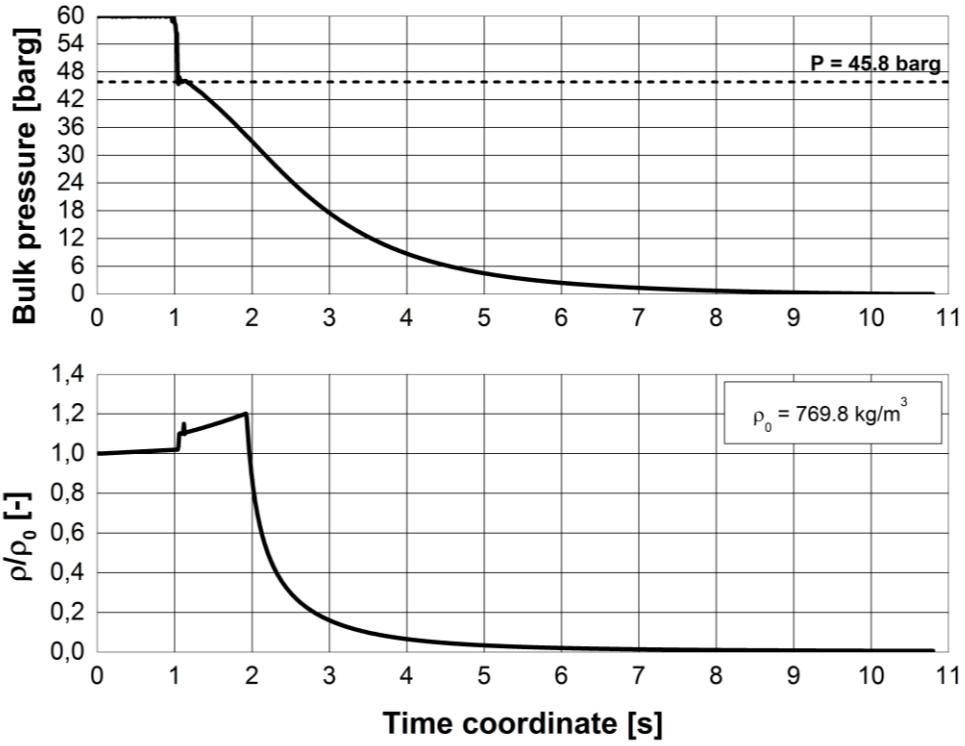

Figure 6.19. *Time profiles of the vessel bulk pressure and of the ratio between the instantaneous mixture density and that pertaining to the initial state. 60 barg, 20 °C expansion. Fourfold orifice size.*

The trend, more clearly detachable in Figure 6.19, develops in four distinct steps:

a. a first stationary period in which the pressure is maintaining its initial value. Even the bulk density is keeping almost unaltered because initial thermal gradients are not so relevant to induce variations in this property. The CO_2 is in its incompressible liquid state;
b. a sudden drop in the pressure is then observed down to a value depending on the orifice size: 54.0 barg for the base case and 45.8 with a fourfold orifice size. A simultaneous density increase is recorded because of the consequent temperature drop;
c. the pressure drop is followed by a monotone pressure decreasing during which the instantaneous bulk mixture density is changing because of the appearance of the vapor phase leading to a multiphase domain. While the dense content is predominant, the pressure evolution is almost linear but, with a growing vapor quantity, compressibility effects arise altering this behavior. A trend similar to that involving a gaseous release is observed. Recorded variations in the pressure trends are observed when the dense content is lowered under the 60 % by mass. At the same time, the density profile is subjected to a relevant decreasing trend following both the pressure and the temperature rapid decline;

d. the CO_2, in its way to the atmospheric conditions, experiences a short time period of stabilization around the triple point pressure that is taking place whenever it is passing down to the SVE region. With respect to the investigated cases, it lasts respectively for 1.6 and 1.4 s after 72.1 and 5.2 s from the release start;

Listed steps have been observed in all the simulation trials performed under an initial dense CO_2 state. Some differences are observed depending on the charging pressure and temperature even if main features are preserved. Experimental trials recently performed by some research groups (see for example: CO_2PipeHaz2009 ([19]), CO_2Pipetrans2013 ([20])) pointed out these blowdown steps. A deeper investigation of the CO_2 thermodynamic states evolution gives results depicted in Figure 6.20-6.21.

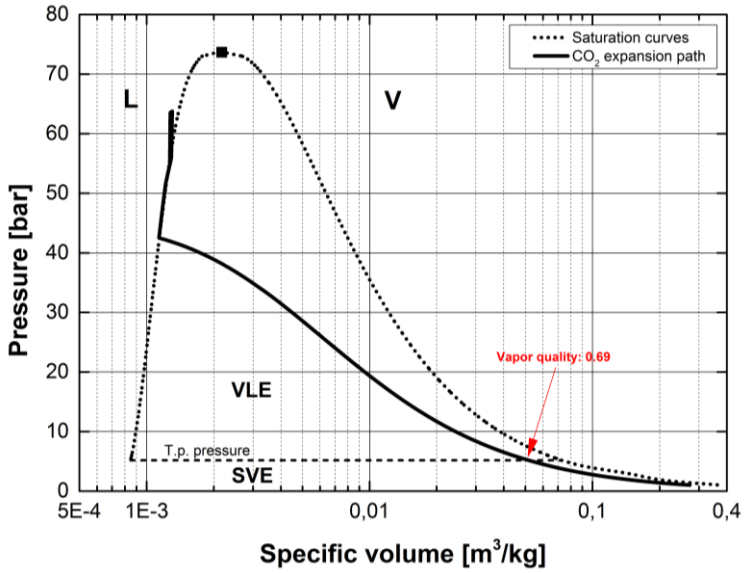

Figure 6.20. *Specific volume-pressure diagram. 60barg, 20 °C expansion. Base case.*

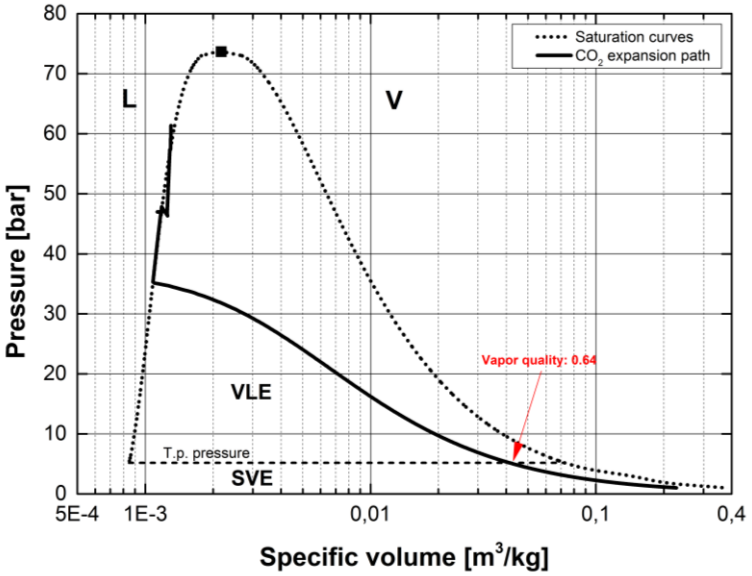

Figure 6.21. *Specific volume-pressure diagram. 60barg, 20 °C expansion. Fourfold orifice size.*

The predicted (v, P) trends are similar in both investigated cases. Being the initial state the same, the CO_2 as already stated is driven to the saturation boundary. However, while the expansion is occurring, the system departs from the phase boundary and depending on the orifice size it gets to the triple point state with a variable vapor content as indicated in Figure 6.20-6.21. The release resulting from the smaller orifice is characterized by a shorter persistence at the saturation conditions and the vapor quality at the triple point pressure is equal to 0.69 (by mass). The pathway in the solid-vapor domain then leads the system to a final vapor content of 0.81 indicating that the final state of the release is characterized by a mixture of dry ice and vapor CO_2.

The increase in the orifice size, i.e. an amplification of the thermal and mechanical dynamics, establishes the conditions for a major liquid content throughout the whole release with a final vapor fraction counted in 0.67. A theoretical fully reversible transformation from the investigated initial state would lead to a final solid-vapor mixture made of 58 % (by mass) of vapor. On the same basis, instead, a development assuming a complete irreversible pathway would have determined a final vapor quality of 0.72.

It has been observed that, depending on the release features, following general remarks hold:

a) once established an initial state, the orifice size is act modifying both the expansion development and the final CO_2 conditions. If the CO_2 charge is liquid, any increase in the orifice size, i.e. an acceleration in the blowdown dynamics, determines a higher instantaneous dense phase content that results in a final solid-rich mixture. The sensitivity of this parameter on the initial charging conditions and the orifice size is reported in Figure 6.22-6.23.

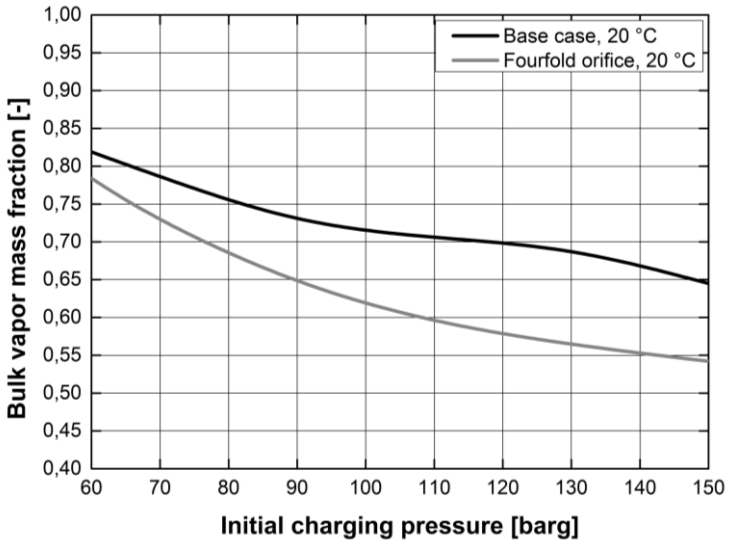

Figure 6.22. *Final expected vapor CO_2 mass fraction in the vessel depending on the initial pressure and the orifice size. Initial temperature: 20°C.*

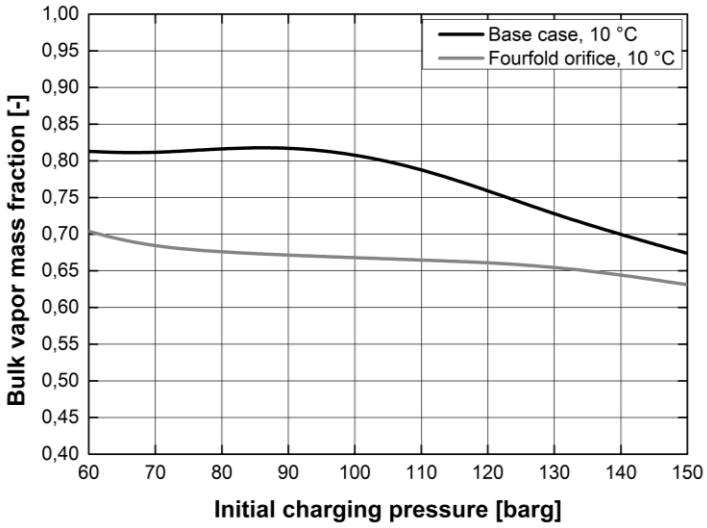

Figure 6.23. *Final expected vapor CO_2 mass fraction in the vessel depending on the initial pressure and the orifice size. Initial temperature: 10°C.*

It is clear how an increase in the charging pressure leads to a major dense final content in the vessel bulk. The pressure domain investigated implies a solid-vapor mixture appearance and, in general, charges up to 150 barg subjected to a release across a fourfold orifice size, experience an increase in the solid content. For a 150 barg, 20 °C expansion, this may amount up to the 46 % by mass against the expected 22 % in the case of 60 barg. Under the charging pressure range (1-150 barg), the base case never results in vapor content lower than 65 % by mass thus requiring a multiphase approach.

It should be noted, instead, that the initial charging temperature is not playing a clearly defined role (Figure 6.22-6.23). Under the base case conditions. The trial concerning an initial temperature of 10 °C leads to a major vapor content with respect to higher charging temperatures when the base case is run. This is not observed enlarging the orifice against which a decrease in the initial temperature results in significant increases in the solid content.

These apparently conflicting trends follow from both the release duration and the nature of the heat transfer mechanisms. It is in fact clear that smaller orifices take the release longer allowing the CO_2 to be subjected to more relevant heat exchanges with the solid walls. This is not happening with larger orifices since the extremely rapid depressurization time scale is limiting these phenomena, tending to adiabatic conditions with the heat reservoir consisting in the CO_2 internal energy. The latter depending also on the initial temperature. On the contrary, smaller orifices are less

sensitive to this parameter and the heat exchanges act leveling the expansion final states;

b) only a part of the depressurization is actually taking place along the liquid saturation border allowing the system to deviate from it once a threshold pressure value is achieved. The degree of development along the saturation line and its duration are sensitive to the initial conditions and the orifice size. Simulations show that larger dependencies are observed in the base case. While the charging pressure is increased, the path along the saturation line is wider (Figure 6.24) and the same effect is induced by the initial temperature. Once the orifice is enlarged, almost saturation conditions are observed at least down to a pressure ratio $P/P_0 = 0.43$ and the charging pressure plays the same role. Once reached these threshold values, pressure profiles generally lose their approximated linearity.

This aspect is relevant when describing the dynamic inside the vessel since it demonstrates that the hypothesis of saturated conditions will not persist during the whole release. The establishment of conditions reported in Figure 6.24-6.25 arises after a time period that ranges within few units of seconds for larger orifices to more than 25 s under the base case, especially at higher initial temperatures.

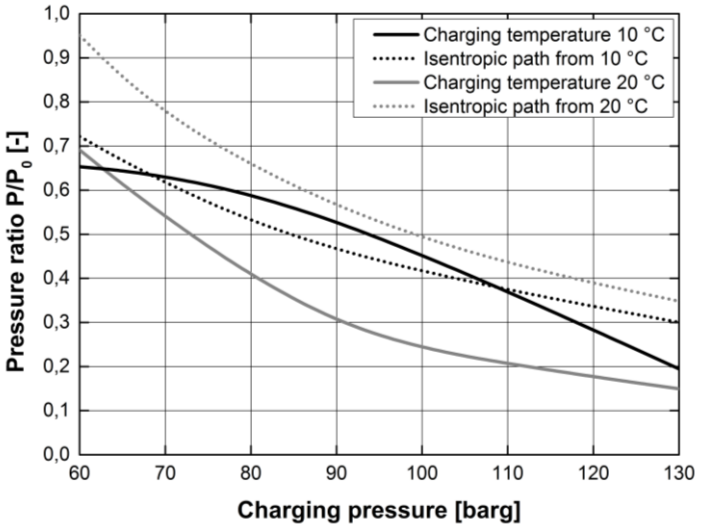

Figure 6.24. *Dimensionless pressure ratio matching the establishment of the saturated conditions. Dependence on the initial charging pressure and temperature. Base case.*

c) Investigated expansions up to 150 barg show a thermodynamic intermediate behavior between the ideal bounding transformations (fully reversible and non). Heat exchanges with solid walls, as previously observed, are mainly observed for longer releases, i.e. with smaller discharge orifices once established the initial charging volume. The

reversibility parameter χ depends on it and increases with larger orifices. Values greater than 0.79 are never observed. With respect to the base cases, a doubled orifice size determines a χ increase that amounts on average up to 14-19 % for pressures up to 80 barg. Above this threshold, the orifice variation is responsible for more restricted alterations, not greater than 10 %.

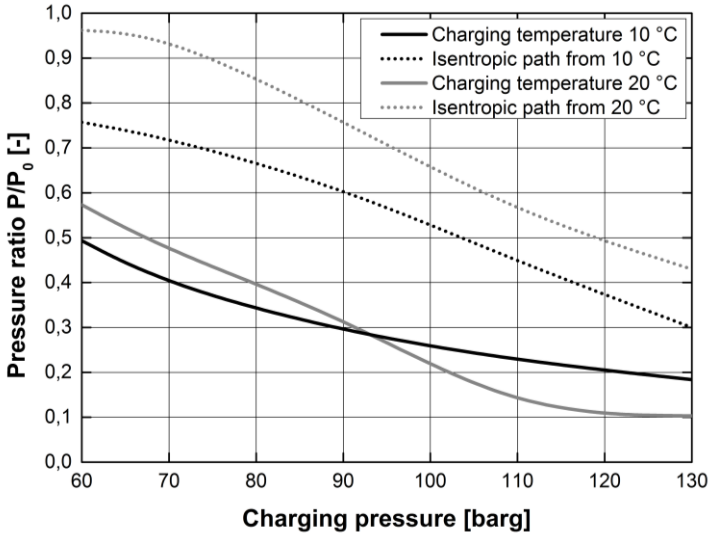

Figure 6.25. *Dimensionless pressure ratio matching the establishment of the saturated conditions. Dependence on the initial charging pressure and temperature. Fourfold orifice size.*

6.3 Simulation of real scale operations

The proposed model has been tested against a real scale domain. The characteristic length scales of CCS and EOR infrastructures are in the region of tens and hundreds of kilometers ([1,9]). This amount is driven by the path from the location source to the storage site or the oil well. In addition, for QRA purposes, also the localization of shut-off valves is a key aspect since they have the function of isolating pipeline sections thus having an impact on the domain size ([1,21]).

6.3.1 CCS and EOR operative conditions

Carbon sequestration established projects are more than 80 worldwide and detailed public information is available for more than 28 as listed in detail in Chapter 1. Table 6.3 gives the indications of the main properties of CO_2-handling infrastructures ([22]).

The longest pipelines are in the Northern America and it should be noted that their average length is longer than in Europe. In addition, bigger pipelines carry larger amounts of CO_2 to be economically viable.

A general QRA investigation usually considers two type of pipeline failure scenarios namely a puncture and a full bore rupture ([1]). Cumulative failure rates of these two types of ruptures are illustrated in Table 6.4 and are depending on the specific study and related statistics ([23]).

Table 6.3. *CO_2-handling infrastructures operative conditions and specs ([22]).*

Parameter	Characteristic range
Length [km]	1.9 – 808
External diameter [mm]	152 – 921
Wall thickness [mm]	5.2 – 27
Capacity designed [Mt/y]	0.06 – 28
Min pressure [bar]	3 – 151
Max pressure [bar]	21 – 200

Different studies employ distinct definitions of puncture rupture. Several of them are suggesting a characteristic hole size of 20 mm ([24,25]) but other investigations make a distinction between pinhole (5-7 mm), small (25 mm), medium (30 mm) and large (100 mm) puncture rupture ([26,27]). The same parameter may also be expressed in terms of puncture to internal pipe diameter ratio ζ. The present analysis deals with ζ values varying from 0.1 to 0.4.

Table 6.4. *CO_2 pipeline ruptures. Cumulative failure rates and distribution ([23]).*

Parameter	Variants		
Cumulative failure rates [incidents km^{-1} $year^{-1}$]	$6.1 \cdot 10^{-4}$	$0.7 \cdot 10^{-4}$	$1.55 \cdot 10^{-4}$
Distribution *rupture : puncture*	0.25 : 0.75	0.25 : 0.75	0.50 : 0.50

6.3.2 Limitation of a vessel blowdown approach in real scale domains

The release from a pressurized domain is, as extensively said, a fully transient phenomenon and the description of the inventory loss is the key point for any hazards quantitative assessment of the pipelines. Therefore, from this point of view, the development of robust and computationally efficient describing models is of primary concern in supporting QRA procedures. Its robustness and efficiency are measured on the capability to capture main

processes that are taking place with an acceptable computation burden. i.e. computational run time.

To face this modeling problems, approaches usually employed are two. The first relies on the more rigorous models while the other is a simplistic approach mainly based on the so called Vessel Blowdown Models (VBM). That formulated in the present work belong to the latter category.

Once a simplistic approach is selected, even if based on the conservation equations, it should be checked against both the experimental data as well as the prediction resulting from more sophisticated ways (*PDEs* based approaches and CFD simulations). This because hypothesis linked to the VBM may lead to erroneous results thus requiring an investigation on their applicability to real case discharges.

Concerning this topic, a good review is that presented by Maghereftheh H. and coauthors ([28]). This work investigates the specific conditions under which the outflow from a pipe can be modeled as a discharge from a vessel through a VBM approach. The comparison is made against a computationally extremely demanding pipeline rupture model (PipeTech) under varying pipe lengths, puncture/pipeline diameter ratios, line pressures and occurrence of two-phase flows.

Main results proposed in ([28]) are collected below:

- as stated by the authors, in the majority of cases, relatively good agreement between the two approaches is observed;
- this degree of agreement increases with a decrease in the diameter ratio and line pressure and growing pipe lengths. Some discrepancies are observed in the latter depressurization stages where the VBM tends to over predict the cumulative mass released;
- the VBM performs well in predicting outflows from a punctured line and in the case of multi-phase releases but is not suitable to describe full bore ruptures;
- an increase in the domain length, with respect to both the puncture and the internal pipe diameter improves the degree of agreement;
- higher charging pressures act deteriorating the VBM performance.

Therefore, the departure of the VBM approach from the predictions of more rigorous models is linked to some parameters that should be taken into account. First among all the geometrical properties of the modeled domain are essential in determining the results.

Another key aspect is related to the model applicability under pumped flow conditions. It is clear that when a release occurs, modern automatic protection systems lead to a pipeline sectioning because of the intervention of the block-valves. The present work deals with the

occurrence of this situation in the sense that only the inventory enclosed by the sectioning valves is subjected to the discharge. It should be underlined that this scenario is the most likely and common when dealing with pipelines depressurizations ([1,9,27,28]).

6.3.3 Model extension results

This section throws light on results obtained from the model application under different operative and geometric conditions. The modeled cases are based on CCS and EOR operative conditions reported in section 5.8.1.

6.3.3.1 Influence of the pipeline length and the ζ parameter

First investigated parameters are those concerning the geometric properties of both the pipeline and the discharge orifice.

These are respectively defined as follows:

a. pipeline length that is varied from 100 to 10000 m;
b. pipeline internal diameter in the range 141.6-867 mm (Table 6.3);
c. pipeline minimum thickness selected according the operative conditions (pressure) and the internal diameter;
d. the ζ parameter, that is the ratio between the orifice and the internal pipe diameter is assumed to be equal to 0.1, 0.2, 0.3 and 0.4 and the orifice diameter is accordingly derived.

Each simulation will imply the selection of specific operative conditions expressed in terms of initial CO_2 pressure and temperature. The CO_2 temperature is conserved at 20 °C as well as the environmental one while investigated operative pressures are equal to 10, 70 and 150 bar.

Figure 6.26-6.27 show respectively the predicted CO_2 bulk and exit temperature and the pressure dynamic with reference to a 100 m long pipeline with an internal diameter of 141.6 mm.

The CO_2 contained in the shortest investigated pipeline domain, subjected to different orifice sizes shows a behavior extremely sensitive to this parameter. VBM predictions show that the total inventory is subjected to a decrease in the temperature whose rapidity and magnitude is depending on the parameter ζ. Greater values of ζ, at the prevailing tested conditions, imply lower bulk CO_2 temperatures because of the incremented mechanical effect related to the depressurization. Starting from 20 °C and increasing ζ, minimum recorded temperatures are respectively equal to 14.2, 4.1, -6.1 and -16.9 °C therefore none of the investigated cases may be intended to be isothermal as it is often assumed in QRA studies concerning “long” pipelines.

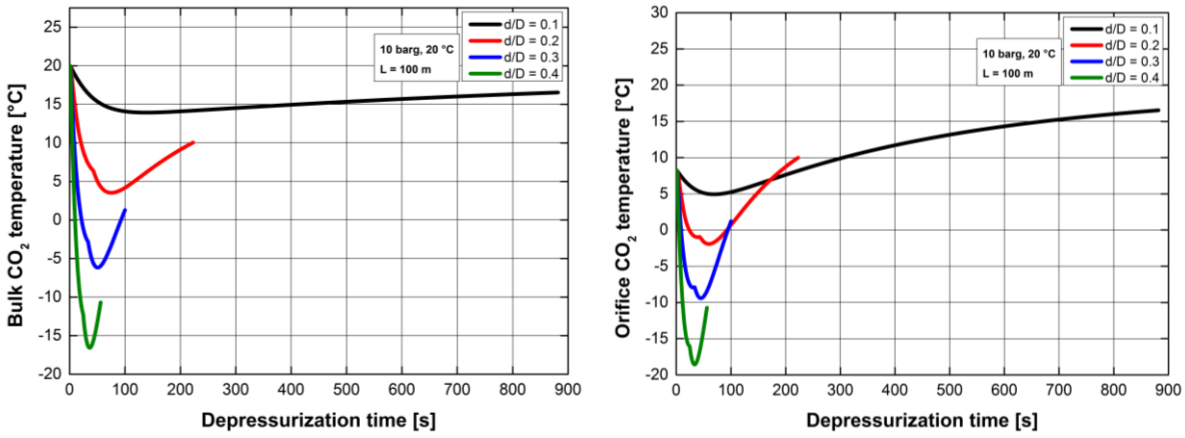

(a) *(b)*

Figure 6.26. *Variation of the CO_2 temperature dynamic following different puncture ruptures. a- internal vessel bulk temperature; b- orifice plane temperature. Internal diameter: 141.6 mm.*

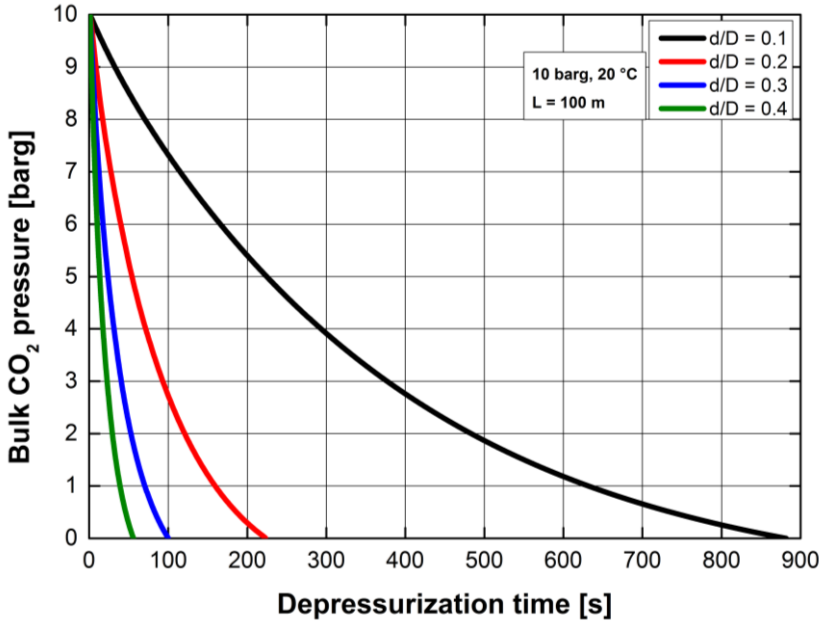

Figure 6.27. *Vessel pressure evolution under different puncture ruptures. Internal diameter: 141.6 mm.*

A similar behavior is observed at the orifice plane at which lower temperatures are recorded because of the expansion transformation.

All performed trials show that the gaseous inventory preserves its initial state and no phase change occurrences are observed also with respect to transient pressure profiles (Figure 6.27). It should be noted however that, given the compressibility properties of the gaseous substance, each release induces large density variations. Different dimensionless density profiles are comparable even under different orifice sizes.

An increase in the pipeline length give the results of Figure 6.28 in the case of 1000 and 10000 m.

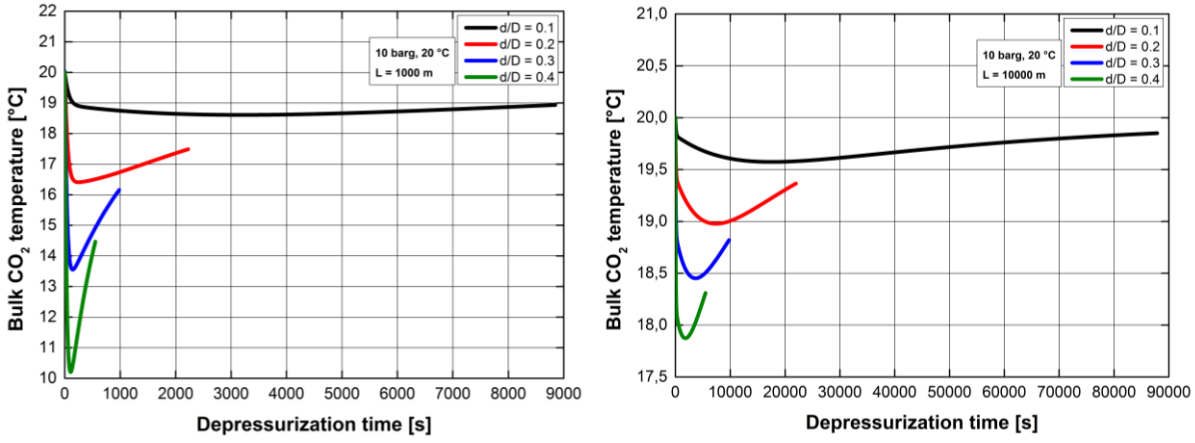

(a) *(b)*

Figure 6.28. *Variation of the CO_2 temperature dynamic following different puncture ruptures. a- 1000 m; b- 10000 m. Internal diameter: 141.6 mm.*

It is interesting to know that, once fixed the initial operative conditions, the increased CO_2 inventory relevantly modifies the internal thermal dynamic. Modifications in the internal bulk CO_2 temperature allow to state that longer pipelines depressurization tends to isothermal conditions.

For example, in the case of 10 km-long pipeline, the internal temperature undergoes a variation limited to 2 °C even with the largest investigated orifice size. This condition, however, falls when the domain length is restricted to 1 km.

In this case the discharge dynamic still shows a significant influence with bulk temperature drops up to 10 °C with larger orifices.

Performed simulations show that the isothermal bulk hypothesis may reasonably apply under the following conditions:

- pipeline length to internal diameter L/d ratio over 60000 while the charging conditions allow for a persistent gaseous phase;
- puncture to internal pipeline diameter ratio up to 0.2 but only for $L/d > 40000$.

Therefore, when allowed, the error committed by implementing the constant temperature depressurization hypothesis produces average errors less than 5 % in what concerning the cumulative mass released.

The latter being a key parameter in determining the predictive model capability ([28]).

Respective cumulative mass profiles are reported in Figure 6.29-6.30.

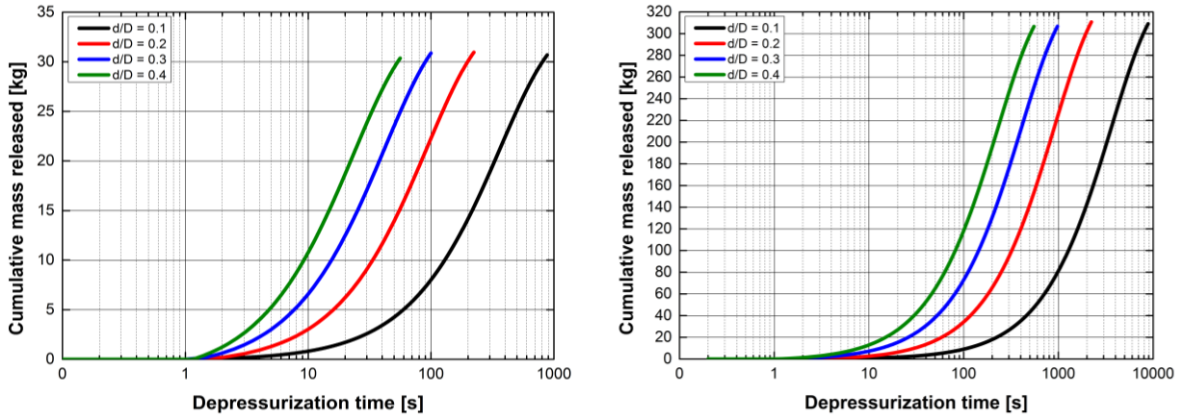

Figure 6.29. *Comparison of time trends (log-scaled) of the cumulative released mass under different conditions. 10 barg, 20 °C expansion. Internal diameter: 141.6 mm. Pipeline lengths: a- 100 m; b- 1000 m.*

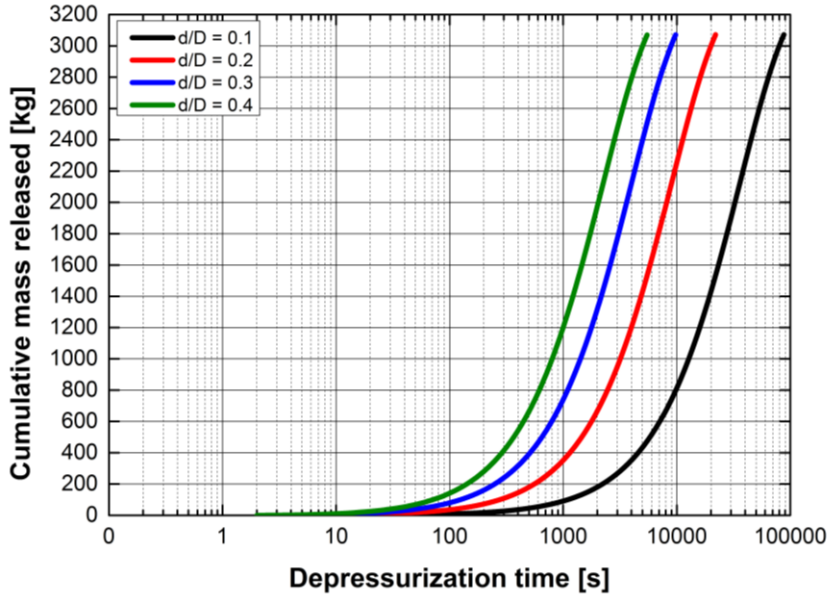

Figure 6.30. *Comparison of time trends (log-scaled) of the cumulative released mass under different conditions. 10 barg, 20 °C expansion. Internal diameter: 141.6 mm. Pipeline length: 10000 m.*

As indicated in Figure 6.29-6.30 the different puncture/pipeline diameter ratios are responsible for the alterations on the inventory released as well as on the total discharge time. Considered the persistent gaseous phase predicted by the model, the qualitative correspondence with data reported in ([28]) should be noted, confirming the method capability. Quantitative values are not matched because data of ([28]) are applied to a release of methane.

In addition, the investigation of the total discharge time with respect to the diameter ratios shows that, once fixed the domain volume and the initial conditions, it decreases with d/D to a power approximately equal to 2. Therefore, the model performance is again confirmed being this behavior expected with gaseous substances.

Further investigations show that an increase in the pipeline internal diameter has the tendency to flatten thermal dynamics because of the increased CO_2 inventory.

Results concerning the maximum internal adopted diameter are reporting in Figure 6.31.

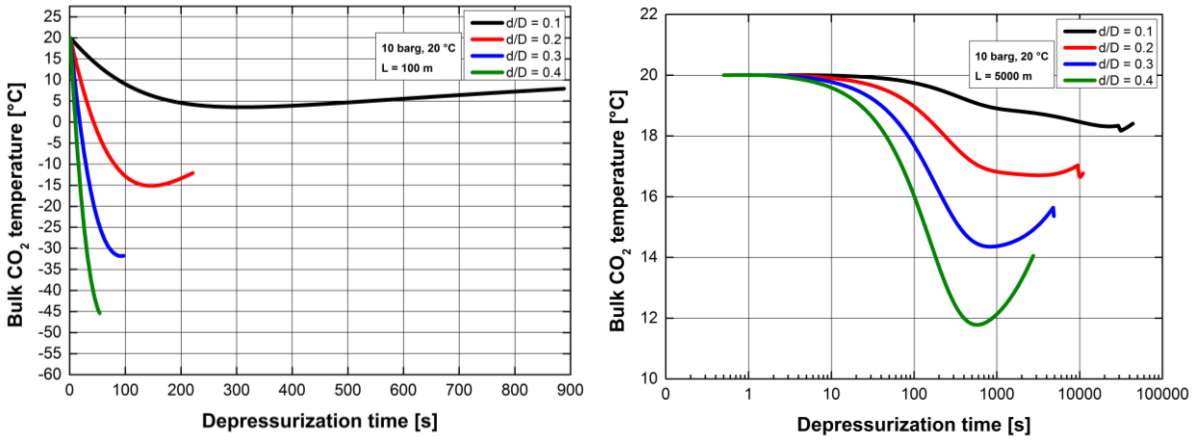

Figure 6.31. *CO_2 bulk temperature dynamic following different puncture ruptures. Internal diameter: 867 mm. Pipeline lengths: a- 100 m; b- 5000 m.*

When the internal diameter is increased, shorter pipeline sections experience wider temperature drops. For example, the exposure of a 100 m long pipeline to an orifice with $d/D = 0.4$ leads to a continuous decline in the bulk temperature that is not observed with smaller opening. In this case, the unloading effectiveness does not allow for the heating effect induced by the solid walls.

The analysis reveals that the walls effect is negligible under the following conditions:

- operative pressures below 45 barg linked to a persistent gaseous phase;
- puncture to internal diameter ratio $d/D > 0.32$;
- pipeline length $L < 1500$ m and internal diameter $D > 450$ mm.

It should be noted that these conditions are subjected to restrictions and stands for necessary conditions not mutually excludable. In this sense, once the investigated pipeline section is satisfying all these features, the influence of the solid walls can be neglected. The error committed taking this assumption is reduced for the systems characterized by higher operative pressures together with larger internal diameter and orifice sizes.

This regular behavior no longer holds whenever the operative pressure is increased over 45 barg. The threshold value is related to a liquid charge that undergoes boiling/sublimation mechanisms once expanded. In this case, all main release descriptive parameters (bulk temperature and pressure, instantaneous bulk dense fraction) are extremely sensitive to the domain and the orifice size. Dimensionless bulk pressure and temperature trends of a pressurized release from 60 barg are reported in Figure 6.32-6.33.

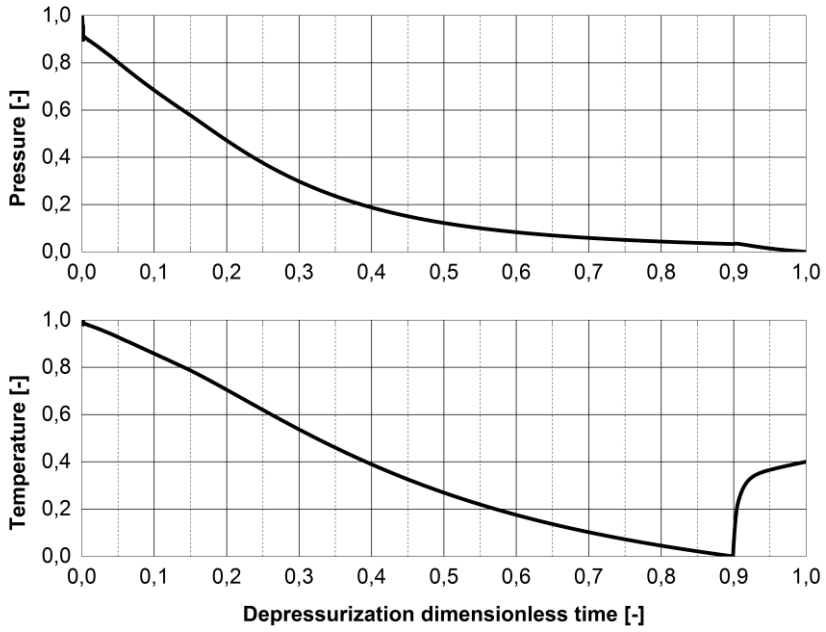

Figure 6.32. *Dimensionless vessel CO_2 pressure and temperature. Pipeline specs: L = 100 m, D = 141.6 mm, d/D = 0.1. 60 barg, 20 °C expansion.*

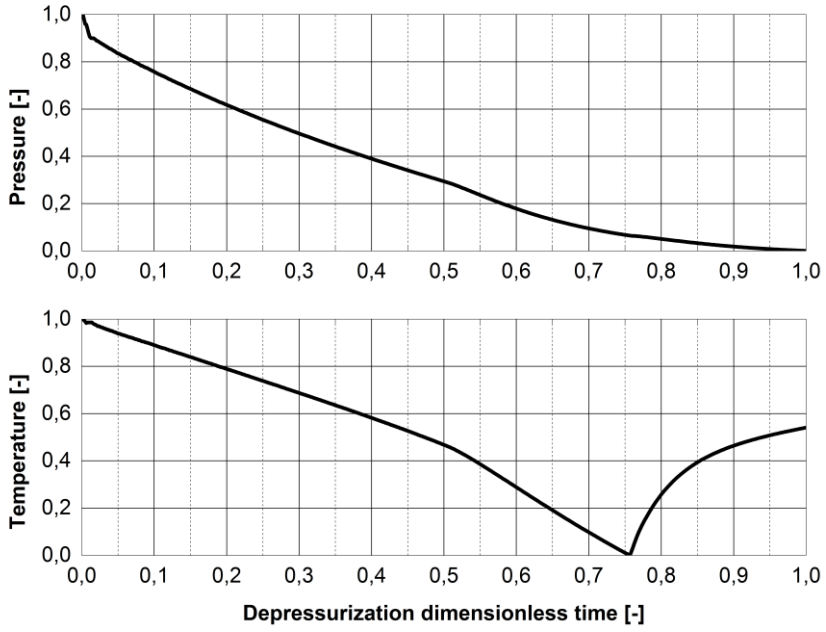

Figure 6.33. *Dimensionless vessel CO_2 pressure and temperature. Pipeline specs: L = 100 m, D = 867 mm, d/D = 0.1. 60 barg, 20 °C expansion.*

Starting from a variation in the internal diameter, once fixed both the pipeline length and the d/D ratio, it may be noted that dynamic trends exhibit some differences.

The cooling phase induced by the depressurization is more limited with an increase in the internal pipeline diameter. Variations arise because in the presence of smaller internal diameters (Figure 6.32) it has been observed that the saturated dense phase longer persists. In

the case of the minimum investigated internal diameter, the dense phase is recorded up to $t^* \cong 0.52$ against $t^* \cong 0.14$ with the largest one and these dimensionless times are corresponding to the single dense phase existence domain. Trials with different charging pressures show that an increase in the pipeline diameter slows the boiling mechanisms once $d/D = 0.1$ and $L < 1500$ m.

If d/D is increased up to 0.4, while the pipeline length unchanged, dynamics are different and results are reported in Figure 6.34-6.35.

The first discrepancy is related to the absence of a late heating process that is instead observed in Figure 6.32-6.33. The occurrence of this temperature variation is due to the total dense phase depletion induced by the boiling/sublimation mechanisms. The reduced heat capacity of the remaining gas linked to the large inventory amount already discharged and the disappearance of latent effects are the main causes of the rapid heating observed mechanism.

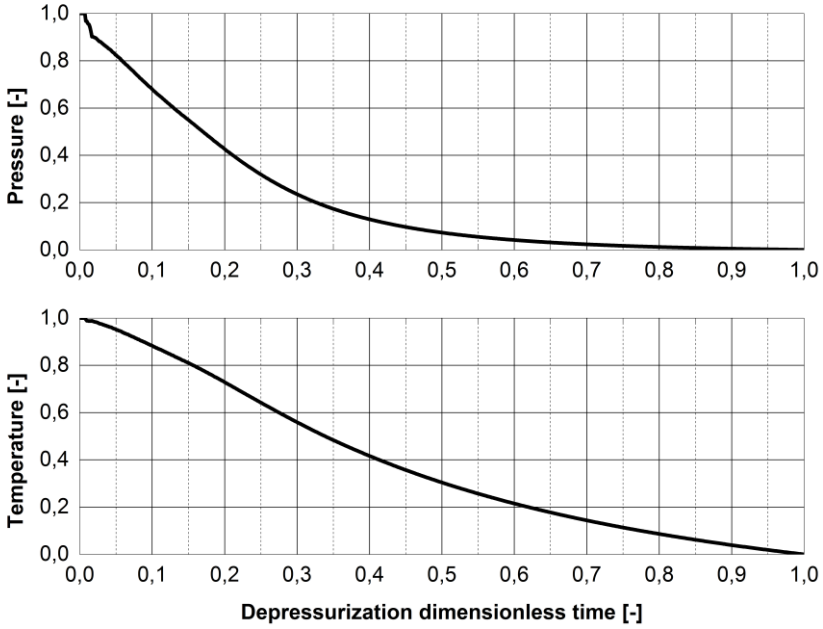

Figure 6.34. *Dimensionless vessel CO_2 pressure and temperature. Pipeline specs: L = 100 m, D = 141.6 mm, d/D = 0.4. 60 barg, 20 °C expansion.*

Both expansions modeled in Figure 6.34-6.35 are characterized by a final bulk state involving a multi-phase mixture respectively made of 35 and 36.8 % dense content (by mass). Given the final bulk conditions, the dense content should be intended representative of solid CO_2. The respective solid contents forecasted at the orifice plane are equal to 28 and 29.5 % (by mass). On the contrary, no solid phase occurrence is observed under the conditions of Figure 6.32-6.33.

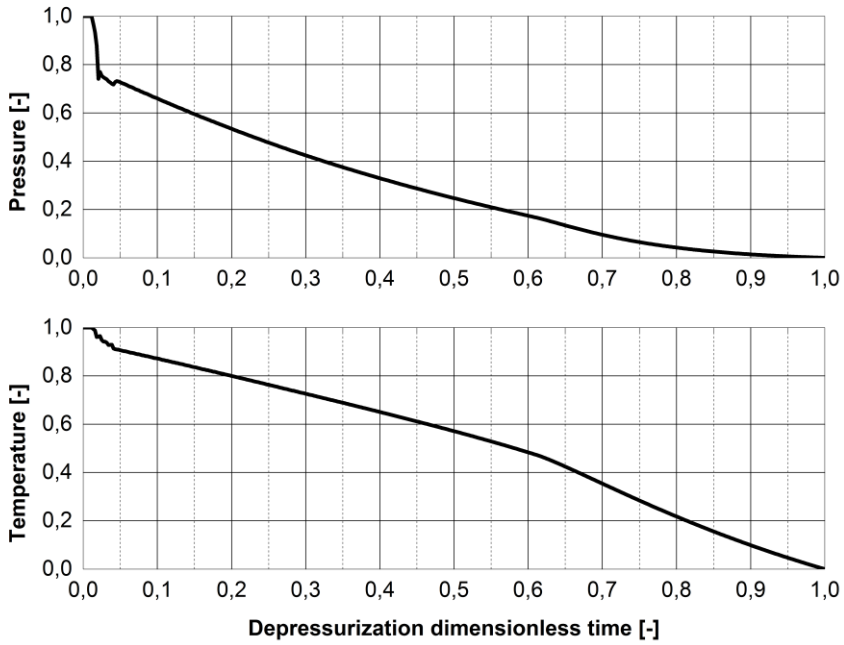

Figure 6.35. *Dimensionless vessel CO_2 pressure and temperature. Pipeline specs: L = 100 m, D = 867 mm, d/D = 0.4. 60 barg, 20 °C expansion.*

Results give reason to state that lower d/D values do not allow the establishment of favorable conditions for the appearance of the solid phase and this has been observed for higher charging pressures (60-150 barg). In fact, the increase in this parameter shows remarkable effects on the aspects that are discussed below.

First of all, it has been observed that under charging pressures from 50 to 150 barg, solid-vapor mixtures are observed only for d/D > 0.28-0.4 depending on this initial parameter. In the case of small ruptures (i.e. $d/D = 0.1$), the formation of solid CO_2 never takes place.

In addition, one of the main consequence of the d/D increase is represented by larger variations in the temperature magnitude and by a decrease in the initial single-phase existence time domain. Results show that the latter is mainly driven by the thermodynamic pathway followed to reach the saturation conditions. Large ruptures imply the occurrence of releases mostly characterized by a development in the VLE or SVE domains while dynamics related to small orifices leave time to the complete boiling of the multi-phase CO_2 mixture. Higher degrees of reversibility are observed with increasing d/D values with highest forecasted levels amounting to 0.79-0.87. In the $d/D = 0.1$ case, longer release times and larger pressure drops decrease this parameter down to 0.64-0.69.

At the same time, a variation in the internal diameter leads to different conclusions. This parameter is related to the total inventory to be discharged but at the same time it drives the investigated orifice size through the d/D ratio. Following Figure 6.36-6.37 give the pressure,

temperature and CO_2 dense fraction trends for a 100 m pipeline with an internal diameter of 141.6 and 867 mm.

It is clear how pipelines with the same lengths subjected to a rapid depressurization are affected by a variation in the internal diameter. The variation in the inventory volume results in a modification in the total release time that is longer for narrower tubes because of the small orifice surface, directly linked to the d/D ratio which, in turn, is depending on the second power of the diameter.

It is interesting to highlight how a variation in this parameter does not alter significantly the initial stages of the depressurization in terms both of the pressure and the temperature. This is observed especially with a low value of d/D (Figure 6.36) with results showing that this behavior holds to pressures up to 150 barg and $d/D < 0.25$. In this sense it may be stated that the expansion transformation to saturated conditions is not affected by the internal pipe diameter magnitude.

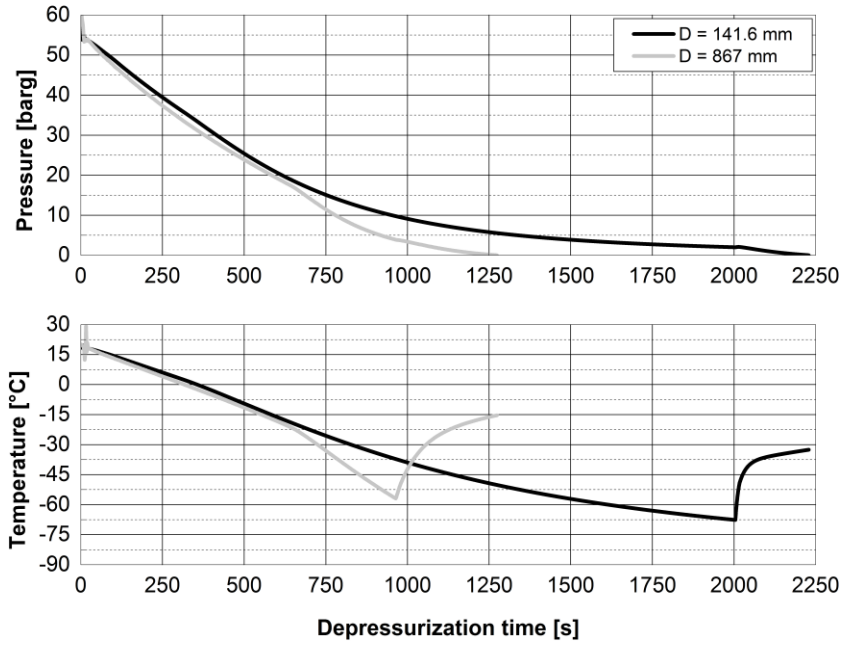

Figure 6.36. *Vessel CO_2 pressure and temperature trends under different internal pipeline diameters. Pipeline length 100 m; $d/D = 0.1$. 60 barg, 20 °C expansion.*

Differences arise when compressible CO_2 occurs both in the form of multi-phase mixture or single phase at the end of some releases. The occurrence of distinct phases then drives the system to different degrees of cooling with lowest temperatures observed under smaller d/D ratios according to a longer persistence of the liquid phase inside the domain.

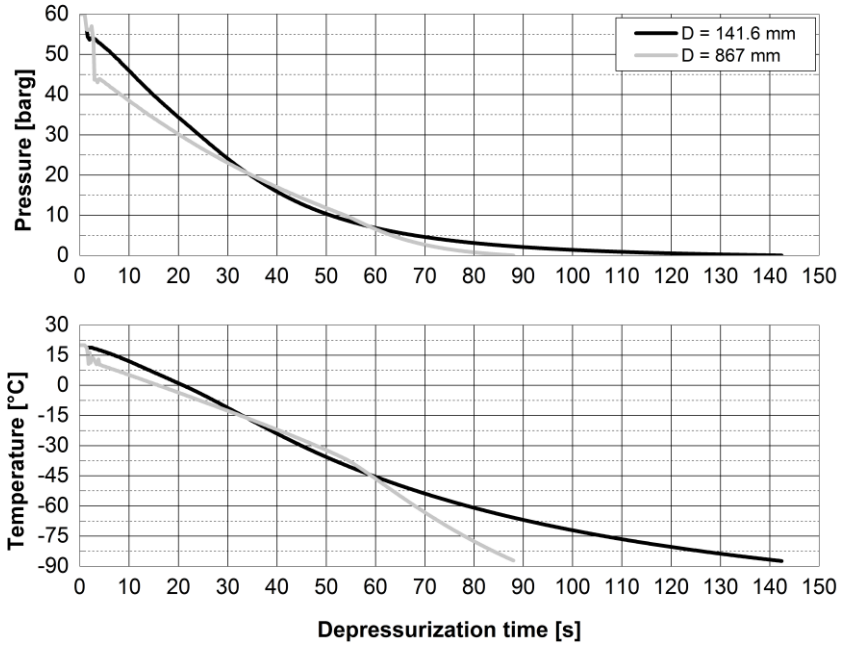

Figure 6.37. *Vessel CO_2 pressure and temperature trends under different internal pipeline diameters. Pipeline length 100 m; $d/D = 0.4$. 60 barg, 20 °C expansion.*

Once the d/D ratio is increased, pressure and temperature dynamics experience deviations also in the initial steps. It may be observed (Figure 6.37) that the blowdown rapidity induced by larger orifice diameters has the tendency to make the minimum reached temperatures comparable even under different internal diameters. These conclusions have been recorded for all the releases which do not allow for a complete boiling/sublimation of the dense CO_2. These are characterized by following conditions:

- charging pressures over 55 barg; a decrease in the operative temperature supports the occurrence of incomplete boiling/sublimation as well as lower external values. In the pressure range 55-150 barg the incomplete boiling/sublimation is virtually always observed for operative temperature below 10 °C;
- shorter pipeline sectors are favorable to the occurrence of this conditions but a key role is played by the d/D ratio that should always be larger than 0.25-0.30.

The geometrical parameter kept unchanged so far is the pipeline length that may be variable depending on situations under QRA analysis. Sectioning operations because of emergency and maintenance purposes are common in the pipeline handling. Being very variable the sectioning lengths, the present work is dealing with the following representative values: 100 m (already investigated), 5000 m and 10000 m.

The effects of the increased pipeline length are investigated in terms of total discharge time and thermal dynamics. Following results apply for pipeline charged at 10, 60 and 150 barg operated at 20 °C.

Results concerning the 10 barg expansions, applied to a pipeline with an internal diameter of 141.6 mm, are reported in Figure 6.38-6.39. Predictions indicate that the pressure evolution is not significantly altered by a variation in the pipeline length and no phase changes are expected even if the inventory amount is changed because of the variated pipeline length. Quantitatively, changes are expected since the total discharge time is extremely sensitive to the pipeline length. For example, results show that the time required to release all the inventory contained in a section pressurized at 10 barg is respectively equal to 15, 710 and 1500 min in the case of 100, 5000 and 10000 m pipeline lengths. When the d/D is increased up to 0.4, this parameter is abated down to 0.92, 45 and 90 min. The main effects of the variation in the pipeline length affect the thermal dynamic as already observed.

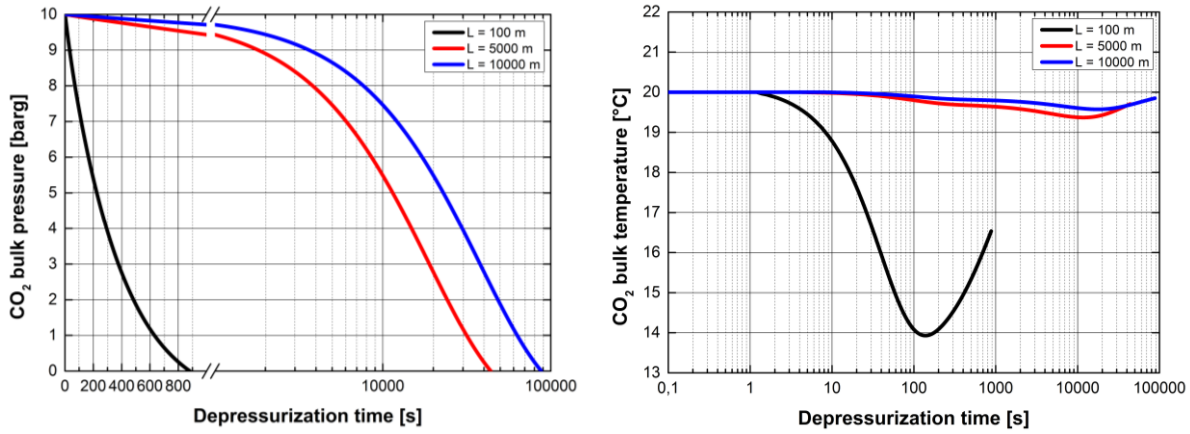

(a) *(b)*

Figure 6.38. *Vessel pressure time evolution under different pipeline lengths. Internal pipeline diameter: 141.6 mm.* $d/D = 0.1$. *a- bulk CO_2 pressure evolution; b- bulk CO_2 temperature evolution. 10 barg, 20 °C expansion.*

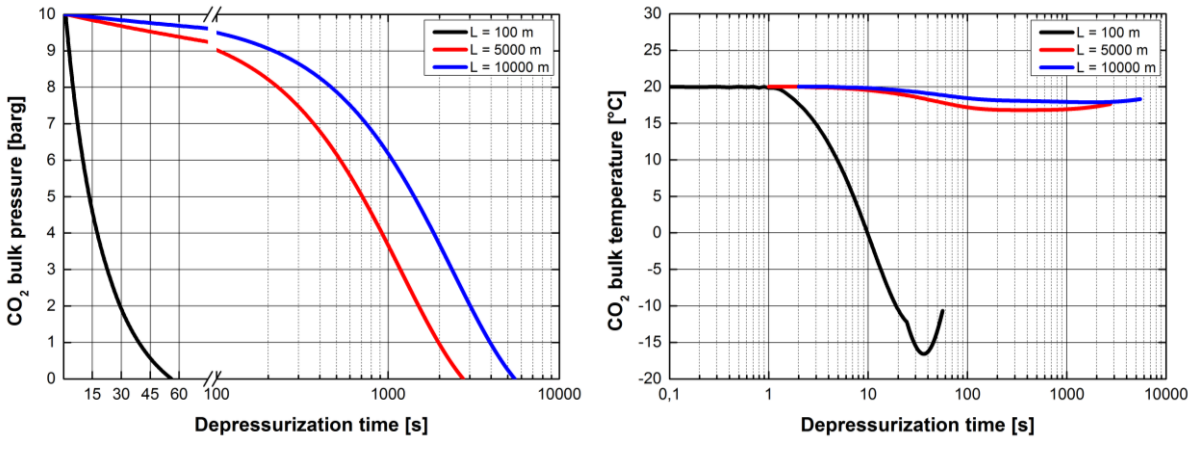

(a) *(b)*

Figure 6.39. *Vessel pressure time evolution under different pipeline lengths. Internal pipeline diameter: 141.6 mm.* $d/D = 0.4$. *a- bulk CO_2 pressure evolution; b- bulk CO_2 temperature evolution. 10 barg, 20 °C expansion.*

Even under different d/D values, i.e. altering the discharge dynamic, an increase in the pipeline length promotes a flattening of the temperature evolution. Higher d/D values oppose it even if still substantial changes are observed (Figure 6.32).

However, when the internal pipeline diameter is increased, the effect of the pipeline length on the temperature evolution is also enhanced. Figure 6.40 shows the temperature tendency when the pipeline diameter is increased up to 867 mm. It may be noted again how shorter pipelines are subjected to the most relevant temperature variations but the isothermal hypothesis no longer holds, especially when the d/D value is increased. It should be underlined that so large pipelines are almost never operated at as such low pressures as 10 barg.

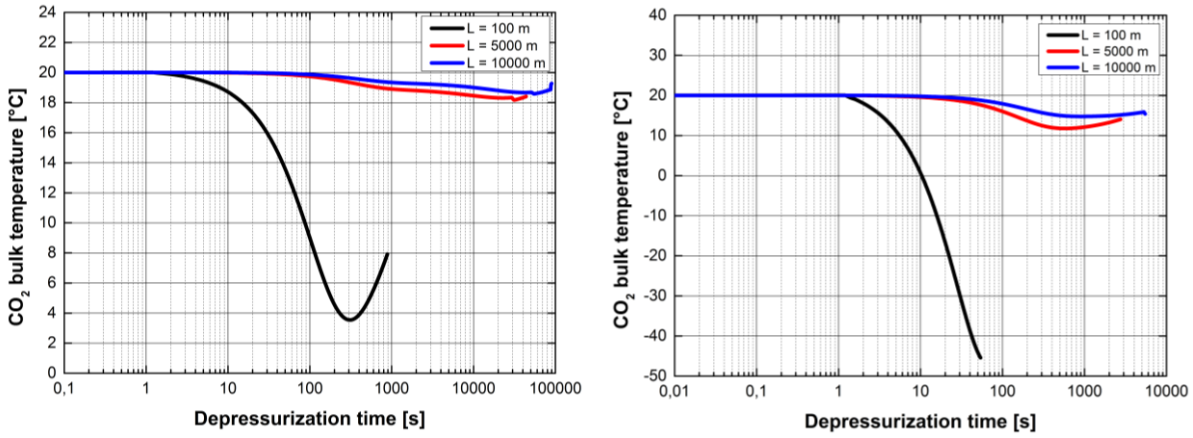

Figure 6.40. *Internal vessel temperature time evolution under varying pipeline lengths. Internal pipeline diameter: 867 mm. a-* $d/D = 0.1$*; b-* $d/D = 0.4$*. 10 barg, 20 °C expansion.*

The CO_2 behavior when subjected to rapid discharges from geometrically varying domains is further investigated at higher charging pressures.

It has been shown that up to 45-50 barg, both the orifice diameter and the pipeline section size are of crucial importance in determining the CO_2 expansion dynamic. As already discussed, higher operative pressures lead to a more complicated behavior in which the boiling/sublimation mechanisms are essential.

Different trials have been run in order to investigate the importance of a geometric parameter variation in the whole dynamic when the CO_2 is expanded from 60 and 150 barg and with therefore an initial dense inventory.

Collected results show that all the investigated geometric parameters (d/D, internal pipeline diameter D and length L) are affecting the following parameters:

- duration of the boiling step;
- dynamics of the system when the whole liquid inventory is exhausted;
- saturation CO_2 properties at the start of the boiling mechanisms.

Starting from a charging pressure of 60 barg, Figure 6.41 collects the results of a 141.6 mm internal diameter pipeline with $d/D = 0.1$.

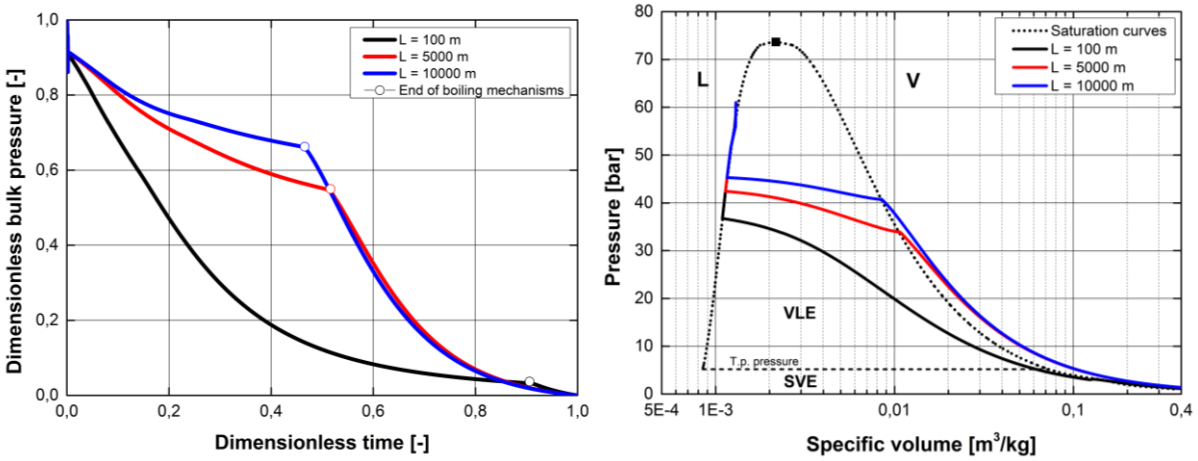

(a) *(b)*

Figure 6.41. *60 barg, 20 °C expansion. Effect on the pressure profiles of a variation in the pipeline length.* $d/D = 0.1$*; pipeline internal diameter: 141.6 mm. a- dimensionless pressure profiles; b- specific volume-pressure curves.*

The pipeline length parameter is mainly governing the whole pressure dynamic giving completely different depressurization profiles. With increasing pipeline lengths, the pressure trend exhibits a characteristic trend that consists of three main steps as it will be deeply discussed later.

By way of introduction, they are briefly explained below:

a. a first step leads the dense CO_2 at the pertaining saturated conditions;
b. a weaker pressure decrease is then expected, corresponding to the boiling mechanism affecting the CO_2 inventory;
c. a final variation in the depressurization trend is matching the occurrence of a gaseous release or a solid-vapor mixture.

The initial step leading to saturated conditions seems not to be affected by the pipeline length as reported in Figure 6.41. This invariability reflects that the expansion to saturated conditions is taking place along similar pathways regardless of the pipeline size. Results show that charging pressures up to 80 barg are linked to depressurization profiles down to the VLE dome characterized by reversibility degrees in the range (0.75;0.84). Initial steps at pressures higher than 80 barg imply slightly smaller values. As it will be discussed later, the main parameter governing this aspect is the charging pressure and the temperature (to a limited extend).

One of the main effects of the increasing pipeline length is a variation in the boiling step duration. As reported in Figure 6.41a, once the length grows, the expansion path in the VLE

dome is shorter as well as the step along the saturation line. The result is that larger CO_2 pipelines involve longer steps that can be modeled as a single gaseous phase release. In addition, with increasing pipeline lengths over 8000-10000 m, the differences in these parameter overlap. The final conclusion is that for half the depressurization time, the releases is in the gaseous state.

It should be noted that the shortest length investigated leads to the appearance of the solid phase that is absolutely not observed in longer pipelines. The 60 barg expansion drives the CO_2 to the SVE domain below the triple point pressure in which the maximum observed solid content fraction is equal to 0.15 (by mass). The solid phase appearance is linked to both the pipeline length and the initial charging conditions. In this sense, predictions show that this occurrence is expected for pipeline length shorter than 2500 m. This parameter increases once the pressure grows (80 barg, 2800 m; 150 barg, 3300 m) as it will be discussed in following sections.

The forecasted exiting mass flow rate, that is essential for the later QRA stages, is sensitive to the pipeline length. This dependence, which does not occur in the case of persistent dense incompressible substances, is only due to the modifications in the pressure and temperature dynamics that are reflected on the mixture quality and its instantaneous density. As an example, the mass flow rate trends expected for a 100, 5000 and 10000 m long pipeline are reported in Figure 6.42.

Different intervals are observed and are more pronounced once the operative pressure and the pipeline length are increased.

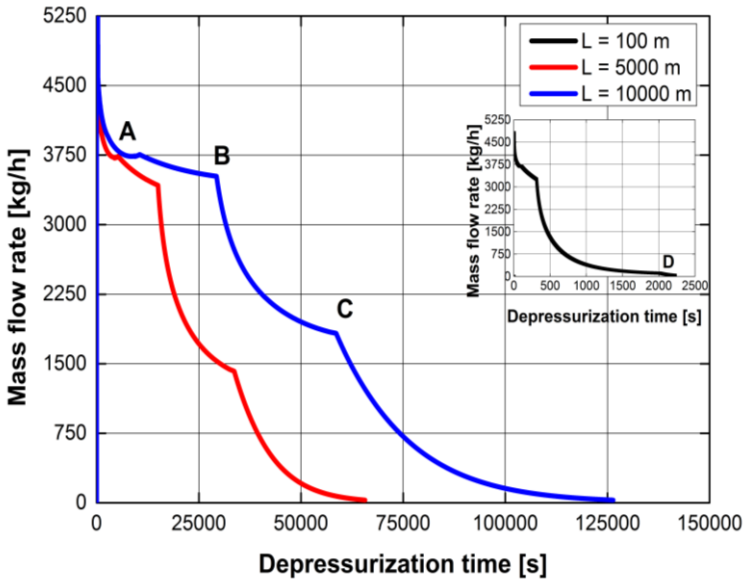

Figure 6.42. *Mass flow rates time trends with respect to different pipeline lengths.* $d/D = 0.1$*; pipeline internal diameter: 141.6 mm. 60 barg, 20 °C expansion.*

Prior to point B, the mass flow rate evolution is almost constant and this step is corresponding to the persistence of the liquid phase in the vessel bulk. Also the mixture quality at the orifice is preserved. After this point, the liquid mass undergoes the boiling mechanism and the mass flow rate trend is subjected to a variation induced by the compressibility effects related to the increasing vapor phase.

At point C, the liquid boiling is complete and the depressurization is that of the gaseous CO_2.

As said, the shortest pipeline drives the profile through an additional point D at which the sublimation of the solid portion ends.

The A-B section is almost preserved even varying pipeline lengths under the condition $L >$ 3000 m and also the trends after point C are comparable if there is no solid phase appearance.

The same pipeline length effects on similar infrastructures are analyzed under the $d/D = 0.4$ condition. Results are collected in Figure 6.43.

It emerges that a variation in the orifice size firstly alters the saturation pressure value at which the multi-phase release starts to occur. Pipelines shorter than 7500 m experience a decrease in this value once d/D is increased; the opposite happens for longer infrastructures. In this way, making clear the inventory amount on the discharge dynamic, the CO_2 remains at saturation conditions longer in reduced domains.

At the same time (Figure 6.43b), the depressurization curves inside the VLE dome are steeper in agreement with the greater incidence of larger orifices. This is also reflected on the pressure evolution in time (Figure 6.43a) that is characterized by longer boiling stages with respect to Figure 6.42a. Despite this trend, no solid phase occurrence is observed in the 5000 and 10000 m pipelines-long.

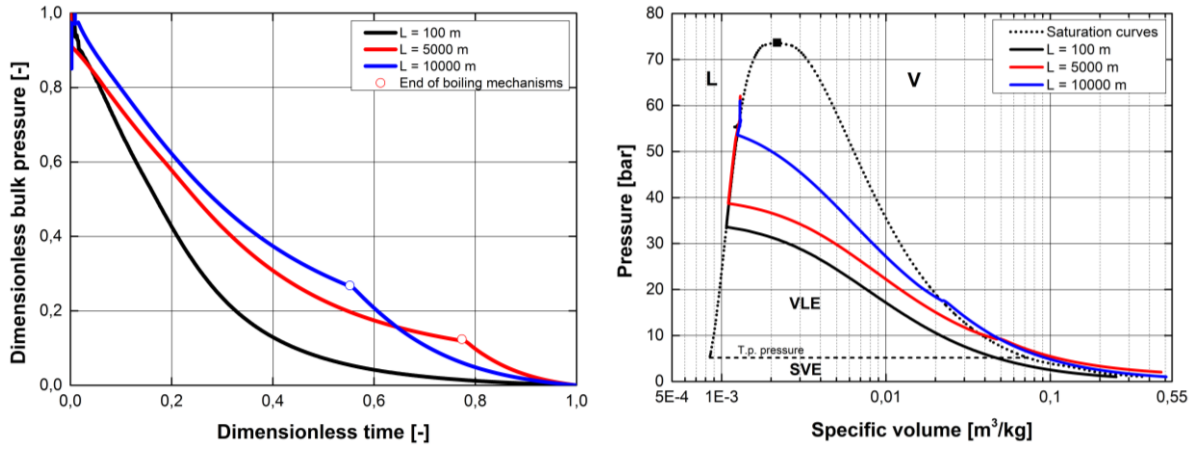

(a) *(b)*

Figure 6.43. *60 barg, 20 °C expansion. Effect on the pressure profiles of a variation in the pipeline length.* $d/D = 0.4$*; pipeline internal diameter: 141.6 mm. a- dimensionless pressure profiles; b- specific volume-pressure curves.*

What happens instead in the case of the shortest pipeline is that an increase in d/D leads to major final solid contents. In the previous investigation, characterized by $d/D = 0.1$, the whole amount of solid has undergone the complete sublimation before the release end. Once d/D is increased up to 0.4, large amounts of dry ice are observed and the final release state is characterized by a multi-phase mixture consisting of up to the 28 % by mass of solid. This final dense content lessens with an increase in the pipeline length and under the investigated conditions, the threshold pipeline length for the occurrence of a final multi-phase mixture is equal to 550 m. Strictly linked to the pressure evolution in time (Figure 6.43a) is that of the temperature in the mass bulk (Figure 6.44-6.45).

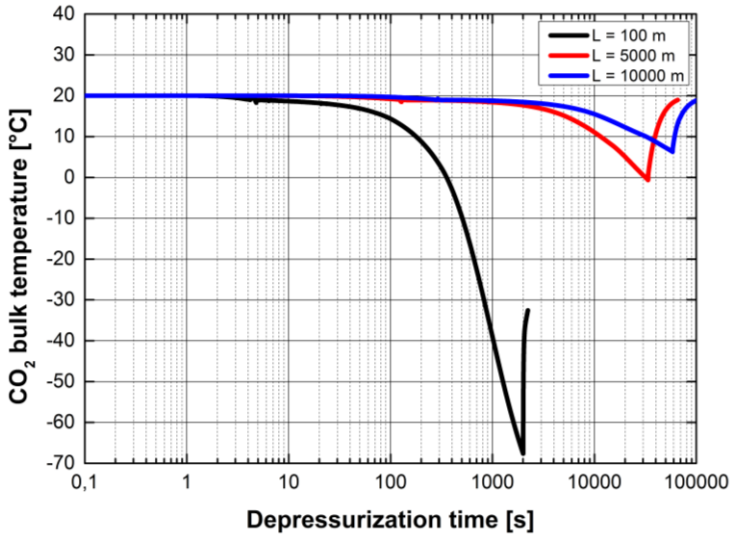

Figure 6.44. *60 barg, 20 °C expansion. Effect on the vessel temperature profiles of a variation in the pipeline length.* $d/D = 0.1$*; pipeline internal diameter: 141.6 mm.*

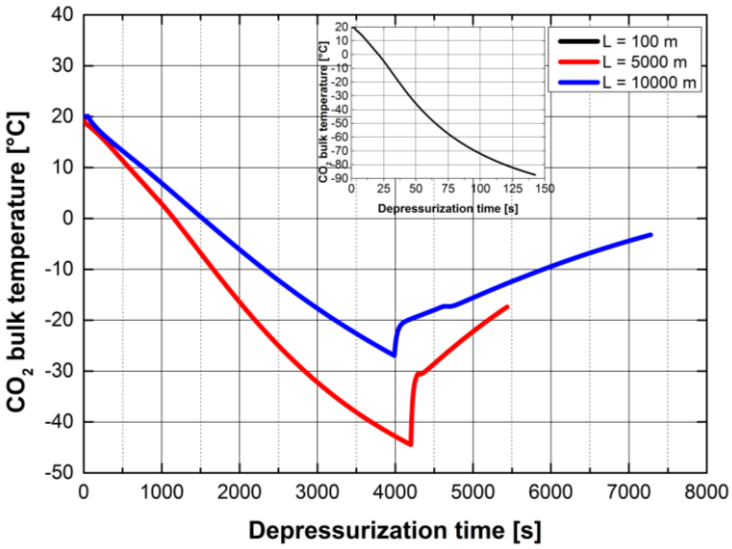

Figure 6.45. *60 barg, 20 °C expansion. Effect on the vessel temperature profiles of a variation in the pipeline length.* $d/D = 0.4$*; pipeline internal diameter: 141.6 mm.*

Results show, however, that an increase in the operative pressure invalidates the isothermal hypothesis as of Figure 6.44-6.45. Under a charging pressure of 60 barg, the 100 m long pipeline experiences temperatures as low as -80 °C without no observed final heating effect, especially under the $d/D < 0.2$ condition. At this initial conditions, nor the longest investigated pipeline sections are subjected to a isothermal blowdown phenomenon with temperature excursions up to 20 °C ($d/D = 0.1$) and 30-40 °C ($d/D = 0.4$).

Following Table 6.5 gives the estimation of average errors committed with the isothermal hypothesis in the blowdown description for different geometries and operative conditions. The error should be intended as the mean integral deviation between the detailed modeled profiles and those based on this assumption.

This error trend reflects the system tendency to be assimilated to an isothermal domain in its bulk section, i.e. far enough from the orifice plane and therefore, given the model assumptions, this condition applies beyond the related *PSSA* control section.

Table 6.5. *Isothermal bulk hypothesis. Error quantification in the predicted profiles with respect to the detailed modeling.*

Pipeline length [m]		**Average error [%]**
Operative pressure [barg]	d/D [-]	
100 m		
10	0.1	12.0
	0.4	36.4
60	0.1	57.9
	0.4	59.2
150	0.1	63.2
	0.4	70.1
5000 m		
10	0.1	5.5
	0.4	24.1
60	0.1	30.5
	0.4	34.7
150	0.1	60.1
	0.4	60.6
10000 m		
10	0.1	4.7
	0.4	26.2
60	0.1	29.1
	0.4	30.4
150	0.1	57.8
	0.4	59.4

More limited errors are expected in the case of lower operating pressures and d/D values, each of them acting as restraints on the thermal dynamic. The first governs the magnitude of the mechanical cooling effect while the latter is strictly linked to its rapidity. Once the pipeline length is increased, the error is lowered because of the improvement in the *VBM* bulk-descriptive approach driven by the increase in the L/D ratio.
Once the initial conditions fall in the dense domain, errors enlarge especially because of the intensified thermal effects going with the liquid CO_2 expansion.

6.3.3.2 Influence of the d/D ratio

The d/D ratio is varied while keeping the pipeline length unchanged. This situation is matching different ruptures affecting a fixed pipeline section.
Differences induced by the variation in this parameter are investigated in terms of the following quantities:

- dimensionless bulk pressure evolution;
- instantaneous specific mixture entropy variation between the bulk and the orifice plane;
- instantaneous dense CO_2 mass fraction in the bulk and at the orifice conditions.

These parameters allow to highlight variances related to a change in the orifice diameter both in terms of mechanical behavior of the system, through the dimensionless pressure trend, and from a thermal perspective (mixture entropy and CO_2 mass fraction).
Results concern a pipeline length of 5000 m, whose magnitude is enough to underline substantial differences when the parameter d/D is changed. The operative pressure is set equal to 60 barg to ensure the occurrence of a multi-phase releases. Same considerations apply for higher charging pressure.
Figure 6.46 collects the dimensionless pressure profiles with respect to a pipeline respectively characterized by an internal diameter of 141.6 and 867 mm.
The d/D incidence on the pressure evolution in the pipeline bulk is relevant with major differences observed in smaller pipelines (Figure 6.46a-6.46b). The increase in the puncture size induces a strengthening in the pressure dynamic with faster declines especially in the dimensionless time range (0;0.8). At $t^* = 0.5$, i.e. when half of the release time has elapsed, the pipeline subjected to $d/D = 0.4$ has lost the 80 % of its initial pressure while the smaller rupture corresponding to $d/D = 0.1$ has not allowed a discharge exceeding the 42 %.

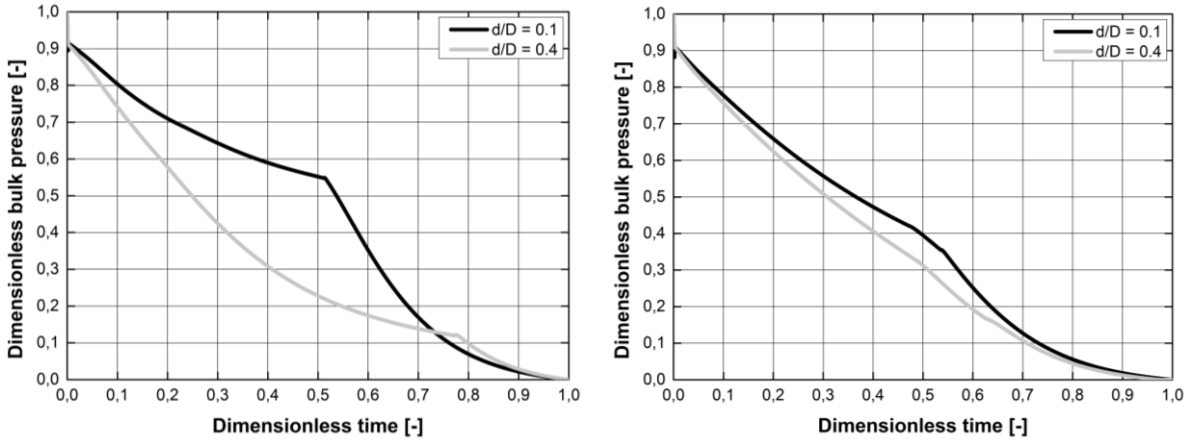

Figure 6.46. *60 barg, 20 °C expansion. Effect of d/D on the dimensionless vessel pressure profile. Pipeline length: 5000 m. Internal diameter: a- 141.6 mm; b- 867 mm.*

These differences are reduced once the pipeline diameter is increased (Figure 6.46b). Pressure profiles are comparable throughout the whole release indicating that the inventory quantity plays a key role in determining its discharge. It should be noted that the investigated variation in the pipeline diameter increases the total CO_2 mass from 60 to 2300 ton. In the first case, the observed total discharge time amounts respectively to 18 and 1.6 h while the latter to 17 and 1.1 h. It is clear that the variation in the d/D parameter significantly reduces the release time even if no relevant differences are observed once the pipeline diameter is increased giving reason to the fact that the first parameter is the governing one. In addition, with respect to Figure 6.46, it is noted again the discrepancies in the multi-phase step duration that is marked by a slope variation driven by the occurrence of phase-change mechanisms. From this perspective, the variation in the d/D acts on the instantaneous dense CO_2 mixture content both in the bulk and at the orifice discharge plane and its investigation is essential since it drives both the thermal and the fluid dynamic.

The instantaneous mixture qualities pertaining to the same modeled releases are reported in Figure 6.47-6.48.

The increase of the d/D on a pipeline of a fixed length firstly results in an enhanced dense content at the orifice plane. This behavior, that is observed for the whole CCS operative pressure range, is governed by two correlated aspects:

- the major pressure dynamics connected to an enlarged orifice diameter;
- the related thermal drop experienced by the CO_2 during the depressurization also enhanced by the persistence of the dense phase, further lowering the instantaneous temperature in its passage to the light phase.

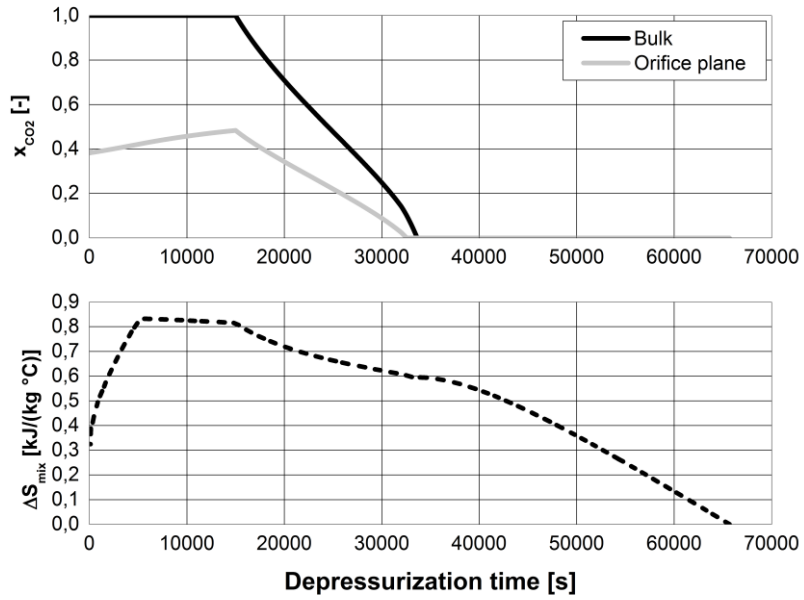

Figure 6.47. *60 barg. Pipeline length: 5000 m. Internal diameter 141.6 mm.* $d/D = 0.1$. *Instantaneous dense CO_2 mixture content (by mass) and difference in the specific mixture entropy between the orifice and the bulk conditions.*

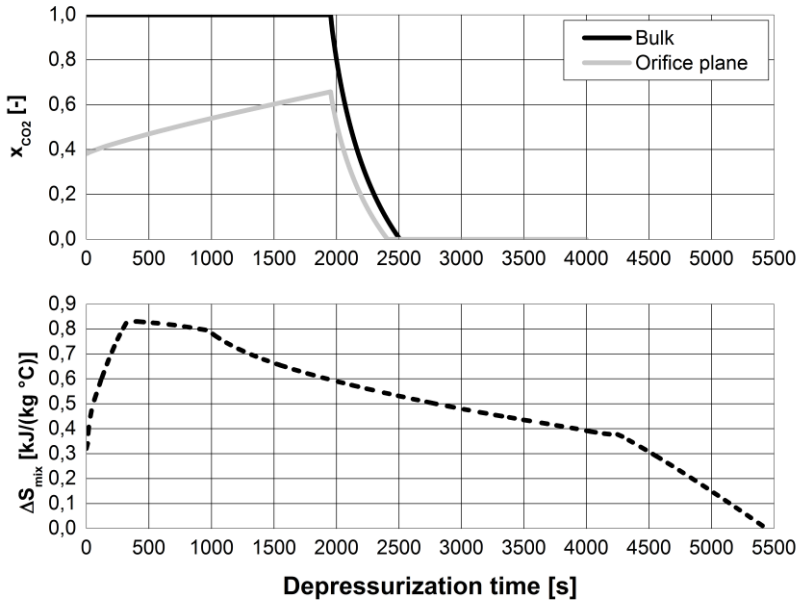

Figure 6.48. *60 barg. Pipeline length: 5000 m. Internal diameter 141.6 mm.* $d/D = 0.4$. *Instantaneous dense CO_2 mixture content (by mass) and difference in the specific mixture entropy between the orifice and the bulk conditions.*

The dense phase content peaks at the orifice are equal respectively to 0.49 and 0.66 with $d/D = 0.1$ and 0.4. The growing dense content at the discharge plane is observed if the solely liquid phase persists in the pipeline bulk because of the thermal effect related to the expansion of a dense-rich mixture. The duration of this step is longer once the d/D grows indicating the occurrence of a release characterized by an increased degree of non-ideality.

Performed trials show that this step is never characterized by the solid phase appearance because pressure levels and specific entropy variations pertaining to the expansion are not allowing this kind of aggregation state. This even in the case of higher charging pressures.
The mixture quality at the orifice starts decreasing with the boiling onset in the bulk (Figure 6.47-6.48) that is testified by the fall in the bulk liquid content. Values pertaining to the discharge location are always smaller than those of the bulk because part of the dense phase undergoes additional boiling mechanisms induced by the pressure drops arising along the discharging way.
Same considerations give reason to the more pronounced quality decline observed in the case of larger d/D values.
From the thermal dynamic perspective, two general main observations emerge.
Firstly, the minimum recorded temperature inside the pipeline is not matching neither the peak in the mixture quality at the orifice nor the the boiling step start. Predictions give reason to state that this occurrence is more precisely taking place at the complete depletion of the liquid phase inside the pipeline. This value is reached much faster than the d/D value is smaller. In addition, moving from previous considerations, this minimum in the temperature is not observed once the expansion does not deplete the dense phase in the pipeline bulk. These observations do not apply for the orifice plane where the temperature excursion is governed by the thermodynamic transformation that is taking place, i.e. the instantaneous enthalpy and entropy variations, but also by the pressure jump existing between the bulk and the orifice plane. The minimum value is recorded at the release start and is almost preserved even under varying geometric parameters since it is strictly linked to the initial physical charging conditions. It ranges between -84 and -79 °C and therefore is always below the equilibrium atmospheric temperature. During the release, the temperature at the orifice increases but with reduced strength while the boiling is occurring in the pipeline bulk and the instantaneous thermal imbalance between the two locations declines because of the reduction in the mechanical pressure driving force.
The second remark is related to the magnitude of the recorded bulk temperatures. Temperature values are sensitive (in addition to the initial charging conditions as it will be discussed later) both to the orifice diameter and the domain size under investigation.
As deeply discussed, following considerations apply:

- the minimum reached temperature decreases with an increase in the d/D ratio;
- longer pipelines experience more limited temperature variations;
- the internal diameter plays different roles in determining the minimum temperature.

Figure 6.49 supports these considerations. It should be noted that in the case of the 5000-m long pipeline, the variation in the internal diameter, i.e. the modification in the CO_2 inventory, does not act uniformly. In fact, when subjected to large ruptures ($d/D > 0.28$), they experience a more limited temperature drop because the rapidity in the discharge phenomenon does not allow for a complete CO_2 cooling. Lowest CO_2 bulk temperatures are recorded in the pipeline characterized by an internal diameter of 141.6 mm at $d/D = 0.4$.

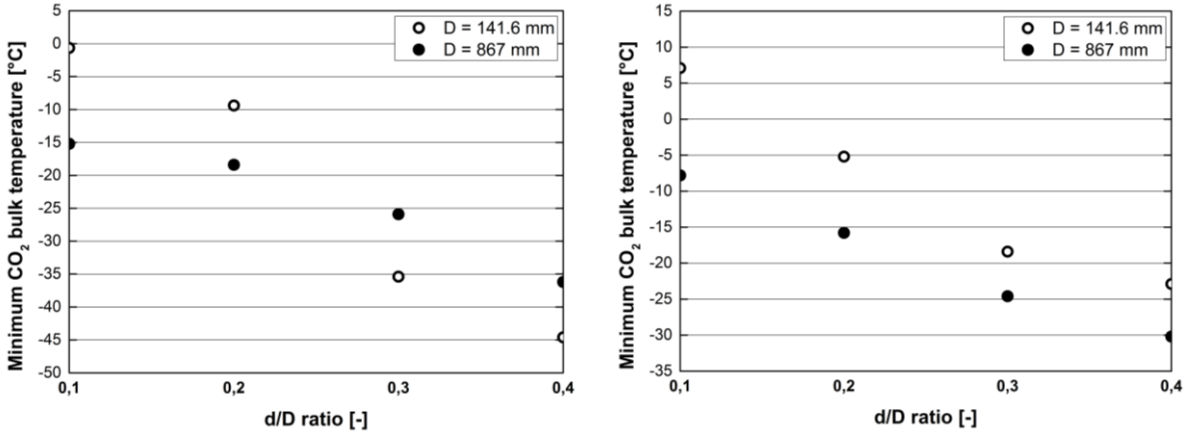

Figure 6.49. *60 barg, 20 °C expansion. Effect of d/D and D on the minimum bulk CO_2 temperature. Pipeline length: a- 5000 m; b- 10000 m.*

A more regular behavior is observed when the pipeline length is increased up to 10000 m since lower temperatures are always observed in larger pipelines. However, as stated, the thermal variations are more limited because of the augmented CO_2 amount to be discharged that is therefore characterized by a greater heat capacity. These conclusions move from the previous considerations.

An increase in the operative pressure acts lowering the temperature values (Figure 6.50). Main differences are observed when the d/D ratio is moderate ($d/D < 0.3$) that is matching the condition under which boiling mechanisms are crucial in determining the thermal dynamic. Above this threshold, the mechanical effect related to the rapid and heavy discharge is no longer negligible with respect to the thermal behavior induced by the phase changes mechanisms. This is the reason why, up to pipeline lengths of 6500 m, minimum recorded temperatures are comparable in the case of $d/D > 0.3$ even under altered operative pressures. 10000 m long pipelines operated at an initial pressure of 150 barg are subjected to a bulk temperature that is abruptly falling down to -87 °C when the internal pipeline diameter and the d/D ratio are respectively equal to 867 mm and 0.4. The growth in the d/D ratio increases the difference in the minimum predicted temperatures because larger ruptures have

a major role on the boiling mechanisms that are also enhanced by the higher charging pressure.

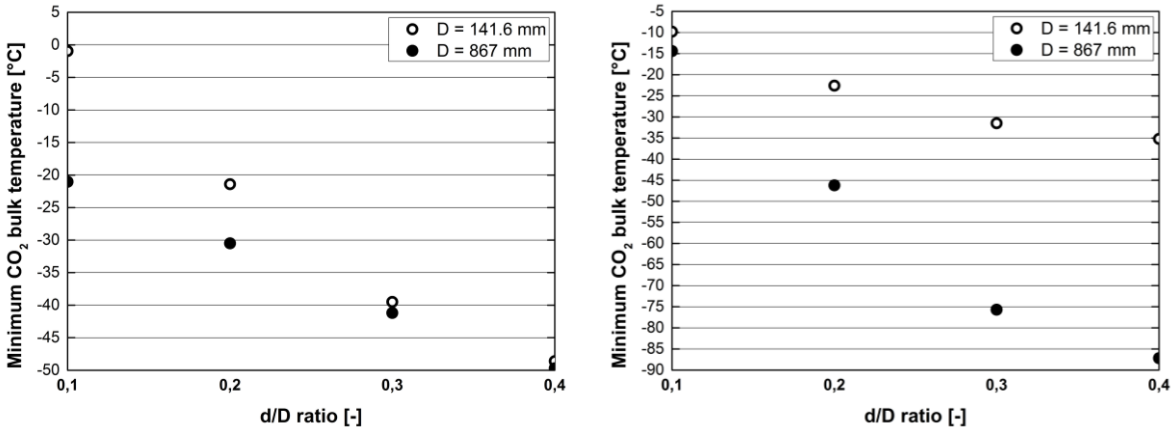

(a) *(b)*

Figure 6.50. *150 barg, 20 °C expansion. Effect of d/D and D on the minimum bulk CO_2 temperature. Pipeline length: a- 5000 m; b- 10000 m.*

6.3.3.3 Influence of the operative conditions

The initial charging conditions are fully described by the bulk CO_2 pressure and temperature. Main effects on the release features of these two combined parameters are investigated in this section.

These conditions are determined by economic and operative reasons and apply at the initial release stages.

Three distinct charging pressures are investigated: 60, 120 and 150 barg. Lower pressures are omitted because many observations in this regard have already been formulated.

Differences are highlighted with respect to a pipeline 5000 m long. The internal diameter value is assumed to be equal to 504.3 mm being the mean value among those listed in Table 6.3.

Following Figure 6.51 applies for a d/D value equal to 0.1.

With reference to Figure 6.51, it should be noted that starting from the liquid conditions, the pressure inside the pipeline rapidly drops down to values in the range 44-60 barg in a few seconds depending on the charging conditions. As said, these values are corresponding to the saturated pressure value that is reached from the initial state following a certain thermodynamic transformation. It is characterized by an increasing degree of reversibility once the charging pressure is enhanced.

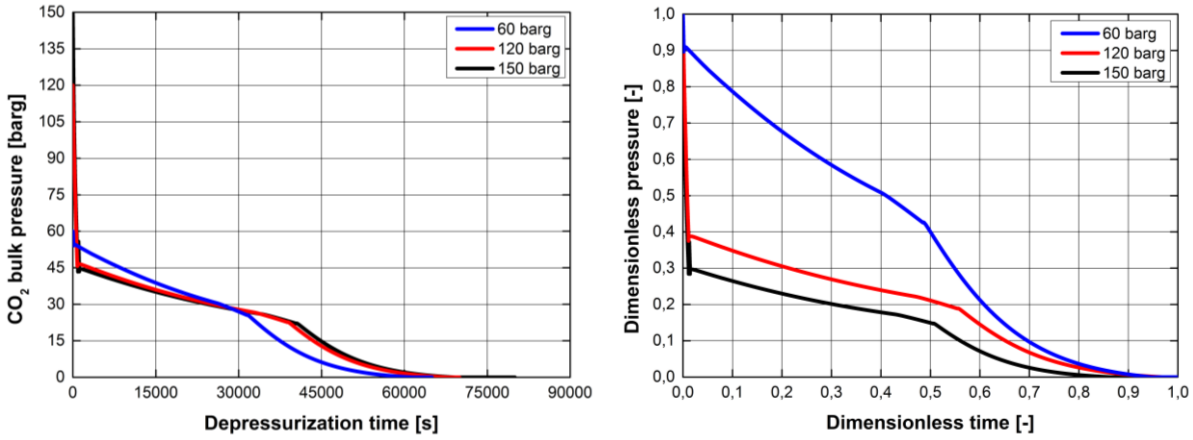

(a) *(b)*

Figure 6.51. *Effect of the charging operative pressure on the expansion development for a 5000 m-long pipeline. Internal diameter: 504.3 mm.* $d/D = 0.1$. *a- time profiles; b- dimensionless profiles.*

The saturation phase is assumed to start when the bulk pressure drop slows down. This is induced by the partial compensation on the released mass due to the boiling mechanisms that are arising once the VLE dome is entered. The related profile alteration is linked to the charging pressure with a tendency to equalize once the initial pressure is high enough. In the present case, this happens for initial pressures over 90 barg.

The decrease rate is altered by this parameter as reported in Figure 6.51b. Profiles give reason to state that, once the saturation state is reached, pipelines characterized by lower charging pressures experience a steepest descent because bulk boiling mechanisms are not enough intense to sustain the mass loss. Once the pressure is increased, phase change mechanisms are strong enough to instantly release a partially equivalent amount of the discharged gaseous mass. Under these conditions, the boiling step is more lasting with respect to the 60 barg example.

Table 6.6 gives representative data of the estimated boiling durations under different specified configurations.

The increase in the operative pressure therefore acts modifying the following parameters:

- time to reach the saturation conditions: higher charging pressures are related to longer times to reach this state;
- time to complete boiling: the time lapse of the phase change is longer in the case of higher charging pressures;
- average discharge mass flow rate during the boiling mechanisms: an increase in the operative pressure leads to smaller released amounts.

Table 6.6. *Main phase-change-related release features under different initial charging pressures and orifice sizes.*

Initial pressure [barg]	d/D [-]	Time to saturated conditions [s]	Time to complete boiling [s]	Average mass flow rate during boiling [kg/s]
150	0.1	1150	40500	11.9
120		1000	39200	12.9
60		160	32000	13.1
150	0.2	315	11550	45.0
120		193	11130	47.4
60		132	9020	49.8
150	0.4	161	3410	187.5
120		134	2820	193.2
60		59	2490	215.0

The first parameter is governed by the thermodynamic pathway induced by the combination of the initial conditions and the d/D ratio. The result is that pipelines charged at higher pressures and subjected to small ruptures will take more time to reach the start of the boiling.

It should be underlined that the transformation followed to the saturated conditions are sensitive to the charging pressure.

It has been observed that a decrease in the initial value leads to major deviations from an ideal isentropic pathway as indicated in Figure 6.52-6.53.

Therefore, the isentropic approximation to the VLE dome is not suitable to describe releases at moderate pressures following small ruptures. Results show that the χ value under these conditions ranges between 0.74 and 0.82.

An increase in the orifice size through the d/D ratio is altering especially the step to saturated conditions as reported in Figure 6.54-6.55 that applies for $d/D = 0.4$.

Major deviations from the isentropic curve are recorded once the orifice diameter is increased and this applies for all the investigated charging pressures.

In addition, lower saturation levels observed with growing d/D ratios are related to the greater discharge rapidity induced by larger orifices.

With respect to the boiling step, it should be underlined that the increase in the charging pressure generally places the relative depressurization path closer to the triple point area thus widening the expansion path that is taking place inside the VLE dome.

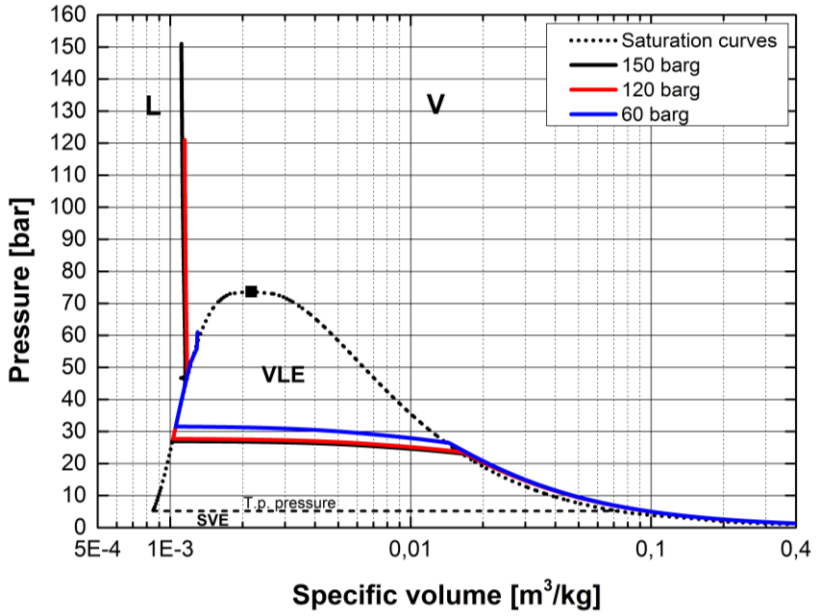

Figure 6.52. *Effect of the charging pressure on the expansion development on a specific volume-pressure diagram. Pipeline length: 5000 m. Internal diameter: 504.3 mm.* $d/D = 0.1$.

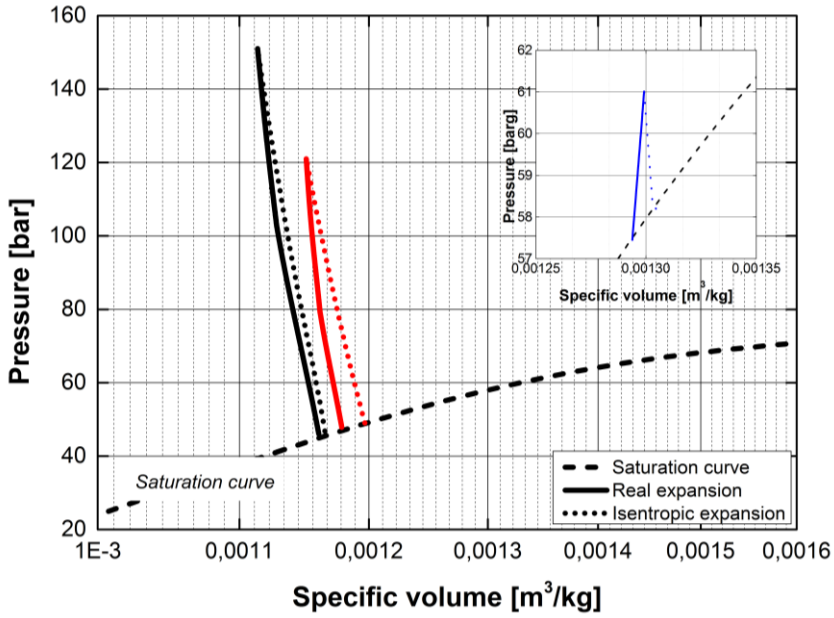

Figure 6.53. *Effect of the charging pressure on the expansion development to saturated conditions on a specific volume-pressure diagram. Pipeline length: 5000 m. Internal diameter: 504.3 mm.* $d/D = 0.1$.

The variation in the initial pressure, however, does not induce modifications on the expansion path beyond the end of the boiling mechanism because this parameter is not the most important in determining the outflow state from the vapor dome. The latter being mainly determined by the pipeline size and by the d/D ratio.

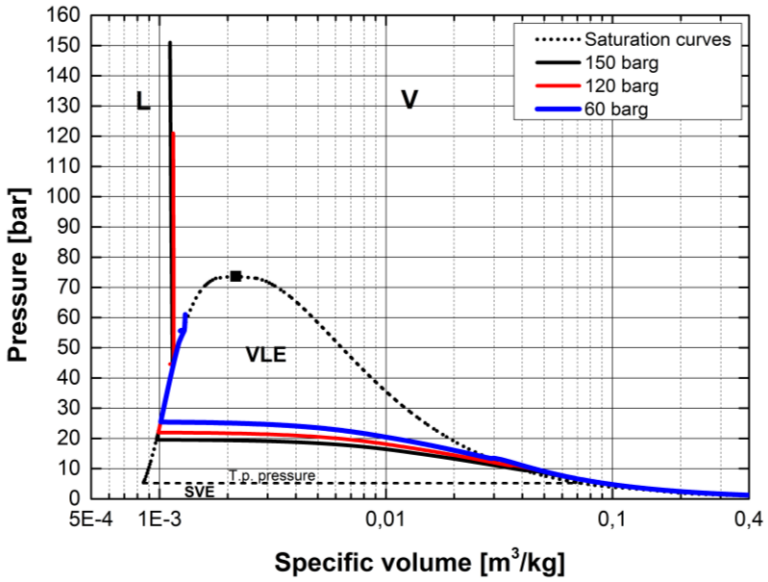

Figure 6.54. *Effect of the charging pressure on the expansion development on a specific volume-pressure diagram. Pipeline length: 5000 m. Internal diameter: 504.3 mm.* $d/D = 0.4$.

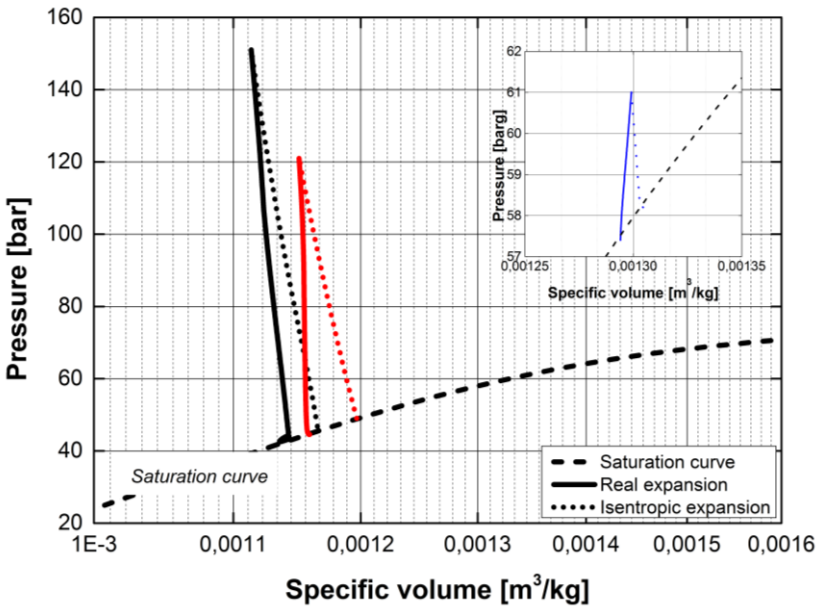

Figure 6.55. *Effect of the charging pressure on the expansion development on a specific volume-pressure diagram. Pipeline length: 5000 m. Internal diameter: 504.3 mm.* $d/D = 0.4$.

A key aspect in the investigation of the initial pressure effects is related to the discharged mass flow rate. It is undisputed that this parameter is determined by the orifice size and by the initial CO_2 conditions. However, in the case of phase change mechanisms this aspect shows some peculiarities that require further investigations.

Profiles concerning the discharged mass flow rate from the pressurized pipeline at 150 barg are reported in Figure 6.56.

All mass flow rate profiles attain their maximum value at the initial release steps when the pipeline pressure is higher. Peaks are equal to 33, 158 and 640 kg/s with reference to d/D values respectively amounting to 0.1, 0.2 and 0.4.

Each peak is followed by a decrease section that leads to an almost steady level that is more pronounced once d/D is decreased, i.e. the release lasts longer. It is clear from Figure 6.56, with respect to $d/D = 0.1$ the development of this *plateau* during which the instantaneous released mass flow is almost constant. Its value is depending on the orifice size and increases once this parameter is enhanced, proving the system capability to release major CO_2 quantities with larger orifices even under boiling conditions. Further details are collected in Table 6.6.

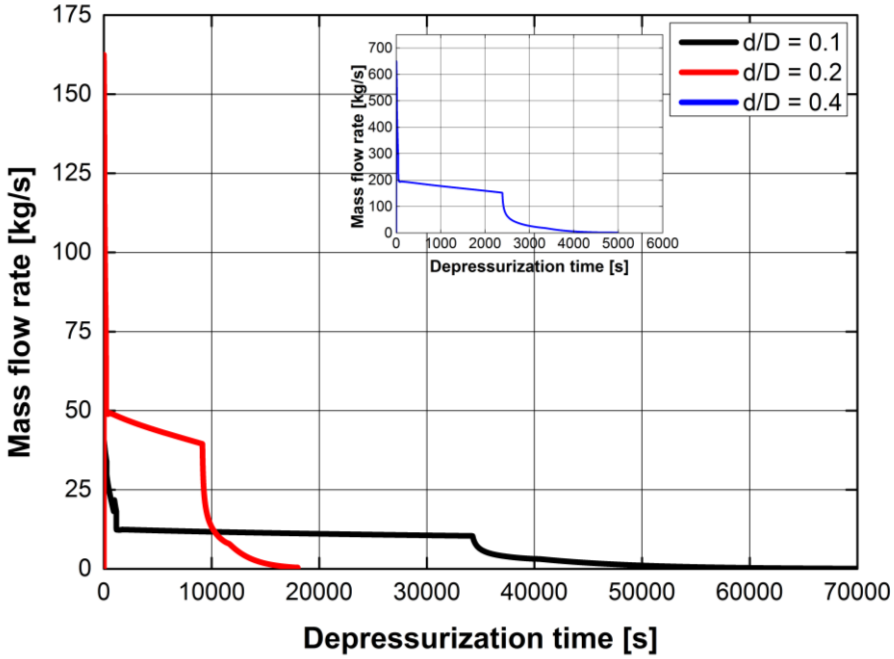

Figure 6.56. *Mass flow rate evolution from a pressurized pipeline at 150 barg and subjected to different orifice sizes. Pipeline length: 5000 m; pipeline internal diameter: 504.3 mm.*

If the operative pressure is lowered, for example down to 120 barg, main differences are observed with respect to the released mass from the vessel.

d/D greater than 0.4 allow for the investigation, inducing sufficiently large variations on the release dynamics.

The time evolution of the instantaneous CO_2 mass inside the 5000-m long pipeline operated at 120 and 150 barg and subjected to a release characterized by $d/D = 0.4$ is reported in Figure 6.57-6.58.

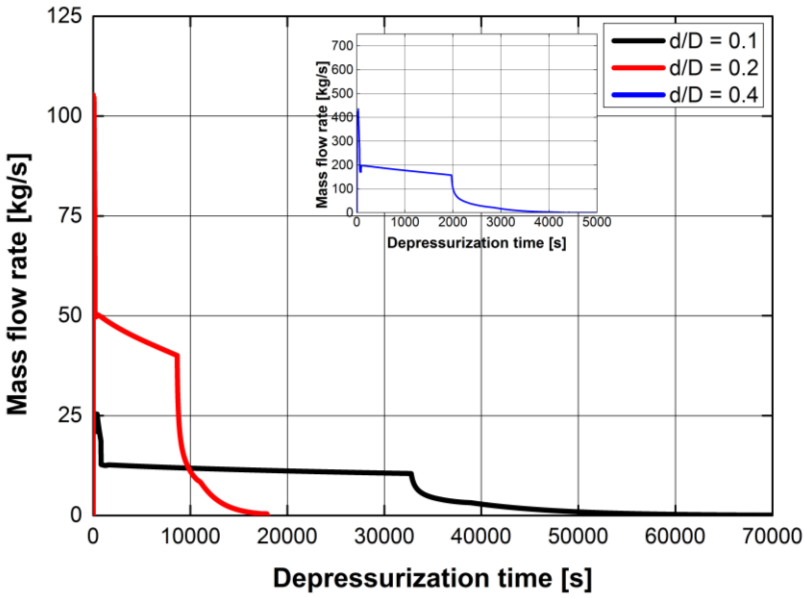

Figure 6.57. *Effect of the charging pressure on the mass flow rate evolution. Pipeline length: 5000 m. Pipeline internal diameter: 504.3 mm. 120 barg, 20 °C expansion.*

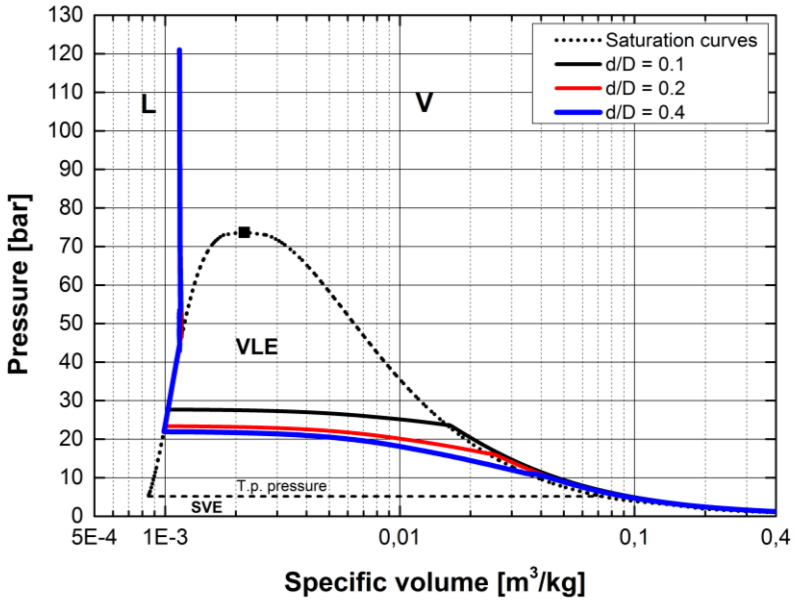

Figure 6.58. *Effect of the charging pressure on the specific volume-pressure profile development. Pipeline length: 5000 m. Pipeline internal diameter: 504.3 mm. 120 barg, 20 °C expansion.*

Other release parameters are instead not preserving their magnitude during the boiling mechanism. In detail, results show that while the mass flow rate is holding, both the vapor and liquid temperatures are changing, the latter experiencing larger variations because the boiling mechanism is extracting energy from the liquid phase. The total mass contained in the vessel, instead, is decreasing almost linearly until the liquid has completely boiled and this is observed every time the CO_2 undergoes a phase change mechanism. The final gaseous release or mixed with solid CO_2, whose content is never above the 20 % by mass, recovers the

peculiar trend specific of a discharge of a light substance. At the same time, the instantaneous dense CO_2 bulk fraction x_{CO_2} is subjected to a decrease whose rapidity is strictly related to the d/D ratio and the charging pressure. At higher values, the decrease in x_{CO_2} is slower leading to a more persistent multiphase mixture.

Finally, the CO_2 bulk density is continually changing throughout the release with highest values detected at the initial steps when also the major mass flow rates are forecasted. Once the boiling mechanisms are occurring in the CO_2 bulk, the mixture density decreases as a result of the gradual increase in the vapor quality. However, it should be underlined that the vapor content is not the only determining factor because the instantaneous bulk temperature, that is variably decreasing, acts inducing density variations. Therefore, the whole density profile is not straightforwardly generalizable even if it shows a decreasing tendency for a large part of the release. A density increase is observed only in the case of very high charging pressures (i.e. above 100 barg) specifically during the expansion to saturated conditions that comes together with relevant temperature drops.

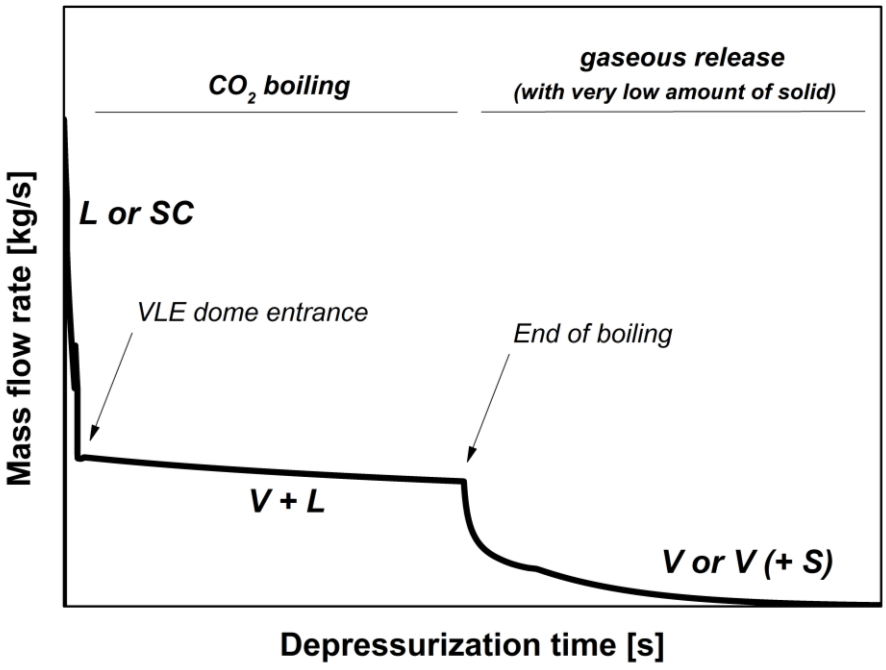

Figure 6.59. *Characteristic qualitative mass flow rate evolution for pressurized pipeline charged with liquid or supercritical CO_2 (L: liquid; SC: supercritical; V: vapor; S: solid).*

Figure 6.59. is to summarize the main features of the mass flow rate evolution for a CO_2 pressurized release subjected to a rapid expansion. This behavior is observed whenever the CO_2 is discharged from a domain that is initially at liquid or supercritical state. Therefore, operative parameters ensuring these aggregation states apply. As previously observed, a

gaseous release will not exhibit the evolution reported in Figure 6.59 but a regular decreasing trend governed only by the density decrease induced by the pressure gradients.

The passage from the VLE to the SVE region, when complied, is characterized by a short period of time during which the CO_2 attests its pressure around that of the triple point. This duration is linked to the dense mass fraction encountered at the triple point pressure but it is of negligible duration (a few seconds) if compared to the total release time. This fact is linked also to the establishment of a new *choked* flow condition corresponding to the entrance in the SVE domain, as discussed in Chapter 3.

General conclusions that are arising from the model application are also confirmed by experimental evidences like those collected by some authors in performing real scale trials ([16,18]).

The other relevant parameter connected with the initial conditions is the operative temperature that may range according to external environmental conditions or technical requirements.

In what concerning this aspect, trials involve the modeling of releases starting from different initial CO_2 temperature conditions considered that in all simulations performed so far has been set at 20 °C. New trials involve an initial operative temperature of 10 °C.

Ignoring the 120 barg pipeline case, Figure 6.60-661 give the pressure and temperature evolutions for a 150 barg pipeline subjected to a rupture of $d/D = 0.1$.

Figure 6.62-6.63 are instead representative of $d/D = 0.4$.

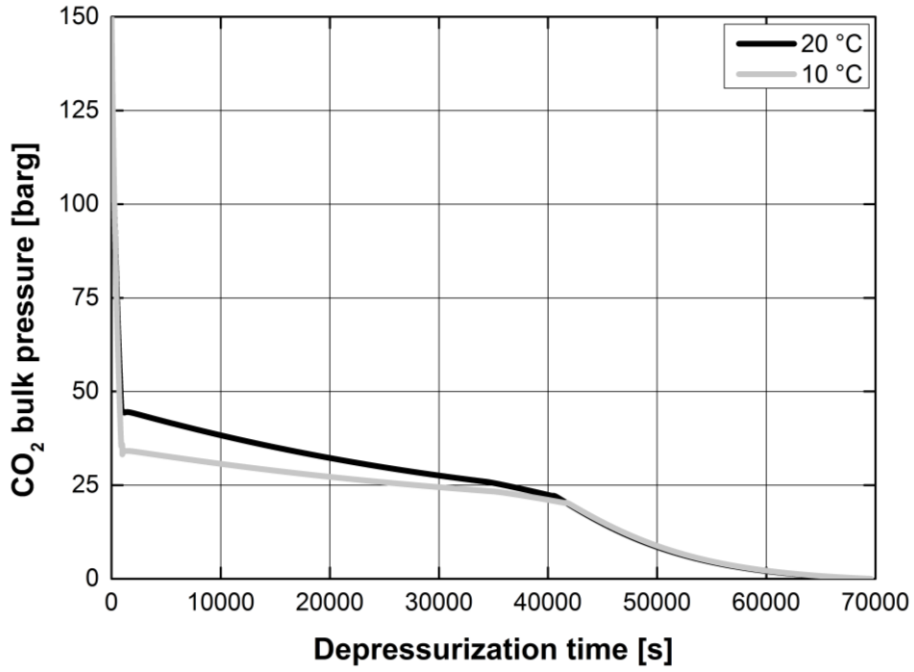

Figure 6.60. *Effect of the operative temperature on the pressure time evolution. Pipeline length: 5000 m; pipeline internal diameter: 504.3 mm.* $d/D = 0.1$. *150 barg expansion.*

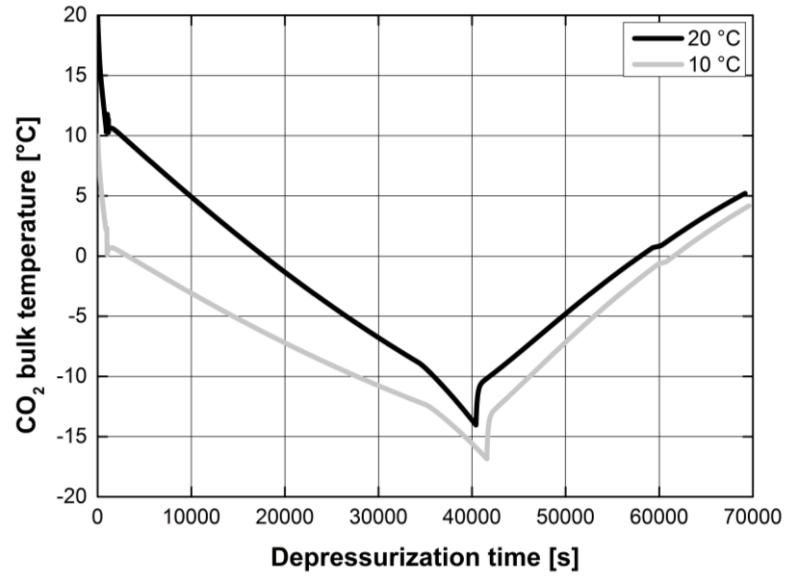

Figure 6.61. *Effect of the operative temperature on the vessel temperature time evolution. Pipeline length: 5000 m; pipeline internal diameter: 504.3 mm.* $d/D = 0.1$. *150 barg expansion.*

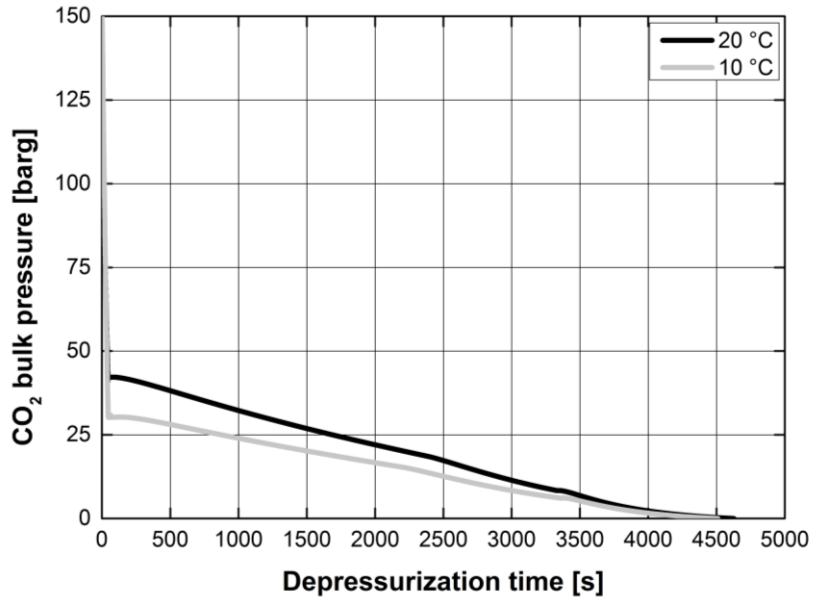

Figure 6.62. *Effect of the operative temperature on the pressure time evolution. Pipeline length: 5000 m; pipeline internal diameter: 504.3 mm.* $d/D = 0.4$. *150 barg expansion.*

As indicated in Figure 6.60-6.61, a decrease in the initial operative temperature is responsible for an altered pressure and bulk temperature profile. Modifications primarily affect the main features of the evolution of the bulk multiphase mixture. Once the initial temperature is decreased also only to 10 °C, both the pathway along the saturation line and the forecasted bulk CO_2 temperature are different.

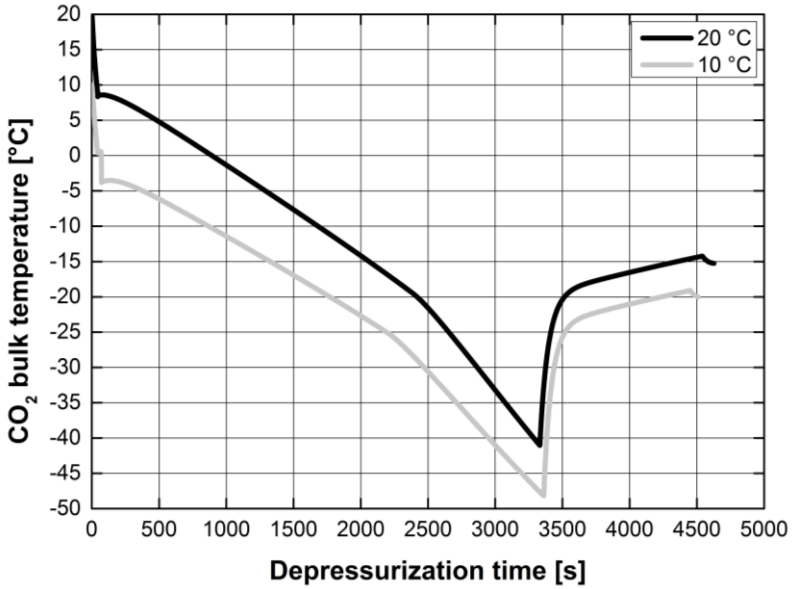

Figure 6.63. *Effect of the operative temperature on the vessel temperature time evolution. Pipeline length: 5000 m; pipeline internal diameter: 504.3 mm.* $d/D = 0.4$. *150 barg expansion.*

In detail, lower initial temperatures prolong the stage at the saturation line as indicated in Figure 6.60-6.62 and this is shown by more reduced pressure values achieved prior to the boiling step. The expect reduction in the case of a d/D value of 0.1 and 0.4 are respectively indicated in Figure 6.64a-6.64b. Even under different d/D values, the effect of an altered initial temperature is the same, tending to give expansions approaching the lower part of the vapor dome.

Consequences are listed below:

- the expansion, started at a lower thermal level, leads to an increased CO_2 cooling that is more pronounced once d/D is increased (Figure 6.61-6.63);
- the minimum recorded bulk temperatures are lower even if the initial temperature discrepancy is not conserved because of the intervention of friction and expansion-related dynamic phenomena. For example, a 150 barg expansion with $d/D = 0.1$ experiences a temperature drop down to -14 °C that is lowered at -16.5 °C with an initial decrease of 10 °C. The respective gap with $d/D = 0.4$ amounts to 8.1 °C;
- the durations of the slower pressure decrease observed in Figure 6.60-6.62 are similar indicating that the temperature is not playing a key role in determining this parameter. The reason is that a change in the initial temperature is not taking significantly away the resulting depressurization paths in the vapor dome. These discrepancies, as observed for other parameters, are enlarged with growing d/D values.;

- the final expansion period, i.e. beyond the VLE dome, is not altered by an initial temperature variation. This because the induced alterations are practically flattened once the CO_2 is going across the VLE region;

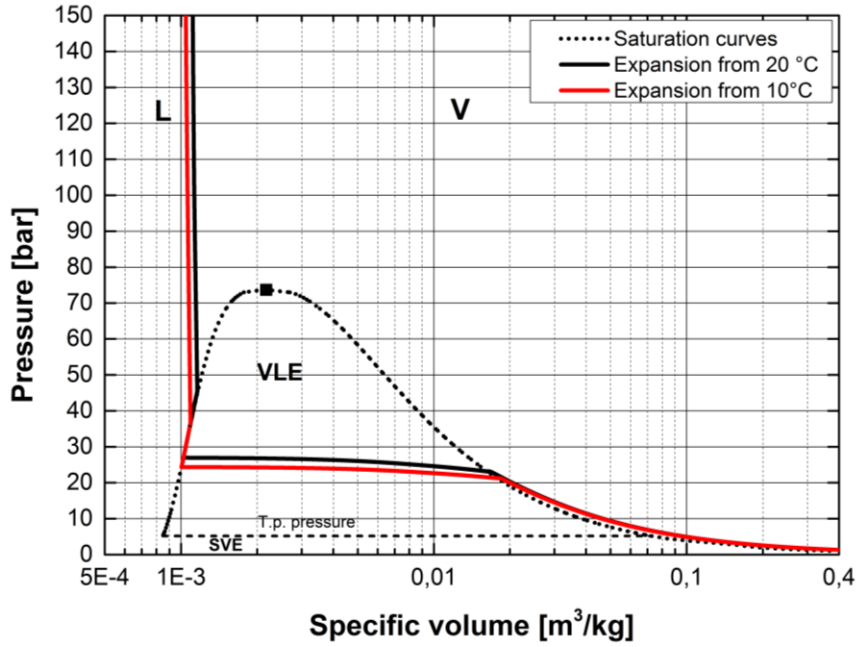

Figure 6.64. *Effect of the operative temperature on the specific volume-pressure curves. Pipeline length: 5000 m; pipeline internal diameter: 504.3 mm.* $d/D = 0.1$. *150 barg expansion.*

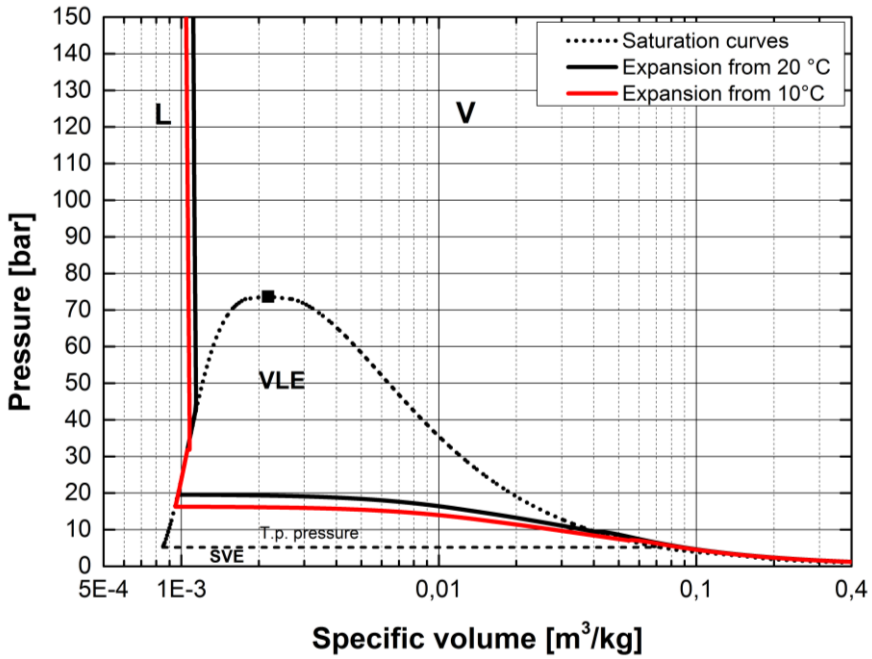

Figure 6.65. *Effect of the operative temperature on the specific volume-pressure curves. Pipeline length: 5000 m; pipeline internal diameter: 504.3 mm.* $d/D = 0.4$. *150 barg expansion.*

Following these more specific considerations, it should also be noted that generally lower temperatures play a key role in determining the total discharge time. Differences, that once again are noticed in the case of smaller pipelines and higher d/D ratios, show that a decrease in the initial operative temperature results in longer total release times. This moves from the fact that the lower thermal content increases the CO_2 density and these differences have an effect on the discharged mass flow rate and therefore to the vessel CO_2 mass evolution.

For example, a release characterized by a large rupture of a 5000-m long pipeline charged at 150 barg lasts for 1.3 h that is decreased at 1.2 h once the initial temperature is lowered of 10 °C.

However, main differences in terms of total discharge times are observed for long pipelines (above 4000 m) and under moderate pressures (below 70-80 barg).

In addition, it is not necessary to emphasize that larger discrepancies are observed for low d/D being the releases derived from small ruptures very similar in terms of global dynamic. In fact, the extremely long discharge times (see, for example, fig. 4.44) act making the total discharge time practically uniform.

However, as it has just been said, a decrease in the operative pressure linked with an initial temperature variation dramatically alters the time required to total discharge. Figure 6.66 specifically refers to a release from 60 barg. Apart from the obvious variations in the depressurization profile of Figure 6.64, the explanation of the variated total release time must be sought in Figure 6.65. In fact, when the charging pressure is moderate, little variations in the initial temperature determine wide density changes.

This sensitivity, in addition to the completely thermodynamic path followed by the CO_2, results in the discrepancies of Figure 6.65.

Density variations are the first parameter acting on the total discharge time which is the same to say on the instantaneous CO_2 mass contained in the pipeline (of constant volume).

However, the further effect on the total discharge time is not primarily due to the final discharge steps, characterized by a low-density CO_2, but differences are arising from the initial path to saturated condition and the initial mechanisms in the VLE dome.

In fact, these are the most relevant steps in determining the discharged mass flow rate from the system because of the high values of the CO_2 density (Figure 6.65) which are reflected in the flow peaks generally observed as indicated in Figure 6.59.

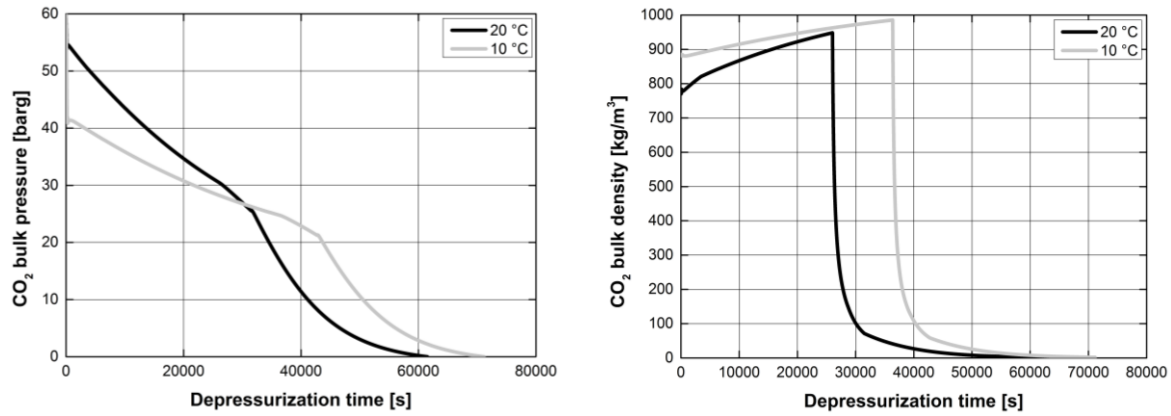

(a) *(b)*

Figure 6.66. *Effect of the operative temperature on the expansion development. 5000 m long pipeline with an internal diameter of 504.3 mm.* $d/D = 0.1$. *a- bulk pressure; b- bulk CO_2 density. 60 barg expansion.*

Therefore, even small density differences in the initial stages determine relevant discrepancies in the instantaneous discharged mass from the vessel and finally in the total discharge time. On this regard, it should be observed that these density variations, in addition to the alterations on the depressurization path, directly act on the remaining CO_2 mass in the vessel beyond the released mass flow rate. The latter being of less immediate understanding in this circumstance.

Under moderate charging pressures, representative dimensionless mass profiles are reported in Figure 6.67. Focusing on the small rupture (Figure 6.67a), the general rise in the CO_2 density induced by the decrease in the initial charging temperature, slows down the discharge phenomenon and to such an extent that when the bulk pressure is halved, only the 60 % of the initial mass has been released. Starting from an initial temperature of 20 °C, the released mass would already equal to 88-90 %.

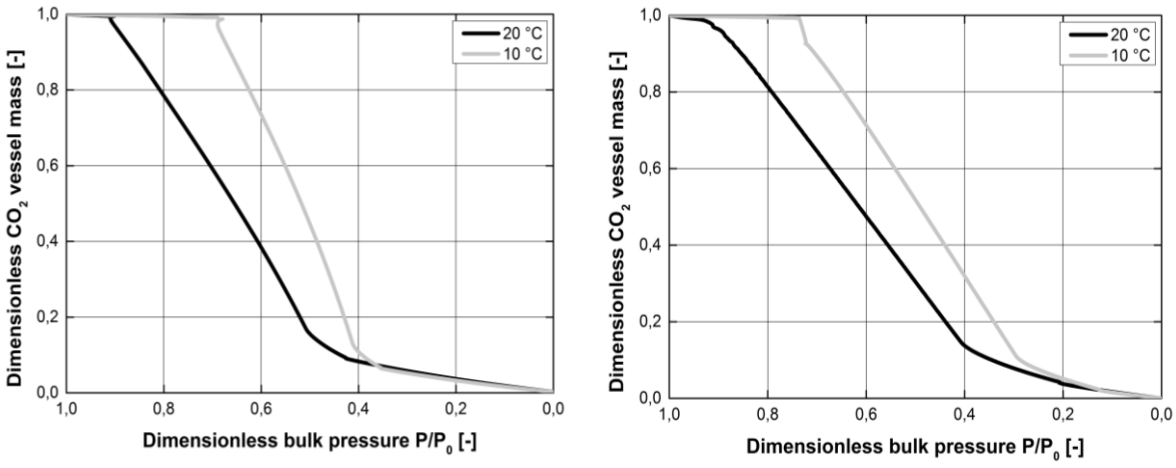

(a) *(b)*

Figure 6.67. *Effect of the operative temperature on the expansion development. 5000 m long pipeline with an internal diameter of 504.3 mm.* $d/D = 0.1$. *a- bulk pressure; b- bulk CO_2 density. 60 barg expansion.*

No relevant alterations are observed above $P/P_0 < 0.4$ because of the similar properties of the discharged CO_2.

This, translated into total release time, prolongs the scenario from 17 to 20 h while keeping both the geometrical parameters and the operative pressure unchanged.

The large rupture (Figure 6.67b) induces differences down to $P/P_0 \cong 0.2$ with a total discharged mass that displays variations up to 25 %. In this case, the total discharge time is varied from 1.1 to 1.3 h.

References to Chapter 6

1. Kornneef, J., Spruijt, M., Molag, M., Ramirez, A., Faaij, A., Turkenburg, W., 2009. Uncertainties in risk assessment of CO_2 pipelines. Energy Procedia, 1(1), 1587-1594.
2. Mahgerefteh, H., Brown, S., Martynov, S., 2012. A study of the effects of friction, heat transfer and stream impurities on the decompression behavior in co2 pipelines. Greenhouse gases: science and technology 2, 369-379.
3. Witlox, H.W.M., Stene, A., Harper, M., Nilsen, S.H., 2011. Modelling of discharge and atmospheric dispersion for carbon dioxide releases including sensitivity analysis for wide range of scenarios. Energy procedia, 4, 2253-2260.
4. Vianello, C., Mocellin, P., Maschio, G., 2014. Study of formation, sublimation and deposition of dry ice from carbon capture and storage pipelines. Chemical Engineering transactions, 36, 613-618.
5. Bird, R.B., Stewart, W.E., Lightfoot, E.N., Transport Phenomena. John Wiley and Sons, 2nd ed., 2007.
6. Russo, P., Parisi, F., 2016. Risk-Targeted Safety Distances of Reinforced Concrete Buildings from Natural-Gas Transmission Pipelines. Reliability Engineering and Safety System, 148, 57-66.
7. Kuby, M.J., Middleton, R.S., Bielicki, J.M., 2011. Analysis of Cost Savings from Networking Pipelines in CCS Infrastructure Systems, Energy Procedia, 4, 2808-2815.
8. Wilson, D.J., Angle, R.P., 1979. The Release and the Dispersion of Gas from Pipeline ruptures. Air Quality Control Branch Pollution Control Division, Alberta.
9. Fannelop, T.K., Ryhming, I.L., 1981. Massive Releases of Gas from Long Pipelines. American Institute of Aeronautics and Astronautics, 6, 132-140.
10. Carter, D.A., 1991. Aspects of Risk Assessment for Hazardous Pipelines Containing Flammable Substances, J. of Loss Prev. Process Ind., 4.

11. Mannan, S., Lees, F.P., 2005. Lees' Loss Prevention in the Process Industries: Hazard Identification, Assessment and Control. Amsterdam, Elsevier Butterworth-Heinemann.
12. EN 10208-2:2009, Steel pipes for pipelines for combustible fluids-technical delivery conditions. Part 2: Pipes of requirement class B.
13. ISO 15589 Parts 1 & 2. Petroleum and natural gas industries-Cathodic protection of pipeline transportation systems.
14. Mazzoldi, A., Hill, T., Colls, J.J., 2008. CO_2 transportation for carbon capture and storage: Sublimation of carbon dioxide from a dry ice bank, International Journal of Greenhouse Gas Control, 2, 210-218.
15. Bouchonneau, N., Sauvant-Moynot, V., Choqueuse, D., Grosjean, F., Poncet, E., Perreux, D., 2010. Experimental testing and modelling of an industrial insulated pipeline for deep sea application, Journal of Petroleum Science and Engineering, 73(1-2), 1-12.
16. Vree, B., Ahmad, M., Buit, L., Florisson, O., 2015. Rapid depressurization of a CO_2 pipeline-an experimental study. International Journal of Greenhouse Gas Control, 41, 41-49.
17. Ahmad, M., Bogemann-van Osch, M., Buit, L., Florisson, O., Hulsbosch-Dam, C., Spruijt, M., Davolio, F., 2013. Study of the thermohydraulics of CO_2 discharge from a high pressure reservoir. International Journal of Greenhouse Gas Control, 19, 63-73.
18. Li, K., Zhou, X., Tu, R., Yi, J., Xie, Q., Jiang, X., 2015. Experimental investigation of CO2 accidental releases from a pressurized pipeline. Energy Procedia, 75, 2221-2226.
19. CO2PipeHaz, 2009. Quantitative failure consequence hazard assessment for next generation CO_2 pipeline: the missing link. In: Description of Work of the Grant Agreement for FP7 Cooperation Work Programme 241346-2-CO2PipeHaz (CP), 1-83. www.co2pipehaz.eu
20. 2013. CO2PIPETRANS Project (DNV).
21. Vianello, C., Mocellin, P., Maschio, G., 2016. Risk assessment of a hypothetical network in UK transporting carbon dioxide. Journal of Loss Prevention in the Process Industries.
22. IEAGHG, CO_2 Pipeline Infrastructure, 2013/18, December, 2013.
23. NEB, Reasons for Decision in the Matter of Souris Valley Pipeline Limited. National Energy Board, Calgary, Canada, 1998.
24. Molag, M., Raben, I.M.E., 2006. Externe veiligheid onderzoek CO2 buisleiding bij Zoetermeer. TNO, Apeldoorn, 2006, 46.

25. CPR, Guidelines for Quantitative Risk Assessment-the Purple Book. Committee for the prevention of Disasters (CPR), VROM, RIVM, The Hague, Netherlands, 1999.
26. Hooper, B., Murray, L., Gibson-Poole, C., 2005. Latrobe Valley CO_2 Storage Assessment, CO2CRC, Melbourne, Australia.
27. Turner, R., Hardy, B., Hooper, b., 2006. Quantifying the risks to the public associated with a CO_2 sequestration pipeline: a methodology & case study. Greenhouse Gas Control Technologies, 8.
28. Mahgerefteh, H., Jalali, N., Fernandez, M.I., 2011. When does a vessel become a pipe. Aiche, 57(12), 3305-3314.

Chapter 7

Non-equilibrium Phenomena in Rapid CO_2 Depressurizations

This section covers the main irreversible sources leading to the occurrence of non-equilibrium mechanisms during a rapid discharge of CO_2. The deviations from the HEM (*Homogeneous Equilibrium Model*), that invokes thermal and mechanical equilibrium between facing phases, are investigated. In addition, the effects of the introduction of the non-equilibrium description are quantified with respect to predicted release parameters.

7.1 Introduction

The applied analysis to rapid CO_2 releases performed so far deals with the fundamental hypothesis of thermodynamic equilibrium (i.e. mechanical and thermal) during the orifice discharge. Practically, this means that conservation equations and the release modeling rely on the HEM approach (*Homogeneous Equilibrium Model*).

However, experimental results show that this modeling approach is not always reliable in describing the blowdown phenomena. In addition, a lack of knowledge exists concerning this topic ([1,2]).

This chapter deals with non-equilibrium related phenomena that may affect the rapid discharge of CO_2 from pressurized domains with specific focus on relaxation phenomena that are arising from a microscopic molecular statistical analysis.

7.2 Features of the HEM approach

The HEM approach, that is Homogeneous Equilibrium Approach ([3]), always assumes that during a rapid phenomenon, like an expansion, following variables among different phases are equal:

- velocity (or local velocity field);
- temperature;
- pressure.

The theoretical basis of this approach relies on the hypothesis that both mass and energy transfers are rapid enough to ensure the equilibrium achievement. It is clear that HEM features find application whenever the releases is characterized by more than one phase as in the case of the CO_2, under the already discussed conditions.
What affects the HEM reliability, i.e. its applicability in QRA procedures concerning the CO_2, is due to all mechanisms that can drive the CO_2 away from the ideal thermodynamic equilibrium ([4,5]) as it will discussed in the following paragraph.
It should be noted that the HEM approach is extensively used in describing the phenomena under investigation for both single and multi-component systems. For example, some authors ([6,7]) have underlined the HEM results agreement with some performed experimental campaign even if, more recently, others have remarked the limitations of this modeling procedure ([8,9]).
Such inaccuracies require therefore a different approach that should move from the analysis and description of main irreversible phenomena occurring during the CO_2 blowdown.

7.3 CO_2 Non-equilibrium thermodynamics

The main concept of the non-equilibrium thermodynamics is related to the general framework that is provided by this branch in describing macroscopic irreversible processes ([5]).
The irreversibility notion is strictly linked to the additional entropy balance equation that is usually employed in this approach, expressing the fact that the entropy is a time-variant variable. Its variability is firstly due to the entropy flow affecting the control volume under investigation and secondly to irreversible phenomena occurring inside it. Therefore, the entropy source is always a non-negative quantity that vanishes once reversible transformations are taking place.
One of the aim of this branch is therefore to relate this entropy source to the various occurring irreversible phenomena.

7.3.1 Main irreversible phenomena in the CO_2 expansion

Irreversible phenomena occurring during a rapid CO_2 expansion are many and have different causes.
Experimental works have revealed, for example, that the metastability of the dense CO_2 near the discharge orifice plays an important role as a source of irreversibility ([6,10]). The metastability is linked to a first-order transition involving latent heat effects and therefore a phase change that in the CO_2 case takes the gas-liquid (boiling/liquefaction) or gas-solid (sublimation) route.

Strictly connected to this aspect are all those which occur during the CO_2 path toward atmospheric conditions and that are listed below:

- nucleation of CO_2 droplets;
- bubble growth;
- crystal formation.

While nucleation and bubble growth are taking place once the CO_2 has entered the vapor-liquid dome, the crystal appearance is expected as the substance crosses the triple point down to atmospheric final conditions. And this only if the previous state resulting from the liquid-gas transition is characterized by a certain final dense CO_2 amount.

All previously listed contribution to the irreversibility will be later discussed and quantified following the approach of some authors ([11]).

In what concerning hazards derived from the CO_2 releases, it should also be underlined that any orifice flow that is accelerated from stagnant to orifice conditions (even under the establishment of sonic flows) is characterized by a certain degree of irreversibility that should be contemplated. Its description relies on the concept of relaxation phenomenon.

In this context, relaxation is intended as the effect resulting from a delay between the application of an external action on the system and its response. This, translated on the CO_2 framework, corresponds to the return of the CO_2 system to equilibrium conditions.

7.3.1.1 Relaxation phenomena in CO_2 expanding systems

A system subjected to a rapid expansion experiences sudden phenomena causing relevant modifications in the molecular energy content and the restoration of the initial system equilibrium will require a characteristic time scale ([5,11]). It is clear that, because of the short residence time (10^{-6}-10^{-4} s), the expansion phenomena may not leave enough time for the system to find equilibrium with the surrounding changing thermodynamic environment.

The relaxation phenomenon is therefore strictly linked with the molecule capacity to store energy and to be subjected to motion. It is known, from the quantum theory, that this is done in three main ways that is through translational, rotational and vibrational motion ([5]). But, because of the triatomic structure of the CO_2, the latter is most significant being its characteristic velocity lower.

However, this velocity, if compared to that characteristic of the release phenomenon, implies following (7.1) :

$$\tau_{vib} \geq \tau_{rel} \quad , \tag{7.1}$$

that is to state that the vibrational non-equilibrium time τ_{vib} is larger or at the limit of the same order of magnitude of that concerning the flow residence time across the discharging orifice τ_{rel}.

From a thermodynamic point of view this means that the vibrational mode is relevant in determining the overall energy content of the system not being negligible during rapid phenomena. As discussed by some authors ([11]), this aspect asks therefore for a vibrational rate equation in which τ_{vib} is quantified as reported in (7.2):

$$\tau_{vib} = \frac{\alpha_1}{P} e^{\left(\alpha_2/T\right)^{1/3}} \quad . \tag{7.2}$$

The (7.2) is derived from a general formulation ([12]) under the approximation of sufficiently low temperature field, compatible to those encountered during pressurized releases. Thus, at a given pressure *P* and temperature *T*, the vibrational characteristic time is estimated once constants α_1 and α_2 are known. These are strictly linked to the CO_2 molecule physical properties and are respectively equal to $4.15 \cdot 10^{-7}$ and 10635.1 K ([11]). Figure 7.1 gives for different temperature values, once fixed a certain pressure level, the τ_{vib} of a CO_2 molecule. The same Figure 7.1 gives an indication of the characteristic average residence times across orifices.

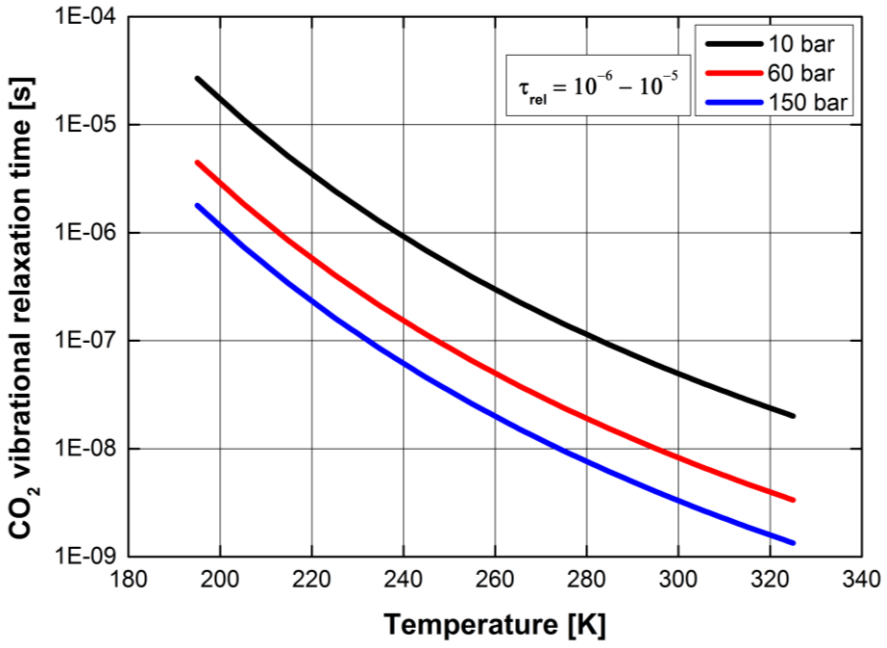

Figure 7.1. *Molecular CO_2 relaxation times under different local temperature and pressure values. The flow across orifices exhibits characteristic times in the order 10^{-6}-10^{-5} s.*

The vibrational relaxation time therefore plays an appreciable role once the comparability between τ_{vib} and τ_{rel} holds and this is achieved under following conditions ([11]):

a) the CO_2 flow field is characterized by temperature gradients;
b) $\tau_{vib} > \tau_{rel}$;
c) the vibrational energy not negligibly contributes to the overall CO_2 internal energy.

A flow from pressurized domains across an orifice ensures condition (a) because of the cooling effect already widely discussed. Condition (b) is met only by large molecules (large is intended with respect to monoatomic or diatomic structures) and by the CO_2 under specific conditions that are sometimes achieved in the release evolution. The last condition is usually not met by molecules that, despite relax slowly, do not have enough vibrational energy at operative conditions. In the case of the CO_2, it is shown that the energy contribution may amount up to 6 % and therefore condition (c) may be met.

7.3.1.2 Subcooled CO_2 and metastability in boiling mechanisms

The expansion from the CO_2 liquid or supercritical region is characterized by a sudden temperature drop. As previously discussed and neglecting the solid appearance, the ideal path during the depressurization is approximated through the following steps:

- an ideal (almost) isothermal expansion to saturated conditions;
- an isothermal and isobaric vaporization to the opposite dome edge.

However, the real transformation deviates from these conditions leading to a superheated liquid state inside the vapor dome up to the spinodal edge as indicated in Figure 7.2.

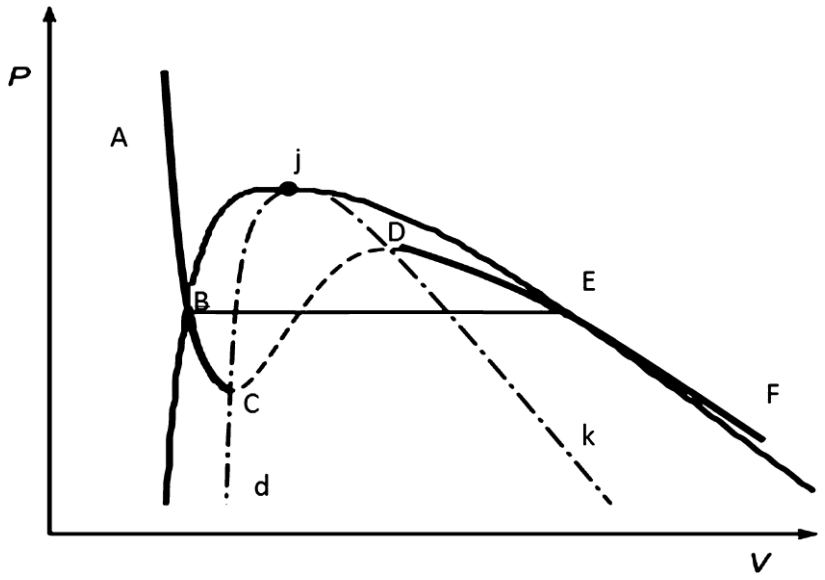

Figure 7.2. *CO_2 metastability curves in the VLE dome and spinodal edges (d – j – k) in a v – P diagram ([11]).*

The passage to the light phase is therefore characterized by the presence of superheated liquid that does not reach the phase transition and this occurrence may be linked to the work required to give rise to a critical bubble inside the mass. Specific reference equations to

estimate this quantity are reported in some sources ([11,12,13]) and show that it is mainly related to the dense phase properties and the degree of superheat.

In addition, the metastability property asks therefore for a free energy jump to be overcome to allow the phase transition.

The most relevant pertaining conclusion, that it will be recovered later, is that these mechanisms come always together with an entropy increase in accordance to non-equilibrium concepts ([5]). This occurrence is defined as structural entropy increase in non-equilibrium phase transition and needs to be quantified to then be inserted in the modeling procedure.

7.3.1.3 Irreversible mechanisms across the triple-point to solid-vapor domain

Starting from the CO_2 phase diagram, any liquid-vapor CO_2 system is subjected to a transition to solid-vapor equilibrium. This is achieved at the triple point being this a three-phase domain. This represents a singularity in the QRA procedures because only a few substances experience the transition occurrence to the solid domain under operative conditions.

The complete CO_2 phase diagram is reported in Figure 7.3 with the solid-vapor region that is located at the bottom.

In what concerning irreversible phenomena at the triple point, some authors ([8]) have forecasted a sharp variation in the vapor mass fraction in the passage to pressures below 5.187 bar. In other words, this gives evidence to the fact that the triple point does not really correspond to the vapor-liquid to the vapor-solid transition equilibrium point. The reason is the same of that applied for the passage across the saturation line of the vapor dome indicating the existence of an energy barrier to be exceeded in the nucleation mechanism. The free energy barrier, expressed in terms of nuclei formation rate J, may be formulated as in (7.3):

$$J = ke^{-\left(\Delta G_c / k_B T\right)} \quad . \tag{7.3}$$

In (7.3), k is the pre-exponential constant, k_B the Boltzmann's constant and ΔG_c the free energy of formation of a nucleos with a critical radius.

Being this occurrence, the resulting vapor and solid phase are not in equilibrium during the nucleation step and following the approach proposed by some authors ([8,11]) this aspect will be included in the model as discussed later.

The specific issues concerning the thermodynamic fundamentals and related discussions are delegated to the scientific source literature ([11]). Some authors ([11,15]), however, proposed the following correlation (7.4) for the work of formation Δw of a critical CO_2 bubble:

$$\Delta w = 16.75 \frac{\sigma^3 T^2}{L_v^2 \rho_v^2 \Delta T^2} \quad , \tag{7.4}$$

In (7.4), σ is the surface tension, L_v the latent heat of vaporization, T is the temperature at the saturation state, ρ_v is the vapor density while ΔT is the degree of superheating.

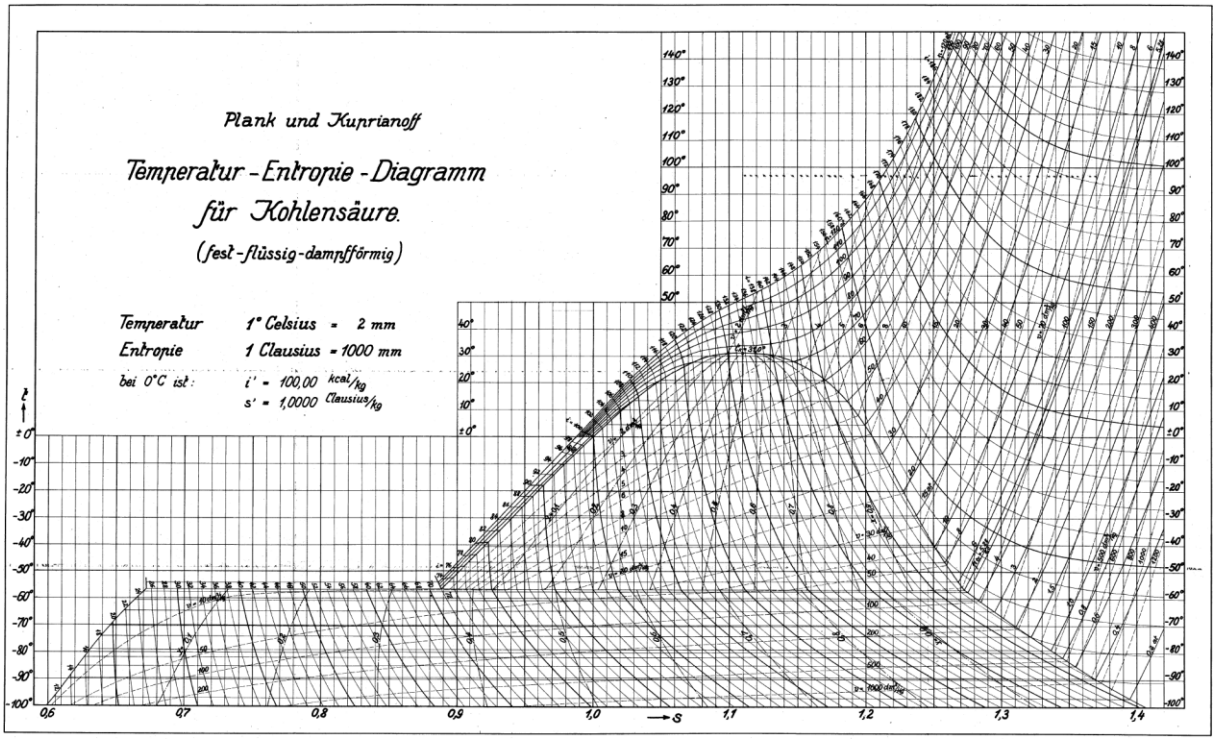

Figure 7.3. *CO_2 (specific) entropy - temperture phase diagram ([14]).*

7.4 The *Homogeneous Relaxation Model* (*HRM*)

Previous considerations result in a modification of the usual *Homogeneous Equilibrium Models* (*HEMs*) that do not take into account any of the irreversibility sources.

The usual approach, giving rise to the *Homogeneous Relaxation Models* family (*HRMs*), consists in the integration of the conservation equations with an additional relation taking into account the entropy generation following the modeled phenomenon ([5]). Practically, not being the entropy a readily accessible quantity, the formulation is based on the vapor mass fraction that is changing also because of the irreversible mechanisms like the non-equilibrium vaporization and nucleation-related issues.

7.4.1 The additional governing equation

The blowdown model, as previously proposed, is based on the conservation equations. In the case of negligible spatial gradients, these are represented by ODEs that require a numerical solving approach.

Once non-equilibrium concepts are to be included, an additional balance equation for the vapor mass fraction x is required ([11]). It is reported in (7.5) in its 1-dimensional formulation depends on the vapor generation rate Λ:

$$\frac{\partial x}{\partial t} + u\frac{\partial x}{\partial z} = \frac{\Lambda}{\rho} \quad . \tag{7.5}$$

A Taylor's expansion around equilibrium conditions, whose pertaining variables are $\bar{}$ superscripted, gives (7.6), τ is the CO_2 relaxation time as previously defined:

$$\frac{Dx}{Dt} = \frac{\bar{x} - x}{\tau} \quad . \tag{7.6}$$

The dependence of the instantaneous CO_2 vapor mass fraction x is therefore given by the following (7.7):

$$x(t) = \bar{x} - (\bar{x} - x|_{t=0})e^{t/\tau} \quad . \tag{7.7}$$

The CO_2 relaxation time τ is expressed in terms of the expected saturation conditions as reported in (7.8):

$$\tau = \tau_0 \left(\frac{x v_{g,sat}}{v}\right)^A \left(\frac{P_0 - P}{P_c - P_0}\right)^B \quad . \tag{7.8}$$

The reference to saturated conditions relies on $v_{g,sat}$ that is the gaseous CO_2 specific volume at the respective point along the saturation curve. In (7.8), while P is the instantaneous system pressure, P_0 is the pressure of the isentropic saturation point with respect to conditions defined by (P, v, x). For the CO_2 case, A = -0.54, B = 1.76 and τ_0 amounts to $2.14 \cdot 10^{-7}$.
The driving force introduced by the HRM approach with the aim of correcting the equilibrium hypothesis is averaged over the relaxation time; this approach essentially preserving the thermodynamic nature.
However, it should be noted that the formulation of (5.5-5.8) is not enough to give a complete description of the whole path to the final conditions across the vapor-liquid dome and the already introduced structural entropy increase should also be estimated.

7.4.2 The configuration probability and structural entropy concepts

Starting from Figure 7.3 it is clear that any expansion path from the liquid or supercritical domain may involve the passage through multi-phase domains. The usual situation is characterized by the occurrence of boiling mechanisms but it is possible that, if the expanding mixture reaches the triple point pressure with a certain amount of liquid, the solid appearance

cannot be ignored. The thermodynamic CO_2 behavior suggests therefore the establishment of conditions suitable for solidification and sublimation phenomena. Their irreversibility effect is quantified in terms of entropy increase that should be intended as a correction factor for all the situations diverging from the equilibrium establishment.

The quantification relies on the statistical rate theory and on the nucleation and sublimation mechanics. Therefore, as proposed by some authors ([5,11]), the approach firstly invokes the entropy definition to then move to the probability quantification related to a change in a certain system configuration.

It is known from the statistical thermodynamic that the probability of occurrence Θ of a certain system configuration (the most probable) is linked to its entropy content by the following relation (7.9) ([16]):

$$S = k_B \ln \Theta \quad . \tag{7.9}$$

Therefore, once a transition from two different configurations i and j is investigated, the expected probability of occurrence is estimated as in (7.10):

$$\Theta_{i \to j} = \Theta_j - \Theta_i = e^{\frac{S_j - S_i}{k_B}} \quad . \tag{7.10}$$

The entropy difference $S_j - S_i$ may be expressed in terms of other thermodynamic functions that are more suitable in the description of the expanding system.

This achieved by considering that the energy conservation law always holds during the expansion that is to assume that the system under investigation is isolated (from the energy point of view). A microscopic enthalpy balance linked to the assumption of no pressure and temperature differences among phases gives (7.11):

$$T_i dS_i = -dg_i \quad . \tag{7.11}$$

The application to the vapor-liquid CO_2 transition leads therefore to:

$$S_v - S_l = -\frac{g_v - g_l}{T} \quad , \tag{7.12}$$

that combined with (7.10) gives the probability to encounter a passage from the liquid to the gaseous phase:

$$\Theta_{l \to v} = e^{-\frac{g_v - g_l}{k_B T}} \quad . \tag{7.13}$$

It should be noted that the eventuality of some vapor to return back to the liquid domain cannot be excluded. The probability of a liquid-vapor transition is thus defined by the (7.14):

$$\Theta_{l\leftrightarrow v} = e^{-\frac{g_v - g_l}{k_B T}} - e^{-\frac{g_l - g_v}{k_B T}} \quad . \tag{7.14}$$

The meaning of (7.14) is that at equilibrium conditions $\Theta_{l\leftrightarrow v} = 0$ because the two constituting terms are equal, i.e. the probabilities are the same. Far from it, however, one of them may prevail on the other like in the case of liquid vaporization for which $\Theta_{l\to v} \gg \Theta_{v\to l}$. The configuration probability flux Π is then expressed depending on the obtained relations considered a Maxwell distribution $f(u)$ of the molecules velocity u:

$$\Pi = \Theta_{l\leftrightarrow v}\int_0^\infty f(u)du = \Theta_{l\leftrightarrow v}\sqrt{\frac{k_B T}{2\pi P M_{CO_2}}} = e^{-\frac{g_v - g_l}{k_B T}}\sqrt{\frac{k_B T}{2\pi P M_{CO_2}}} \quad . \tag{7.15}$$

7.4.3 Estimation of the structural entropy increase in the liquid-vapor transition

The structural entropy increase is postulated during a phase transition as reported in (7.10) and correspondingly, a variation in the Gibbs free energy is expected.

Along an isentropic depressurization path, some authors ([8]) reflected on the fact that the entropy conservation is not generally conceivable in open systems. In other words, a non-equilibrium driving force is expected dealing with an entropy increase and a variation in the system enthalpy. The sequence provides that the entropy increase and therefore that of the vapor mass fraction is linked to the distance between the constant enthalpy line and the isentropic curve.

The variation in the kinetic energy, that during the release is subjected to a relevant increase, tends to reduce this gap ([8]).

The estimation of the mass fraction variation because of non-equilibrium phenomena relies on the differential interphase energy balance. It is supposed that all involved heat is transferred between the interested phases. Given x_l the instantaneous liquid mass fraction, $c_{p,l}$ the liquid specific heat and L_v the latent vaporization heat, (7.16) expresses the energy balance:

$$x_l(T)c_{p,l}(T)dT = L_v(T)dx_l \quad . \tag{7.16}$$

The (7.16), before the numerical integration, is rearranged to give (7.17):

$$\frac{c_{p,l}(T)}{L_v(T)}dT = \frac{dx_l}{x_l(T)} \quad . \tag{7.17}$$

The integration is performed between the initial CO_2 conditions at the saturation border and those pertaining to the triple point location leading to (7.18):

$$\int_{T^{sat}}^{T_{tp}} \frac{c_{p,l}(T)}{L_v(T)} dT = \int_{1}^{x_{l,tp}} \frac{dx_l}{x_l(T)} \quad . \tag{7.18}$$

As indicated, (x.18) is integrated between the saturation temperature T^{sat} at which $x_l(T) = x_l(T^{sat}) = 1$ and the triple point condition characterized by a liquid quality equal to $x_{l,tp}$.

7.4.4 Estimation of the structural entropy increase in the solid-vapor transition

Once the triple point is reached, the CO_2 undergoes a solid-vapor transition. However, the final liquid-vapor point is not matching that pertaining to the solid-vapor region because of the occurrence of irreversible mechanisms strictly linked to the establishment of a nucleation barrier to be overcome.

The entropy increase occurring at the triple point location can be assessed by means of the Richard's rule ([8]) from which the nucleation entropy variation ΔS_{nucl} is equal to:

$$\Delta S_{nucl} = \frac{L_v(T_{tp})}{T_{tp}} \quad . \tag{7.19}$$

This entropy increase is represented in Figure 7.4 between point C and D.

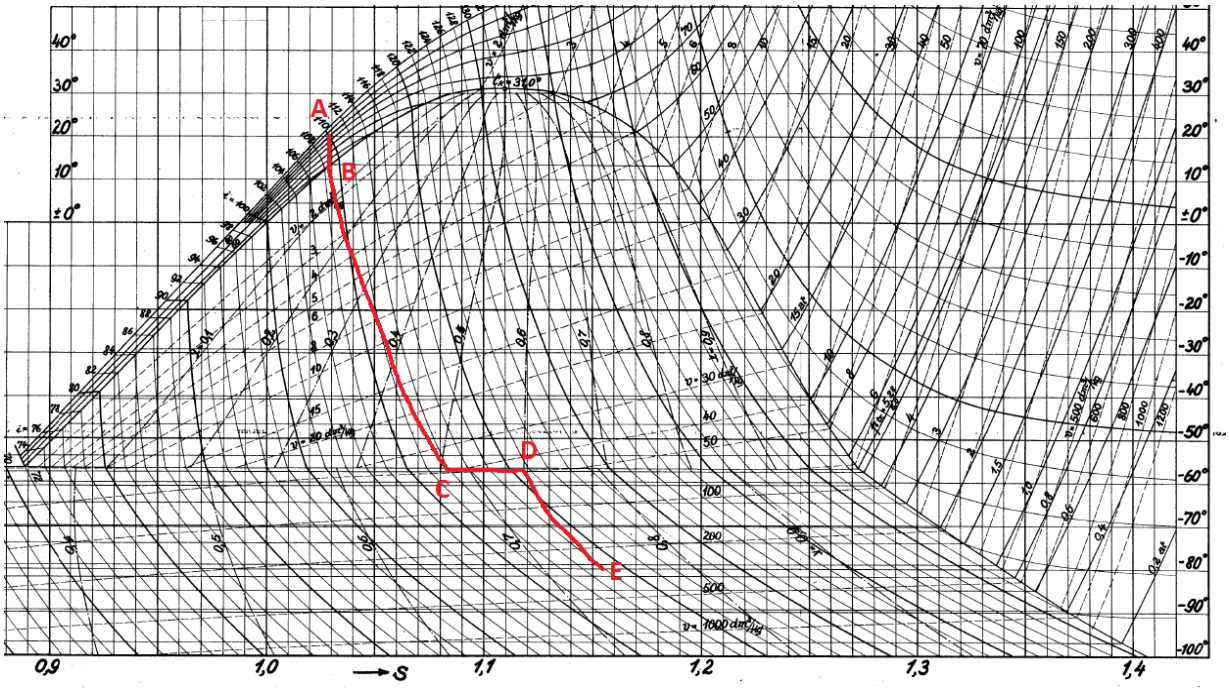

Figure 7.4. *Typical CO_2 atmospheric expansion on a entropy-temperature phase diagram ([14]) with the indication of the representative points along the depressurization path. From point C to D an entropy increase is expected because of the occurrence of irreversible phenomena.*

Considering Figure 7.4, the representative expansion starts from point A in the liquid domain down to point B which is located on the saturation line. As previously observed, specific CO_2 conditions may lead to a depressurization path initially following this curve to then move inside the VLE dome. Then the depressurization, with instantaneously variable mixture quality, reaches the triple point pressure (point C). The establishment of an energy nucleation barrier induces an entropy increase before the passage into the solid-vapor region. Finally, the system, characterized by a new incremented entropy content (D), reaches the atmospheric pressure corresponding to point E.

It should be noted that a phase diagram is only representative of equilibrium states. Therefore, in this sense, point D is not matching an equilibrium state because it is linked to a metastable condition that cannot be represented in a thermodynamic phase diagram. The linked enthalpy variation that is occurring because of the entropy variation is thus only apparent ([8]). Instead, the entropy change is irreversible and due to the liquid-solid transition across a nucleation energy barrier as defined in (7.3).

The modeling of the quality variation in the solid-vapor domain is performed in the same way as that formulated in the previous section. Therefore, considering the solid CO_2 properties, the same differential energy balance of (7.17) give the following integrated relation that holds from the triple point temperature to atmospheric conditions:

$$\int_{T_{atm}}^{T_{tp}} \frac{c_{p,s}(T)}{L_s(T)} dT = \int_{x_{s,atm}}^{x_{l,tp(D)}} \frac{dx_l}{x_l(T)} \quad . \tag{7.20}$$

where $c_{p,s}$ is the solid CO_2 specific heat, L_s is the latent sublimation heat and $x_{l,tp(D)}$ is intended as the liquid fraction at the triple point pressure corresponding to the increased entropy state formulated as in (7.19).

7.5 Incorporation of non-equilibrium issues to the developed model

This section is devoted to the results collection derived from the insertion of the discussed non-equilibrium issues. Specifically, the blowdown model has been complemented by the following non-equilibrium related aspects:

a. the structural entropy increase during the passage in the VLE dome because of nucleation-related phenomena;
b. the structural entropy increase at the triple point in the passage from the liquid-vapor to the solid-vapor region;
c. the presence of a relaxation time τ between the facing CO_2 phases evaluated as in (7.8);

7.5.1 Non-equilibrium expansion paths from dense to atmospheric conditions

Results concerning the variations in the expansion path followed by the CO_2 from stagnation conditions to atmospheric parameters are investigated in terms of taken up state variables.

The initial state, that is fully defined by the couple (P_0, T_0) or any other state variable couple, is matching the operative CO_2 conditions already discussed in the previous chapter. It pertains to the single-phase liquid or supercritical CO_2 because in real systems, as observed, an initial gaseous state very rarely results in a multiphase mixture under the investigated operative conditions.

The expansion from the initial state to the saturated conditions is not affected by non-equilibrium aspects since the domain is made of a unique phase not subjected to phase change mechanisms. Therefore, the predicted path toward the vapor dome boundary is untouched and it is matching the final conditions forecasted by the model and, as known, characterized by a certain (variable) degree of reversibility through the χ parameter.

Once the saturation point is reached and therefore with the appearance of a multiphase system, each facing phase is experiencing its own thermal dynamic depending on the instantaneous CO_2 relaxation time τ.

On this light, moving from the investigated expansion paths from the dense domain, further investigations are performed especially in what concerning the deviations introduced by the previously discussed additional non-equilibrium modeling hypothesis.

The initial investigation deals with the prediction of the pressure and temperature profiles of each phase that may occur during the discharge phenomenon. The occurrence of non-equilibrium phenomena are analyzed in terms of instantaneous temperature difference ΔT between the facing phases and, in detail, it is expressed as follows:

$$\Delta T = T_{dense\ phase} - T_{gaseous\ phase} \quad . \tag{7.21}$$

As a starting point, two representative transformations are investigated moving from an initial pressure of 60 and 150 barg. These are respectively matching the fully reversible and irreversible transformation that is a value of χ respectively equal to 1 and 0. This link to ideal transformations has been selected in order to primarily throw light on the expected thermal discrepancies that are affecting the facing phases.

Representative domain size is kept unchanged except for the pipeline length that is varied between 100 and 1000 m. At the same time, the d/D ratio is assumed to match a small (0.1) and a large rupture (0.4).

Figure 7.5 outlines the bulk ΔT evolution for a 100-m pipeline operated at 60 barg and 20 °C subjected to a small rupture. Results refer respectively to a completely irreversible (a) and reversible (b) transformation. Figure 7.6 is derived from the same expansion subjected to a large rupture.

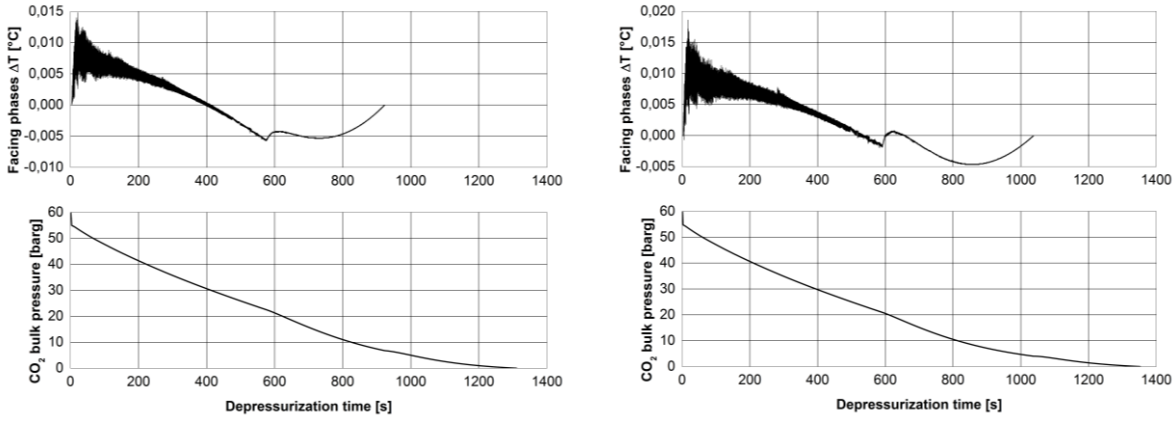

(a) *(b)*

Figure 7.5. *60 barg, 20 °C expansion with* $d/D = 0.1$. *Instantaneous temperature difference as expressed in (7.21) with respect to: a- completely irreversible, b- completely reversible transformation.*

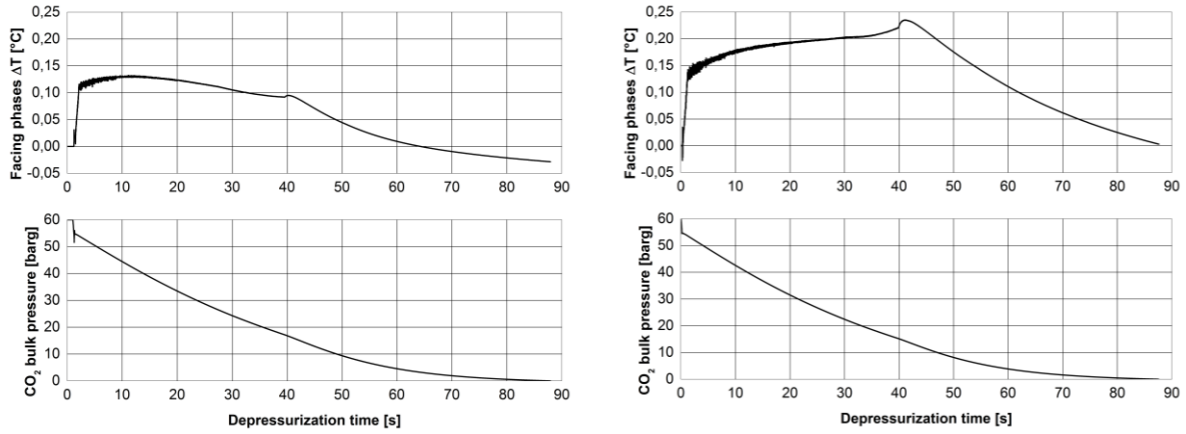

(a) *(b)*

Figure 7.6. *60 barg, 20 °C expansion with* $d/D = 0.4$. *Instantaneous temperature difference as expressed in (7.21) with respect to: a- completely irreversible, b- completely reversible transformation.*

Figure 7.5-7.6 show that both the orifice size and the supposed transformation nature are inducing modifications on the equilibrium between facing phases. The introduction of the aforementioned irreversible mechanisms leads to a difference in their instantaneous temperatures.

The hypothesis of fully reversible transformation gives more restrained temperature differences with respect to the imposition of an irreversible mechanism. The deviation is more effective with larger orifice sizes since the induced temperature gradients are larger as

observed in the previous chapters. These observations are valid for all the investigated releases involving a liquid charge.

More precisely it should be noted that a variation in the orifice size has the effect of increasing the temperature differences up to one orders of magnitude. With respect to Figure 7.5-7.6, the increase of d/D from 0.1 to 0.4 leads to a amplification of temperature gradients from a maximum value of 0.01 to 0.12.

Under the conditions related to Figure 7.5-7.6, temperature alterations with respect to the equilibrium profiles are almost negligible. The negligibility is measured upon the induced density variations that, with a ΔT amounting to fractions of a degree centigrade, are almost insensitive to the introduction of the non-equilibrium approach. Predictions show that the maximum density percentage variation under the altered thermal field is restricted to 1-2 %. At the same time, the depressurization profile is not experiencing any variation and therefore also the total discharge time is conserved. However, as already observed, the introduction of a different expansion path influences the total discharge time that is larger with a release through a small orifice.

Once the orifice size is increased and the temperature difference enlarges (Figure 7.5), a modification in the depressurization path is observed even if not so significant. Temperature differences between facing phases are wider mainly because of the incremented and more rapid boiling mechanisms induced by large pressure gradients.

It should also be mentioned that in the initial steps of the release evolution, the dense phase is always characterized by a higher thermal content that tends to decrease with the pressure decline. This is due to the incorporation of metastability phenomena in the process description that are strictly linked to the boiling onset at temperatures slightly higher than the saturation level.

The whole temperature difference trend, that is varying with d/D once the initial operative conditions and the pipe geometry are fixed, can be generally considering the steps below indicated.

Firstly, the initial increase is occurring when the CO_2 is expanding along the saturation line. Because of the lack of equilibrium, the pathway is not matching the VLE border but is located in its close proximity, inside the dome. This means that very low amount of vapor is produced even if boiling mechanisms are taking place. The produced vapor has always a temperature lower than that of the liquid bulk. Results show that the location of the pathway with respect to the dome border is primarily depending upon the initial charging pressure. Higher values matching larger d/D values tend to increase the gap between the effective pathway and that along the saturation curve. Corresponding ΔT values are larger. Starting from a pressure of

150 barg with $d/D = 0.4$, results give $\Delta T_{max} \cong 4.2\,°C$ that is lowered to 2.9 °C with $d/D = 0.1$.

Subsequent ΔT evolution is depending on the specific release features, especially in what concerning the dense phase content, but some common aspects can be underlined and directly exported from Figure 7.5-7.6. Focusing on Figure 7.5, a subsequent ΔT is observed and is taking place again during the decrease near the saturation border. This trend tends to vanish once the expansion definitively moves to the facing VLE border, i.e. when the instantaneous produced vapor is increasing. At this point, some simulations show that the liquid mass is colder than the produced light phase ($\Delta T < 0$) and this occurrence is more likely under increasing irreversible conditions (Figure 7.5a). Following the expansion evolution, the next ΔT trend is not regular but the tendency is to restore the thermal equilibrium. This is corresponding to the boiling occurrence inside the VLE dome and therefore to increasing vapor quality. As indicated in Figure 7.5, final steps are characterized by $\Delta T = 0$ because of the presence of the only gaseous phase.

This trend, even if qualitatively depending on the releases specs, is observed when the release is not producing a final bi-phase mixture. The latter determining a different ΔT evolution as indicated in Figure 7.6. The initial development is similar to that previously discussed but the tendency is to have a dense phase almost always warmer than the produced light phase. In addition, a discontinuity is observed at about $\mathrm{t} \approx 40$ s matching the departure from the VLE liquid border. A similar decreasing trend is then observed following the boiling occurrence but differences arise because the release evolution leads the CO_2 in the solid-vapor domain that is achieved once $P < P_{tr}$.

Additional simulations show that an increase in the CO_2 domain, i.e. in the pipeline length up to 1000 m, plays a role in modifying the magnitude of ΔT. In fact, the ΔT experienced by the CO_2 in 1000 m-long pipelines, are slightly increased with a maximum amplification amounting to about 2 times.

However, the main governing parameter on the ΔT magnitude is the charging pressure. In fact, an increase in the operative pressure up to 150 barg determines clear variations both in the ΔT magnitude and profile.

As a title of example, Figure 7.7 gives the ΔT trend of a 100 m-long pipeline charged at 150 barg subjected to a large rupture.

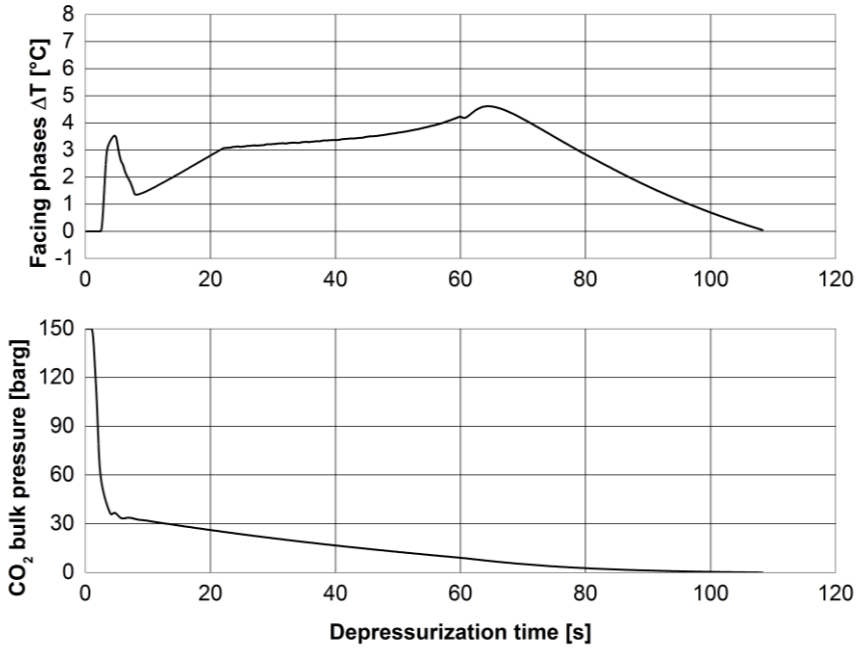

Figure 7.7. *150 barg, 20 °C expansion with* $d/D = 0.4$*. Instantaneous temperature difference as expressed in (7.21) with respect to a completely reversible transformation.*

It is clear how the introduction of the non-equilibrium hypothesis once the operative pressure is enhanced is a decisive factor in governing the release dynamics. The enhanced operative pressure is acting enlarging the thermal disequilibrium between the facing phases that, as indicted in Figure 7.7, may amount up to 2-4 °C with largest gaps growing with the occurrence of the boiling mechanisms. The forecasted ΔT_{max} tendency with respect to the operative pressure is reported in Figure 7.8.

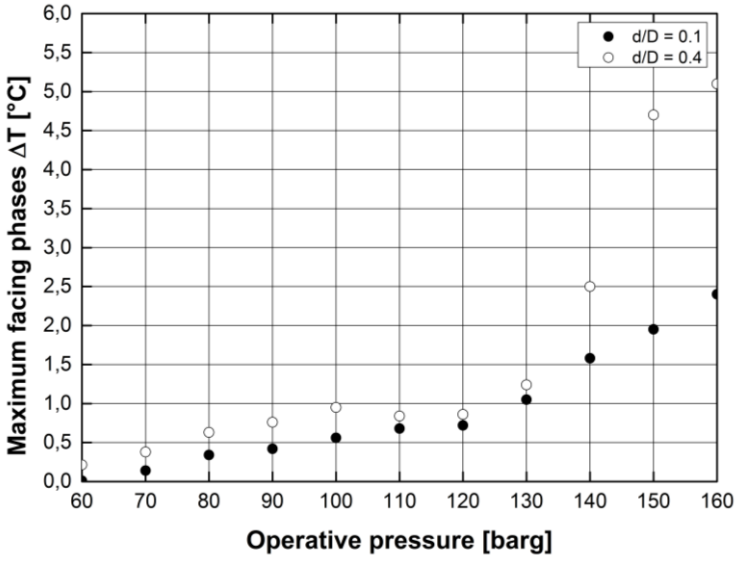

Figure 7.8. *Maximum predicted temperature difference between facing phases under different initial operative pressures and orifice sizes.*

The difference in the phases temperatures becomes apparent over 100 barg corresponding to $\Delta T > 0.5\,°C$ but enlarges considerably for higher pressure values. In the EOR and CCS operative range, ΔT may amount up to 5.2 °C under the condition of $d/D = 0.4$. The effect of the d/D increase is significant over a pressure of 140 barg.

The CO_2 carried in longer pipelines experience a similar rising trend with respect to both the operative pressure and orifice size but the temperature difference is never larger than 8-9 °C.

In addition, no relevant effects are laid at the initial operative temperature in the usual operative range.

It is interesting to investigate the consequences related to these temperature difference on the main release parameters to throw light on the convenience of complicating the model by means of non-equilibrium concepts.

The analysis is performed with respect to widest recorded temperature differences, i.e. for a 100 m-long pipeline charged at 150 barg and subjected to a large rupture. The expansion is supposed to occur following a fully reversible transformation and the comparison with the neglecting non-equilibrium effects is performed.

The occurrence of a temperature difference is primarily acting on the instantaneous phase specific volume that is directly linked to the mass flow rate discharged from the system. The comparison with the base case neglecting non-equilibrium features is reported in Figure 7.9. The representation is referred to the light phase since the dense one is almost insensitive to ΔT of this order of magnitude.

As depicted in figure 7.9, two are the main effects related to the introduction of a non-equilibrium approach.

The first one is related to a difference in the instantaneous density mixture that is evident at the boiling onset (between 55 and 60 s in Figure 7.9). The prediction of a certain degree of non-equilibrium between phases is responsible for a delay in the boiling mechanisms as testified by the delayed density decreased that is due to the vapor production. The subsequent boiling evolution, if compared in dimensionless terms, shows some differences and this is also testified by the varied dense quality evolution of Figure 7.9. It should be noted that the dense content evolution is indicating that the final release states are determining a solid-vapor mixture. The appearance of the solid CO_2 is observed at a dimensionless time in the range 0.61-0.64.

The predicted instantaneous dense mixture content is always higher than that predicted without assuming non-equilibrium phenomena. However, once the CO_2 has passed the triple point pressure, the predicted solid content is lower than the corresponding equilibrium value and this is testified by the reducing gap between the quality curves of Figure 7.9.

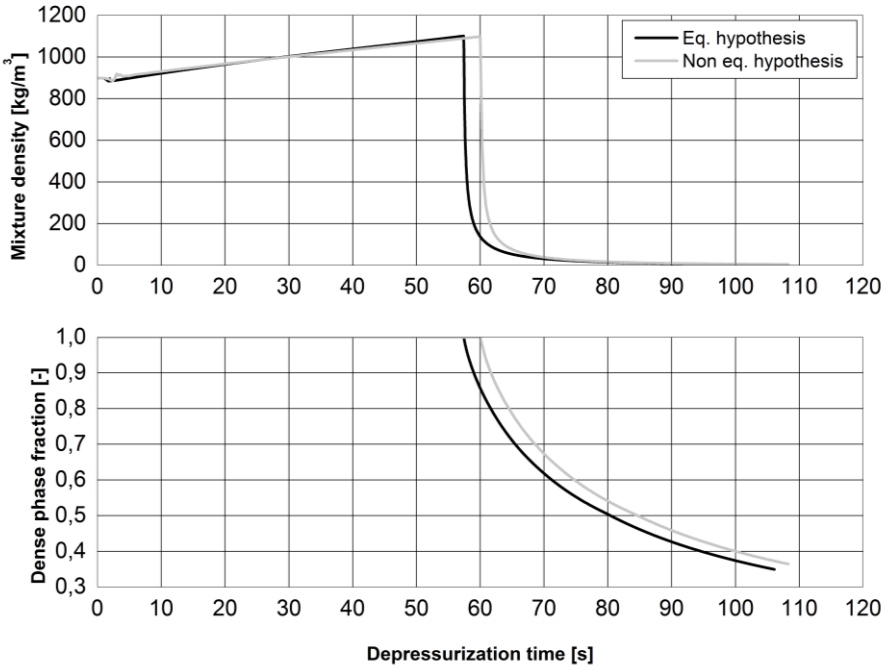

Figure 7.9. *Predicted bulk instantaneous mixture density and dense quality following the equilibrium and non-equilibrium hypothesis.*

The reason is due to the structural entropy increase across the triple point as modeled in (7.19-7.20). In this sense, the passage across the triple point is corresponding to an entropy increase required to overcome the energy barrier related to the nuclei formation. The energy conservation principle therefore imposes a new entropic state.

Practically, results show that this occurrence is altering the pathway inside the solid-vapor region resulting in a final altered solid content with respect to equilibrium predictions.

The quantification of this entropy jump shows that this amounts to 0.159 kJ kg^{-1} K^{-1} and depending on the post-expanded state at the triple point, the quality variation from the liquid to the solid amount has different magnitudes. The resulting pathway evolution is therefore altered leading to modified atmospheric conditions. Results are discussed below.

Different depressurizations from fixed operative conditions (pertaining to the dense domain) are performed starting from 60 to 150 barg. In addition, different initial temperatures have been considered always with respect to usual working conditions.

Following Table 7.1 lists the CO_2 characteristic states along the depressurization path pertaining to the triple and the atmospheric final point.

The first relevant result is related to the generalized increase in the triple point vapor fraction. Because of the predicted structural entropy increase, the forecasted increase is in the range 0.09 – 0.16 indicating that, at the triple point, the real mixture is characterized by a lower

dense content. The final state along the triple point locus is the result of the altered expansion mechanism that is starting from a state pertaining to the metastable region.

Table 7.1. *Predicted CO_2 states along the completely reversible depressurization path under equilibrium and non-equilibrium hypothesis.*

Initial conditions		Equilibrium triple point vapor quality [-]	Non - equilibrium triple point vapor quality [-]	Atmospheric vapor quality [-]	Atmospheric post – expanded temperature [°C]
P_0 [barg]	T_0 [°C]				
60	20	0.401	0.489	0.652	-81.5
60	10	0.353	0.448	0.625	-82.1
60	0	0.286	0.395	0.598	-84.6
100	20	0.351	0.505	0.658	-90.8
100	10	0.314	0.412	0.589	-92.5
100	0	0.264	0.365	0.561	-95.2
150	20	0.344	0.451	0.634	-96.6
150	10	0.302	0.395	0.587	-97.1
150	0	0.251	0.358	0.568	-99.5

It should be considered that the boiling process starts inside the vapor dome and therefore the initial state is not matching the saturated one and, in addition, the pathway evolution along the saturation curve is not observed. The location of this metastable point depends on the initial CO_2 conditions. Predictions give reason to state that this subcooled state is almost matching the saturation pressure but its thermal content is lower. Only by way of explanation, this state is mapped on a pressure-specific volume diagram in Figure 7.10 even if the diagram is representative of equilibrium states that are not therefore pertaining to this metastable condition.

Figure 7.10 shows that releases starting from an initial pressure above about 50 barg are giving a metastable state involving a certain degree of subcooling. An increase in the storage pressure is enlarging this gap even if the expected thermal difference is keeping almost unchanged and in the range 2.5-7 °C.

Results are confirming that, once the CO_2 has reached this metastable state, the boiling mechanism takes place driving it through an almost constant quality curve down to a new point. The following effective boiling transformation is then responsible to the pathway down to the triple point pressure whose pertaining states are listed in the second column of Table 7.1.

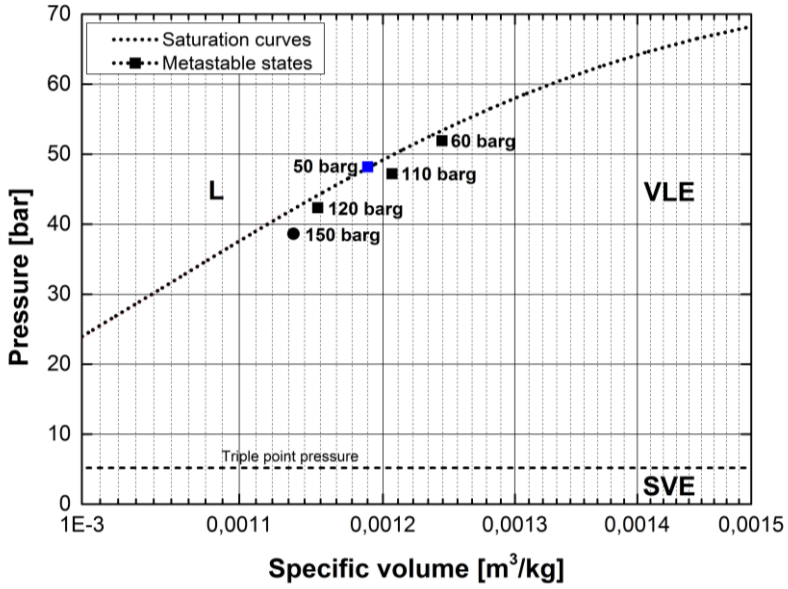

Figure 7.10. *Vapor-liquid metastable states following depressurizations from specified initial CO_2 pressures.*

The enrichment in the light phase below this pressure value is mainly governed by this metastable state as well as the final mixture temperature. The latter is significantly below the atmospheric equilibrium value (-78.4 °C) and this is also testified by many of the investigated experimental trials ([17,18]). This result is due to the incorporation of latent heat effects as well as the non-equilibrium aspects discussed above and it is clear how the isentropic mechanism, usually involved in QRA studies, is in this way overcome. However, as discussed by some authors ([11]), the isentropic expansion is not preserved only in the vapor-liquid region down to the triple point pressure. More precisely, the expansion reversibility degree is lower in that region with respect to the solid-vapor domain.

In this sense, results give reason to state that a completely reversible transformation is not allowable in the description of the CO_2 expansion from pressures above 50-60 barg. Simulations show that the degree of reversibility is changing between 0.82-0.94 and 0.96-0.98 in the passage across the triple point. The increase in the reversibility once the solid phase is appeared is due to the limited change in the mixture quality after the triple point as observed in Figure 7.9. From a thermodynamic perspective, the expansion is almost occurring in an adiabatic way and the very small mixture vapor content variation results therefore in a conservation of the mixture entropy.

It should be noted, with respect to Table 7.1, that the initial charging temperature is determining the atmospheric post-expanded conditions but is not substantially altering the reversibility degree of the expansion.

7.5.2 Practical implications of the introduction of non-equilibrium features

The introduction of the non-equilibrium description may have some results on the practical perspective in the release modeling. As observed, the incorporation of the discussed features, alters the pathway evolution, the behavior in the bi-phase domains, the passage across the triple point and the final atmospheric state.

The QRA requirement, however, does not pay attention to the detailed mechanisms but to the comprehensive effect on the release dynamic and its main parameters then used to assess the substance dispersion (released flow rate, released mixture quality and total discharge time).

Therefore, on this perspective, the variations in these main parameters will be discussed with respect to the base case involving the equilibrium hypothesis.

The released flow rate is sensitive to the instantaneous mixture density which in turn is influenced by the following parameters:

- mixture quality;
- expansion pathway, i.e. instantaneous pressure gradients and temperature magnitude;
- orifice size.

The first two points involve aspects related to the expansion nature while the latter is strictly related to the domain under investigation. However, even passing through the mass flux (massive flow rate of substance per unit cross section), the dependence from the orifice size does not fall. This because the orifice size through the d/D ratio is influencing both the expansion pathway and the non-equilibrium effects magnitude and finally the instantaneous CO_2 state.

The conditions pertaining to moderate charging pressure (P < 60-80 barg), short pipelines (L < 500-800 m) and small ruptures are put aside because of negligible comprehensive non-equilibrium effects on the global discharge dynamics.

Focusing on large ruptures, following Figure 7.11 it is clear the effect of the introduction of the non-equilibrium description. The main consequence is a deep alteration of the discharged mass flow rate, i.e. the mass evolution in time.

The alteration is observed for both the light and the dense phase and the non-equilibrium features are determining a delay in the phase-change mechanisms. Globally, the total discharge time is longer and results show that this increase may amount up to 45 %. This is the result of the effect of the thermal unbalances between the facing phases leading to a gap in the instantaneous density whose effect is then observed in the discharged mass flow rate. The additional variation in the expansion pathway is also responsible for the alterations in the depressurization dynamics especially in what concerning the pressure profile and the boiling

start point. The metastable states observed in Figure 7.10 are determining different evolutions inside the vapor dome.

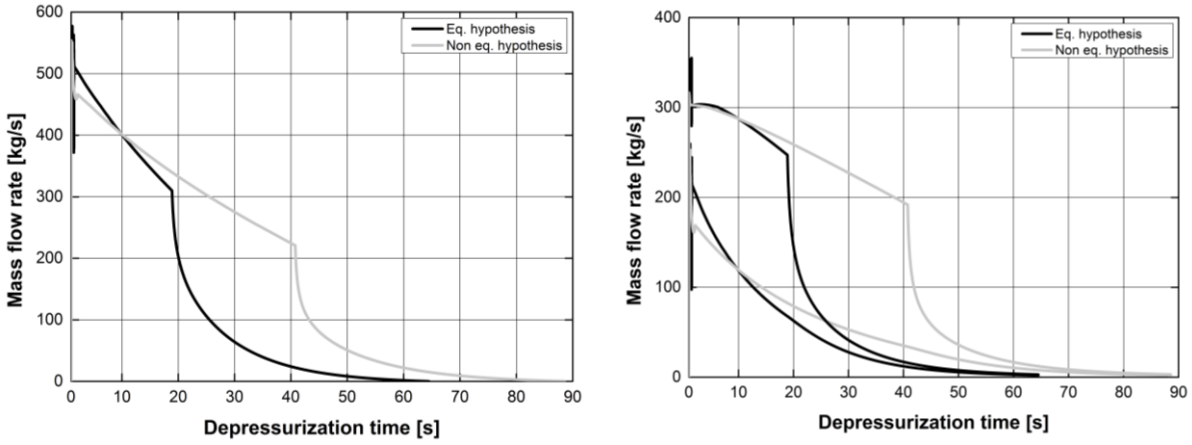

Figure 7.11. *Effect of the non-equilibrium hypothesis on a- the total discharged mass flow rate; b-light and dense phase mass flow rates. 100 m pipeline, $d/D = 0.4$, 60 barg and 20 °C.*

Resulting CO_2 dense fractions are reported in Figure 7.12 with respect to the bulk and the orifice state.

The general behavior observed in Figure 7.12 shows that the equilibrium trend leads to final states characterized by a higher vapor content even if boiling mechanisms are brief. In addition, forecasted orifice dense mass fractions are lower if the non-equilibrium hypothesis is neglected with peaks at 0.55-0.78 depending on the initial charging pressures.

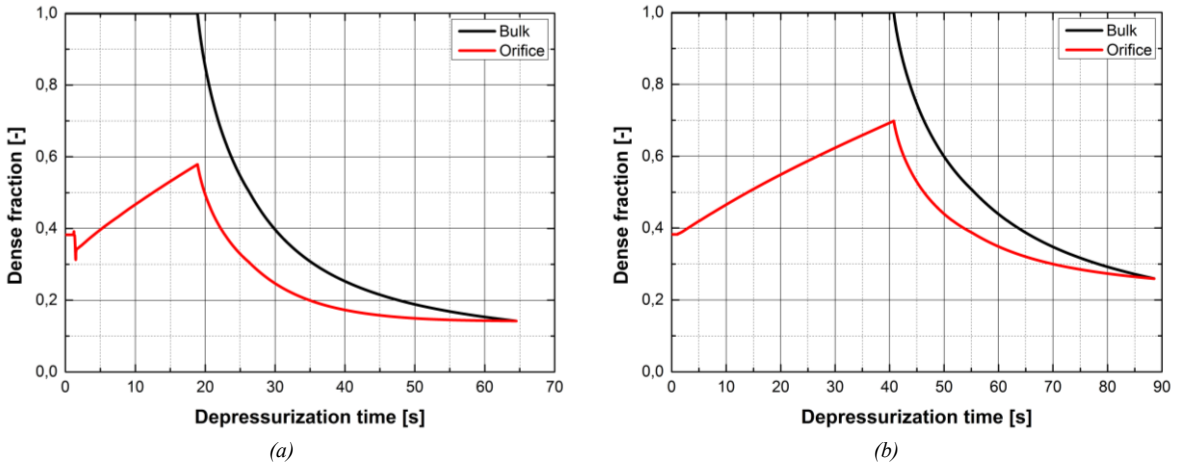

Figure 7.12. *100 m pipeline, $d/D = 0.4$, 60 barg and 20 °C. a- equilibrium; b- non equilibrium mas dense fraction.*

From a QRA perspective, the incremented amount of the orifice dense fraction is essential in determining the subsequent atmospheric near-field dispersion since part of the liquid and finally of the solid phase (after the passage across the triple point pressure) will give a sublimating dry ice bank soil deposition.

Once the pipeline length is increased, for example up to 1000 m, observed gaps in the total discharge time are more limited. Results show that a general increment in the total CO_2 inventory induced by a domain size increase, has the effect of reducing the influences of the non-equilibrium issues on the time-to-complete discharge. Observed phase change plateau is still sensitive to the adopted hypothesis and the instantaneous mixture density exhibits lower values compared to the 100-m long pipeline giving therefore reason to the longer release time.
From the CO_2, dense fraction perspective, the lack of equilibrium is not altering the fact that solid CO_2 is observed at the orifice only for pipeline lengths below 1500 m subjected to d/D > 0.3 and P > 55 barg. The only difference is related to the lower expected amount of solid CO_2 throughout the whole release because of the varied expansion pathway. In general, the difference amount in the cumulative solid released mass is below 5-8 % with respect to the base case.
Results pertaining to pipelines operated at higher pressures, show discrepancies depending on the release orifice size. For operative pressures up to 150 barg, this threshold value is equal to 0.25 and it discriminates the system behavior under the non-equilibrium hypothesis.
Ruptures that are taking place with $d/D < 0.25$ induce differences in the blowdown dynamics only in the case of very short pipelines (i.e. $L < 500\,m$). In this case, main differences are observed in the phase change steps, especially in what concerning the boiling phase. Longer times-to-boiling-end are expected whose increase is directly related to the charging pressure. On a dimensionless basis, this parameter ranges between 2 to 10 % in the range 60-150 barg. The released mass flow rate during boiling is consequently lower than the base case but it is negligibly affecting the subsequent dispersion step;
Under the condition $d/D > 0.25$, major differences in the main blowdown parameters are observed with a decreasing pipeline length. The thermal differences between the facing phases have the result of globally lowering the dense phase amount that is discharged from the system. The QRA procedure therefore should deal with the occurrence of mixtures that are rich in the light phase primarily because of the enhanced boiling mechanisms. Following Table 7.2 gives the time averaged value of the dense quality that is discharged from pipelines with indicated specifications.
Table 7.2 is also giving the forecasted percentage variation in the total discharge time with respect to the base case neglecting non-equilibrium sources.
Differences in the total discharge time predictions are linked to the varied phase densities but are always below the 10 % under pipeline lengths above 1000 m.

Table 7.2. *Expected CO_2 dense mixture quality discharged from the specified pipeline under the non-equilibrium hypothesis.*

Initial conditions [barg]	Pipeline length [m]	d/D [-]	Dense quality [-]	Total discharge time variation [%]
80	1000	0.3	0.24	+4.5
80	1000	0.4	0.28	+5.1
80	10000	0.3	0.21	+1.5
80	10000	0.4	0.23	-0.1
120	1000	0.3	0.26	+4.9
120	1000	0.4	0.31	+5.2
120	10000	0.3	0.24	+1.5
120	10000	0.4	0.26	+0.5
150	1000	0.3	0.28	+9.1
150	1000	0.4	0.33	+9.0
150	10000	0.3	0.24	+3.5
150	10000	0.4	0.25	+3.1

It should be noted however that the percentage datum is strictly linked to the investigated scenario being the discharge time sensitive to the orifice and the pipeline size.

To conclude, the introduction of the non-equilibrium features alters the QRA predictions.

The negligibility of this approach is applicable only for specific real situations but once employed it is clear that the further model improvement and complication should be assessed with respect to the QRA purposes.

The inclusion of supplementary equations will increase the computational burden that is reflected on a run time rise up to +20 %.

However, as discussed, some scenarios are mainly driven by the occurrence of non-equilibrium phenomena and a QRA analysis neglecting these aspects will lead to wrong predictions.

This specifically applies to very short pipeline segments subjected to large ruptures or under increasing operative pressures. In such situations, inaccuracies should be expected especially in what concerning the instantaneous vapor quality at the orifice, the mixture density and therefore the total discharge time.

However, it should be noted that very short pipelines are generally the result of very intensive sectioning interventions or are matching pipeline stacks inside industrial sites. The practical interest of these situations should however be discussed since they may be of very limited hazard impact.

References to Chapter 7

1. Kornneef, J., Spruijt, M., Molag, M., Ramirez, A., Faaij, A., Turkenburg, W., 2009. Uncertainties in risk assessment of CO_2 pipelines. Energy Procedia, 1(1), 1587-1594.
2. Bird, R.B., Stewart, W.E., Lightfoot, E.N., Transport Phenomena. John Wiley and Sons, 2nd ed., 2007.
3. Mahgerefteh, H., Brown, S., Martynov, S., 2012. A study of the effects of friction, heat transfer and stream impurities on the decompression behavior in CO_2 pipelines. Greenhouse gases: science and technology 2, 369-379.
4. Zemansky, 1968. Heat and Thermodynamics. Mc-Graw Hill Book Company.
5. De Groot, S.R., Mazur, P., 1984. Non-equilibrium Thermodynamics, Dover Books, Leiden, NL.
6. Witlox, H.W.M., Harper, M., Oke, A., 2009. Modelling of discharge and atmospheric dispersion for carbon dioxide releases, Journal of loss prevention in the process industries, 22, 795-502.
7. Webber, D.M., 2011. Generalizing two-phase homogeneous equilibrium pipeline and jet models to the case of carbon dioxide. Journal of loss prevention in the process industries, 24, 356-360.
8. Martynov, S., Brown, S., Mahgerefteh, H., Sundara, V., 2013. Modelling choked flow for CO2 from the dense phase to below the triple point. International journal of Greenhouse Gas Control, 19, 552-558.
9. Engelmeier, L., Pollak, S., Kilzer, A., Weidner, E., 2012. Jet cutting with liquid carbon dioxide, 10th International Symposium on Supercritical Fluids, San Francisco, USA.
10. Witlox, H.W.M., Stene, A., Harper, M., Nilsen, S.H., 2011. Modelling of discharge and atmospheric dispersion for carbon dioxide releases including sensitivity analysis for wide range of scenarios. Energy procedia, 4, 2253-2260.
11. Benintendi, R., 2014. Non-equilibrium phenomena in carbon dioxide expansion, Process Safety and Environmental Protection, 92, 47-59.
12. Vincenti, W.G., Kruger, C.H., 1965. Introduction to Physical Gas Dynamics, Wiley.
13. Lu, Zh.Q., 2002. Two-phase flow and boiling heat transfer. Tshinghua University Press, Beijing.
14. Plank, R., Kuprianoff, J., 1929. Die thermischen Eigenschaften der Kohlensaure im gasformingen, flussigen und festen Zustand, Mitteilung aus dem Kaltetechnischen Institut der Technischen Hochschule, Berlin.
15. Lu, Zh. Q., 2002. Two-phase flow and boiling heat-transfer. Tshinghua University Press, Beijing.
16. Le Bellac, M., Mortessagne, F., Batrouni, G.G., 2010. Equilibrium and non-equilibrium statistical thermodynamics, Cambridge University Press, UK.

17. CO_2PipeHaz, 2009. Quantitative failure consequence hazard assessment for next generation CO_2 pipeline: the missing link. In: Description of Work of the Grant Agreement for FP7 Cooperation Work Programme 241346-2-CO2PipeHaz (CP), 1-83. www.co2pipehaz.eu
18. 2013. CO_2PIPETRANS Project (DNV).

Chapter 8

Model Application to Some Real Existing CCS and EOR Projects

8.1 Introduction

In the present section, the proposed model is applied to existing CO2 handling infrastructures. Selected technical data and declared operative conditions are derived from the technical documentation and are used in the model, without any modifications, to obtain specific release parameters profiles and values that may be used in QRA procedures.

Following data are derived and reported:

- pressure, density and total mass flow rate profiles in time;
- dense fraction profiles in time in the pipeline bulk and at the orifice;
- total discharge time;
- average mass flow rate during phase change mechanisms and their duration in time;
- occurrence of solid phase;
- minimum reached temperature in the pipeline bulk.

Pipelines sectors are supposed to be 1000 and 5000 m long and accidental ruptures small and large that is respectively with $d/D = 0.1$ and 0.4.

Three existing CCS and EOR projects are considered:

1 Cortez Pipeline (Kinder Morgan), Texas-United States of America;

2 Canyon Reef Carriers Pipeline (Kinder Morgan), Texas-United States of America;

3 Snøhvit Pipeline (Statoil), Norway-Europe.

8.2 Infrastructures' specifications

8.2.1 Cortez pipeline, U.S.A.

Table 8.1. *Project 1 specifications.*

Location	Operator	Capacity [Mton/yr]	Length [km]	Diameter [mm]	Pressure [bar]	CO_2 source	Year
TX, USA	Kinder Morgan	19.3	803	726 (30")	186	McElmo Dome	1984

8.2.2 Canyon Reef Carriers pipeline, U.S.A.

Table 8.2. *Project 2 specifications.*

Location	Operator	Capacity [Mton/yr]	Length [km]	Diameter [mm]	Pressure [bar]	CO_2 source	Year
TX, USA	Kinder Morgan	4.4	352	400 (16")	140	Gasification plant	1972

8.2.3 Snøhvit pipeline, Norway.

Table 8.3. *Project 3 specifications.*

Location	Operator	Capacity [Mton/yr]	Length [km]	Diameter [mm]	Pressure [bar]	CO_2 source	Year
NORWAY, EUROPE	Statoil	0.7	153	200 (8")	100	Amine CO_2 plant	2006

8.3 Simulations results. Cortez pipeline, U.S.A.

8.3.1 1000 m, small rupture

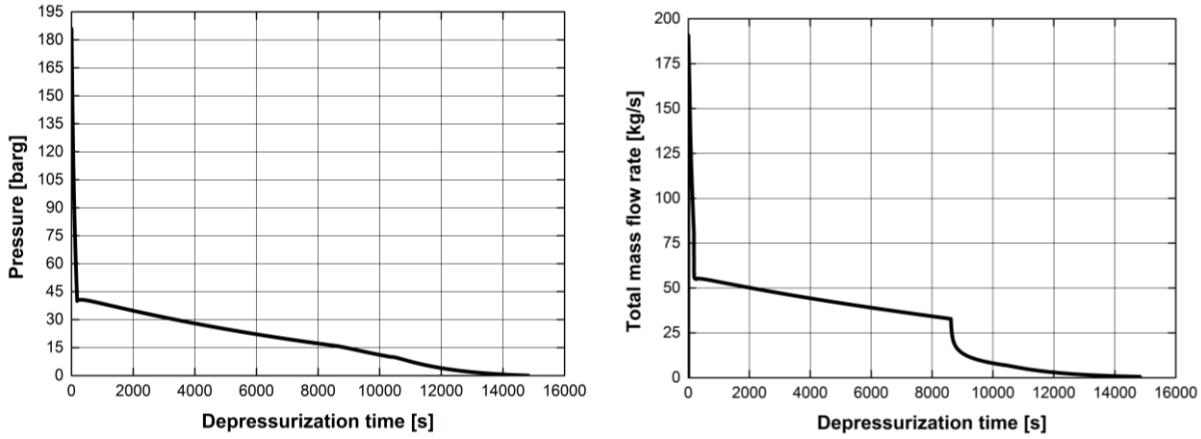

(a) *(b)*

Figure 8.1. *a- pressure time evolution; b- total released mass flow rate time evolution.*

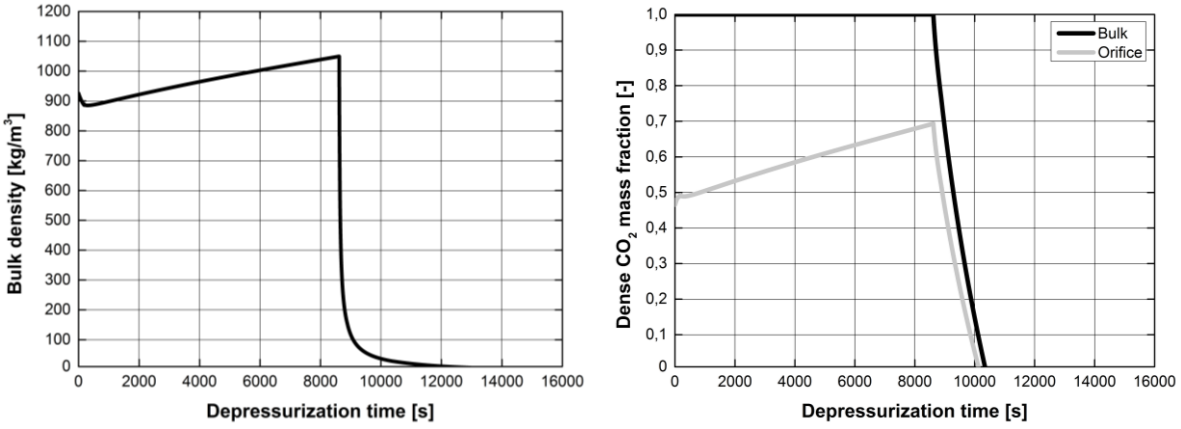

(a) *(b)*

Figure 8.2. *a- bulk density time evolution; b- dense CO_2 mass fraction time evolution.*

Total discharge time	3.7 h
Time to complete bulk boiling	2.1 h (57%)
Average mass flow rate during bulk boiling	3.22 kg/s
Occurrence of solid phase	no
Average expansion degree of reversibility χ	0.76
Minimum bulk temperature	-11 °C
Total average computational runtime	18 min

8.3.2 1000 m, large rupture

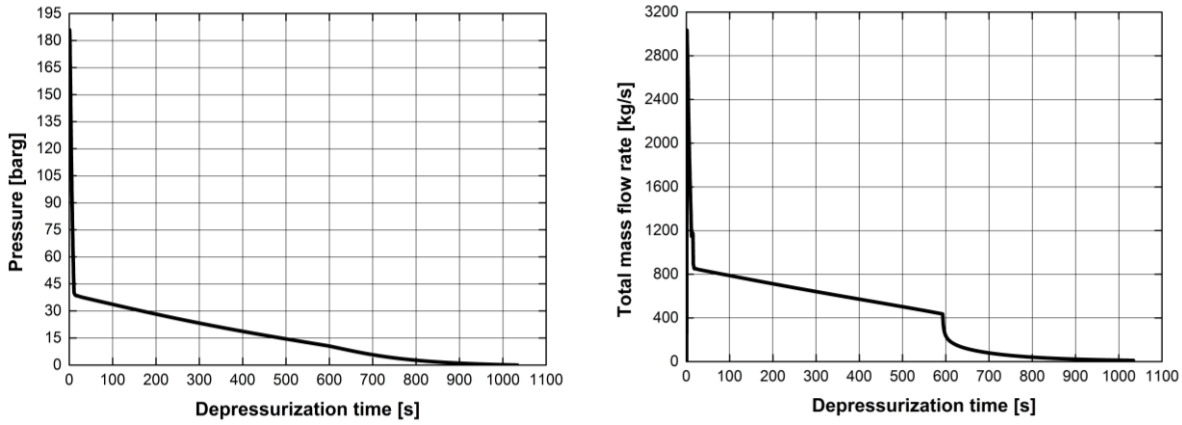

(a) *(b)*

Figure 8.3. *a- pressure time evolution; b- total released mass flow rate time evolution.*

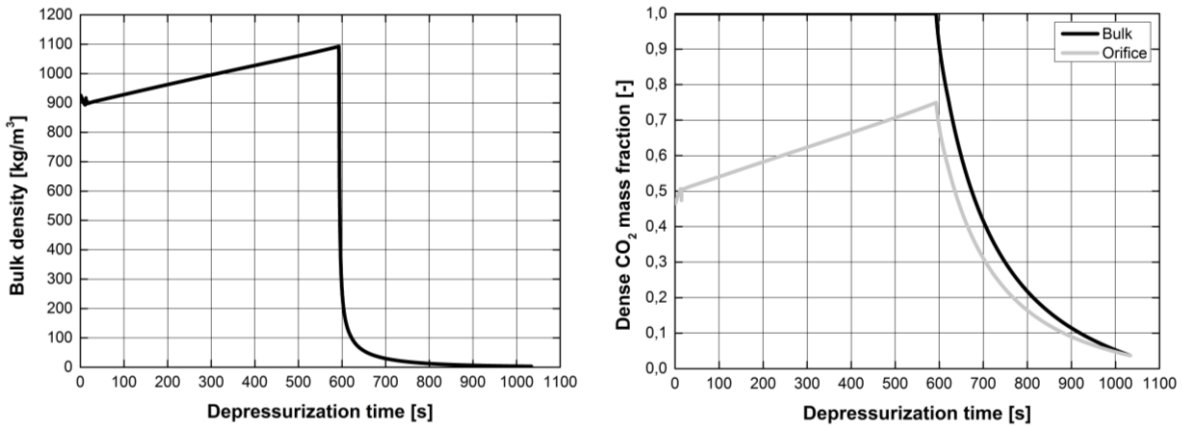

(a) *(b)*

Figure 8.4. *a- bulk density time evolution; b- dense CO_2 mass fraction time evolution.*

Total discharge time	0.34 h
Time to complete bulk boiling	0.28 h (82%)
Average mass flow rate during bulk boiling	28.1 kg/s
Occurrence of solid phase	yes (bulk and orifice), after 0.23 h
Average expansion degree of reversibility χ	0.83
Minimum bulk temperature	-60 °C
Total average computational runtime	14 min

8.3.3 5000 m, small rupture

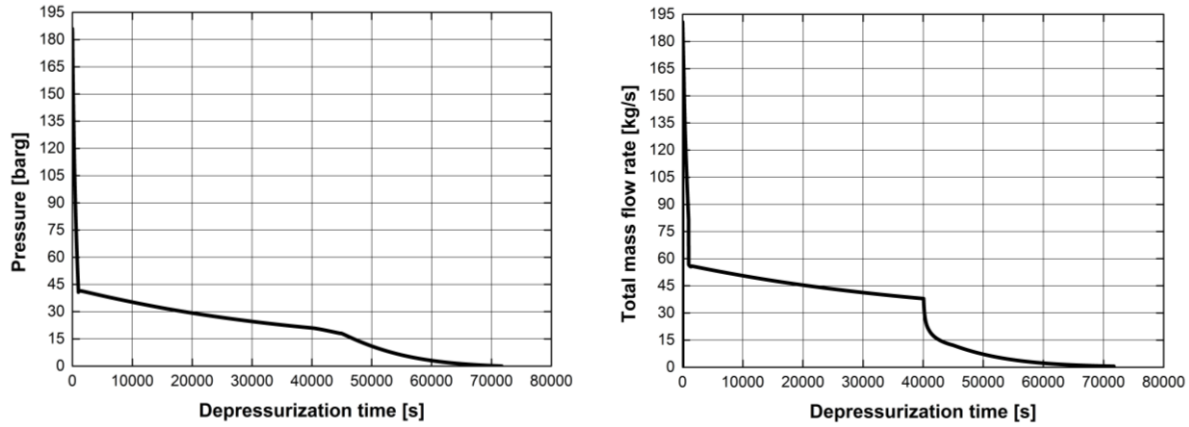

(a) *(b)*

Figure 8.5. *a- pressure time evolution; b- total released mass flow rate time evolution.*

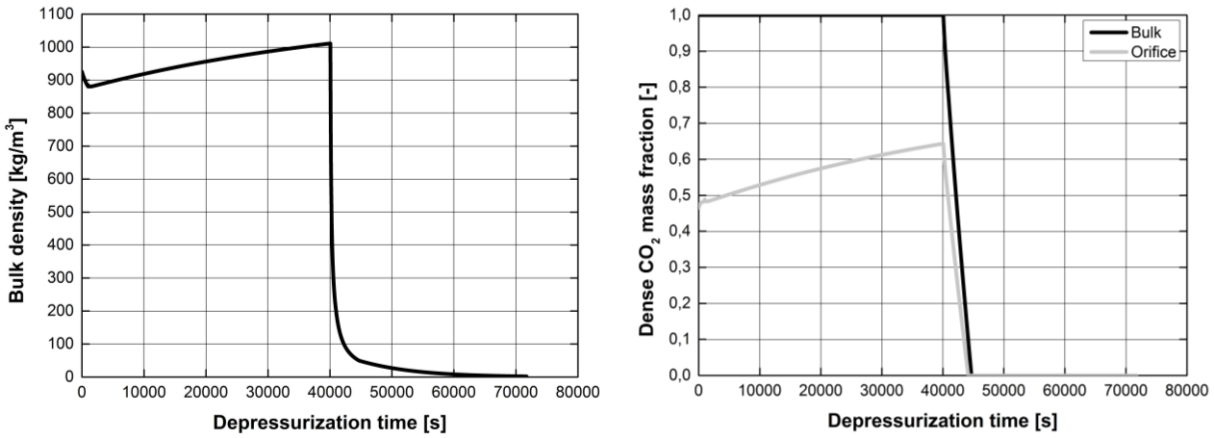

(a) *(b)*

Figure 8.6. *a- bulk density time evolution; b- dense CO_2 mass fraction time evolution.*

Total discharge time	17.6 h
Time to complete bulk boiling	9 h (51%)
Average mass flow rate during bulk boiling	3.6 kg/s
Occurrence of solid phase	no
Average expansion degree of reversibility χ	0.77
Minimum bulk temperature	-0.4 °C
Total average computational runtime	26 min

8.3.4 5000 m, large rupture

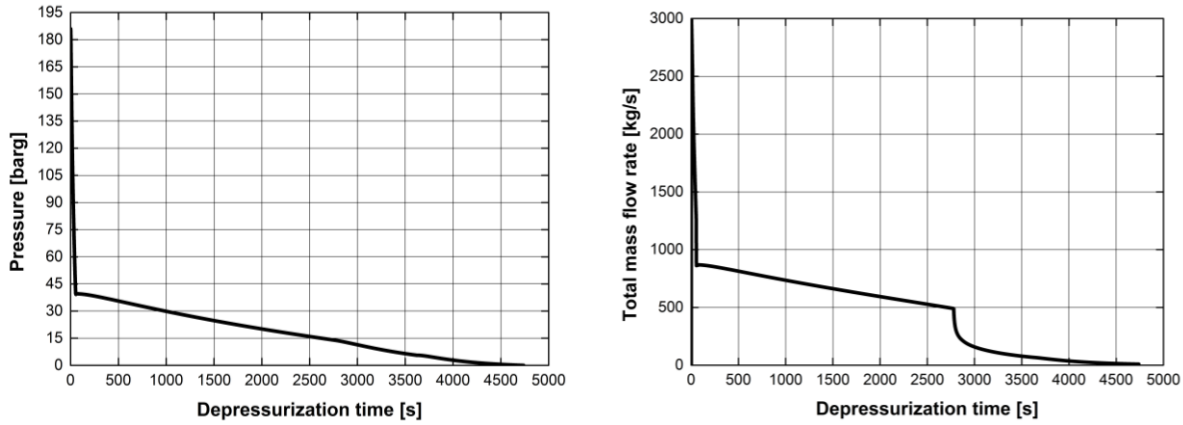

(a) *(b)*

Figure 8.7. *a- pressure time evolution; b- total released mass flow rate time evolution.*

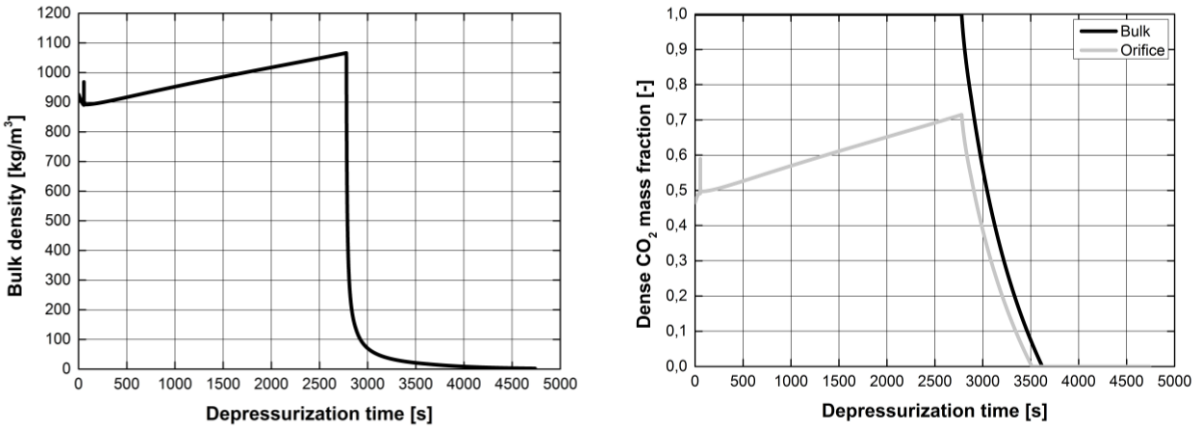

(a) *(b)*

Figure 8.8. *a- bulk density time evolution; b- dense CO_2 mass fraction time evolution.*

Total discharge time	1.5 h
Time to complete bulk boiling	1 h (67 %)
Average mass flow rate during bulk boiling	39 kg/s
Occurrence of solid phase	no
Average expansion degree of reversibility χ	0.81
Minimum bulk temperature	-54.2 °C
Total average computational runtime	25 min

8.4 Simulations results. Canyon Reef Carriers pipeline, U.S.A.

8.4.1 1000 m, small rupture

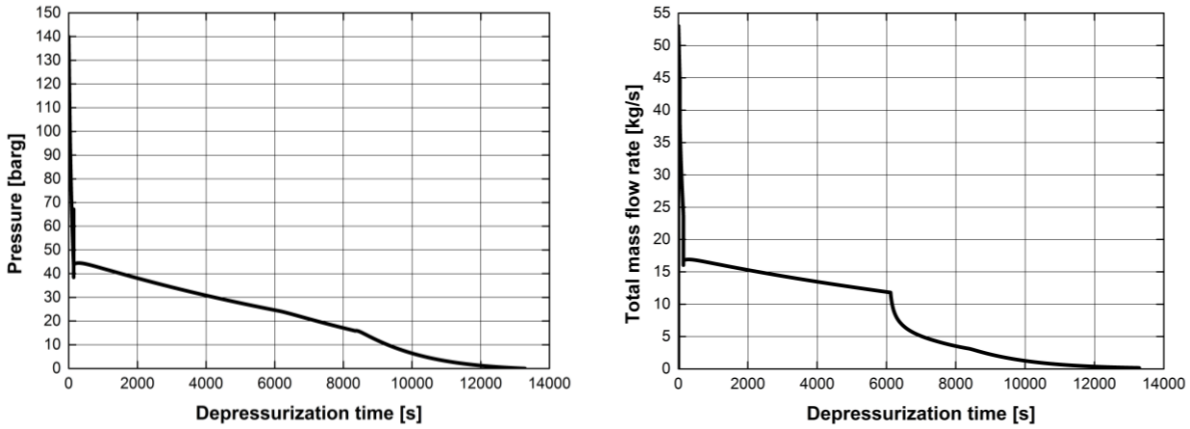

(a) *(b)*

Figure 8.9. *a- pressure time evolution; b- total released mass flow rate time evolution.*

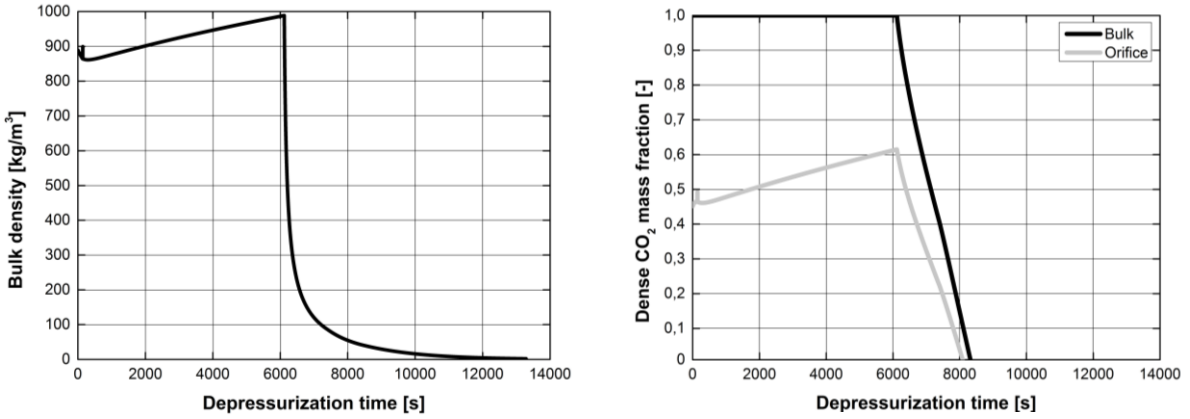

(a) *(b)*

Figure 8.10. *a- bulk density time evolution; b- dense CO_2 mass fraction time evolution.*

Total discharge time	3.4 h
Time to complete bulk boiling	2.3 h (6%)
Average mass flow rate during bulk boiling	12.2 kg/s
Occurrence of solid phase	no
Average expansion degree of reversibility χ	0.73
Minimum bulk temperature	-24.4 °C
Total average computational runtime	16 min

8.4.2 1000 m, large rupture

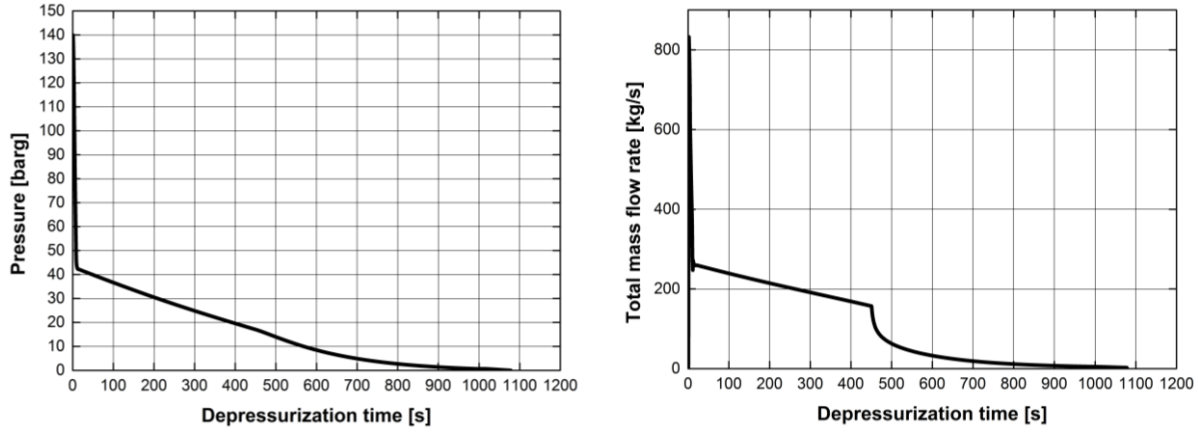

(a) *(b)*

Figure 8.11. *a- pressure time evolution; b- total released mass flow rate time evolution.*

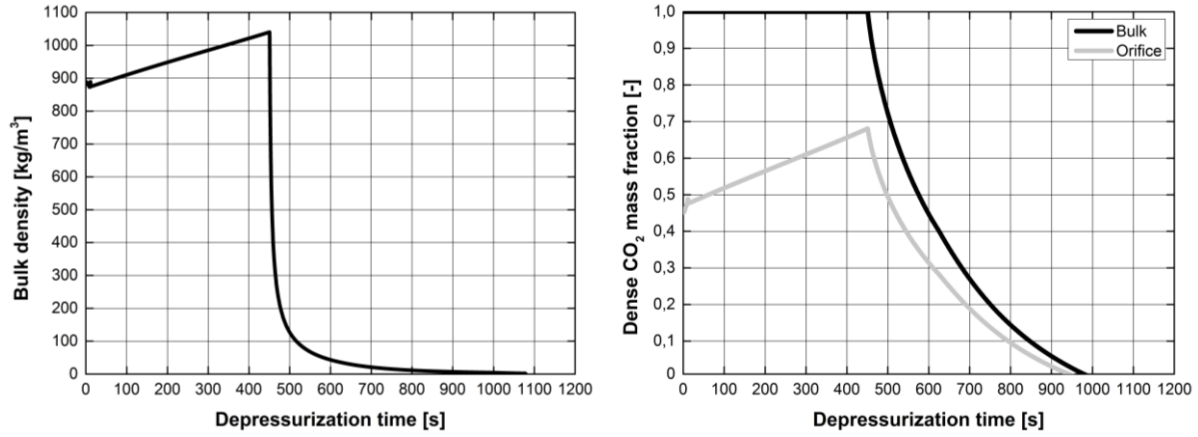

(a) *(b)*

Figure 8.12. *a- bulk density time evolution; b- dense CO_2 mass fraction time evolution.*

Total discharge time	0.3 h
Time to complete bulk boiling	0.28 h (94%)
Average mass flow rate during bulk boiling	111.4 kg/s
Occurrence of solid phase	yes (bulk and orifice), after 0.18 h
Average expansion degree of reversibility χ	0.85
Minimum bulk temperature	-81.1 °C
Total average computational runtime	15 min

8.4.3 5000 m, small rupture

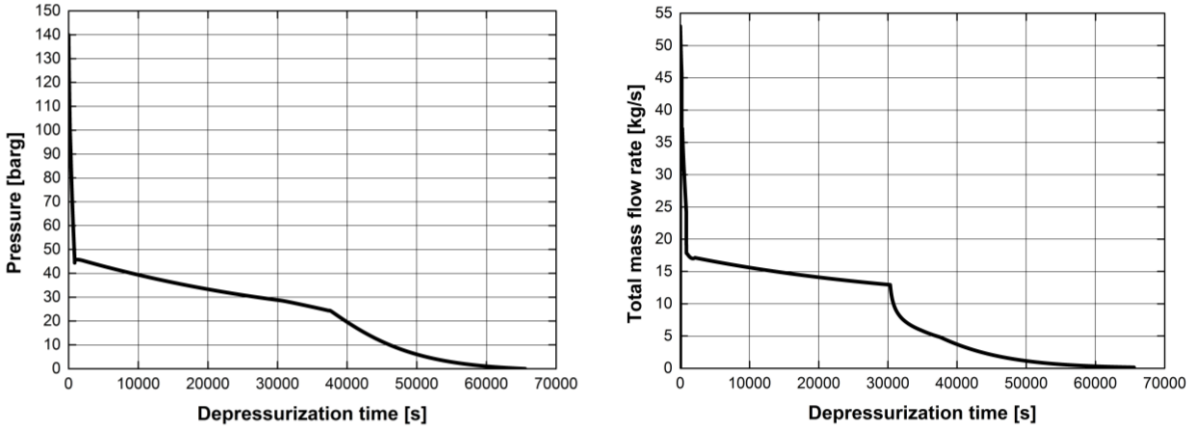

(a) *(b)*

Figure 8.13. *a- pressure time evolution; b- total released mass flow rate time evolution.*

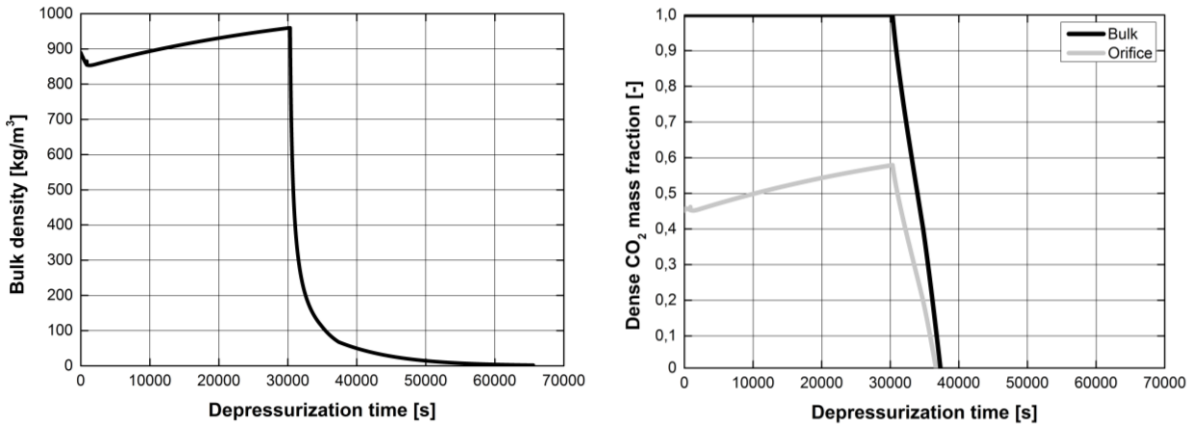

(a) *(b)*

Figure 8.14. *a- bulk density time evolution; b- dense CO_2 mass fraction time evolution.*

Total discharge time	18.2 h
Time to complete bulk boiling	10.4 h (57%)
Average mass flow rate during bulk boiling	13.8 kg/s
Occurrence of solid phase	no
Average expansion degree of reversibility χ	0.75
Minimum bulk temperature	-11.0 °C
Total average computational runtime	31 min

8.4.4 5000 m, large rupture

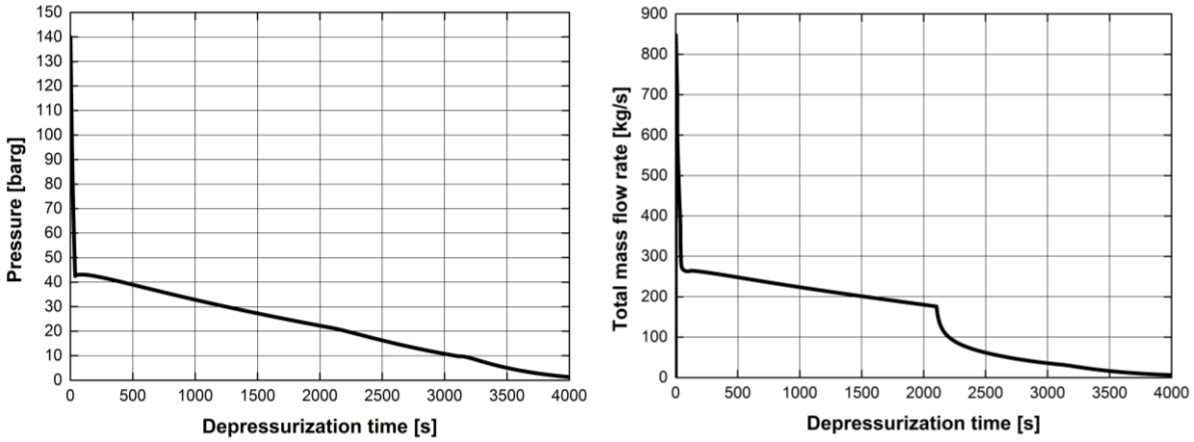

(a) *(b)*

Figure 8.15. *a- pressure time evolution; b- total released mass flow rate time evolution.*

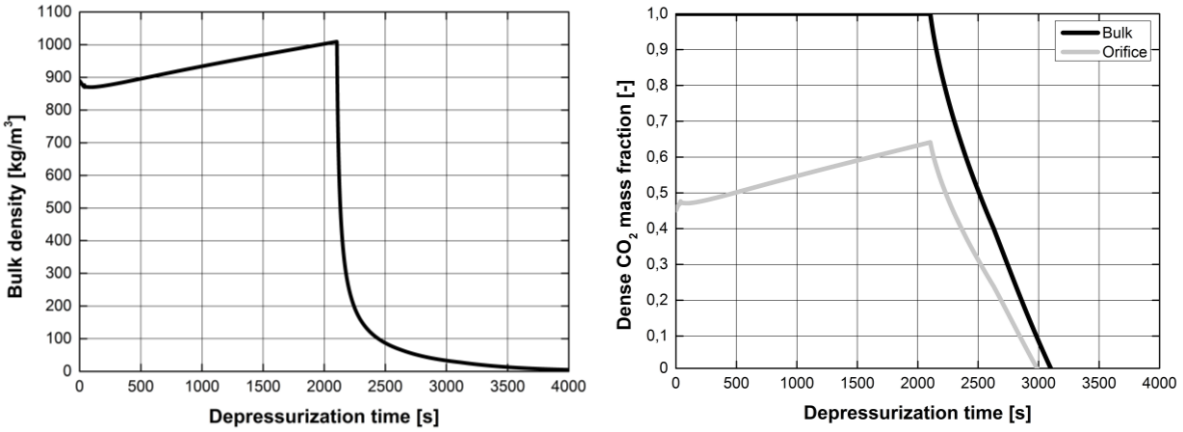

(a) *(b)*

Figure 8.16. *a- bulk density time evolution; b- dense CO_2 mass fraction time evolution.*

Total discharge time	1.1 h
Time to complete bulk boiling	0.87 h (79%)
Average mass flow rate during bulk boiling	173.8 kg/s
Occurrence of solid phase	no
Average expansion degree of reversibility χ	0.84
Minimum bulk temperature	-38.4 °C
Total average computational runtime	21 min

8.5 Simulations results. Snøhvit pipeline, NORWAY

8.5.1 1000 m, small rupture

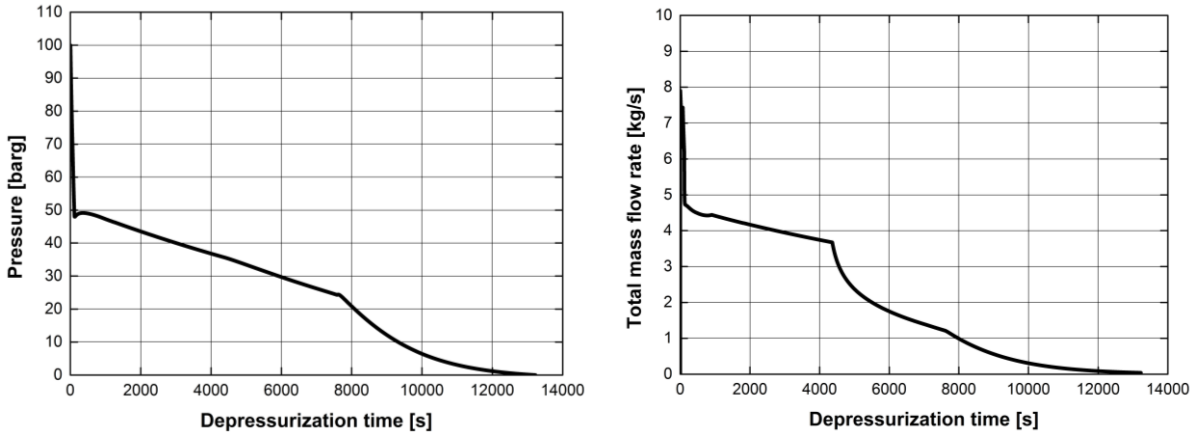

(a) *(b)*

Figure 8.17. *a- pressure time evolution; b- total released mass flow rate time evolution.*

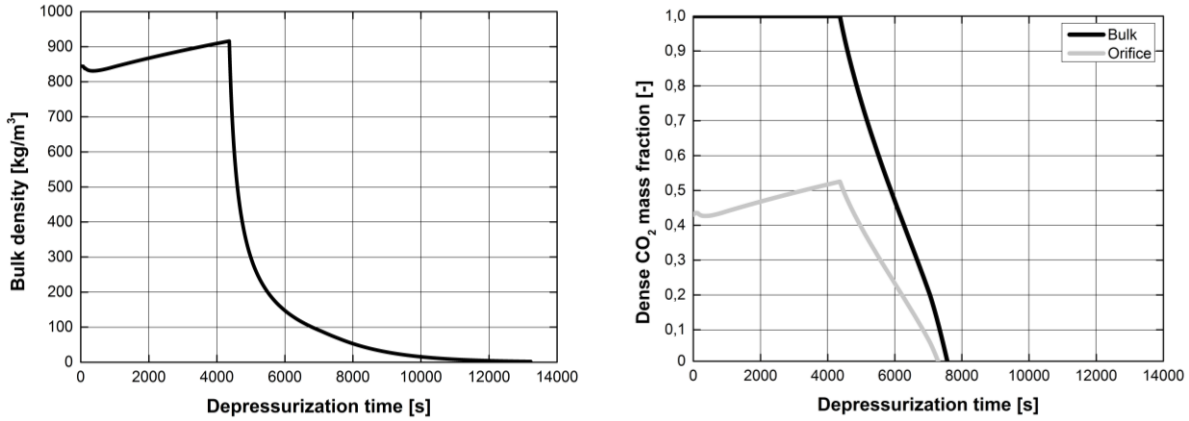

(a) *(b)*

Figure 8.18. *a- bulk density time evolution; b- dense CO_2 mass fraction time evolution.*

Total discharge time	3.7 h
Time to complete bulk boiling	2.1 h (57%)
Average mass flow rate during bulk boiling	3.2 kg/s
Occurrence of solid phase	no
Average expansion degree of reversibility χ	0.71
Minimum bulk temperature	-11.2 °C
Total average computational runtime	21 min

8.5.2 1000 m, large rupture

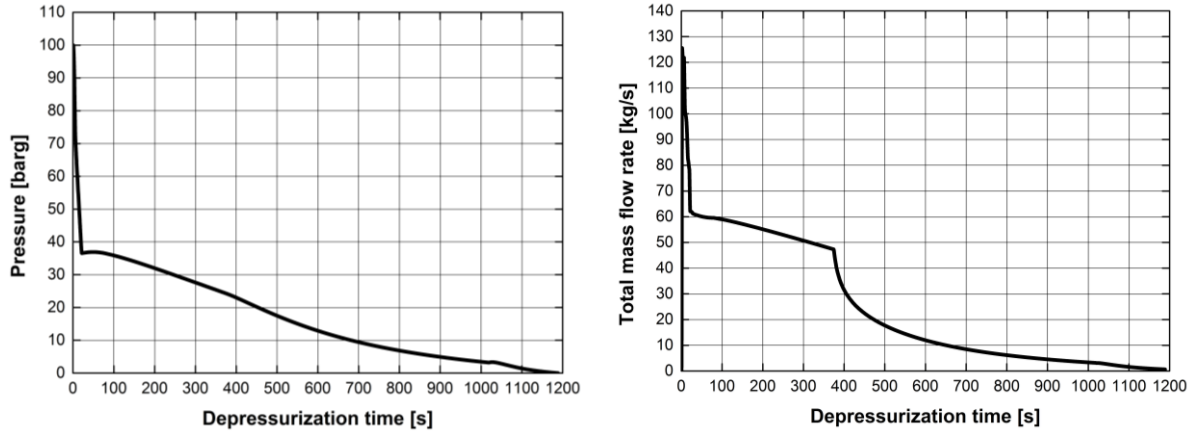

(a) *(b)*

Figure 8.19. *a- pressure time evolution; b- total released mass flow rate time evolution.*

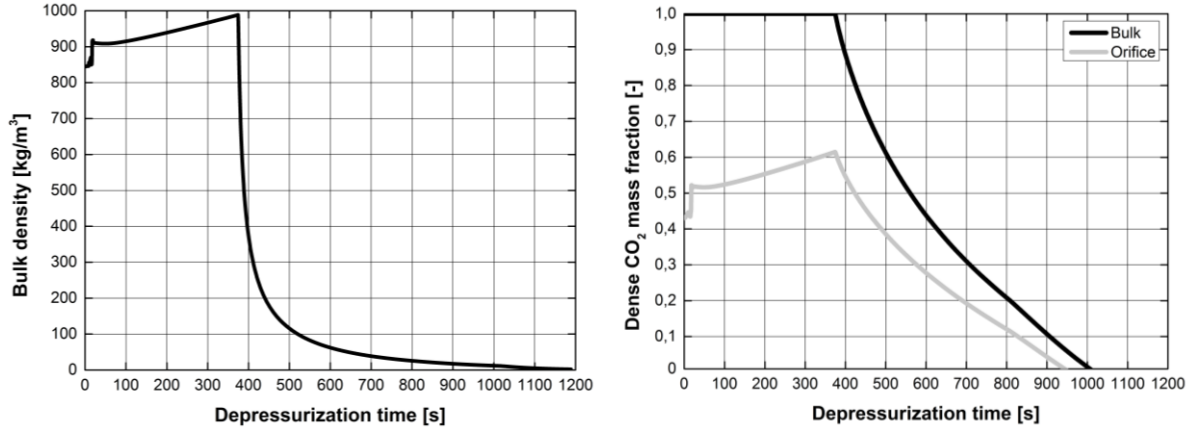

(a) *(b)*

Figure 8.20. *a- bulk density time evolution; b- dense CO_2 mass fraction time evolution.*

Total discharge time	0.3 h
Time to complete bulk boiling	0.28 h (94%)
Average mass flow rate during bulk boiling	28.2 kg/s
Occurrence of solid phase	yes (bulk and orifice), after 0.23 h
Average expansion degree of reversibility χ	0.86
Minimum bulk temperature	-60.2 °C
Total average computational runtime	15 min

8.5.3 5000 m, small rupture

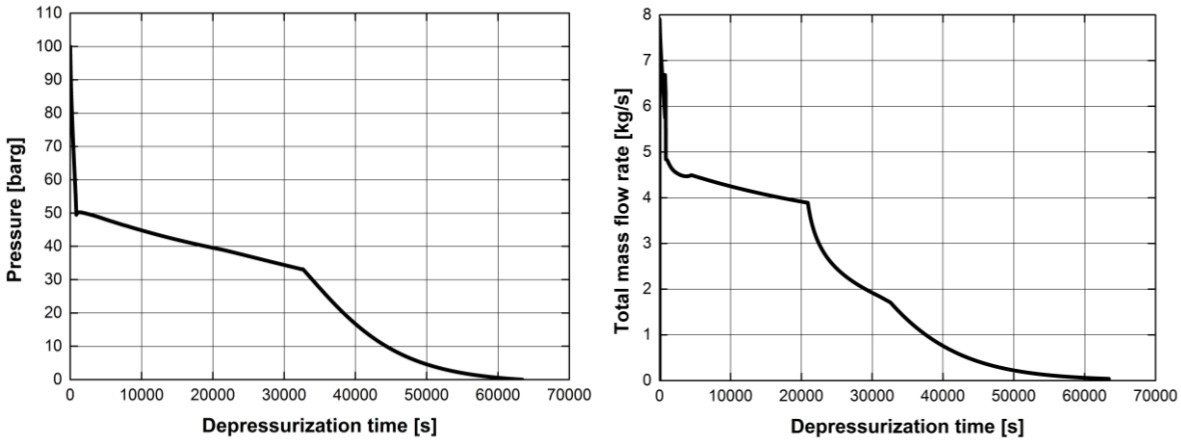

(a) *(b)*

Figure 8.21. *a- pressure time evolution; b- total released mass flow rate time evolution.*

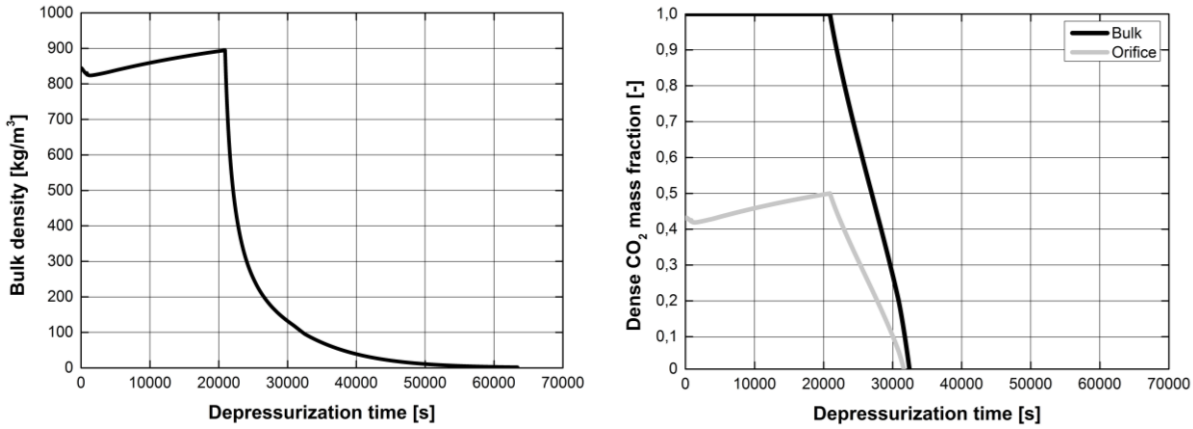

(a) *(b)*

Figure 8.22. *a- bulk density time evolution; b- dense CO_2 mass fraction time evolution.*

Total discharge time	17.6 h
Time to complete bulk boiling	9.0 h (51%)
Average mass flow rate during bulk boiling	3.6 kg/s
Occurrence of solid phase	no
Average expansion degree of reversibility χ	0.77
Minimum bulk temperature	-0.5 °C
Total average computational runtime	31 min

8.5.4 5000 m, large rupture

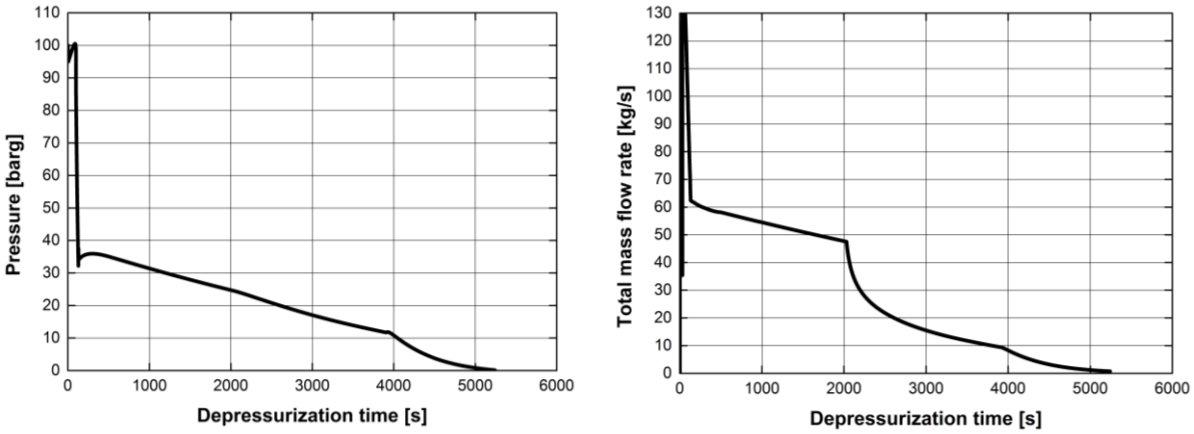

(a) *(b)*

Figure 8.23. *a- pressure time evolution; b- total released mass flow rate time evolution.*

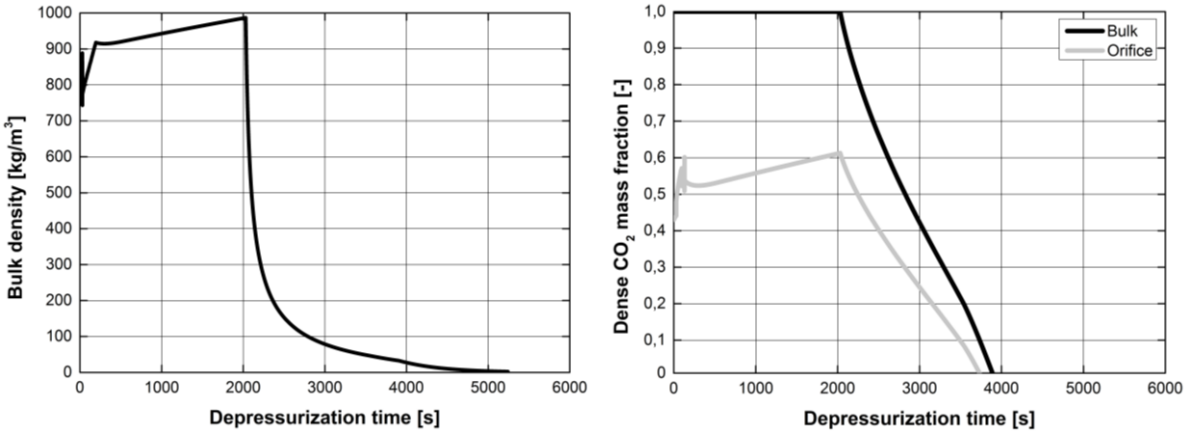

(a) *(b)*

Figure 8.24. *a- bulk density time evolution; b- dense CO_2 mass fraction time evolution.*

Total discharge time	1.5 h
Time to complete bulk boiling	1.09 h (73%)
Average mass flow rate during bulk boiling	38.4 kg/s
Occurrence of solid phase	no
Average expansion degree of reversibility χ	0.82
Minimum bulk temperature	-32.8 °C
Total average computational runtime	27 min

Conclusions

The deployment of CO_2 handling infrastructures for Carbon Sequestration and Enhanced Oil Recovery purposes may determine hazards that are mainly linked to the asphyxiating nature of this substance. The transportation step, that is performed via dedicated large pressurized pipeline networks, is one of the most critical in what concerning risks.

Unlike more established processes and techniques, the QRA procedures applied to the CCS and the EOR chains reveals knowledge gaps leading to significant inaccuracies.

Gaps are related to the unavailability of reliable and comprehensive models able to describe the release evolution from pressurized domains. In fact, the peculiar CO_2 thermodynamic behavior, invoking even all three aggregation states (gaseous, liquid and solid), usually invalidates traditional available models. In addition, the lack of specific experimental data makes it difficult to have tools to drive any model development.

In view of the above, an experimental investigation and the development of a comprehensive depressurization model have been carried out.

The self-collected experimental data has allowed for the investigation of the pressure and the temperature dynamics during a rapid depressurization as well as the variation of the total discharge time with respect to the initial charging conditions. Charging pressures up to 70 barg have been investigated.

Results show specific thermal dynamics that are resulting from two competitive mechanisms: the mechanically-induced cooling and the heat transfer processes with the solid walls. Depending on the initial conditions, the relative magnitude changes leading to minimum temperatures inside the vessel not matching neither an isenthalpic nor an isentropic expansion. Detailed investigations show also that the pressure profiles experience slope variations once the dense CO_2 phase occurs inside the vessel thus giving rise to phase-change mechanisms. Alterations are also observed with respect to the discharge mass flow rate and therefore the total discharge time.

The laboratory-scale experimental investigation has allowed for the collection of specific parameters like the discharge coefficient and details on the expansion thermodynamic nature that have been used to close the proposed model checking its results against the experimental data.

The model development has moved from the detailed analysis of the CO_2 once subjected to large pressure gradients. The theoretical investigation has highlighted the occurrence of multiple choked flow conditions, each pertaining the vapor-liquid and the vapor-solid

mixtures that need to be implemented in the model structure. Then, a thermodynamic approach has pointed out the operative conditions leading to multi-phase releases showing that even at moderate pressures (P > 40 barg) and under gaseous charges, liquid and solid CO_2 may be expected especially with isentropic processes. It should be noted that in QRA's procedure, the occurrence of the solid phase is considered as an extremely unlikely scenario thus giving rise to unacceptable inaccuracies.

The proposed comprehensive model is based on a set of conservation equations, thermodynamic relations, heat-transfer and phase-change constitutive relations as well as on robust equations of state covering all the CO_2 aggregation states. The selected numerical approach allows for the check of the choked flow conditions establishment and the collection of all the main parameters and profiles needed for the QRA purposes.

The test against the experimental data reveals a good qualitative and quantitative agreement especially with respect to the pressure profiles. The results extension shows that the initial charging pressure plays a key role in determining the whole depressurization path especially in the dimensionless time $0.1 < t* < 0.5$. At the same time, differences in the thermal dynamics are observed with transformations whose reversibility index ranges between 0.25 and 0.80.

The model extension procedure has allowed for the analysis of the domain size and the operative conditions incidence on the main release parameters. Results show that the orifice size affects not only the minimum recorded temperature in the bulk but also the depressurization path inside the VLE and SVE dome that is followed by a decrease in the reversibility content with larger discharge orifices. This has been observed for CO_2 pipelines operated at $P < 50$ barg. In addition, at such low pressures, the influence of warmer walls on the expansion development and nature cannot be neglected. At the same time, a detailed analysis gives reason to state that for charging pressures higher than 40 barg, the appearance of the dense phase inside the vessel is almost always expected. Whenever it occurs, a mixed influence of the orifice size and the charging conditions leads to an alteration of the thermal dynamics, the phase transition occurrence and the instantaneous mixture quality and density. This results in a whole discharge dynamic mainly governed by two competitive mechanisms: the bulk boiling/sublimation mechanisms and the actual mass discharge due to the pressure gradients. Because of this, a final peculiar and recurring depressurization profile is achieved with different slope changes linked to the passage in VLE and across the triple point to the SVE domain.

Further analysis show that final expected solid contents, depending on the initial pressure and the orifice size, may amount up to 45 % by mass especially in the operative pressure range

from 60 to 150 barg. It has also been observed that in larger pipelines the bulk isothermal hypothesis may apply under the condition $L/D > 60000$ or in smaller domains but with $d/D < 0.2$. Wall effects on the thermal dynamic determination are negligible for $P < 45$ barg, $L < 1500$ m, $D > 450$ mm and $d/D > 0.32$. At the same time, pipelines charged with dense CO_2 experience modifications in some specific phase-change-related parameter depending again on the operative pressure and the orifice size. For example, the transformation to saturated conditions is affected by both and it is never matching an isentropic path. The resulting peculiar mass flow rate time evolution shows more last boiling mechanisms with large ruptures. The latter are responsible for thermal dynamic variations leading to more pronounced cooling effects that result in lower bulk CO_2 temperatures. In this sense, the strong dependence of the total release time on the initial temperature (variations up to 30 %) has emerged but only for long pipelines subjected to small ruptures and that are operated at $P < 80$ barg.

Model predictions in what concerning the alterations induced by a variation in the pipeline length and internal diameter show that longer pipelines experience brief boiling steps while an increase in the pipeline diameter enhances the dense content at the orifice. In these situations, the minimum expected bulk temperature is matching the complete depletion of the bulk liquid phase and ranges between -89 and -80 °C. Lower observed temperatures with respect to atmospheric levels are due to latent heat-related effects and are also confirmed in available large-scale data.

The solid formation in the pipeline bulk and/or at the orifice plane is not negligible for $L <$ 1500 m, $d/D > 0.3$ and $P > 55$ barg thus disproving usually adopted QRA hypothesis in CCS and EOR hazard investigation.

Finally, the model completion with non-equilibrium features has underlined that this approach can be omitted in extremely short pipelines ($L <$ 500-800 m) operated at low pressure ($P <$ 60-80 barg) but subjected to small ruptures ($d/D <$ 0.1-0.15). In all other cases, non-equilibrium effects determine large differences in the expected mixture quality and post-expanded temperatures resulting in vapor-richer mixtures that are linked to longer release times (up to +45 %).

To conclude, this work has allowed for the development of a comprehensive model to be used in QRA's studies applied to CO_2-handling infrastructures. Some of the existing knowledge gaps have been filled making available a complete and reliable model. Its well-balanced compromise between the degree of detail and the requested computational burden makes it suitable to be used both in planning and in emergency situations without relying on inaccurate or even more sophisticated and time-demanding models.

Nomenclature

Chapter 2

A	Helmholtz free energy (J)
A^{IG}	Helmholtz free energy ideal-gas contribution (J)
A^{R}	Helmholtz free energy residual contribution (J)
A_i, P^i, b_{ij}	SWEoS polynomial coefficients
a, b, c, d, q, r	YEoS parameters
a, b, ε	PREoS terms
a_r, b_r, c_r, d_r	(2.19) constants
k_1, k_2	(2.23) parameters
N_i	i-component total number of moles (mol)
P	Pressure (Pa)
P_c	Critical point pressure (Pa)
R	Universal gas constant (J/(mol K))
S	Total system entropy (J/kg)
T	Temperature (K)
T_c	Critical point temperature (K)
T_r	Reduced temperature (-)
U	Total system energy (J)
V	Total system volume (m^3)
v	Specific volume (m^3/kg)
v_r	Reduced specific volume (-)
Z_c	Critical compressibility factor (-)
μ_j	j-component electrochemical potential (J/mol)
ρ	Density (kg/ m^3)
ρ_r	Reduced density (-)
φ	Acentric factor (-)

Chapter 3

a_i	(3.84) parameters
c	Speed of sound (m/s)

C_P	Specific heat at constant pressure (J/(kg K))
C_P^0	Specific heat at constant pressure in the ideal-gas state (J/(kg K))
dQ_{irr}	Irreversible heat flow contribution to (3.73)
e	Specific energy (J)
e_0	Initial specific energy magnitude (J)
e^t	Total internal energy (J/kg)
$\boldsymbol{g}$	Gravity acceleration vector
G	Mass flux (kg/(m^2 s))
G_{choked}	Mass flux at choked conditions (kg/(m^2 s))
h	Specific enthalpy (J/kg)
h^t	Total specific enthalpy (J/kg)
h_0	Stagnation specific enthalpy (J/kg)
h_m	Mixture specific enthalpy (J/kg)
m	System mass (kg)
$\dot{m}_n$	mass flow rate across the system borders (kg/s)
$\hat{\boldsymbol{n}}$	Normal versor
$\dot{Q}$	Heat flow rate (J/s)
P	Pressure (Pa)
P_{amb}	Ambient pressure (Pa)
P_{choked}	Pressure at choked conditions (Pa)
P_{tp}	Triple-point pressure (Pa)
s	Specific entropy (J/kg)
s_m	Mixture specific entropy (J/(kg K))
T	Temperature (K)
T_{tr}	Triple point temperature (K)
T_{iso-s}	(3.87) dummy integration variable (K)
u	Velocity (m/s)
$\boldsymbol{u}$	Velocity vector
U	Total system internal energy (J)
$\widehat{U}$	Specific system internal energy (J)
u_{l-v}	Liquid-vapor mixture velocity (m/s)
u_{s-v}	Solid-vapor mixture velocity (m/s)
u_{s-l-v}	Mixture velocity at the triple point condition (m/s)
u_0	Initial velocity magnitude (m/s)
V	Specific volume (m^3/kg)

v_m	Mixture specific volume (m^3/kg)
$\dot{W}_s$	Shaft work per unit time (J/s)
x_i	i-component mass fraction
Z	Compressibility factor (-)
α	(3.34) constant
γ	Generic potential energy
δ, ϑ	(3.96) variables
μ_{JT}	Joule-Thomson coefficient (K/Pa)
ρ_0	Initial density magnitude (kg/ m^3)
φ	System potential energy (J)

Chapter 4

a_i, N, n	(4.2) coefficients
f	Friction factor (-)
P^{exp}	Experimental pressure value (bar)
Re	Reynolds number (-)
S_1	Stagnation transversal section (m^2)
S_2	Orifice transversal section (m^2)
T^{exp}	Experimental temperature value (°C or K)
x	Measurement distance (m)
y	(4.2) observed value
ΔP	Pressure loss (Pa)
ΔT	(4.1) temperature difference (°C)
γ_d	Discharge coefficient
ρ_1	Density at stagnation conditions (kg/m^3)
ρ_2	Density at orifice conditions (kg/m^3)

Chapter 5

A	Generic transversal section (m^2)
$A_{int,v}$	Internal vessel surface area (m^2)
$A_{i,END}$	End caps vessel exposed surface (m^2)

$\widetilde{c_v}$	Constant-volume specific heat (J/(kg K))
C_w	Wall heat capacity (J/K)
G	Mass flux (kg/(m^2 s))
G_{choked}	Mass flux at choked conditions (kg/(m^2 s))
Gr	Grashof number (-)
h	Specific enthalpy (J/kg)
$h_{i,END}$	Heat transfer coefficients related to $A_{i,END}$ (W(m^2 K))
L_D	Domed-vessel characteristic length (m)
L_{ev}	Vaporization latent heat (J/kg)
m_V	Vapor mass (kg)
m_L	Liquid mass (kg)
m_S	Solid mass (kg)
$\dot{m}_0$	CO_2 mass flux (kg/(m^2 s))
Nu	Nusselt number (-)
P_0	Vessel pressure (Pa)
PM	CO_2 molecular weight (g/mol)
Pr	Prandtl number (-)
$\dot{q}_v$	Heat flux at the vessel wall (J/(s m^2))
Ra	Rayleigh number (-)
T_0	Internal vessel temperature (K)
T_V	Vapor temperature (K)
T_w	Internal wall temperature (K)
u	Velocity (m/s)
$\widetilde{u_0}$	Specific internal energy (J/kg)
u_{conv}	Convection-driven processes characteristic velocity
u_{sold}	Solidification-driven processes characteristic velocity
U_i	Overall heat transfer coefficient (W(m^2 K))
β	(5.45) gaseous volume fraction (-)
γ	Heat capacities ratio (-)
γ_d	Discharge coefficient
ϑ, γ	(5.36) parameters
ξ_i	(5.48) Lagrange-based polynomial parameters
ρ_0	CO_2 density inside the vessel (kg/m^3)
ρ_w	Wall density (kg/m^3)

$\rho_{L,ev}$	Evaporated liquid density (kg/m^3)
σ	Surface tension (N/m)
χ	Reversibility coefficient (-)
φ	(5.11) parameter

Chapter 6

I_L	(6.1) integrated variable
L	Pipeline length (m)
$\dot{m_{out}}$	Mass flow (kg/s)
P	Pressure (Pa)
P_0, P_L	Pressure values at boundary conditions (Pa)
u	Velocity (m/s)
ΔH_{comb}	Combustion heat (J/kg)
ϑ	Radiated heat fraction (-)
τ_{atm}	Atmospheric transmissivity (-)
ω	(6.1) parameter

Chapter 7

$c_{p,l}$	Liquid specific heat (J/(kg K))
$c_{p,s}$	Solid specific heat (J/(kg K))
g	Gibbs' free energy (J/kg)
J	Nuclei formation rate (1/s)
k	Pre-exponential factor
k_B	Boltzmann's constant (m^2 kg/(s^2 K))
L_v	Vaporization latent heat (J/kg)
L_s	Sublimation latent heat (J/kg)
P	Pressure (Pa)
P_c	Critical pressure (Pa)
P_0	Isentropic pressure (Pa)
T	Temperature (K)
T_{tp}	Triple point temperature (K)
$v_{g,sat}$	Gaseous CO_2 specific volume at saturated conditions (m^3/kg)

x	Vapor mass fraction (-)
$\bar{x}$	Equilibrium vapor mass fraction (-)
x_l	Liquid fraction (-)
α_1, α_2	(7.2) constants
ΔG_c	Formation free energy (J)
ΔS_{nucl}	Nucleation entropy variation (J/kg)
ΔT	Superheating degree (K)
Δw	Bubble formation work (J)
Λ	Vapor generation rate (kg/s)
Θ	Probability of a state-occurrence (-)
ρ_v	Vapor density (kg/m^3)
σ	Surface tension (N/m)
τ_{rel}	Characteristic relaxation time (s)
τ_{vib}	Characteristic vibrational time (s)